Energy Storage & Conversion : Waste Heat Recovery in Microgrids by a free piston stirling engine

Mahdi Majidniya

Thèse

Présentée à

Université de Lorraine

École doctorale SIMPPÉ: Sciences et Ingénierie des Molécules des Produits des Procédés et de l'Énergie

par

Mahdi MAJIDNIYA

pour obtenir

le grade de Docteur

Spécialité "Énergie et Mécanique"

ENERGY STORAGE & CONVERSION: WASTE HEAT RECOVERY IN MICROGRIDS BY A FREE PISTON STIRLING ENGINE

Soutenance le 2 Décembre 2021

Composition de la commission d'examen :

Président :	M. Fei GAO,	Professeur, Université de Technologie de Belfort Montbéliard (FEMTO-ST)
Rapporteurs :	M. François LANZETTA,	Professeur, Université de Franche-Comté (FEMTO-ST)
	Mme. Lavinia GROSU,	MCF-HDR, Université Paris Nanterre (LEME)
Examinateurs :	M. Babak NAHID-MOBARAKEH,	Professeur, McMaster University (MARC)
	Mme. Christelle PERILHON,	MCF-HDR, Conservatoire national des arts et métiers (Lifse)
	M. Abdelhamid KHEIRI,	MCF-HDR, Université de Lorraine (LEMTA)
Directeur :	M. Benjamin REMY,	Professeur, Université de Lorraine (LEMTA)
Co-directeur :	M. Thierry BOILEAU,	MCF, Université de Lorraine (LEMTA)
Invité :	M. Majid ZANDI,	Associate Professor, Shahid Beheshti University (REDSBU)

A côté de la difficulté est, certes, une facilité !

SUMMARY

In this study, a combined system of an FPSE and a PMLSM is investigated. First, a linear model (an already developed model in literature) and a nonlinear model (a new applied model in the present study) of the FPSE are developed, and the results of these models are compared. Then the most suitable model for the study, is chosen. It is shown that the linear model cannot identify the realistic behavior of the FPSE; thus, the nonlinear one should be used. After that, the nonlinear FPSE model is validated with available experimental results. After validating the FPSE model, two scenarios, including a decoupled one (an already existed one in literature) and a coupled one (a newly introduced method in the present study), are considered to study the enthalpy pumping loss on the FPSE system. Then the best scenario for the enthalpy pumping, which is the coupled one, is chosen based on the results. After that, the FPSE system is coupled with the presented PMLSM model. In order to combine the thermodynamic model of the FPSE and the electrodynamic model of the PMLSM, their dynamic equations are combined. Then, the thermo-electro-dynamic equations are solved, and the coupled system is controlled in MATLAB Simulink®. Controlling such a system makes it possible to avoid conditions leading to FPSE instability. Moreover, it is feasible to control the system in transient operating modes to get the best performance. After combining FPSE with PMLSM, two control methods are introduced, and their results are compared. These control methods are based on identifying the reference parameters. Then, an application of such a system is presented. This system is used as a waste heat recovery in a tri-generation system. The power source of this tri-generation system is a Solid Oxide Fuel Cell (SOFC) which is combined with a Double Effect Absorption Chiller (DEACH) for cooling production and a heat exchanger for providing the thermal needs. Finally, a study of the sensitivity to the parameters of such a system is performed. Using this analysis provides information concerning the sensitivity of such a system to different parameters.

ACKNOWLEDGEMENTS

Thank you to….

My supervisors, who shaped my scientific life, but not only that…

My thesis committee, who helped me to evaluate and improve my work…

My family, who always supported me. I owe them all the times that was for them, but I put on the thesis…All the times that it did not go well, but they were there…All the times that they prayed for me…

My friends, who helped me to adapt to this new life in this new country…

Thank you all…

Without you, it would not have been possible.

Mahdi Majidniya

December 2021

Nancy-France

CONTENTS

LIST OF TABLES

LIST OF FIGURES

LIST OF ABBREVIATIONS AND ACRONYMS

A	Area, m^2
$a; b; c$	Reaction extents, mol/s
$\underline{A}; \underline{B}; \underline{C}; \underline{D}; \underline{E}$	Constants
B_v	Friction coefficient
C	Clearance, m
C_f	Darcy friction factor
C_p	Heat transfer coefficient at constant pressure, J/(kg.K)
C_v	Heat transfer coefficient at constant volume, J/(kg.K)
d	Diameter, m
F	Force, N
Fr	Faraday constant, 96487 C/mol
h	Convective heat transfer coefficient, $W/(m^2.K)$
H	Enthalpy (J/kg)
i	Current, A; Current density, A/m^2
i_0	Exchange current density, A/m2
i_l	Limiting current density, A/m^2
K	Reaction equilibrium constant
L	Inductance, mH
LHV	Lower Heating Value, J/kg
l	Length, m
$M; m$	Mass, kg

Greek symbols

λ	Specific heat ratio
ΔG	Gibbs free energy changes, J/mol
μ	Dynamic viscosity, Pa.s
η	Efficiency
θ	Angle
Υ	Pre-exponential factor, A/m^2
ρ	Density, kg/m^3
τ	Pole pitch, m
ψ_f	Flux linkage, Wb
ω	Frequency, rad/s

Index and exponent

0	Standard state
$a; b; c; d; q; \alpha; \beta$	Axis
Act	Activation
An	Anode
b	Buffer
c	Compression
Ca	Cathode
$Conc$	Concentration
cy	Cylinder

$\dot{m}$	Mass flow rate, kg/s	D	Displacer
$\dot{n}_j^i$	Molar flow rate of component i in channel j, mol/s	e	Expansion
n_e	Number of electrons	el	Electric
P	Pressure, Pa	em	Electromagnetic
Pr	Prandtl number	eq	Equilibrium
$\dot{Q}$	Heat transfer rate, W	gs	Gas spring
Q_{rxn}	Reaction heat, J	h	Heater
R	Gas constant, Radius, m	k	Cooler
r	Resistance, Ω	Ohm	Ohmic
Re	Reynolds number	P	Power piston
$\overline{\overline{Re}}$	Recirculation ratio	pr	Product
S	Entropy, J/K	R	Regenerator
T	Temperature, K	r	Reforming
u	Velocity, m/s	re	Reactant
U_f	Fuel utilization factor	rev	Reversible
U_{ox}	Air utilization factor	rod	FPSE Rod
V	Volume, m^3	s	Shifting
$\dot{V}$	Volumetric rate, m^3/s	*Abbreviation*	
v	Voltage, V	FPSE	Free Piston Stirling Engine
X^i	Molar concentration of component i	PMLSM	Permanent Magnet Linear Synchronous Machine
x	Displacement, m	IRSOFC	Internal Reforming Solid Oxide Fuel Cell
$\dot{x}$	Velocity, m/s	DEACH	Double Effect Absorption Chiller
Xm	Mass concentration		

$\ddot{x}$ Acceleration, m/s^2

List of Appendices

1 INTRODUCTION

1.1 Background

To date, the most common energy networks, for example, the energy network that exists in France, are based on a centralized supplier-consumer structure. In this structure, always the energy is produced by a centralized supplier and is fed to consumers. Today, with the help of renewable energies, consumers can locally produce their energy. This energy production can disrupt the network function. To solve this problem, the project of Internet Of Energy (IOE) is introduced in UL-ENSEM (Université de Lorraine-L'École Nationale Supérieure d'Électricité et de Mécanique) coupled with the TIE (Territoire Industrie Énergie) scientific chair (LEMTA-CNRS). IOE is moving from the conventional centralized/unidirectional networks to the decentralized/bidirectional ones. The schematic of IOE and its comparison with common energy systems are shown in Figure 1.1.

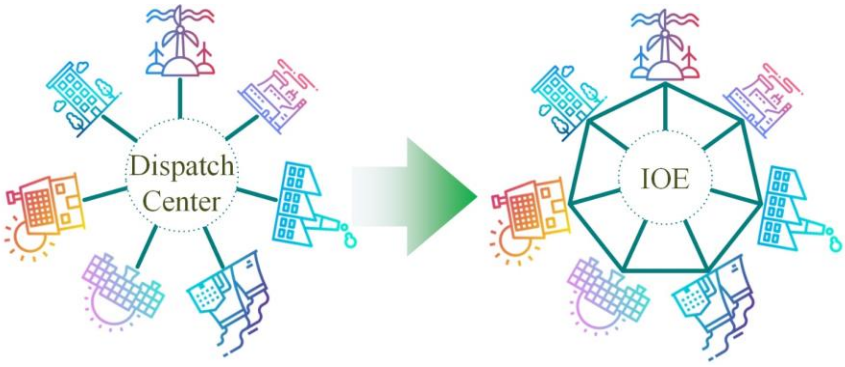

Figure 1.1: Schematic of IOE and common energy network

Through IOE, the connections between consumers with a supplier and also other consumers will be a dynamic/multidirectional one. It means, by an effective control strategy, a consumer through the IOE can feed another consumer to satisfy its demands without disrupting the network function.

IOE concept is a wide/multidisciplinary content that should be divided into different sections. These sections can be identified as energy capture, energy conversion, energy distribution/transportation, energy storage, and control systems. Each section also can be divided into some subsections; for example, the energy conversion section can be divided into system modeling and system optimization subsections. The control section also can be divided into each system control and controlling the integration of the systems/network. Another point is that for each section, different systems/methods can be applied. Also, there are different control and optimization methods that can be used. The systems that are defined in the IOE project and needed to be controlled are shown in Figure 1.2.

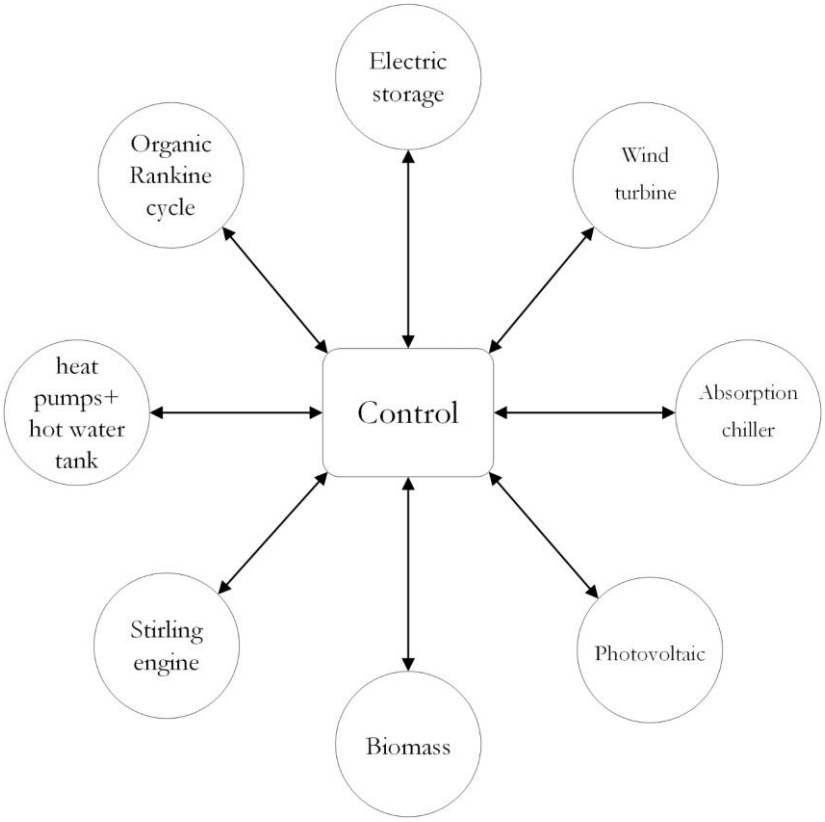

Figure 1.2: IOE control schematic

One crucial point that should be noted is that the working conditions of the systems are dynamic, so the models should be the detailed dynamic ones to be capable of predicting the realistic behavior of the systems/network.

In the present thesis, as a part of the IOE project, the study was done in three sections: energy conversion section, control section, and optimization section.

From the energy conversion point of view, different systems can be studied, including the Stirling engine and Organic Rankine Cycle (ORC). ORC is a closed-loop cycle that compared to conventional steam turbine Rankine cycle has the following advantages [1,2]:

- Compatible with lower temperature heat sources.
- Longer lifetime.
- Less maintenance is required.
- Smaller and cheaper heat exchangers are needed that results in a smaller system.

Stirling engine is also a closed-loop system with the following advantages:

- Silent and practically vibrationless operation [3].
- Minimal pollution. Due to external combustion, the fuel can be burned more sufficiently [4].
- The maximum attainable efficiency compared to heat engines operating between the same temperature difference [3].
- Since it is an external combustion system, the energy source may be of almost any form whatever, so long as it is available at a sufficiently high temperature. Stirling engines can be run on solar energy [5,6], high-temperature fuel cells [7,8], gasification systems [9], combustion systems [10], and also many industries that directly or indirectly deal with thermal energy like steel or chemistry industries [11].
- High reliability [3].
- Mechanical simplicity [3].
- The highest specific work output of any closed regenerative cycle [3]

Since, in comparison with the ORC, Stirling has higher potential efficiency, higher specific work output, higher reliability, and the advantage of mechanical simplicity [3], the focus of the present study will be on this system and its adapted alternator.

From the control point of view, an alternator with a dedicated control system will be introduced for the Stirling engine. Furthermore, from the optimization point of view, the system's performance considering the control parameters will be optimized.

Now, the energy conversion system will be introduced, and the selection of the proposed system will be justified.

1.2 Stirling Engine

As it was already discussed, due to the many advantages of the Stirling engine, it is an interesting option for waste heat recovery or direct transformation of thermal energy to electricity. Especially in the current period due to energy demand increment, a lot of thermal-based systems are developed to produce it. In these methods, a heat source is converted into electricity. This kind of conversion can be divided into two categories: 1- nonrenewable power plants extracting energy from fossil fuels or nuclear fission; 2- renewable power plants such as geothermal or solar power plants. Such systems, less or more, are always accompanied by heat loss. Recovering this waste heat is important for energy efficiency, economic, and environmental points of view. Thus, choosing the right waste heat recovery system is very critical [12]. In the research of such a heat recovery system, many vital parameters should be considered, including efficiency, cost, environmental effect, and reliability. Thus, the Stirling engine can be used as an auxiliary system to recover the waste heat from thermal-based systems or as the primary energy conversion system due to its many advantages.

To have an idea of the Stirling engine cycle, the P-V (Pressure-Volume) and T-S (Temperature-Entropy) diagrams of an ideal Stirling engine are shown in Figure 1.3.

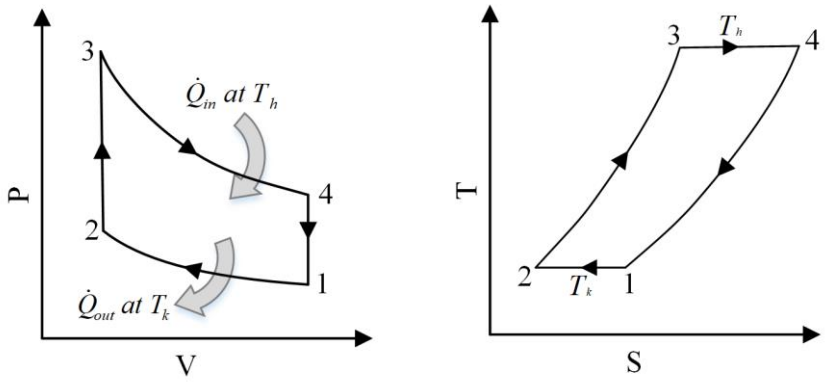

Figure 1.3: P-V and T-S diagrams of an ideal Stirling engine

The 1-2 process is an isothermal compression. During this process, the heat will be removed from the engine at the cold source temperature, which is equal to T_k. The 2-3 process is an isochoric one that the working gas passes through the regenerator. The 3-4 process is an isothermal expansion process. During this process, the heat will be added to the engine at the hot source temperature, which is equal to T_h. The 4-1 process, like 2-3 one, is an isochoric process. During this process, the working gas passes through the regenerator. At this step, the working gas gives heat to the regenerator that will be recovered during the 2-3 process [3]. From the practical point of view, the ideal Stirling cycle cannot be reproduced. First, it is extremely difficult to achieve isothermal working condition with conventional heat exchangers. Then, there are always non-idealities and irreversibilities associated with friction and leakage losses. However, even if the ideal cycle can not be achieved, these systems are still interesting for electricity production [3,8,13].

One of the main applications of Stirling engines is for Combined Heat and Power (CHP) systems [8]. Figure 1.4 shows a 3-kW beta-type Stirling engine built by Thorsen et al. [14] in 1996 at the Technical University of Denmark.

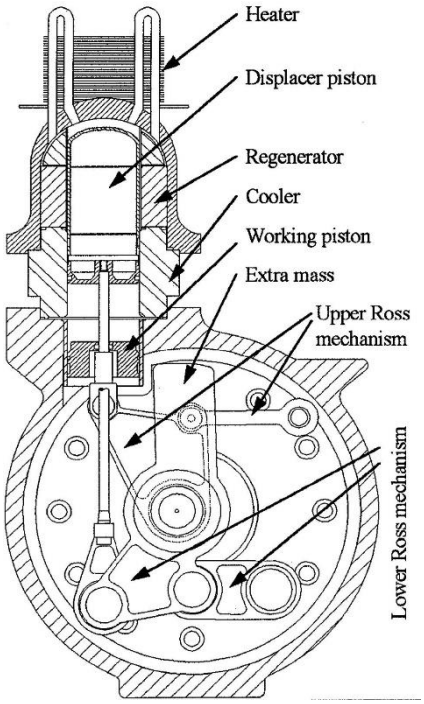

Figure 1.4: The 3-kW Stirling engine developed by Thorsen et al. [14]

The goal of the presented Stirling engine in Figure 1.4 was simultaneous production of electricity and heating for Danish single-family houses. The working gas was helium, and the fuel was natural gas. The electrical efficiency of this system at Helium mean pressure of 8.5 MPa and outlet cooling water temperature of 35°C was 23% [14].

The Technical University of Denmark and its cooperative partners, in 1996, also began to develop and optimize a 35-kW biomass-powered CHP plant [15–17]. This system is shown in Figure 1.5.

Figure 1.5: The 35-kW Stirling engine developed in 1996 [18]

The system, which is shown in Figure 1.5, is based on a four-cylinder double-acting Stirling engine that the cylinders were parallel in a square arrangement. The working gas is Helium with a mean pressure of 4.5 MPa. The electrical efficiency and the combined efficiency of this system were 9.2% and 90.0%, respectively.

Sato et al. [19] also built a wood-powered 55-kW Stirling engine CHP plant and carried out demonstration tests. This system is shown in Figure 1.6.

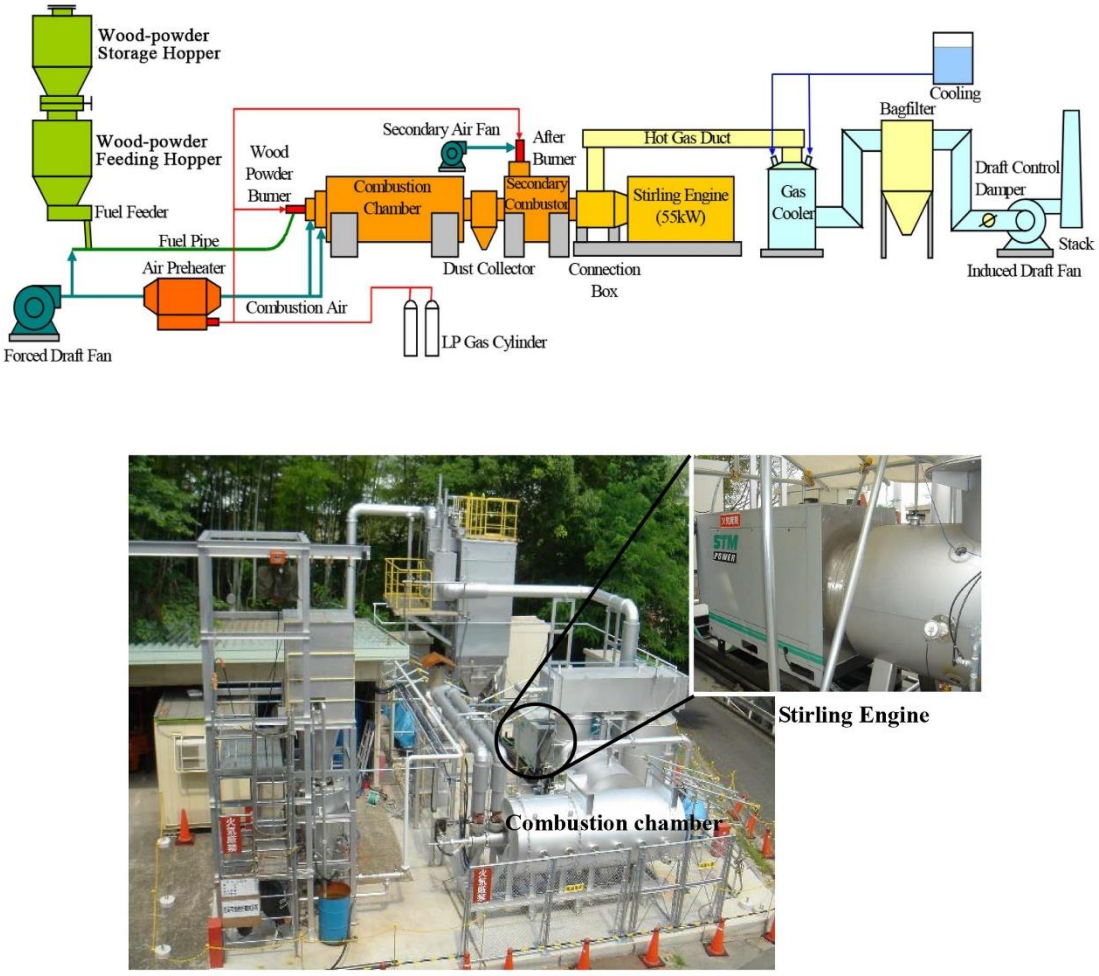

Figure 1.6: The 55 kW wood power fuelled CHP system by Sato et al. [19]

The problem with the wood power-fueled Stirling engine, which is shown in Figure 1.6, was unavoidable ash-fouling problems in SE heater tubes and fins. To avoid this problem, which generally appears while the Stirling engine uses biomass fuel, fluidized-bed was introduced for such systems. A system that used this idea was a Stirling-based CHP unit built by Urciuolo et al. [20]. This system is shown in Figure 1.7.

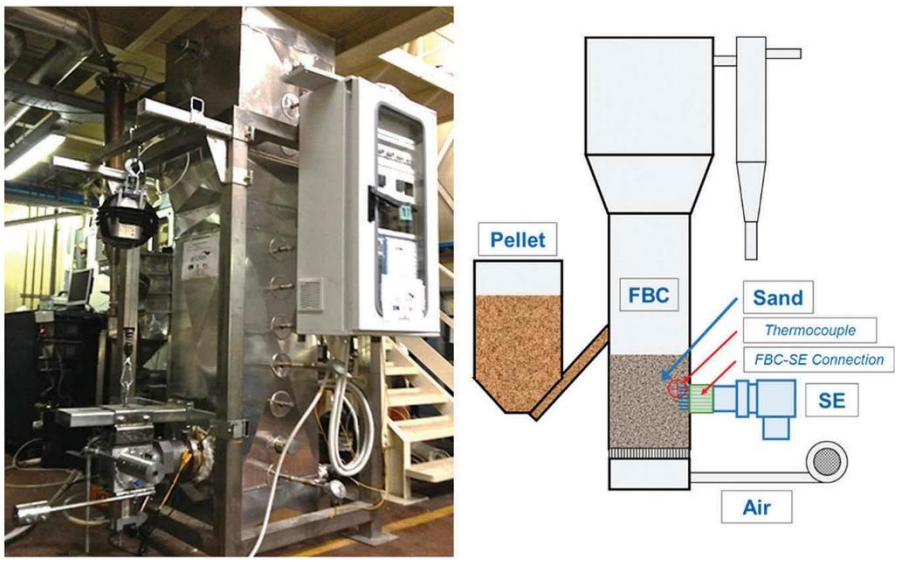

Figure 1.7: The fluidized-bed CHP based system built by Urciuolo et al. [20]

Another similar system based on the fluidized-bed, which was based on the hybrid solar-biomass CHP was introduced by Angrisani et al. [21], which is shown in Figure 1.8.

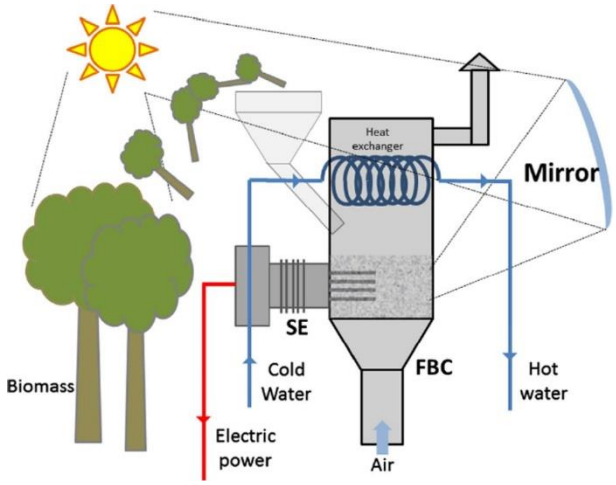

Figure 1.8: Hybrid solar-biomass system proposed by Angrisani et al. [21]

Besides all the experimental setups that were already built and tested, there are also some commercialized micro-CHP systems based on the Stirling engines. The WhisperGen Stirling Mk5 unit built by Whisper Tech, a New Zealand firm, is one of these systems. This system could produce 1 kW of electricity and 13-14 kW of heating [4]. This system is shown in Figure 1.9.

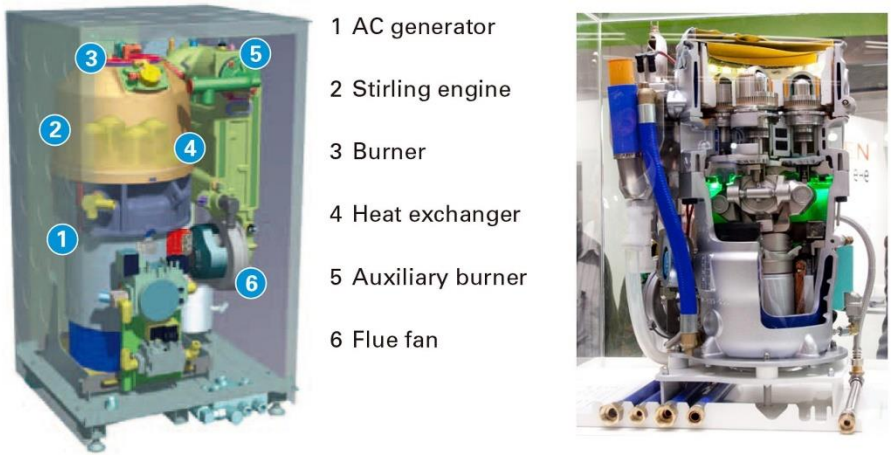

Figure 1.9: The WhisperGen Stirling Mk5 unit [4,22]

Another commercialized system is the SOLO V161 micro-CHP unit by SOLO Stirling GmbH, which is shown in Figure 1.10. This system could work with natural gas or liquefied petroleum gas as fuel. This system could generate 2-9 kW of electricity and 22-30 kW of heating. The electrical and overall CHP efficiencies of this system were 22-24% and more than 90%, respectively [4].

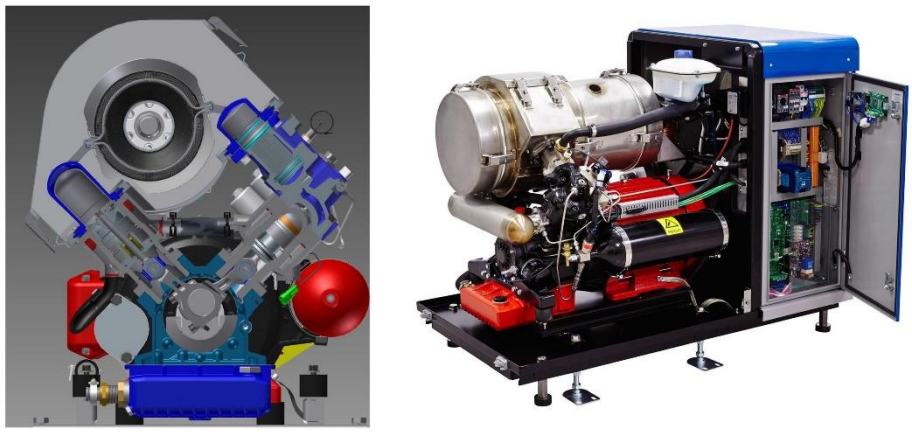

Figure 1.10: The SOLO V161 micro-CHP unit [4,23]

Microgen system, which is developed by the UK company BG Group, is another commercialized Stirling engine micro CHP system. It was expected that several home-appliance manufacturers, including Senertec, Remeha, Brötje, Baxi, and Viessmann to market their micro-CHP units by integrating the Microgen unit [4]. This unit could produce 1.1 kW of electricity and 15-36 kW of heating. The electrical and thermal efficiencies of this system were

13% and 90%, respectively [4]. The micro-CHP Ecogen by Baxi, which is fueled by natural gas, is shown in Figure 1.11.

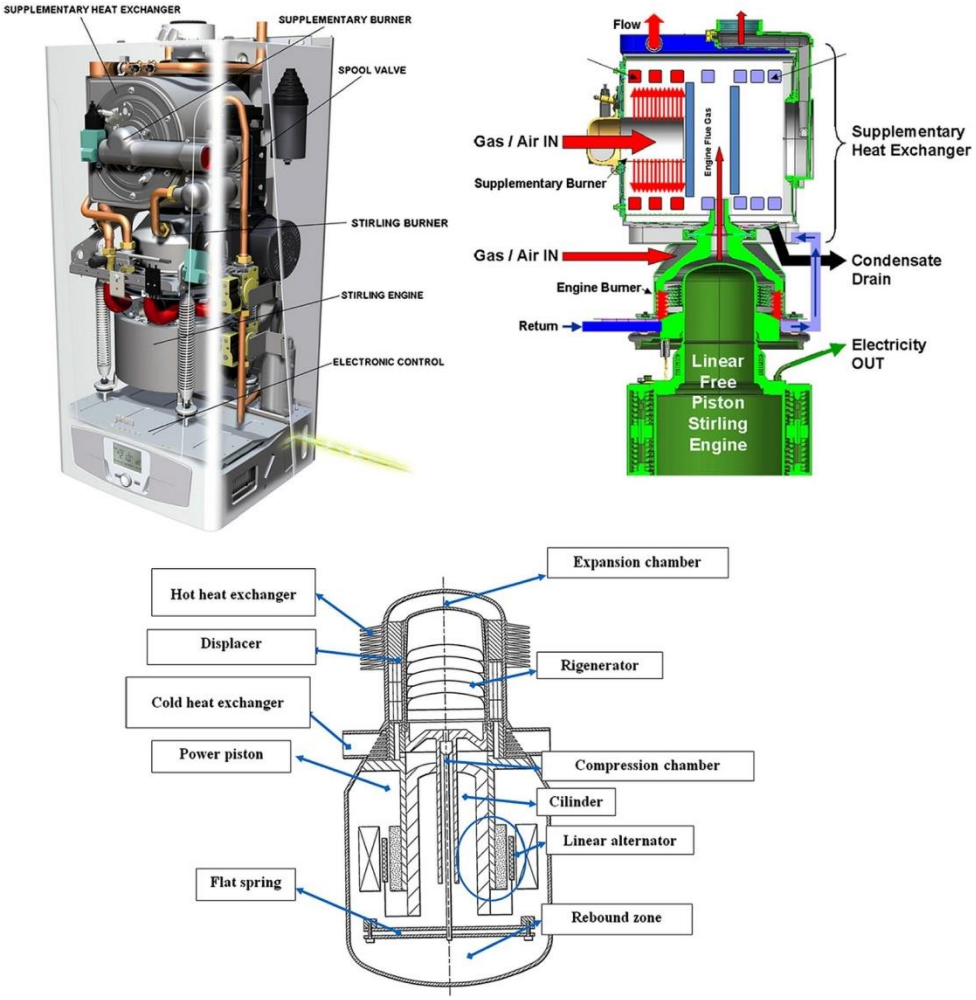

Figure 1.11: The micro-CHP Ecogen by Baxi [24]

The Infinia Corporation developed a 1-kW FPSE (refer to RG-1000) that was incorporated in micro-CHP products manufactured by Ariston Thermo Group, Bosch Thermotechnik, Enatec in Europe, and Rinnai in Japan since 2000 [4,25]. The Ariston 1-kW Stirling engine-based micro CHP system could produce 4-35 kW of heating, and its CHP efficiency was higher than 98% in condensing mode [26]. Qnergy acquired Infinia in 2013. Qnergy micro CHP systems using the SmartBoiler series could produce 2.8-7.2 kW of electricity and up to 46 kW of heating. The electrical and CHP efficiencies were 15.3% and 99%, respectively. The 1-kW Stirling engine-based micro CHP and Qnergy micro-CHP unit are shown in Figure 1.12.

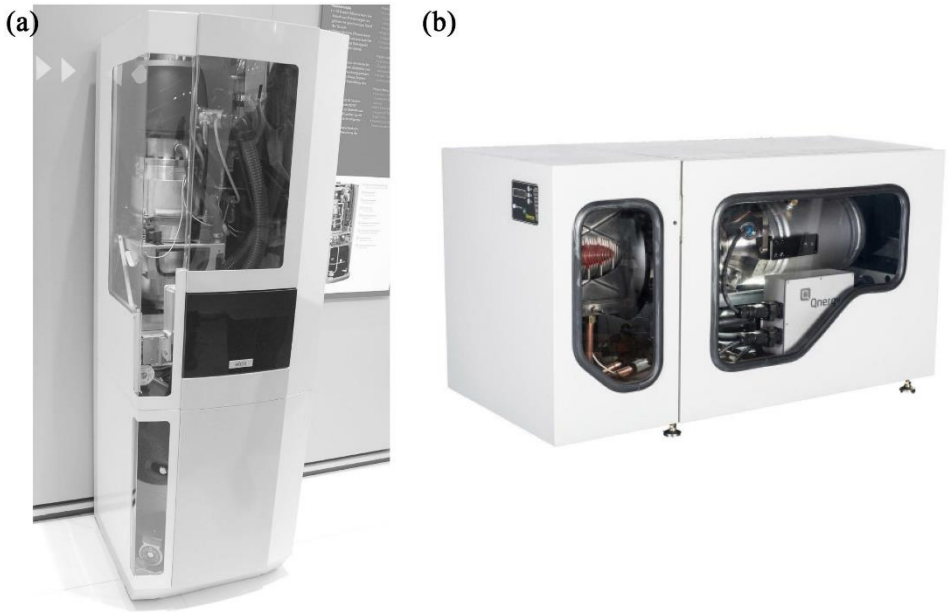

Figure 1.12: (a) Ariston 1-kW micro-CHP unit and (b) Qnergy micro-CHP unit [4,27]

All the studied and built Stirling engines, from the mechanical configuration point of view, can be categorized into three groups: Alpha, Beta, and Gamma [28]. A simplified schematic of the Alpha engine is shown in Figure 1.13.

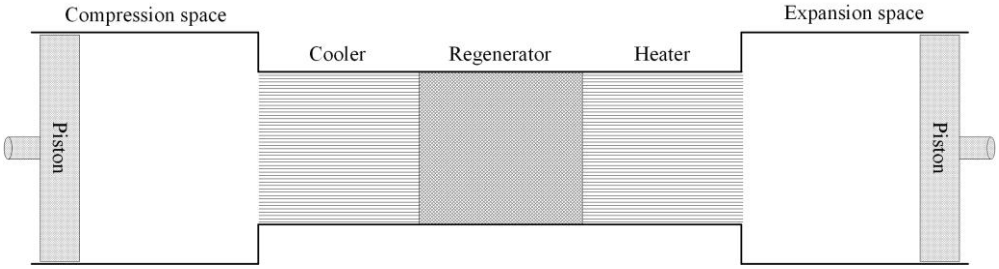

Figure 1.13: The Alpha type Stirling engine [3]

As shown in Figure 1.13, the Alpha engine consists of two separate spaces with pistons inside them. Since there are two pistons, compared to single-piston engines (Beta and Gamma), it needs more sealing, and there is a higher risk of leakage [29]. Since in these engines compared to other types, a higher compression ratio can be obtained at the same volume, higher power can be extracted [30]. An example of an Alpha Stirling engine is the Ross Yoke drive engine which is shown in Figure 1.14. This mechanism was invented by Andy Ross [3].

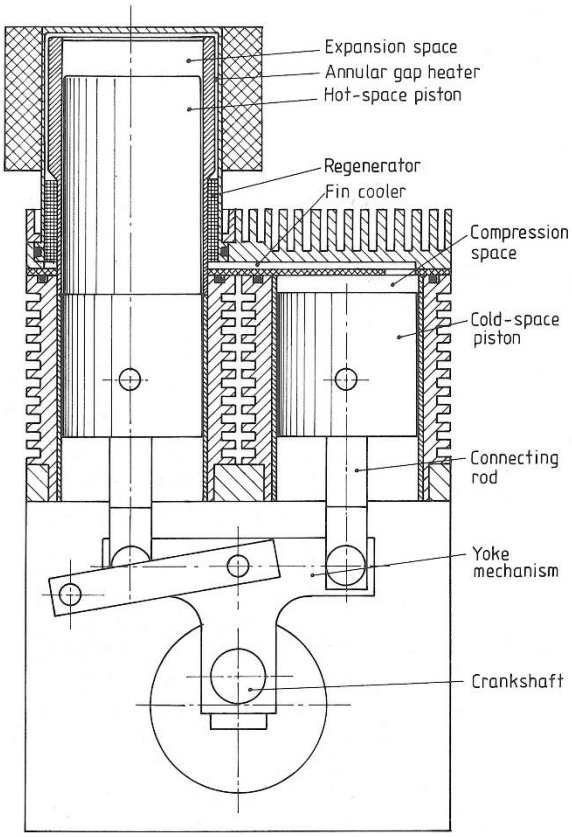

Figure 1.14: The Ross Yoke drive engine [3]

The Ross Yoke drive engine uses a conventional crank mechanism driving two pistons through a yoke linkage. Due to this specific type of connection, the engine is much more compact. Also, this connection causes the rods to travel in an almost straight path and as a result, the side thrust of the pistons is reduced. Thus, there will be less friction, longer sealing life, and more available power [30].

The second type of Stirling engine is the Beta type whose schematic is shown in Figure 1.15.

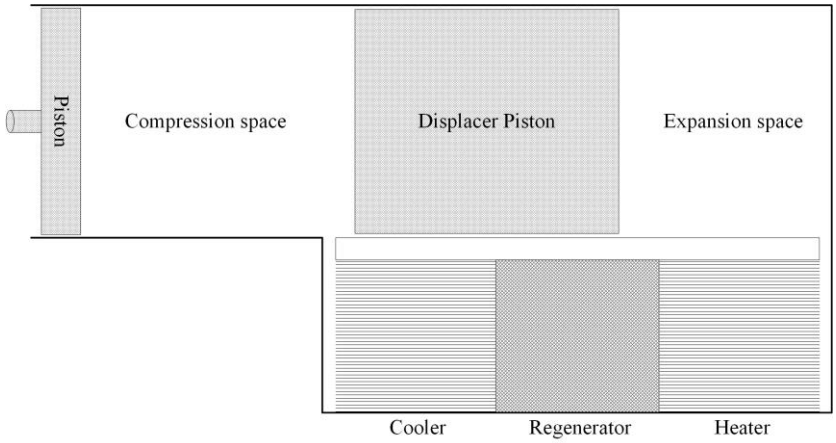

Figure 1.15: The Beta type Stirling engine [3]

As can be seen in Figure 1.15, there are one piston and one displacer that are located in the same cylinder. The displacer transfers the working gas between compression and expansion spaces through the cooler, regenerator, and heater. Beta Stirling engines, compared to other types, are more compact. This feature makes it suitable for applications that the space is limited. However, the power-volume ratio may be smaller than other types [30]. A well-known Beta type engine is the Rhombic drive one whose schematic is shown in Figure 1.16. This mechanism was invented by R J Meijer in 1959 [31].

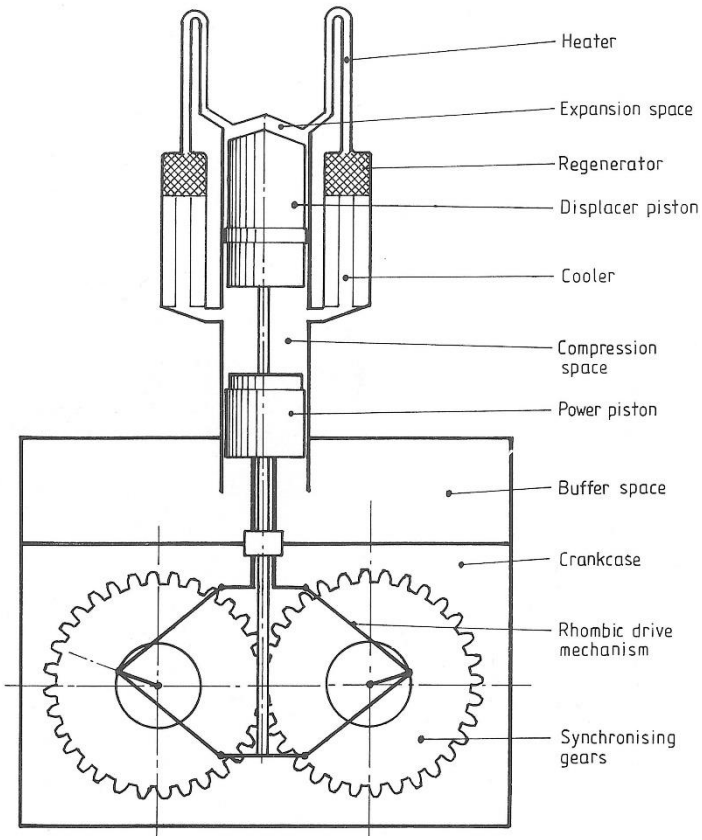

Figure 1.16: The Rhombic drive engine [3]

For the Rhombic drive engine, there is no side force for the pistons. Furthermore, the static and dynamic balancing in the single-cylinder arrangement is attained, allowing vibrationless high-speed operation. However, the disadvantage of the Rhombic drive mechanism is its complexity [3].

The last type of Stirling engine in this category is the Gamma type shown in Figure 1.17.

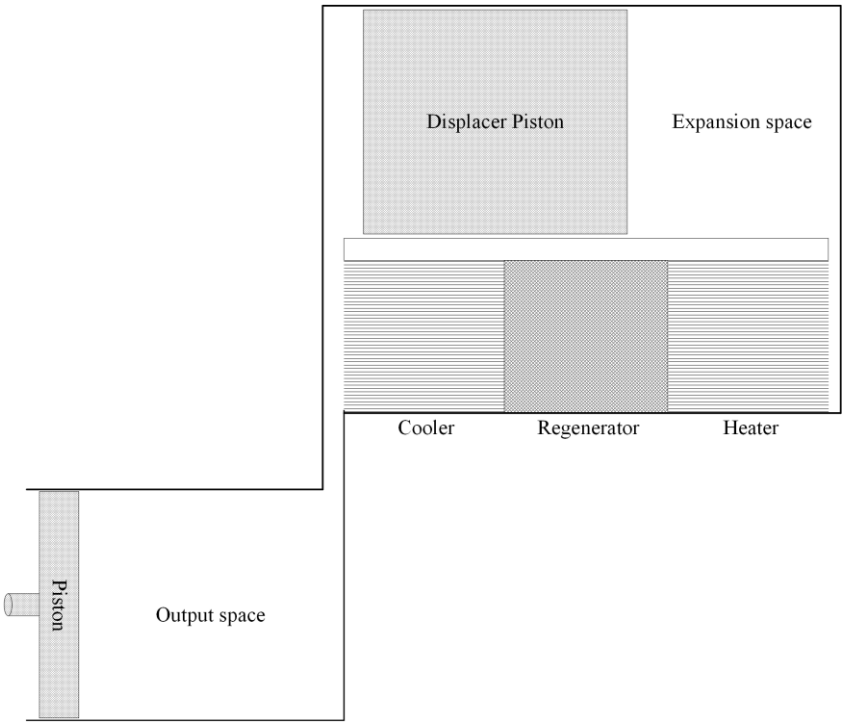

Figure 1.17: The Gamma type Stirling engine [3]

As shown in Figure 1.17, the Gamma engine, like the Beta engine, has one displacer and one piston. The only difference is that they are located in different cylinders. In this engine, unlike the Alpha one, only one cylinder is needed to be sealed. Also, the dead volume in the Gamma engine is larger than other engines that causes lower specific power compared to them. Thus, this engine is preferred in applications that the advantage of having separate cylinders outweighs the power disadvantage [3]. An example of the Gamma engine is the Ringbom engine which is shown in Figure 1.18. This engine was built by Ossian Ringbom in 1907 [32].

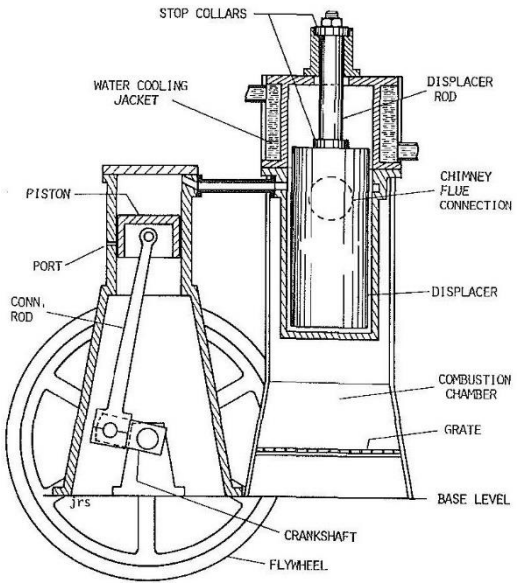

Figure 1.18: The Ringbom engine [32]

The Ringbom engine is in the category of Gamma engine. The only difference between this engine and conventional Gamma engine is that generally, the displacer and the piston are connected mechanically. However, in the Ringbom engine, the displacer is guided by a rod and only the piston is connected to a flywheel.

From another point of view which is based on the connection method between the piston and displacer, the Stirling engines can be categorized into kinematic and free-piston ones [33,34]. In kinematic engines, known as conventional Stirling engines, there is a mechanical connection between two pistons through a series of mechanical elements such as cranks, connecting rods, and flywheels. Examples of such engines are shown in Figure 1.19.

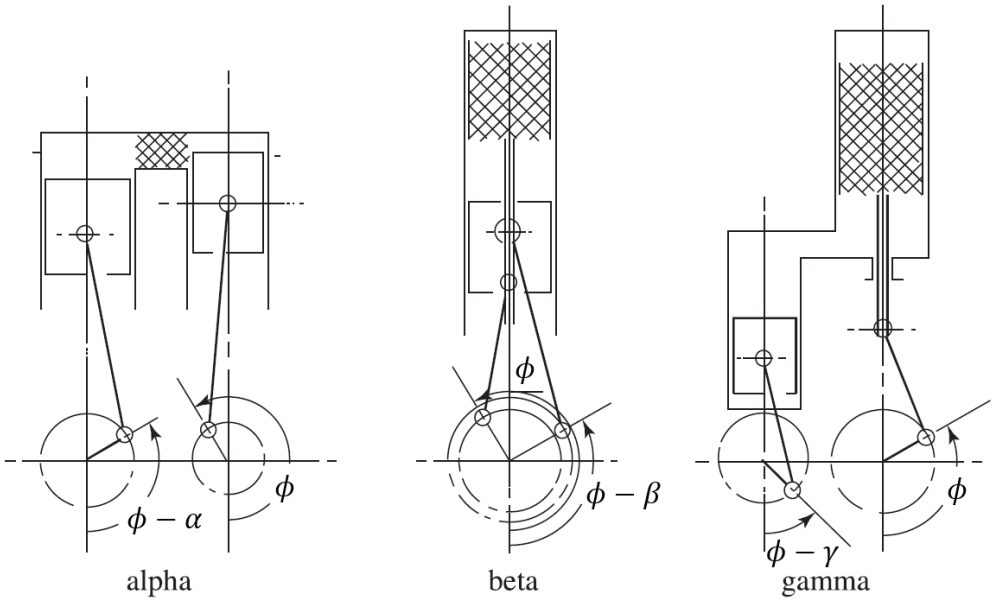

Figure 1.19: Alpha, Beta, and Gamma engines with kinematic configuration [35]

In free-piston engines, the pistons are synchronized by their dynamic behavior and the variations of working gas pressure. There is a strong coupling between mechanical-dynamics and thermodynamics in free-piston engines to identify the system performance [3]. Thus, for such a system, if a model is going to be developed, it should consider all these aspects. The Free Piston Stirling Engine (FPSE), which was invented by W.T. Beale in 1964 [36], has the advantages of simplicity, low cost, ultra-reliability, compactness, lightweight, and freedom of gas leakage over conventional Stirling engine [3,37–39]. The schematic of a Beta-type FPSE is shown in Figure 1.20.

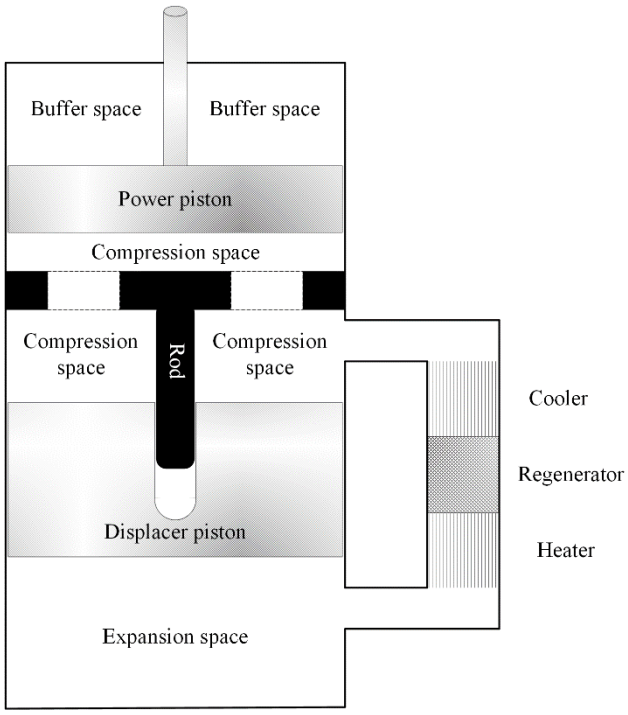

Figure 1.20: The Beta type FPSE [3]

Since the Beta type FPSE has the advantages of Beta type Stirling engine and Free Piston Stirling Engine at the same time, it is the most popular FPSE. Sunpower RE-1000 engine is an example of such a system that its schematic is shown in Figure 1.21. Due to all the advantages of this, the focus of the present study is also on it.

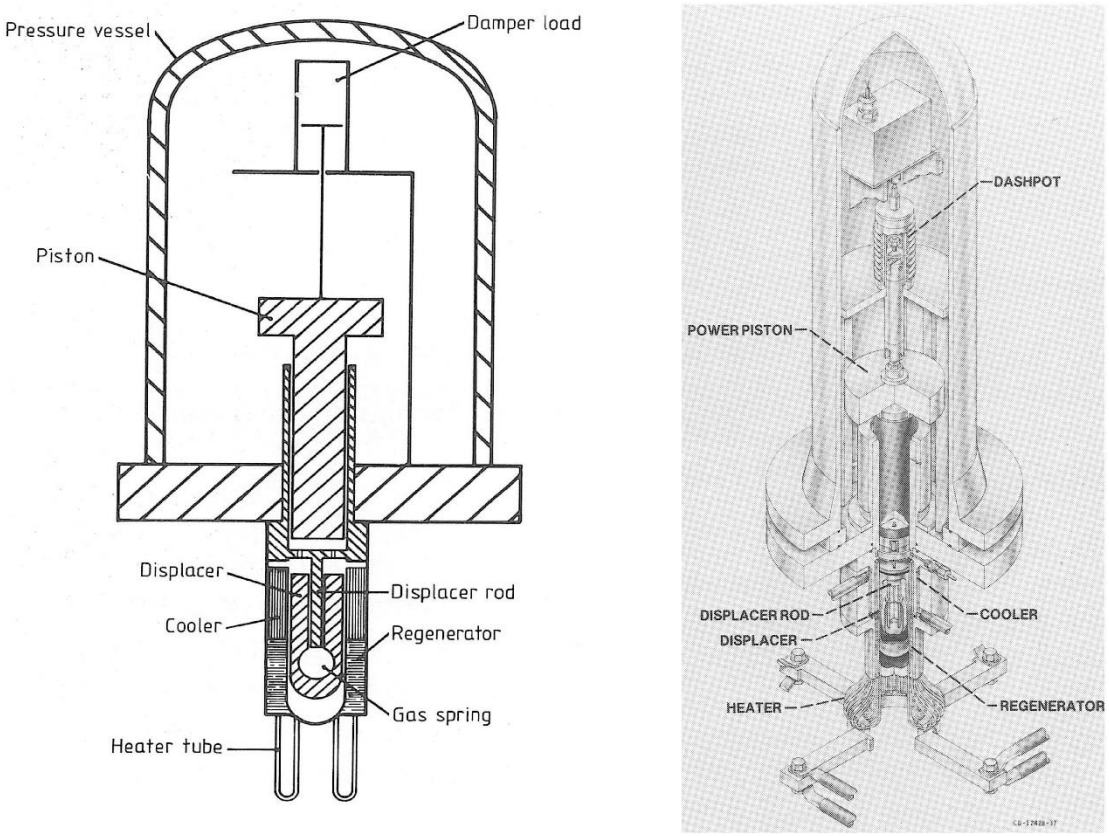

Figure 1.21: The Sunpower 1 kW FPSE [3]

As can be seen in Figure 1.21, there is a damper load at the end of the piston rode to apply the required force through a linear movement of the piston. In practice, to extract energy from the linear movement of the piston in the form of electricity, a linear generator is used which is generally described as a damper [40,41]. This linear generator will be discussed in the next section.

1.3 Linear Generator

Due to the higher performance of linear machines compared to the rotary ones, they are being developed in many applications incorporating linear movement, especially when energy efficiency is a vital requirement. Thanks to advances in linear machine technology, the gearboxes and similar systems that were used to transform linear movement to rotary one and vice versa are not needed anymore, and direct-drive linear electromechanical conversion is attained [42].

The advantages of linear machines in comparison with the machines with linear-rotation conversion, besides the energy efficiency, are as following:

- High velocity. In linear-rotation movement conversion, which is used in rotary machines, this velocity is limited [42].
- High acceleration. The linear rotation conversion in rotary machines leads to chain inertia increment that affects the dynamic of the electromechanical system. Thanks to the direct mechanical coupling of the linear machine and its prime mover, higher acceleration can be obtained [42].
- High accuracy of position sensing [42].
- High lifetime with less maintenance [42].

There are different types of linear generators. The linear generator can be a three-phase or a one-phase one. Also, it can be induction or a permanent magnet. Since a three-phase generator needs less wire than the equivalent one-phase one, a three-phase generator is chosen [43]. Also, between induction and permanent magnet linear generators, due to the higher efficiency of the permanent magnet one, this type of generator is selected [44]. Thus, a three-phase Permanent Magnet Linear Synchronous Machine (PMLSM) is chosen as the linear generator to be coupled with the FPSE. A schematic of such a system is shown in Figure 1.22.

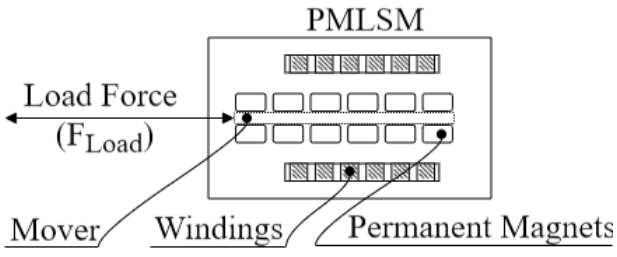

Figure 1.22: The PMLSM schematic

The load force, which is shown in Figure 1.22, comes from the FPSE system through a rigid rod that connects the PMLSM mover to the FPSE piston. Thus, the dynamic model of the PMLSM is needed to study this connection. Also, the electrical model of the PMLSM is needed to calculate the output power.

To obtain the required response for the PMLSM system, a control system is needed to be used besides this system. This control system is shown in Figure 1.23.

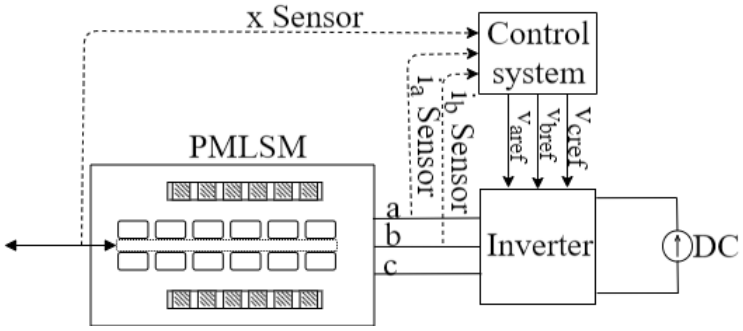

Figure 1.23: The schematic of the PMLSM besides its control system

As can be seen in Figure 1.23, a control system and also an inverter are coupled with the PMLSM. The control system, that will be explained later in detail, is working based on three sensors: two current sensors and one position sensor. An inverter, which is a power electronic device, that allows to convert DC voltage into AC voltage and vice-versa. This converter can be controlled in a way to ensure a motor or a generator behavior of the PMLSM. As the PMLSM is a three phase machine, a three phase inverter is used. A schematic of a three-phase inverter is shown in Figure 1.24.

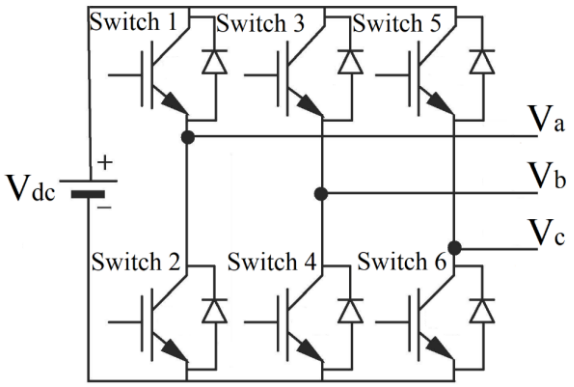

Figure 1.24:Schematic of a three-phase inverter [45]

As can be seen in Figure 1.24, a three phase inverter consists of six transistors and six diodes The control of the switches is realized by the output of the control system [45]. In general, a standard three-phase inverter has eight valid switch states. The controlling of the switches is done through Pulse Width Modulation (PWM) methods [45]. In the present study, the inverter is modeled as a gain equal to 1. This is due to the choice which is made concerning the PWM control method that allows to model the inverter as a unit gain [46].

The general form of PMLSM equations in $a-b-c$ frame can be written as [47]:

$$[v_{a,b,c}] = [L_{a,b,c}]\left[\frac{di_{a,b,c}}{dt}\right] + [r][i_{a,b,c}] + \dot{x}_{mover}\left[\frac{d\psi_{a,b,c}}{dt}\right] \quad 1.1$$

In Equation 1.1, v is the voltage, L is the inductance, i is the current, r is the resistance, $\dot{x}_{mover}$ is the mover velocity, and ψ is the flux linkage. In general, due to the hard controlling of the PMLSM in the three-phase $(a-b-c)$ frame directly, the mathematical model is written in $d-q$ frame using Park and Concordia transformations. These transformations convert the stationary phase coordinate system $(a-b-c)$ to the rotary one $(d-q)$ that by assuming Y as current or voltage, can be expressed as [12]:

$$\begin{bmatrix} Y_\alpha \\ Y_\beta \end{bmatrix} = \sqrt{\frac{2}{3}}\begin{bmatrix} 1 & -1/2 & -1/2 \\ 0 & \sqrt{3}/2 & -\sqrt{3}/2 \end{bmatrix}\begin{bmatrix} Y_a \\ Y_b \\ Y_c \end{bmatrix} \quad 1.2$$

$$\begin{bmatrix} Y_d \\ Y_q \end{bmatrix} = \begin{bmatrix} \cos\theta & \sin\theta \\ -\sin\theta & \cos\theta \end{bmatrix}\begin{bmatrix} Y_\alpha \\ Y_\beta \end{bmatrix} \quad 1.3$$

$$\begin{bmatrix} Y_\alpha \\ Y_\beta \end{bmatrix} = \begin{bmatrix} \cos\theta & -\sin\theta \\ \sin\theta & \cos\theta \end{bmatrix}\begin{bmatrix} Y_d \\ Y_q \end{bmatrix} \quad 1.4$$

$$\begin{bmatrix} Y_a \\ Y_b \\ Y_c \end{bmatrix} = \sqrt{\frac{2}{3}}\begin{bmatrix} 1 & 0 \\ -1/2 & \sqrt{3}/2 \\ -1/2 & -\sqrt{3}/2 \end{bmatrix}\begin{bmatrix} Y_\alpha \\ Y_\beta \end{bmatrix} \quad 1.5$$

With Equations 1.2-1.5, the transformation from $(a-b-c)$ frame to $(d-q)$ frame and vice versa, is possible. The value of θ for these equations can be calculated as [12]:

$$\theta = \int \frac{\pi}{\tau}\dot{x}_{mover}\, dt = \frac{\pi}{\tau}x_{mover} \quad 1.6$$

Which τ is the pole pitch. Finally, based on the developed transformation, the PMLSM system can be modeled in $d-q$ frame, in motor convention, as following [12]:

$$v_d = L_d\frac{di_d}{dt} + ri_d - \frac{\pi}{\tau}\dot{x}_{mover}L_q i_q \quad 1.7$$

$$v_q = L_q\frac{di_q}{dt} + ri_q + \frac{\pi}{\tau}\dot{x}_{mover}\left(L_d i_d + \sqrt{3/2}\,\psi_f\right) \quad 1.8$$

$$F_{em} = \frac{\pi}{\tau}\left(\sqrt{3/2}\,\psi_f i_q + \left(L_d - L_q\right)i_d i_q\right) \quad 1.9$$

$$m_{mover}\ddot{x}_{mover} = F_{em} - B_v\dot{x}_{mover} - F_{load} \quad 1.10$$

$$Power_{em} = F_{em}\dot{x}_{mover} \quad 1.11$$

$$Power_{el} = v_q i_q + v_d i_d \quad 1.12$$

In these equations, F_{em} is the electromagnetic force, ψ_f is the flux linkage, $Power_{em}$ and $Power_{el}$ are the electromagnetic and electrical power, respectively. Equation **1.10** will be used to identify the dynamic linkage between the FPSE and the PMLSM. Figure 1.25 shows how to use the PMLSM equations through a block diagram.

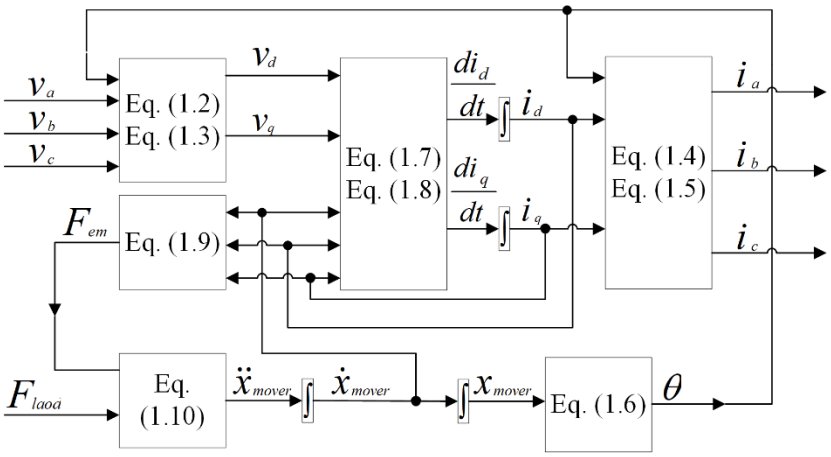

Figure 1.25: The PMLSM model block diagram

F_{load} is the input and $v_a, v_b,$ and v_c voltages are the results of the system control applied by the inverter. Also, $i_a, i_b,$ and i_c will be used in the control model. Now to have the required behavior of the system, it should be controlled. The control system will be explained in detail in chapter 3.

1.4 FPSE-PMLSM Combined System

All the presented aspects in sections 1.2 and 1.3 make the FPSE-linear alternator combined system an interesting and essential topic to study. A schematic of such a system with a Permanent Magnet Linear Synchronous Machine as the generator is shown in Figure 1.26.

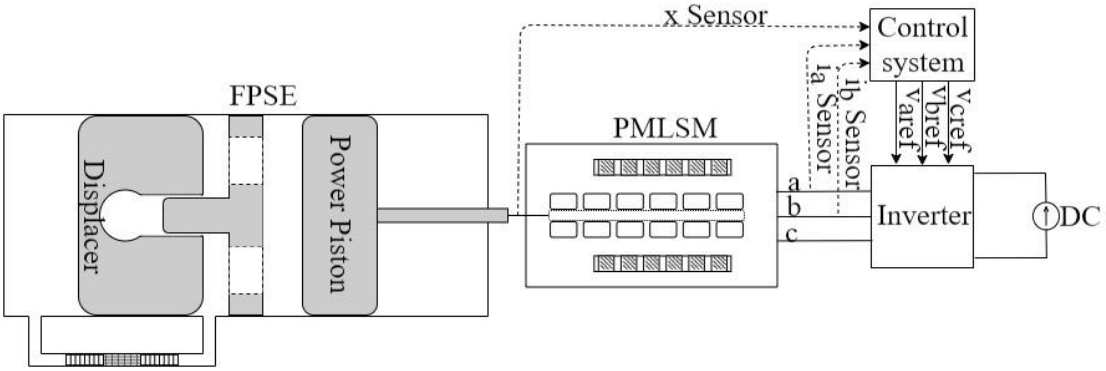

Figure 1.26: The FPSE-PMLSM combined system schematic

The system which is shown in Figure 1.26, is the main system that is going to be analyzed in the present study. There are also other studies that focused on such a similar system. Most of these studies analyzed the combined system by only focusing on one part of it and did not study the whole system in detail. To have more realistic system behavior and develop a more efficient control method to improve its efficiency and stability, it is necessary to study the thermodynamic, mechanic, and electric behavior of the system at the same time with fine models.

Studies that focused on analyzing a linear alternator for FPSE and did not model it in detail are a large part of such studies. Kim et al. [48] theoretically and experimentally designed and studied a linear oscillatory single-phase permanent magnet generator that can be used with an FPSE. They analyzed different types of linear generators to find the suitable one for FPSE. Their focus was on the linear generator, and they did not present a model for FPSE. Zheng et al. [49] also, by defining two simple equations to calculate the force and the power of the FPSE and presenting a linear model for a three-phase Permanent Magnet Linear Synchronous Machine (PMLSM), studied the control strategies that can be applied during starting and generating modes. They also studied their control methods experimentally. In the experimental setup, due to limitations, they used a brushless DC motor as a prime mover engine to simulate FPSE and convert rotary motion to linear one by using a crankshaft mechanism. Dang et al. [44,50,51] theoretically and experimentally in three different papers studied and optimized a tubular linear induction generator to be used with FPSE. They did not propose a model for FPSE and only focused on the generator system. Hew et al. [52], without presenting a model for FPSE or linear generator, experimentally studied a 5 kW linear generator to be used in FPSE.

Besides the previous studies that focused on the linear alternator, some studies did not model it in detail and just presented it as a damper next to the FPSE. Boucher et al. [40] analytically studied a linear model of a dual FPSE combined with a PMLSM modeled as a damper. Their model was a linear dynamic one, and they did not provide the generator or the thermic model. Karabulut et al. [41] also proposed and analyzed the thermal and dynamic behavior of a Martini type FPSE with a linear model. In their model, they identified the alternator as a damper for FPSE and did not analyze it in detail. Ye et al. [53,54] used the response surface methodology and the artificial neural network to predict the FPSE performance based on a linear FPSE model. They did not provide a generator model and did not consider the thermic model of the FPSE. Zare et al. [55], studied an FPE based on its linearized model. They also used describing function and genetic algorithm for this analysis. They studied the FPSE results and validated them with an experimental setup. They modeled only the dynamic system and also did not provide a model for the generator.

Furthermore, some studies presented a linear model of a combined FPSE-linear alternator system. Zheng et al. [56], in continuation of their previous study [49], presented a combined system of an FPSE with a 1 kW PMLSM. In their study, they presented a linear model for FPSE. For the experimental setup, due to the limitations, they used a brushless DC motor combined with a crankshaft mechanism to model FPSE. Zhu et al. [57] used thermoacoustic theory to develop a linear model of a micro-CHP system consisting of a β-type FPSE acoustically coupled with a linear alternator. They also built an experimental setup to validate their theoretical model. In all these studies, even studies that analyzed both FPSE and PMLSM in detail, they used a linear model for FPSE.

Only a few studies of a combined FPSE-linear alternator system have been done, and all have used the simplified systems. Thus, a comprehensive analysis of such a system seems necessary. Using nonlinear thermodynamic equations of the FPSE combined with the PMLSM model makes the system more realistic and possible to study the instabilities of the FPSE in such combination. In addition, as it will be shown later, the linear model of FPSE is not the most reliable model to study the system in all operating conditions.

2 FPSE MODELING

In order to study the FPSE system in detail and have an appropriate estimation of the system stability and control parameters, its accurate model should be developed. There are dynamic and thermic models and also linear and non-linear ones [11,12,58,59]. Since the FPSE works as a heat recovery system and is mechanically connected to a linear generator, both dynamic and thermic models are required. Here, first, the linear and nonlinear dynamic models of the FPSE will be developed and then the best one will be chosen. Then, the dynamic model will be coupled with the thermic one. At the end, after validation, the results of the nonlinear thermodynamic model will be analyzed. It should be noted that the modeled FPSE is based on the Sunpower RE-1000 system [60].

2.1 Dynamic Analysis

The schematic of the Free Piston Stirling Engine (FPSE) system is shown in Figure 2.1.

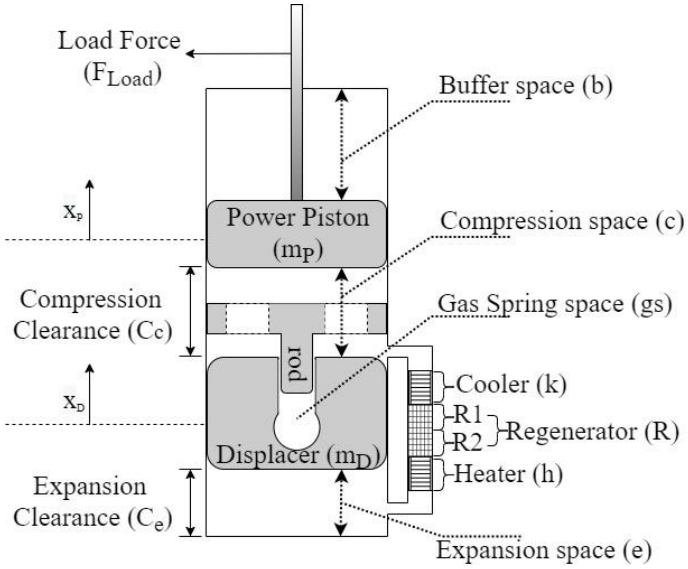

Figure 2.1: Schematic of the FPSE

As it is shown in Figure 2.1, the power piston and displacer piston are two moving pistons of the FPSE. The dynamic equations of the system come from the Newton's second law applied to pistons. The spaces around these pistons are buffer space, compression space, gas spring space, and expansion space. Through pressure balances between pistons and spaces around them, the dynamic equations of the system can be written as:

$$m_P \ddot{x}_P = A_P(P_c - P_b) - F_{Load} \tag{2.1}$$

$$m_D \ddot{x}_D = A_D P_e - (A_D - A_{rod})P_c - A_{rod}(P_{gs}) = A_D(P_e - P_c) + A_{rod}(P_c - P_{gs}) \tag{2.2}$$

In these equations, the mechanical frictions between pistons and cylinder, and FPSE casing displacements are not taken into account. In these equations, m is the mass, $\ddot{x}$ is the acceleration, A is the area, P is the pressure, and F_{Load} is the load force. All the indexes (P, $c, b, D,\ e, rod$ and gs) were also defined in Figure 2.1. The compression space pressure can be calculated based on the mass conservation in the system (constant total mass of the gas inside the system M_{gas}^{total} without leakage) and ideal gas law considering the instantaneous volumes (V_i) and temperatures (T_i) of the gas at each space [3]:

$$P_c = M_{gas}^{total} R \left(\frac{V_c}{T_c} + \frac{V_e}{T_e} + \frac{V_h}{T_h} + \frac{V_k}{T_k} + \frac{V_{R1}}{T_{R1}} + \frac{V_{R2}}{T_{R2}}\right)^{-1} \tag{2.3}$$

The reason that the regenerator is divided into two parts ($R1$ and $R2$) is to have a more precise model of it [3]. For heater, cooler, and regenerator, the volumes are constant, but for the compression and expansion spaces, their instantaneous volumes can be calculated as:

$$V_c = A_P(x_P + C_c) - (A_D - A_{rod})x_D \quad 2.4$$

$$V_e = A_D(x_D + C_e) \quad 2.5$$

C_c and C_e are compression and expansion clearance, respectively which were shown in Figure 2.1. The instantaneous temperature calculations will be discussed in the next section.

Other parameters required to solve Equations **2.1** and **2.2** are buffer and gas spring spaces' pressures. For buffer and gas spring, the quasi static adiabatic assumption can be applied, and their pressures can be calculated as [3]:

$$P_i = P^{mean}\left(V_i^{mean}/V_i^{\text{instantaneous}}\right)^{\lambda}; \quad i: b, gs \quad 2.6$$

Instantaneous volumes of the buffer and the gas spring are as:

$$V_b^{\text{instantaneous}} = V_b^{mean} - A_P x_P \quad 2.7$$

$$V_{gs}^{\text{instantaneous}} = V_{gs}^{mean} - A_{rod} x_D \quad 2.8$$

The last required parameter to solve Equations **2.1** and **2.2** is the pressure difference between expansion and compression spaces which is equal to the pressure drop (ΔP) between these two spaces:

$$P_e - P_c = \Delta P \quad 2.9$$

This pressure drop is due to the gas flow through cooler, regenerator, and heater that can be calculated as following [3,12]:

$$\Delta P_i = \frac{1}{2}\rho_i \left(\frac{C_{f_i} l_i}{d_i^{hydraulic}}\right) u_i |u_i| ; \quad i: h, k, R1, R2 \quad 2.10$$

C_f is the Darcy friction factor, l is the length of each space, and u is the gas velocity. The hydraulic diameter ($d^{hydraulic}$) for the heater and the cooler can be defined as:

$$d_i^{hydraulic} = \frac{4A_i}{Wetted\ perimeter_i} ; \quad i: h, k \quad 2.11$$

For the wire mesh porous media of the regenerator, the hydraulic diameter can be calculated as [12]:

$$d_R^{hydraulic} = \frac{d_{wire} \times Porosity}{1 - Porosity} \quad 2.12$$

Darcy friction factors based on the Reynolds number (Re) according to the Majidniya et al. [12] study are presented in Table 2.1.

Table 2.1: Darcy friction factor [12,61,62]

For heater and cooler:	$Re < 2000$	$C_f = 64/Re$
	$Re > 2000$	$C_f = 0.316Re^{-0.25}$
For regenerator:	$Re < 60$	$C_f = 4 \times 10^{(1.73-0.93 \log Re)}$
	$60 < Re < 1000$	$C_f = 4 \times 10^{(0.714-0.365 \log Re)}$
	$Re > 1000$	$C_f = 4 \times 10^{(0.015-0.125 \log Re)}$

Reynolds number can be calculated as:

$$Re_i = \frac{\rho_i u_i d_i^{hydraulic}}{\mu_i}; \quad i: h, k, R1, R2 \quad 2.13$$

Dynamic viscosity and gas density of Helium based on its temperature and pressure at each space can also be calculated as [63]:

$$\mu_i = 3.674 \times 10^{-7} T_i^{0.7}; \quad i: h, k, R1, R2, e, c \quad 2.14$$

$$\rho_i = \frac{48.14 P_i \times 10^{-5}}{T_i (1 + 0.4446 P_i \times 10^{-5} / T_i^{1.2})}; \quad i: h, k, R1, R2, e, c \quad 2.15$$

The pressure of the gas at each space, based on the calculated pressure drops (Equation **2.10**) also can be calculated as [3,11]:

$$P_k = P_c + \frac{\Delta P_k}{2} \quad 2.16$$

$$P_{R1} = P_k + \frac{\Delta P_k}{2} + \frac{\Delta P_{R1}}{2} \quad 2.17$$

$$P_{R2} = P_{R1} + \frac{\Delta P_{R1}}{2} + \frac{\Delta P_{R2}}{2} \quad 2.18$$

$$P_h = P_{R2} + \frac{\Delta P_{R2}}{2} + \frac{\Delta P_h}{2} \quad 2.19$$

$$P_e = P_h + \frac{\Delta P_h}{2} \tag{2.20}$$

Finally, instant gas velocity in the heater, cooler, and regenerator should be calculated. It is assumed that the variation of the total volume of the gas inside the system causes gas to pass through the heater, cooler, and regenerator at the same time, and based on that, the instantaneous gas velocity can be calculated as [3,11]:

$$u_i = \frac{\dot{V}_{tot}}{A_i}; \quad i: h, k, R1, R2 \tag{2.21}$$

The total gas volume variation is due to the volume variations of the gas in compression and expansion spaces that can be calculated as:

$$\dot{V}_c = A_P \dot{x}_P - (A_D - A_{rod})\dot{x}_D \tag{2.22}$$

$$\dot{V}_e = A_D \dot{x}_D \tag{2.23}$$

$$\dot{V}_{tot} = \dot{V}_c - \dot{V}_e = A_P \dot{x}_P - (2A_D - A_{rod})\dot{x}_D \tag{2.24}$$

Now, to solve Equations 2.1 and **2.2**, since some of the dynamic parameters are affected by temperature or temperature dependent (including instantaneous volumes and pressures which has a direct effect on the pistons' movement), the thermic model of the system should be developed to be coupled with the presented dynamic one. Also, the isothermal assumption with the constant temperature in all the spaces can be used. This method is an easy method to apply but not a precise one and does not provide all the required information, for example the heat exchangers' heat transfers or spaces' temperature variations, concerning the FPSE operating condition.

2.1.1 Linear and Nonlinear Analysis

Here, two methods for solving the dynamic equations of the FPSE are studied and the results are compared to choose the best one. The common method that was generally used by authors [40,41,56,57] was based on the linearized dynamic equations. In this method, all the dynamic equations were linearized and then the set of dynamic equations were solved. Another method which is a new method developed by author and presented here, is the nonlinear method that the nonlinear equations are used directly and solved without any

linearization and simplification. The linearization will be explained and then its results will be presented.

The first equation that will be linearized is Equation **2.3**. By replacing V_c and V_e with their relations of equation 2.4 and 2.5, respectively, Equation 2.3 will be as:

$$P_c = M_{gas}^{total} R \left(\frac{A_P(x_P + C_c) - (A_D - A_{rod})x_D}{T_c} + \frac{A_D(x_D + C_e)}{T_e} + \frac{V_h}{T_h} + \frac{V_k}{T_k} + \frac{V_{R1}}{T_{R1}} + \frac{V_{R2}}{T_{R2}} \right)^{-1} \quad 2.25$$

Equation **2.63** can be simplified as following [3]:

$$P_c = \frac{M_{gas}^{total} R}{\mathbb{Z}} \left(1 + \frac{A_P x_P - (A_D - A_{rod})x_D}{\mathbb{Z} T_c} + \frac{A_D x_D}{\mathbb{Z} T_e} \right)^{-1} \quad 2.26$$

$$\mathbb{Z} = \frac{A_P C_c}{T_c} + \frac{A_D C_e}{T_e} + \frac{V_h}{T_h} + \frac{V_k}{T_k} + \frac{V_{R1}}{T_{R1}} + \frac{V_{R2}}{T_{R2}} \quad 2.27$$

With the condition of $\left(\frac{A_P x_P - (A_D - A_{rod})x_D}{\mathbb{Z} T_c} + \frac{A_D x_D}{\mathbb{Z} T_e} \right) \ll 1$ which is usually satisfied easily [3], Equation **2.26** can be linearized as follows using Binomial theorem and ignoring the second-order terms [3]:

$$P_c \cong \frac{M_{gas}^{total} R}{\mathbb{Z}} \left(1 - \frac{A_P x_P - (A_D - A_{rod})x_D}{\mathbb{Z} T_c} - \frac{A_D x_D}{\mathbb{Z} T_e} \right) \quad 2.28$$

Since the charge pressure is equal to the mean pressure in working spaces, Equation **2.28** can be rewritten as:

$$P_c \cong P^{mean} \left(1 - \frac{A_P x_P - (A_D - A_{rod})x_D}{\mathbb{Z} T_c} - \frac{A_D x_D}{\mathbb{Z} T_e} \right) \quad 2.29$$

Now, by replacing the instantaneous volumes of Equation 2.6 with their values of Equations 2.7 and 2.8 following equations can be obtained:

$$P_b = P^{mean} \left(\frac{V_b^{mean}}{V_b^{mean} - A_P x_P} \right)^{\lambda} = P^{mean} \left(1 - \frac{A_P x_P}{V_b^{mean}} \right)^{-\lambda} \quad 2.30$$

$$P_{gs} = P^{mean} \left(\frac{V_{gs}^{mean}}{V_{gs}^{mean} - A_{rod} x_D} \right)^{\lambda} = P^{mean} \left(1 - \frac{A_{rod} x_D}{V_{gs}^{mean}} \right)^{-\lambda} \quad 2.31$$

Again, with the same method of linearization that was used for P_c, the linearized form of Equations **2.30** and 2.31 will be as:

$$P_b = P^{mean}\left(\frac{V_b^{mean}}{V_b^{mean} - A_P x_P}\right)^{\lambda} = P^{mean}\left(1 + \lambda\frac{A_P x_P}{V_b^{mean}}\right) \quad 2.32$$

$$P_{gs} = P^{mean}\left(\frac{V_{gs}^{mean}}{V_{gs}^{mean} - A_{rod} x_D}\right)^{\lambda} = P^{mean}\left(1 + \lambda\frac{A_{rod} x_D}{V_{gs}^{mean}}\right) \quad 2.33$$

The final parameter that should be linearized is the pressure drop which was shown in Equation 2.10. The linearization method of the pressure drop is different from what has been done for other terms [3]. First of all, it is assumed that the variation of the gas density by pressure can be neglected. Then, since the pressure drop effect on the system is similar to the damping effect, an equivalent linear damper that dissipates the same amount of energy should be found [3]. Thus, the dissipated energy by the actual damping should be equal to the dissipated energy by the linear damping. Their values will be compared in a quarter cycle [64]. Replacing the pressure drop (ΔP) with a linear damper that its equivalent coefficient is equal to $C^{Linear damping}$, means:

$$\Delta P_i = C_i^{Linear damping} u_i \; ; \quad i: h, k, R1, R2 \quad 2.34$$

By assuming a sinusoidal displacement, the flow velocity (u) can be estimated as:

$$u_i = U_i \cos \omega t \; ; \quad i: h, k, R1, R2 \quad 2.35$$

Now, the dissipated energy by the damper, which is the right side of Equation 2.34, can be calculated as:

$$Dissipated\ Energy = \int_0^{\frac{\pi}{2}} \left(C_i^{Linear damping} u_i\right)\frac{u_i}{\omega} d(\omega t) \; ; \quad i: h, k, R1, R2 \quad 2.36$$

U_i is the flow velocity amplitude. Putting Equation 2.35 in 2.36 will give the following equation:

$$Dissipated\ Energy = \frac{C_i^{Linear damping} U_i^2}{\omega}\int_0^{\frac{\pi}{2}} (\cos \omega t)^2 d(\omega t) = \frac{\pi}{4}\frac{C_i^{Linear damping} U_i^2}{\omega} \; ; \quad i: h, k, R1, R2 \quad 2.37$$

Now, for the left side of Equation 2.34, which is the pressure drop (ΔP), the dissipated energy can be calculated as:

$$Dissipated\ Energy = \int_0^{\frac{\pi}{2}} \left(\frac{1}{2} \rho_i \left(\frac{C_{f_i} l_i}{d_i^{hydraulic}} \right) u_i |u_i| \right) \frac{u_i}{\omega} d(\omega t)\ ; \quad i: h, k, R1, R2 \tag{2.38}$$

In the first quarter, the value of the flow velocity is assumed to be positive. By using the same assumption of Equation **2.35**, Equation **2.38** can be calculated as follows:

$$Dissipated\ Energy = \frac{1}{3} \rho_i \left(\frac{C_{f_i} l_i}{d_i^{hydraulic}} \right) \frac{U_i^3}{\omega}; \quad i: h, k, R1, R2 \tag{2.39}$$

Now, by using Equations 2.37 and 2.39, the linear damper coefficient can be calculated as:

$$C_i^{Lineardamping} = \frac{4}{3} \frac{\rho_i}{\pi} \left(\frac{C_{f_i} l_i}{d_i^{hydraulic}} \right) U_i; \quad i: h, k, R1, R2 \tag{2.40}$$

Thus, the linearized pressure drop will be as following:

$$\Delta P_i = \frac{4}{3} \frac{\rho_i}{\pi} \left(\frac{C_{f_i} l_i}{d_i^{hydraulic}} \right) U_i u_i\ ; \quad i: h, k, R1, R2 \tag{2.41}$$

u_i can be calculated based on Equation 2.21. U_i can be calculated based on the Equation **2.24** and assuming a sinusoidal movement for displacer ($X_D\ sin(\omega t + \phi)$) and piston ($X_P\ sin(\omega t)$) as following:

$$U_i = \frac{Net\ volumetric\ flow\ rate\ amplitude}{A_i} = \frac{\omega \sqrt{(A_P X_P)^2 + (2A_D - A_{rod})^2 X_D^2 - 2(2A_D - A_{rod}) A_P X_P X_D \cos\phi}}{A_i}\ ; i: h, k, R1, R2 \tag{2.42}$$

It should be noted that to find the constant value of C_{f_i} that can be used in the linear model, U_i which has a constant value will be used to calculate Re.

Finally, the first right term of Equation 2.2 which is $A_D(P_e - P_c) = A_D \Delta P$ can be linearized as:

$$A_D \Delta P = C_P^{damping} \dot{x}_p + C_D^{damping} \dot{x}_D \tag{2.43}$$

$$C_P^{damping} = A_P A_D \mathbb{C} \tag{2.44}$$

$$C_D^{damping} = -2(2A_D - A_{rod}) A_D \mathbb{C} \tag{2.45}$$

$$\mathbb{C} = \sum_{i:h,k,R1,R2} \frac{4}{3}\frac{\rho_i}{\pi}\left(\frac{C_{f_i} l_i}{d_{hydraulic\ i}}\right)\frac{U_i}{A_i} \quad 2.46$$

Now, the final linearized form of Equations 2.1 and 2.2 can be written as follows:

$$\ddot{x}_P = K_{PP}x_P + K_{PD}x_D + D_{PP}\dot{x}_P + D_{PD}\dot{x}_D \quad 2.47$$

$$\ddot{x}_D = K_{DP}x_P + K_{DD}x_D + D_{DP}\dot{x}_P + D_{DD}\dot{x}_D \quad 2.48$$

$$K_{PP} = \frac{A_P^2}{m_P} P^{mean}\left(\frac{1}{T_k\mathbb{Z}} + \frac{\gamma}{V_b^{mean}}\right) \quad 2.49$$

$$K_{PD} = -\frac{A_P^2}{m_P\mathbb{Z}} P^{mean}\left(\frac{1}{T_h} - \frac{(1 - A_{rod}/A_P)}{T_k}\right) \quad 2.50$$

$$D_{PP} = -\frac{C_{Load}}{m_P} \quad 2.51$$

$$D_{PD} = 0 \quad 2.52$$

$$K_{DP} = -\frac{A_P A_{rod} P^{mean}}{m_D T_k \mathbb{Z}} \quad 2.53$$

$$K_{DD} = -\frac{A_{rod}}{m_D} P^{mean}\left(\frac{A_P}{T_h\mathbb{Z}} - \frac{(A_p - A_{rod})}{T_k\mathbb{Z}} + \frac{\gamma A_{rod}}{V_{gs}^{mean}}\right) \quad 2.54$$

$$D_{DP} = C_P^{damping}/m_D \quad 2.55$$

$$D_{DD} = C_D^{damping}/m_D \quad 2.56$$

C_{Load} in Equation 2.51 is the coefficient of the damping load force, which can be described as the following equation:

$$F_{Load} = C_{Load}\dot{x}_P \quad 2.57$$

It should be noted that this force is not a part of the system and is an artificial load. The choice of the load is arbitrary but it is commonly made as Equation 2.57 because it is easy to model and well adapted to the oscillating system.

Now, the linear and nonlinear dynamic models of the FPSE will be solved and the results will be compared. To have a better look of the main differences between two models, their main dynamic equations which are Equations 2.1, 2.2, 2.47, and 2.48 are repeated in Table 2.2.

Table 2.2: FPSE linear and nonlinear dynamic equations

Nonlinear	$m_P\ddot{x}_P = A_P(P_c - P_b) - F_{Load}$ $m_D\ddot{x}_D = A_D P_e - (A_D - A_{rod})P_c - A_{rod}(P_{gs}) = A_D(P_e - P_c) + A_{rod}(P_c - P_{gs})$
Linear	$\ddot{x}_P = K_{PP}x_P + K_{PD}x_D + D_{PP}\dot{x}_P + D_{PD}\dot{x}_D$ $\ddot{x}_D = K_{DP}x_P + K_{DD}x_D + D_{DP}\dot{x}_P + D_{DD}\dot{x}_D$

To develop these models, some assumptions are made that are only valid for the current section (2.1.1). The first one is that the dynamic models will be solved with the isothermal assumption. It means that the temperatures of all spaces are constant. The gas temperature in the heater, cooler, and regenerator will be equal to the wall temperatures in these spaces. Also, the temperature of the gas in the expansion and compression spaces will be equal to the heater and cooler temperatures, respectively. Furthermore, to have a similar situation in linear and nonlinear simulation, for both cases, Re was calculated based on U_i . The method of U_i calculation was explained after Equation 2.42. Also, at this analysis, maximum displacer and piston strokes are assumed to be equal to 9×10^{-3} m and 8.3×10^{-3} m, respectively. These values are selected based on the nonlinear dynamic results to have comparable cases and are only valid for the linear analysis. The phase shift between displacer and piston that are at a frequency of 30 Hz is also assumed to be equal to $42.5°$ [3]. This assumption is only needed for the linear analysis to calculate some parameters (**2.42**) which uses the repetition procedure for solution and for the nonlinear analysis this phase shift will be calculated.

For simplification, only at this analysis which is developed in the current section, it is also assumed that the regenerator is not divided into two parts. To calculate the gas temperature in the regenerator, it is assumed that the temperature variation in the regenerator is linear, as it is shown in Figure 2.2. This assumption is not far from reality [3,65].

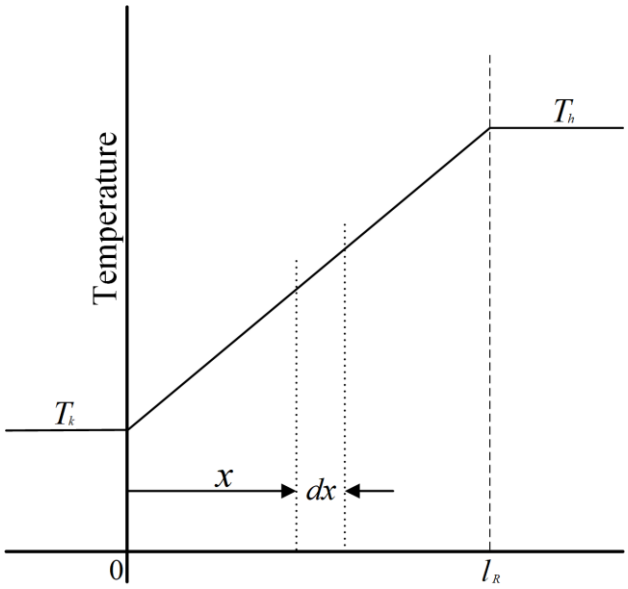

Figure 2.2: Linear temperature profile in the regenerator

Based on Figure 2.2, the linear temperature distribution between heart and cooler in regenerator (T_R) can be expressed as the following equation:

$$T_R(x) = \frac{(T_h - T_k)x}{l_R} + T_k \qquad 2.58$$

Then the total mass of the gas (m_R) in the regenerator void volume (V_R) can be calculated as:

$$m_R = \int_0^{V_R} \rho dV_R \qquad 2.59$$

Since $V_R = A_R l_R$, for a constant free flow area of A_R, it can be written $dV_R = A_R dx$. Also, based on the ideal gas law, it can be written that $P = \rho RT \rightarrow \rho = P/(RT)$. Now Equation 2.59 can be rewritten as:

$$m_R = \frac{PA_R}{R} \int_0^{l_R} \frac{dx}{\frac{(T_h - T_k)x}{l_R} + T_k} = \frac{PV_R}{R} \frac{\ln(T_h/T_k)}{T_h - T_k} \qquad 2.60$$

Also, the ideal gas law in the regenerator based on the mean effective temperature in the regenerator T_R can be written as:

$$PV_R = m_R R T_R \qquad 2.61$$

Now, the regenerator mean-effective-temperature based on Equations 2.60 and 2.61 can be calculated as:

$$T_R = \frac{T_h - T_k}{\ln(T_h/T_k)} \qquad 2.62$$

It should be noted that all the assumptions that were made, including the isothermal condition, method of Re calculation, maximum strokes, phase shift, frequency, and the number of regenerator sections, are only the assumptions that are used in the current section (2.1.1) to compare the linear and nonlinear models and are not valid for the next sections.

Now, based on the explained assumptions and input data of Table 2.3, the results of the two simulation methods will be presented. It should be noted Table 2.3 is a reference table for the PMLSM and FPSE models that will be developed later and the input data will be the same as the Table 2.3.

Table 2.3: FPSE input data [8,12,13,60]

A_R	$8.745\ cm^2$	d_{wire}	$0.00889\ cm$	$Number\ of\ Tubes_h$	34
A_R^{wetted}	$0.2019\ cm^2$	Gas	$Helium$	P^{mean}	$70\ bar$
C_c	$1.83\ cm$	l_D	$15.19\ cm$	$Passage\ size_k$	$5.1 \times 38\ cm$
C_e	$1.861\ cm$	l_h	$18.34\ cm$	$Porosity$	75.9 %
C_p	$5195\ J/(kgK)$	l_k	$7.92\ cm$	T_h^{wall}	$814.3\ K$
C_v	$3117\ J/(kgK)$	l_R	$6.44\ cm$	T_k^{wall}	$322.8\ K$
d_D	$5.67\ cm$	m_D	$0.426\ kg$	V_b^{mean}	$2615\ cm^3$
d_h	$0.2362\ cm$	m_P	$6.2\ kg$	V_{gs}^{mean}	$37.97\ cm^3$
d_P	$5.718\ cm$	M_{gas}^{total}	$0.0014\ kg$	V_R	$56.37\ cm^3$
d_{rod}	$1.663\ cm$	$Number\ of\ passages_k$	135	$Wetted\ Perimeter_k$	$115.2\ cm$

The results of the linear and nonlinear models are presented in Figure 2.3. In Figure 2.3, the displacer and piston displacements over time for both models are shown.

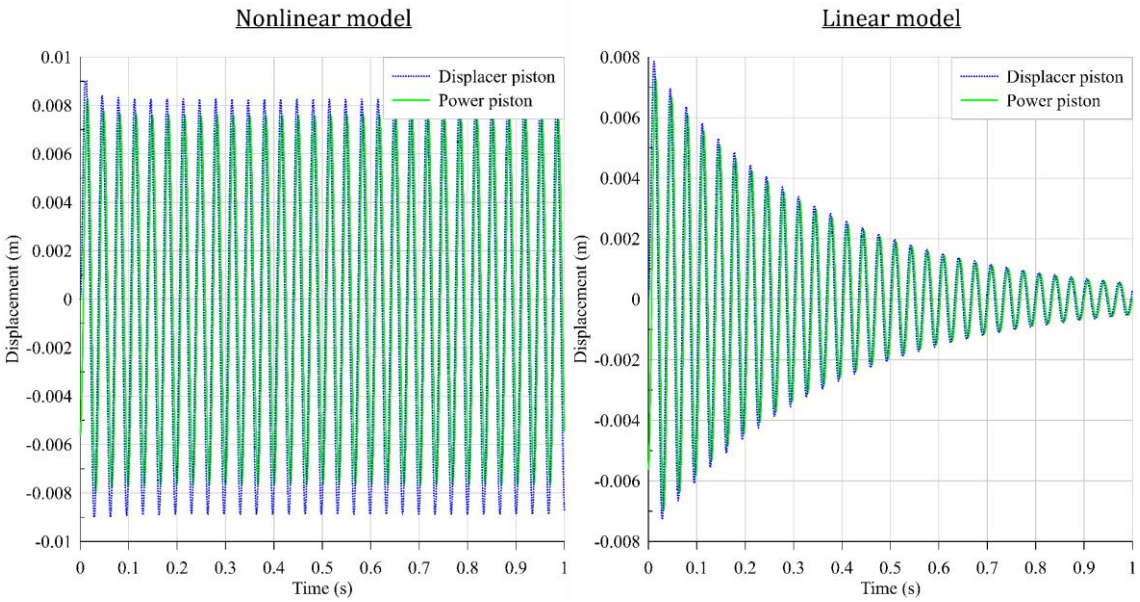

Figure 2.3: Linear and nonlinear models' results

As shown in Figure 2.3, the results of the nonlinear model are getting steady after a few cycles, but for the linear model, it is not the case. Since the linear model never gets steady and finally, the system stops working, which is not what happens in reality (in reality the system has a steady oscillating behavior [3,60]), the linear model cannot predict the realistic behavior of the FPSE. Thus, the nonlinear model will be used for modeling the FPSE system.

It should be noted that as it was already discussed, the nonlinear model is a new applied model by author in the present study.

2.2 Thermal Analysis

In order to have a precise estimation of the FPSE behavior, its thermic model is developed here to be coupled with the dynamic one. For the thermic model, the following conservation of energy equation should be solved for each space [3,11]:

$$\dot{Q}_{in} + \left(\dot{m}C_pT\right)_{in} - \left(\dot{m}C_pT\right)_{out} - Power_{out} = C_v\frac{d}{dt}(mT) \qquad 2.63$$

By this equation, the gas temperature in each space can be calculated. Expansion and compression spaces are assumed to be isolated and the only heat transfers with the

environment happen through the heater, cooler, and regenerator. These heat transfers which are through the walls can be calculated as [3,11]:

$$\dot{Q}_{in\ i} = h_i A_{wetted\ i}(T_{wall\ i} - T_i); \quad i: h, k, R1, R2 \tag{2.64}$$

$$h_i = \frac{C_{fi}}{4} \times \frac{Re_i \mu_i C_p}{2 d_{hydraulic\ i} Pr_i}; \quad i: h, k, R1, R2 \tag{2.65}$$

$$Pr_i = \frac{0.7117 \times T_i^{-(0.01-1.42\times10^{-4}\times P_i\times10^{-5})}}{1 + 1.123 \times 10^{-3} \times P_i \times 10^{-5}}; \quad i: h, k, R1, R2 \tag{2.66}$$

Now, based on Figure 2.1, the conservation of energy equation for each space is reformulated as follow to be used for each space temperature calculation [3,11]:

$$\dot{T}_c = \left(\frac{\dot{m}_{k\ to\ c} CpT_{kc} - \dot{W}_P}{Cv} - \dot{m}_{\ c} T_c\right) / m_c \tag{2.67}$$

$$\dot{T}_k = \left(\frac{\dot{Q}_{in\ k} + \dot{m}_{c\ to\ k} CpT_{ck} + \dot{m}_{R1\ to\ k} CpT_{R1k}}{Cv} - \dot{m}_{\ k} T_k\right) / m_k \tag{2.68}$$

$$\dot{T}_{R1} = \left(\frac{\dot{Q}_{in\ R1} + \dot{m}_{k\ to\ R1} CpT_{kR1} + \dot{m}_{R2\ to\ R1} CpT_{R2R1}}{Cv} - \dot{m}_{\ R1} T_{R1}\right) / m_{R1} \tag{2.69}$$

$$\dot{T}_{R2} = \left(\frac{\dot{Q}_{in\ R2} + \dot{m}_{R1\ to\ R2} CpT_{R1R2} + \dot{m}_{h\ to\ R2} CpT_{hR2}}{Cv} - \dot{m}_{\ R2} T_{R2}\right) / m_{R2} \tag{2.70}$$

$$\dot{T}_h = \left(\frac{\dot{Q}_{in\ h} + \dot{m}_{R2\ to\ h} CpT_{R2h} + \dot{m}_{e\ to\ h} CpT_{eh}}{Cv} - \dot{m}_h T_h\right) / m_h \tag{2.71}$$

$$\dot{T}_e = \left(\frac{\dot{m}_{h\ to\ e} CpT_{he} - \dot{W}_D}{Cv} - \dot{m}_e T_e\right) / m_e \tag{2.72}$$

In these equations, $\dot{m}_{i\ to\ j}$ is the gas mass flow rate from space *i* to space *j*. This mass flow, based on the conservation of mass equation between spaces, and according to Figure 2.1, can be written as [3,11]:

$$\dot{m}_{k\ to\ c} = -\dot{m}_{c\ to\ k} = \dot{m}_c \tag{2.73}$$

$$\dot{m}_{R1\ to\ k} = -\dot{m}_{k\ to\ R1} = \dot{m}_c + \dot{m}_k \tag{2.74}$$

$$\dot{m}_{R2\ to\ R1} = \dot{m}_c + \dot{m}_k + \dot{m}_{R1} \tag{2.75}$$

$$\dot{m}_{h\ to\ e} = -\dot{m}_{e\ to\ h} = \dot{m}_e \tag{2.76}$$

$$\dot{m}_{R2\ to\ h} = -\dot{m}_{h\ to\ R2} = \dot{m}_e + \dot{m}_h \quad 2.77$$

$$\dot{m}_{R1\ to\ R2} = \dot{m}_e + \dot{m}_h + \dot{m}_{R2} \quad 2.78$$

Based on these equations, the relation between the gas flow rate passes through boundaries and gas mass variations in each space is known. Also, the instantaneous mass of gas in each space can be calculated as:

$$m_i = \rho_i V_i; \quad i: h, k, R1, R2, e, c \quad 2.79$$

Furthermore, T_{ij} which is the temperature of the gas passing through the boundary, can be identified based on the gas flow direction. It means if the gas flows from space i to space j, $\dot{m}_{i\ to\ j}$ will be positive and $T_{ij} = T_{ji} = T_i$, otherwise, $T_{ij} = T_{ji} = T_j$.

2.3 Thermodynamic Analysis

After developing dynamic and thermic models of the FPSE, they should be coupled to develop the thermodynamic one. With the thermodynamic model, it would be possible to study the FPSE behavior in detail. The thermodynamic model provides information about the pistons' movements, gas temperatures in different spaces, the thermal balance of the system, and the FPSE output power.

There are two important points that should be considered while developing a model. The first is about knowing the equations and the relations between them, and the second is the order in which the equations must be solved. The first point was already presented in sections 2.1 and 2.2. Here the second point, which is about linking the equations of each section, will be discussed. This linking will help to use the equations in an appropriate order to get to the requested results.

The first things that should be clarified are the inputs and outputs of the system as it is shown in Figure 2.4.

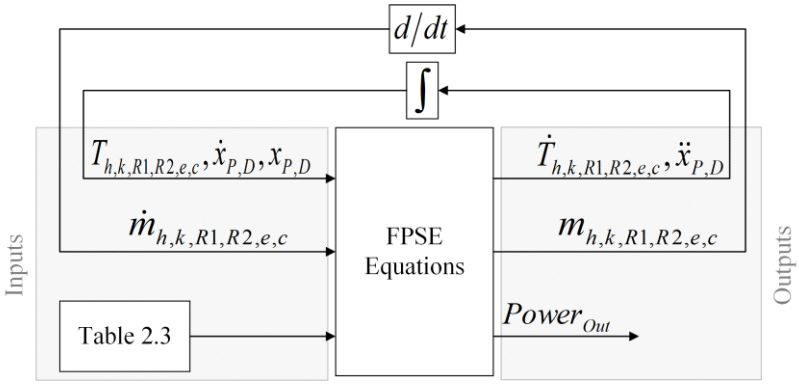

Figure 2.4: Inputs and outputs of the FPSE model

Two sets of inputs can be seen in Figure 2.4: variable and constant inputs. Variable inputs are the inputs calculated by integration or derivation of the outputs at each time step. Constant inputs are initial values and the parameters that were already shown in Table 2.3. In should be noted that in Figure 2.4 the integral sign can represent one or two integrations.

It should be noted that the wall temperatures in the regenerator (T_{R1} and T_{R2}) were calculated based on the linear temperature distribution assumption as was shown in Figure 2.2. Now, to link the equations, the suggested order to use the equations and develop the FPSE model is presented in Table 2.4.

Table 2.4: FPSE modeling steps

1	Eq. 2.24	12	Repeat 4-11 with new ρ
2	Eq. 2.21	13	Eq. 2.6
3	Eq. 2.14	14	Eq. 2.1
4	Eq. 2.13	15	Eq. 2.2
5	Eq. 2.4	16	Eq. 2.79
6	Eq. 2.5	17	Eq. 2.73-2.78
7	Eq. 2.3	18	Eq. 2.66
8	Eq. 2.10	19	Eq. 2.65
9	$\Delta P = \sum \Delta P_i$	20	Eq. 2.64
10	Eq. 2.16-2.20	21	Eq. 2.67-2.72

11	Eq. 2.15

To start the procedure of Table 2.4, since the pressure in each space is unknown, it is assumed to be equal to the mean pressure and an initial value of ρ (function of P_i) was used. Then after recalculating ρ in step 11 with calculated P_i values from step 9, steps 4-11 will be repeated until the new calculated ΔP has a difference less than 1% compared to the old one.

Now, the results of the FPSE thermodynamic modeling will be presented and studied. First, to show the reliability of the presented model, it is validated with existed experimental results of Schreiber et al. [60] at the same working condition and input data of Table 2.3. The validation results are shown in Table 2.5.

Table 2.5: FPSE validation

	Experimental [60]	Theoretical
Power (W)	1000	1001
Frequency (Hz)	30.2	28.84
Phase Shift (°)	47.6	34.51
Piston Stroke (cm)	2.32	2.97
Displacer Stroke (cm)	2.55	2.45
Efficiency (%)	27.4	28.74

As can be seen in Table 2.5, the FPSE model is valid. Now, the thermodynamic results of the FPSE modeling at the same conditions of Table 2.5 will be presented. First, to show the transition from transient operation to steady-state operation, the pistons' displacements and velocities from transient to steady-state are shown in Figure 2.5 and Figure 2.6.

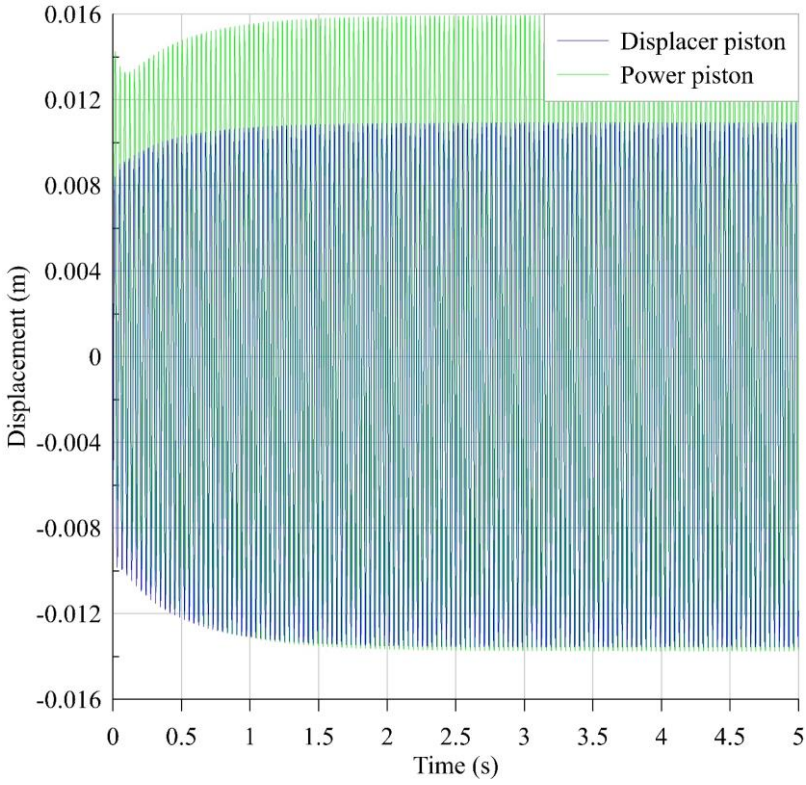

Figure 2.5: Pistons' displacements from transient to steady-state

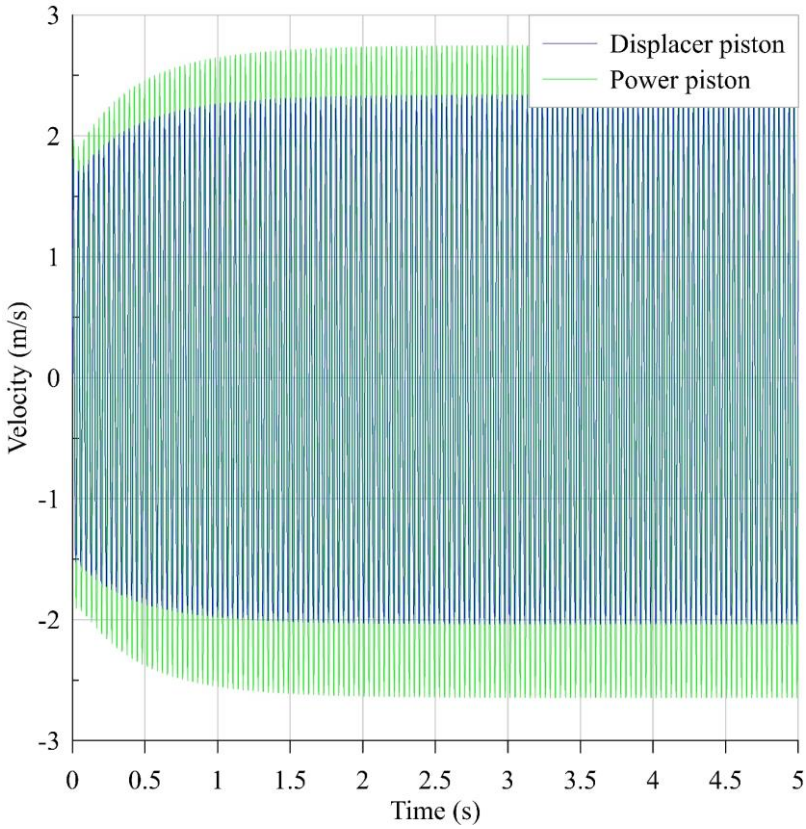

Figure 2.6: Pistons' velocities from transient to steady-state

As can be seen in Figure 2.5 and Figure 2.6, the system will find its steady-state in less than 5 seconds. Furthermore, the Pressure-Volume diagrams for expansion and compression spaces are shown for the same period of time of Figure 2.5 and Figure 2.6 in Figure 2.7 and Figure 2.8.

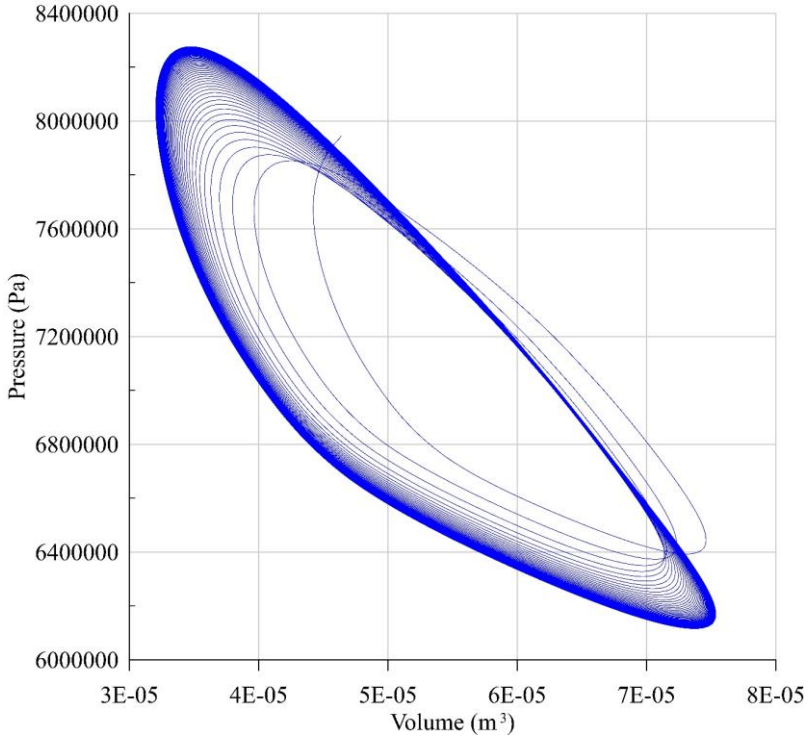

Figure 2.7: P-V diagram of compression space

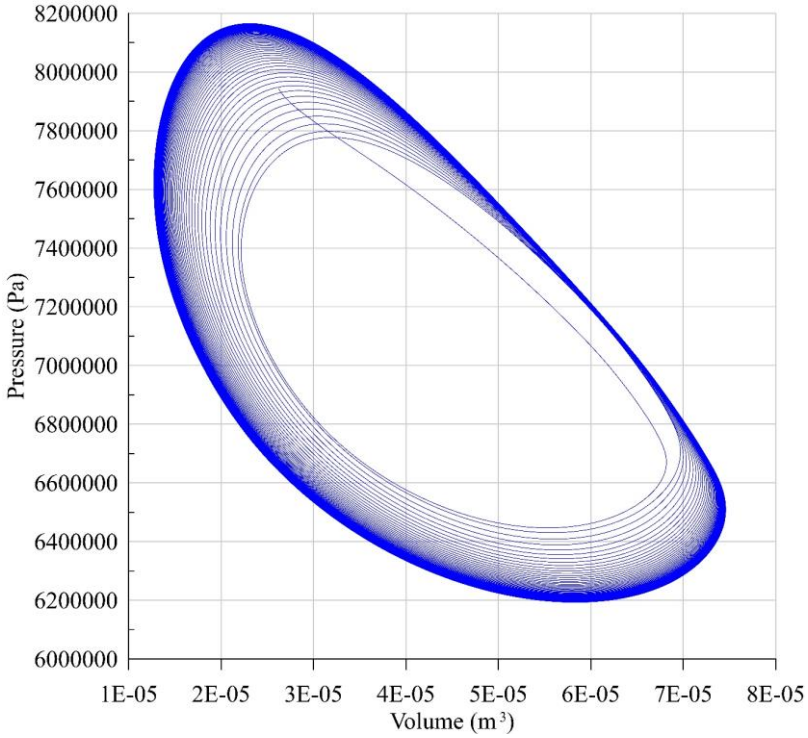

Figure 2.8: P-V diagram of expansion space

In Figure 2.7 and Figure 2.8, from another point of view, the transition from transient to steady-state operation can be seen. To have a better look at the system behavior in the transient state, the results of the FPSE modeling at the first 0.5 seconds are presented in Figure 2.9 - Figure 2.14.

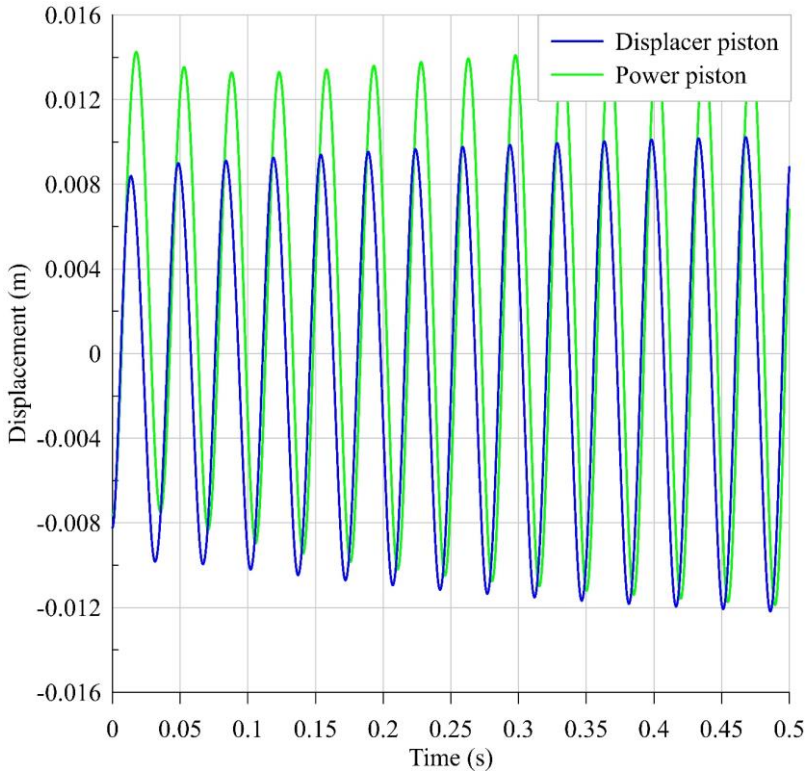

Figure 2.9: Pistons' displacements in the transient state

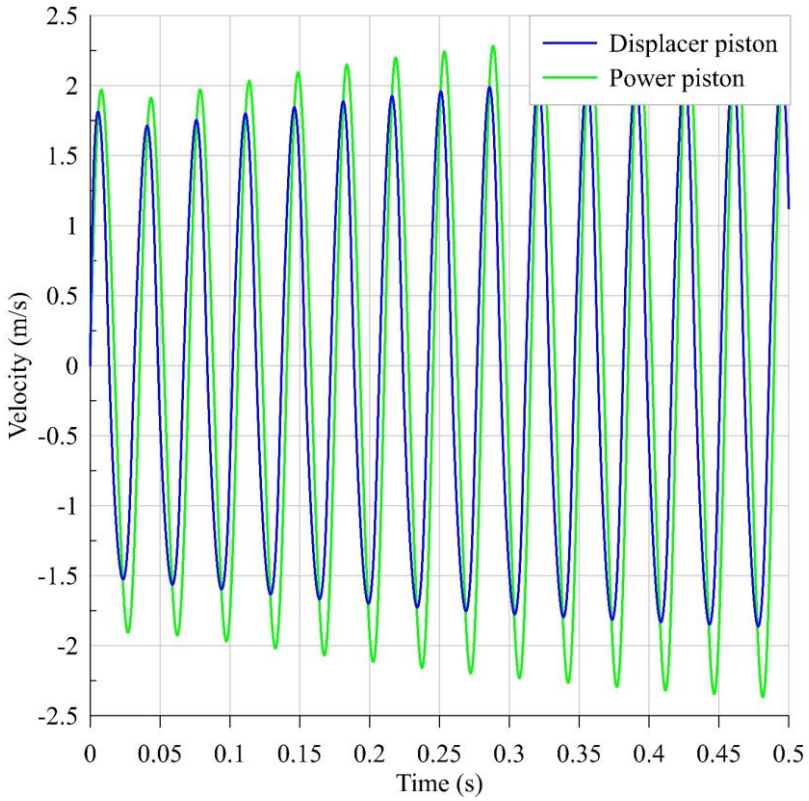

Figure 2.10: Pistons' velocities in the transient state

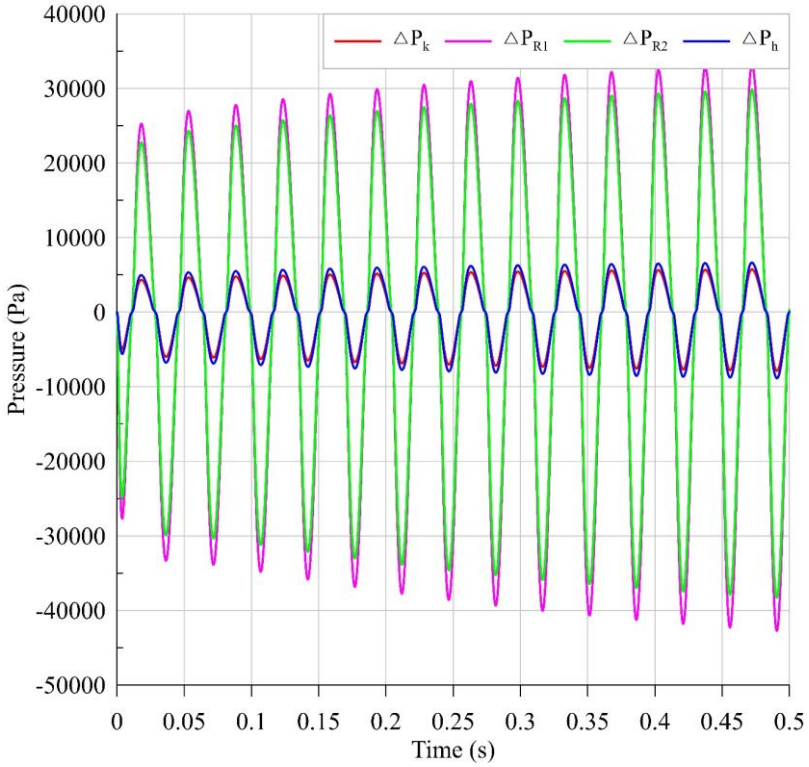

Figure 2.11: Pressure drops in the transient state

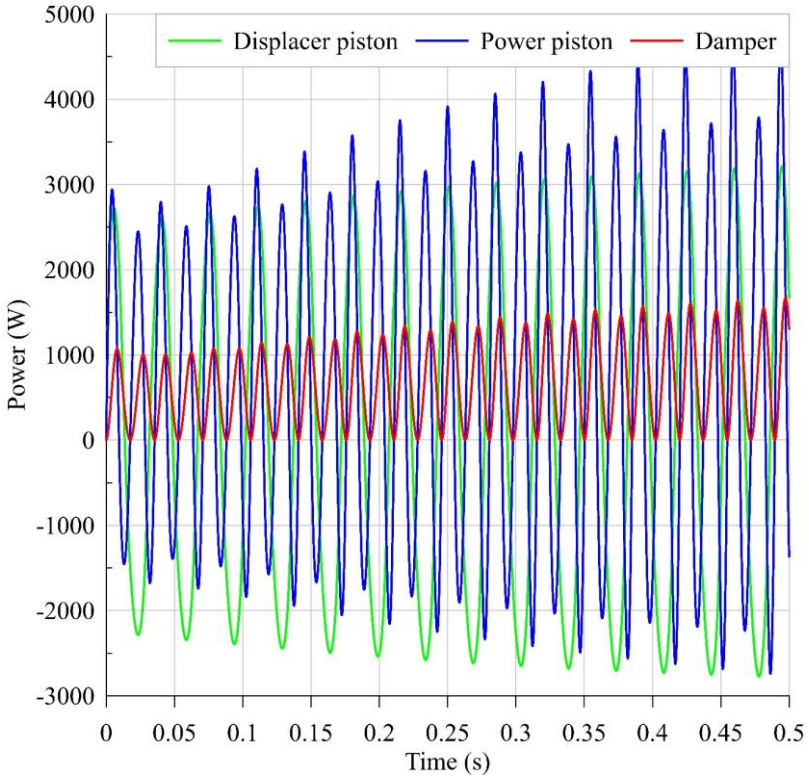

Figure 2.12: Pistons and damper work in the transient state

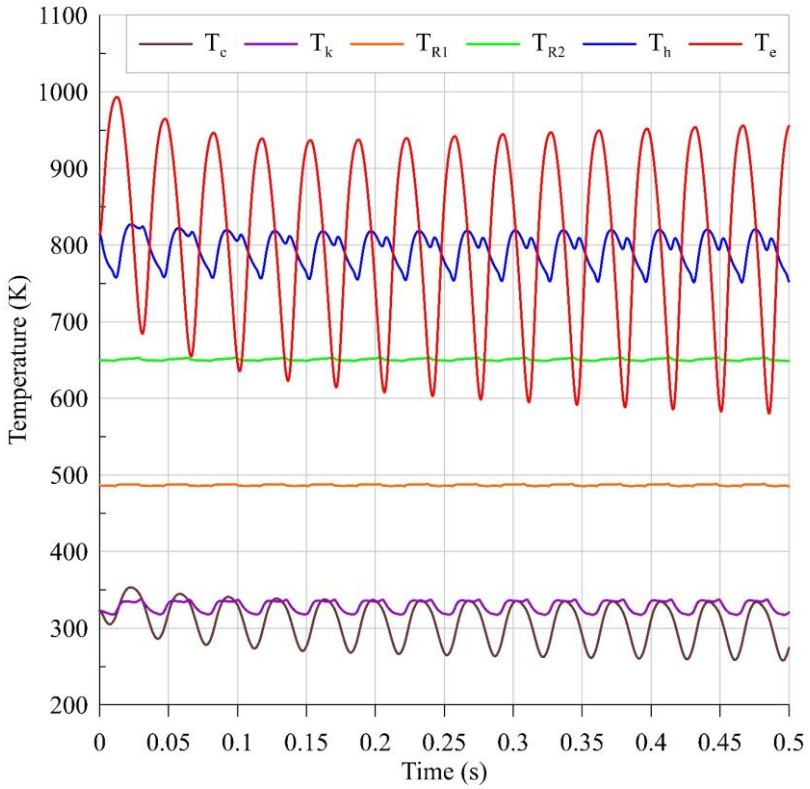

Figure 2.13: Spaces' temperature variations in the transient state

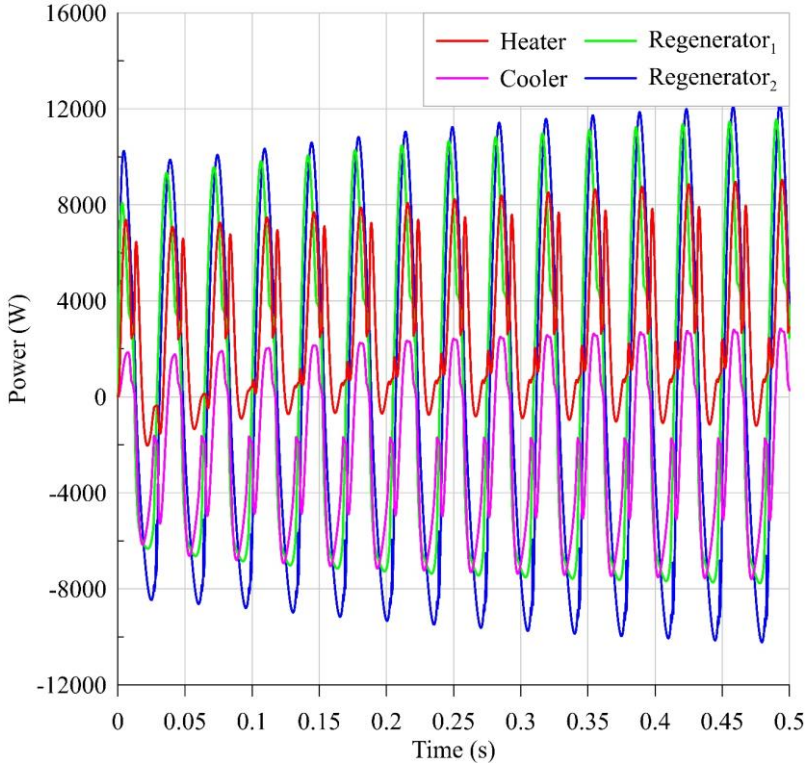

Figure 2.14: Spaces' heat transfer in the transient state

Now, to show the steady-state response, the same results are presented for one steady-state cycle in Figure 2.15 - Figure 2.20.

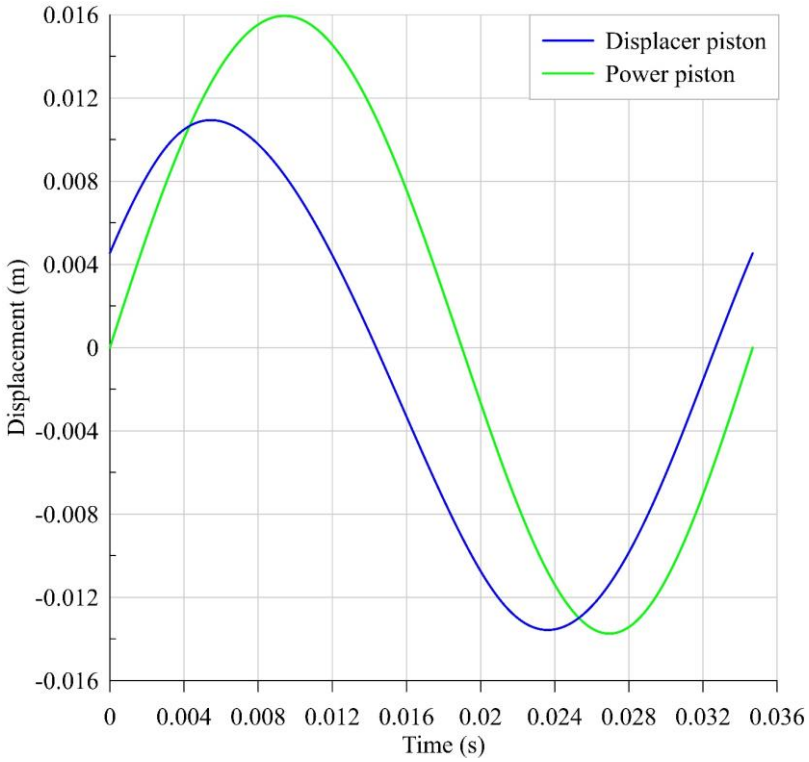

Figure 2.15: Pistons' displacements in one steady-state cycle

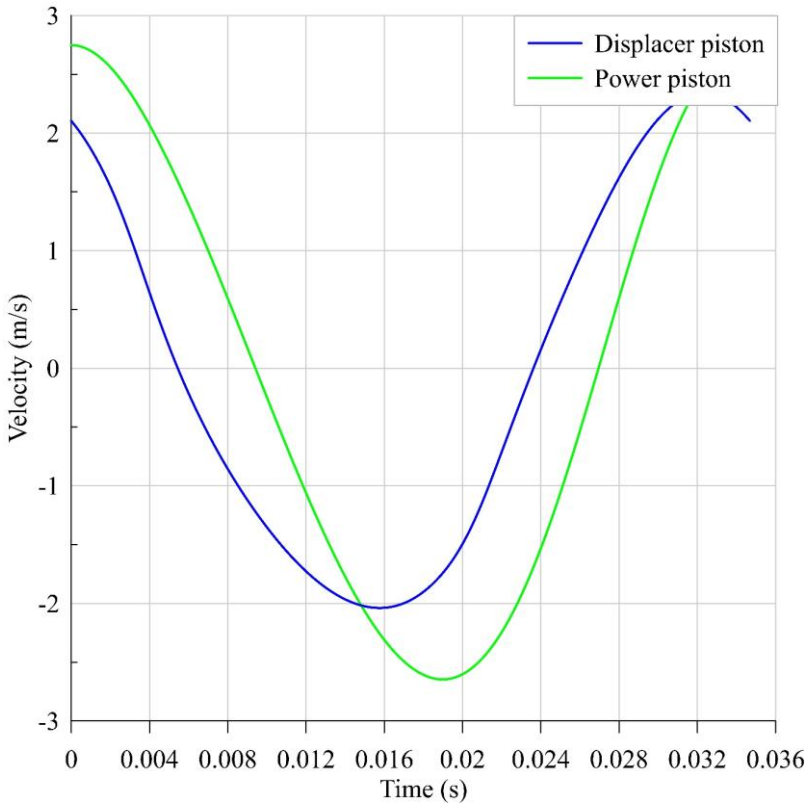

Figure 2.16: Pistons' velocities in one steady-state cycle

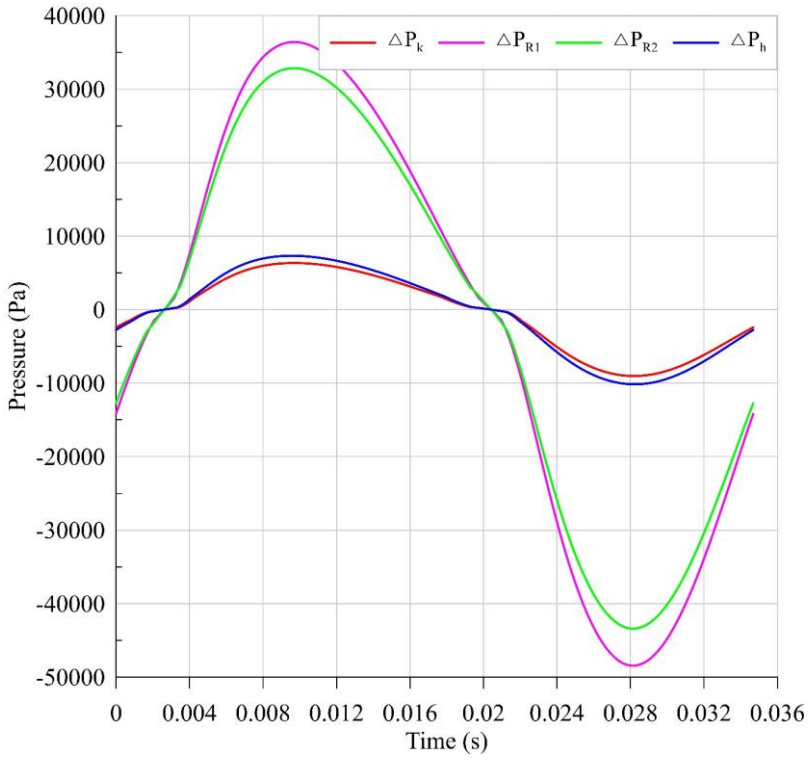

Figure 2.17: Pressure drops in one steady-state cycle

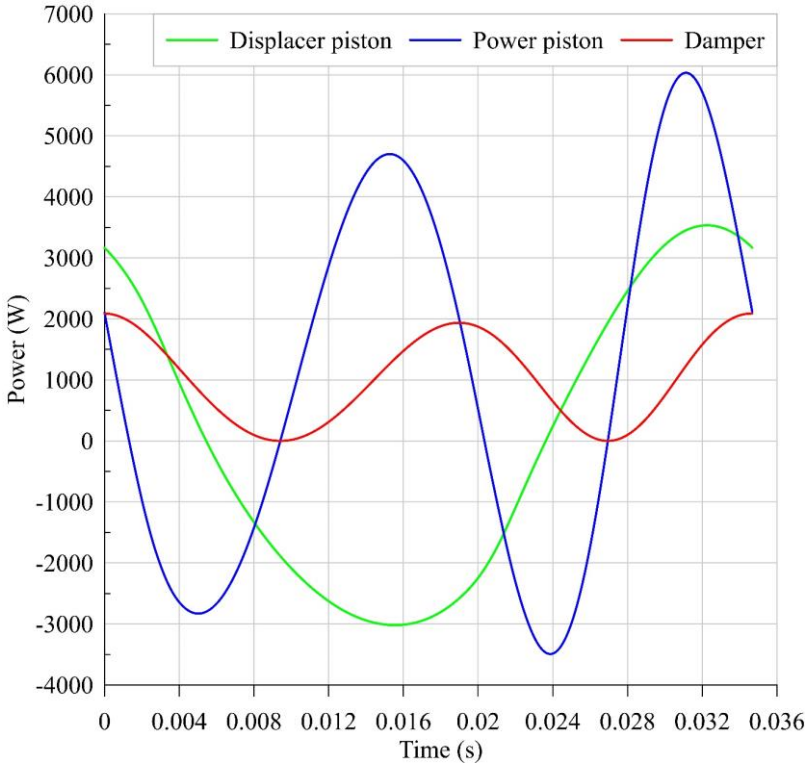

Figure 2.18: Pistons and damper work in one steady-state cycle

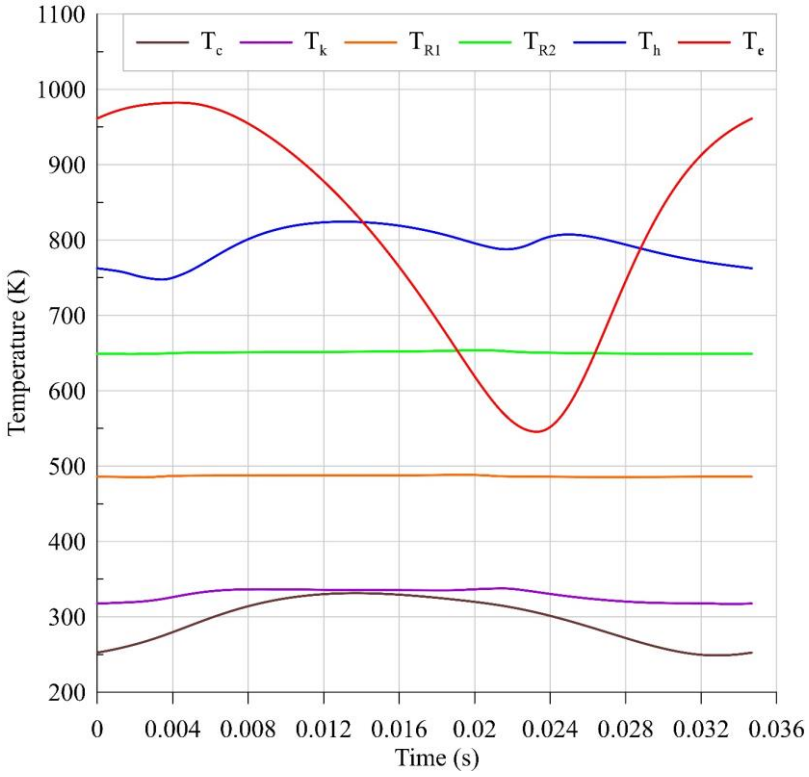

Figure 2.19: Spaces' temperature variations in one steady-state cycle

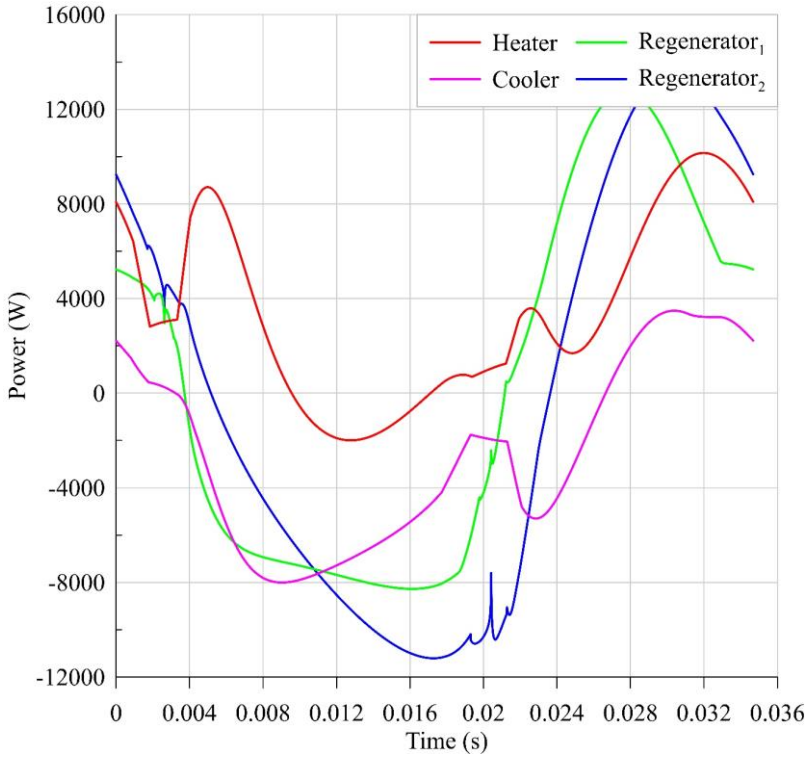

Figure 2.20: Spaces' heat transfer in one steady-state cycle

As shown in pistons' displacements and velocities figures (Figure 2.5, Figure 2.6, Figure 2.9, Figure 2.10, Figure 2.15, and Figure 2.16), the behavior of the system, as it is expected, is almost sinusoidal.

As can be seen in Figure 2.11 and Figure 2.17, the regenerator, due to its porous media, has the highest pressure drop. Furthermore, the pressure drop in the heater and cooler are at the same order of magnitude and smaller compared to the regenerator pressure drop.

The pistons and damper work are shown in Figure 2.12 and Figure 2.18. Here, the meaning of the pistons and damper work is the work which is done on them. The damper work can be calculated based on Equation 2.54. The pistons work can also be calculated based on Figure 2.21 and the following equation (the parameters which were used in this equation were defined in Figure 2.21):

$$\dot{W}_{piston} = A(P_1 - P_2)\dot{x} \qquad 2.80$$

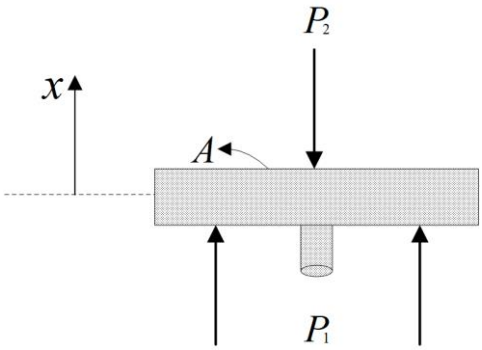

Figure 2.21: A piston and pressures around it

The variation of gas temperature in different spaces is also shown in Figure 2.13 and Figure 2.19. As can be seen in these figures, due to the porous media of the regenerator, and its thermal storage characteristic, its temperature is almost constant. Also, expansion space has the maximum variation of the temperature. This variation directly affects the heater temperature, which causes it to have a higher variation than the cooler temperature. In general, temperature variation in the heater and cooler compared to the expansion and compression spaces are smaller due to the constant wall temperature assumption that was made and also the constant volumes of these spaces.

At the end, the heat transfer of different spaces is shown in Figure 2.14 and Figure 2.20.

2.4 Enthalpy Pumping Loss

One of the most important parameters in heat-work conversion machines, like the Stirling engine, is their internal energy losses. These losses have a significant impact on the machine's performance and decrease its efficiency. Thus, taking these losses into account when modeling heat-work conversion machines is very important to have accurate results. Now, that a precise thermodynamic model of the FPSE system was developed, the effect of this loss on the system can be studied.

Displacer gap losses have been underestimated in the Stirling engines in the past [66]. These losses can be divided into two categories: enthalpy pumping and shuttle effect [3,66]. The first is significant, especially for FPSEs, because, due to stability and starting issues, these systems usually use relatively higher clearances around pistons [67,68]. This clearance causes gas leakage between expansion and compression spaces, which results in the so-called

enthalpy pumping [69,70]. Also, each time that the displacer moves from one side to another side, it absorbs some heat from the hot side and rejects it to the cold side. This last effect is called the shuttle heat transfer or loss [69,70]. Since the enthalpy pumping directly affects the pressure variation and energy balance of the expansion and compression spaces due to the gas leakage between them, the focus will be on the enthalpy pumping in the FPSE.

Enthalpy pumping happens due to the short-circuit-like flow between the compression and the expansion spaces. This short-circuit-like flow through the cylinder-displacer gap is due to the instantaneous pressure difference between the compression and expansion spaces as well as to the displacer periodic motion. First of all, one had to notice that the enthalpy pumping value affects the performance of the Stirling engine: less enthalpy pumping means better engine performances and vice versa. However, the enthalpy pumping does not directly represent a value to be deduced from the computed engine useful work obtained without this gap flow effects.

Two methods may be used to compute the enthalpy pumping that are the one-way or decoupled method, or the two-way or coupled method. In fact, the gas flow through the displacer gap and the compression-expansion spaces pressure difference are interconnected, and each affects the other, as will be shown in the following sections. In the coupled method, which is an iterative method, the gas leakage flow computed in each iteration is used to correct the spaces' pressure difference for the next iteration. Here, the results given by the coupled and the decoupled models will be compared and the best one will be chosen. The decoupled method was generally considered by recent researchers [69,70], while the coupled method is a new method which is developed in the present study.

2.4.1 Decoupled Model

The decoupled model developed here is an adaptation of the general study of Mabrouk et al. [69,70] to the special case of the FPSE. This method is based on the extraction of the required data (velocities, pressures, and displacements of the different interior components and spaces) from the developed FPSE model and uses them to calculate the enthalpy pumping loss. Then the displacer gap gas flow is computed as well as the resulting enthalpy leakage. The flowchart of the decoupled model is shown in Figure 2.22.

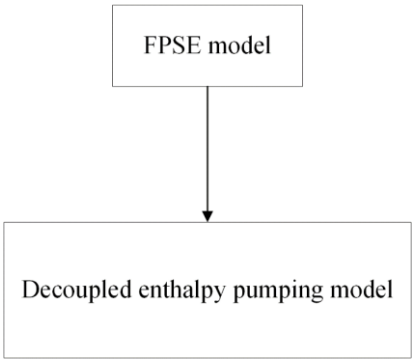

Figure 2.22: Flowchart of the decoupled enthalpy pumping model

As can be seen in Figure 2.22, there is no coupling here since the engine thermodynamic simulation and the displacer-cylinder gap flow computations are performed sequentially without any computation iterative schema. The schematic of the gap with respected coordinates is shown in Figure 2.23.

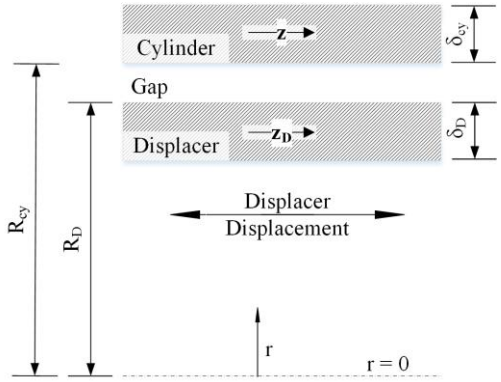

Figure 2.23: Displacer gap coordinates

The formulation of the momentum and energy equation of the fluid flowing in the gap is developed based on the coordinates shown in Figure 2.23. As can be seen in Figure 2.23, two coordinates are defined: one stationary coordinate (z), related to the cylinder, and one moving coordinate (z_D), related to the displacer. δ_{cy} and δ_D are thermal penetration depths in cylinder and displacer.

It is assumed that the temperature variation along z and z_D axis is linear with a slope equal to $\Gamma = \left(T_e^{average} - T_c^{average}\right)/l_D$. The average temperatures of expansion and compression spaces are assumed to be equal to the heater and cooler wall temperatures, respectively. Also, since the decoupled analysis is complicated, the constant temperature assumption for spaces is applied. It means, the non-linear dynamic model of section 2.1.1 with the isothermal

assumption is used for the decoupled calculation. Based on these assumptions, and also on the fact that the gas flow between the compression and the expansion spaces related to the displacer displacement introduces a periodic boundary condition on the cylinder and the displacer surfaces. The respective displacer and cylinder temperatures can be divided, with respect to the time t, into an oscillating part and a constant part. They can be identified as [69]:

$$T_{cy}(z,r,t) = T_{ref} - \Gamma z + \tilde{T}_{cy}(r,t) \quad 2.81$$

$$T_D(z_D,r,t) = T_{ref} - \Gamma z_D + \tilde{T}_D(r,t) \quad 2.82$$

$$z_D = z - x_D(t) \quad 2.83$$

$$T_D(z,r,t) = T_{ref} - \Gamma z + \Gamma x_D(t) + \tilde{T}_D(r,t) \quad 2.84$$

$$T_f(z,r,t) = T_{ref} - \Gamma z + \tilde{T}_f(r,t) \quad 2.85$$

T_{ref} is the reference temperature, which is the cylinder temperature at $z = 0$, and $x_D(t)$ is the displacer position.

For the fluid flow into the cylinder-displacer gap, based on the periodic displacer motion, and the compression and expansion spaces pressure variations, and assuming fully developed flow in the gap, the gas pressure, the gas flow velocity, the displacer position, and the displacer velocity can also be defined as:

$$P_f(z,t) = P_0(z) + \tilde{P}_f(z,t) \quad 2.86$$

$$u_f(r,t) = \tilde{u}_f(r,t) \quad 2.87$$

$$x_D(t) = \tilde{x}_D(t) \quad 2.88$$

$$u_D(t) = \tilde{u}_D(t) \quad 2.89$$

Notice that for the Stirling general case, the displacer position $x_D(t)$, that appears in Equations 2.84 and 2.88, is imposed by the engine mechanism following a predefined choice (e.g., Rhombic mechanism). For the present case of FPSE, this displacer position is not imposed but obeys the dynamic model that was defined by the developed model.

With the hypothesis mentioned above of laminar and fully developed flow in the gap, the momentum and energy equations for the fluid flow inside the gap can be written as [69]:

$$\frac{\partial \tilde{u}}{\partial t} = -\frac{1}{\rho_{f0}}\frac{\partial \tilde{P}}{\partial z} + \upsilon_{f0}\left(\frac{\partial^2 \tilde{u}}{\partial r^2} + \frac{1}{r}\frac{\partial \tilde{u}}{\partial r}\right) \quad 2.90$$

$$\frac{\partial \tilde{T}_f}{\partial t} + \frac{\partial T_{f0}}{\partial z}\tilde{u} - \frac{T_{f0}\beta_0}{\rho_{f0}Cp_{f0}}\frac{\partial P}{\partial t} = \alpha_{f0}\left(\frac{\partial^2 \tilde{T}_f}{\partial r^2} + \frac{1}{r}\frac{\partial \tilde{T}_f}{\partial r}\right) \quad 2.91$$

Heat conduction in displacer and cylinder can be considered by the following equations:

$$\frac{\partial T_{cy}}{\partial t} = \alpha_{cy0}\left(\frac{\partial^2 T_{cy}}{\partial r^2} + \frac{1}{r}\frac{\partial T_{cy}}{\partial r}\right) \quad 2.92$$

$$\frac{\partial T_D}{\partial t} = \alpha_{D0}\left(\frac{\partial^2 T_D}{\partial r^2} + \frac{1}{r}\frac{\partial T_D}{\partial r}\right) \quad 2.93$$

To solve all these equations, the boundary conditions should be defined. For the gas velocity, the non-slip boundary condition is applied:

$$u_f(R_D, t) = u_D(t) \quad 2.94$$

$$u_f(R_{cy}, t) = 0 \quad 2.95$$

Relating to the conductive heat transfer with respect to the radial direction in the displacer and the cylinder, since the frequency of the surface periodic boundary layers in the cylinder and the displacer are relatively high, the respective penetration depths, δ_{cy} and δ_D, are small. Hence, one may assume that in the cylinder and displacer, the respective penetration depths, δ_{cy} and δ_D are steady and are not affected by the gas flow inside the gap. It gives the two following boundary conditions:

$$\tilde{T}_{cy}(R_{cy} + \delta_{cy}, t) = 0 \quad 2.96$$

$$\tilde{T}_D(R_D - \delta_D, t) = 0 \quad 2.97$$

On the contact surfaces with the flowing gas, it can be assumed that the temperature of the latter is equal to the respective surface temperature of the cylinder and the displacer:

$$T_{cy}(z, R_{cy}, t) = T_f(z, R_{cy}, t) \quad 2.98$$

$$T_D(z, R_D, t) = T_f(z, R_D, t) \quad 2.99$$

On these contact surfaces, one had to consider also the heat flux continuity. It gives the two following boundary conditions:

$$K_{cy0}\frac{\partial T_{cy}(z,R_{cy})}{\partial r} = K_{f0}\frac{\partial T_f(z,R_{cy})}{\partial r} \quad 2.100$$

$$K_{D0}\frac{\partial T_D(z,R_D)}{\partial r} = K_{f0}\frac{\partial T_f(z,R_D)}{\partial r} \quad 2.101$$

At this level, all the governing Equations (2.81 to 2.93) and the boundary conditions (2.94 to 2.101) are known for the cylinder, the displacer, and the fluid that flows in the gap. Hence, the system of the equations can be solved.

2.4.1.1 Analytical solution of the developed decoupled model

Since the system has a periodic behavior, the variables can be expressed as the Fourier series [71]. By considering complex notation, Equations 2.81 to 2.89 can be re-written as:

$$T_D^*(z,r,t) = T_{ref} - \Gamma z + \Gamma x_D(t) + \sum_{n=1}^{\infty} T_{Dn}^*(r)e^{i\omega nt} \quad 2.102$$

$$T_{cy}^*(z,r,t) = T_{ref} - \Gamma z + \sum_{n=1}^{\infty} T_{cyn}^*(r)e^{i\omega nt} \quad 2.103$$

$$T_f^*(z,r,t) = T_{ref} - \Gamma z + \sum_{n=1}^{\infty} T_{fn}^*(r)e^{i\omega nt} \quad 2.104$$

$$P_f^*(z,t) = P_0(z) + \sum_{n=1}^{\infty} P_{fn}^*(z)e^{i\omega nt} \quad 2.105$$

$$u_f^*(z,r,t) = \sum_{n=1}^{\infty} u_{fn}^*(r)e^{i\omega nt} \quad 2.106$$

$$x_D^*(t) = \sum_{n=1}^{\infty} x_{Dn}^*(z)e^{i\omega nt} \quad 2.107$$

$$u_D^*(t) = \sum_{n=1}^{\infty} u_{Dn}^*(z)e^{i\omega nt} \quad 2.108$$

Now by rewriting Equations 2.90 to 2.93 in complex notation, it would be possible to solve them analytically. By reformulating these equations, the result is as:

$$\frac{\partial^2 u_{fn}^*}{\partial r^2} + \frac{1}{r}\frac{\partial u_{fn}^*}{\partial r} - \frac{in\omega}{\nu_{f0}}u_{fn}^* = \frac{1}{\rho_{f0}\nu_{f0}}\frac{\partial P_{fn}^*}{\partial z} \quad 2.109$$

$$\frac{\partial^2 T_{fn}^*}{\partial r^2}+\frac{1}{r}\frac{\partial T_{fn}^*}{\partial r}-\varepsilon_n^2 Pr T_{fn}^*=-\frac{i}{n\omega}\frac{\partial T_{f0}}{\partial z}\varepsilon_n^2 Pr u_{fn}^*-\varepsilon_n^2 Pr\frac{T_{f0}\beta_0}{\rho_{f0}Cp_{f0}}P_{fn}^* \quad 2.110$$

$$\frac{\partial^2 T_{cyn}^*}{\partial r^2}+\frac{1}{r}\frac{\partial T_{cyn}^*}{\partial r}-\varepsilon_n^2 Pr\sigma_{cy}T_{cyn}^*=0 \quad 2.111$$

$$\frac{\partial^2 T_{Dn}^*}{\partial r^2}+\frac{1}{r}\frac{\partial T_{Dn}^*}{\partial r}-\varepsilon_n^2 Pr\sigma_{D}T_{Dn}^*=0 \quad 2.112$$

In these equations, $\varepsilon_n=\sqrt{in\omega/\nu_{f0}}$, $\sigma_{cy}=\alpha_{f0}/\alpha_{cy0}$, and $\sigma_D=\alpha_{f0}/\alpha_{D0}$. All these equations have analytical solutions. Equation 2.109 is a modified Bessel equation and its solution is [72]:

$$u_{fn}^*=-\frac{1}{i\rho_{f0}n\omega}\frac{\partial P_{fn}^*}{\partial z}+E_nI_0(\varepsilon_n r)+D_nJ_0(\varepsilon_n r) \quad 2.113$$

I_0 and J_0 are first-order and second-order modified Bessel functions. The boundary conditions of Equations 2.94 and 2.95 can be re-written as:

$$u_{fn}^*(R_D,t)=u_{Dn}^*(t) \quad 2.114$$

$$u_{fn}^*(R_{cy},t)=0 \quad 2.115$$

Based on these boundary conditions, E_n and D_n can be calculated as:

$$E_n=\frac{\frac{1}{i\rho_{f0}n\omega}\frac{\partial P_{fn}^*}{\partial z}\left[J_0(\varepsilon_nR_{cy})-J_0(\varepsilon_nR_D)\right]+u_{Dn}^*J_0(\varepsilon_nR_{cy})}{I_0(\varepsilon_nR_D)J_0(\varepsilon_nR_{cy})-I_0(\varepsilon_nR_{cy})J_0(\varepsilon_nR_D)} \quad 2.116$$

$$D_n=\frac{\frac{1}{i\rho_{f0}n\omega}\frac{\partial P_{fn}^*}{\partial z}\left[I_0(\varepsilon_nR_D)-I_0(\varepsilon_nR_{cy})\right]}{I_0(\varepsilon_nR_D)J_0(\varepsilon_nR_{cy})-I_0(\varepsilon_nR_{cy})J_0(\varepsilon_nR_D)}+\frac{u_{Dn}^*}{J_0(\varepsilon_nR_D)-J_0(\varepsilon_nR_{cy})} \quad 2.117$$
$$\times\left(1-\frac{J_0(\varepsilon_nR_{cy})\left[I_0(\varepsilon_nR_D)-I_0(\varepsilon_nR_{cy})\right]}{I_0(\varepsilon_nR_D)J_0(\varepsilon_nR_{cy})-I_0(\varepsilon_nR_{cy})J_0(\varepsilon_nR_D)}\right)$$

These parameters are a function of the gas pressure gradient in the gap and also displacer velocity, which both govern the fluid in the gap. Finally, the gas velocity can be calculated as:

$$u_f(z,r,t)=\sum_{n=1}^{\infty}Real(u_{fn}^*)\,cos(n\omega t)-\sum_{n=1}^{\infty}Imaginary(u_{fn}^*)\,sin(n\omega t) \quad 2.118$$

Equations 2.110 to 2.112 also can be solved as follows:

$$T_{fn}^{*} = -\frac{\Gamma \frac{\partial P_{fn}^{*}}{\partial z}}{\rho_{f0}(n\omega)^2} + i\frac{Pr}{Pr-1}\frac{\Gamma}{n\omega}[E_n I_0(\varepsilon_n r) + D_n J_0(\varepsilon_n r)] + F_n I_0\left(\varepsilon_n r\sqrt{Pr}\right) + G_n J_0\left(\varepsilon_n r\sqrt{Pr}\right) + \frac{T_{f0}\beta_0}{\rho_{f0} Cp_{f0}} P_{fn}^{*} \quad 2.119$$

$$T_{cyn}^{*} = N_n I_0\left(\varepsilon_n r\sqrt{Pr\sigma_{cy}}\right) + O_n J_0\left(\varepsilon_n r\sqrt{Pr\sigma_{cy}}\right) \quad 2.120$$

$$T_{Dn}^{*} = Q_n I_0\left(\varepsilon_n r\sqrt{Pr\sigma_{D}}\right) + S_n J_0\left(\varepsilon_n r\sqrt{Pr\sigma_{D}}\right) \quad 2.121$$

In these equations, F_n, G_n, N_n, O_n, Q_n, and S_n can be calculated based on the boundary conditions that were already mentioned in Equations 2.96 to 2.101. These boundary conditions with complex notation are:

$$T_{cyn}^{*}(R_{cy} + \delta_{cy}, t) = 0 \quad 2.122$$

$$T_{Dn}^{*}(R_{D} - \delta_{D}, t) = 0 \quad 2.123$$

$$T_{cyn}^{*}(z, R_{cy}, t) = T_{fn}^{*}(z, R_{cy}, t) \quad 2.124$$

$$T_{Dn}^{*}(z, R_{D}, t) + \Gamma x_{Dn}^{*} = T_{fn}^{*}(z, R_{D}, t) \quad 2.125$$

$$K_{cy0}\frac{\partial T_{cyn}^{*}(z, R_{cy})}{\partial r} = K_{f0}\frac{\partial T_{fn}^{*}(z, R_{cy})}{\partial r} \quad 2.126$$

$$K_{D0}\frac{\partial T_{Dn}^{*}(z, R_{D})}{\partial r} = K_{f0}\frac{\partial T_{fn}^{*}(z, R_{D})}{\partial r} \quad 2.127$$

By using these boundary conditions, analytically or numerically, the values of F_n, G_n, N_n, O_n, Q_n, and S_n can be calculated.

Finally, the temperatures can be calculated as follows:

$$T_D(r, z, t) = T_{ref} - \Gamma z + \Gamma x_D + \sum_{n=1}^{\infty} Real(T_{Dn}^{*})\cos(n\omega t) - \sum_{n=1}^{\infty} Imaginary(T_{Dn}^{*})\sin(n\omega t) \quad 2.128$$

$$T_{cy}(r, z, t) = T_{ref} - \Gamma z + \sum_{n=1}^{\infty} Real\left(T_{cyn}^{*}\right)\cos(n\omega t) - \sum_{n=1}^{\infty} Imaginary\left(T_{cyn}^{*}\right)\sin(n\omega t) \quad 2.129$$

$$T_f(r,zt) = T_{ref} - \Gamma z + \sum_{n=1}^{\infty} Real\left(T_{fn}^*\right) cos(n\omega t) - \sum_{n=1}^{\infty} Imaginary\left(T_{fn}^*\right) sin(n\omega t) \quad 2.130$$

Now, based on the presented analytical solution, and assuming that the gas is perfect, computation of the gas velocity and temperature in the gap can be done, and the enthalpy pumping can be calculated.

2.4.1.2 The Enthalpy pumping expression and computation

In the specialized published works [69,70], the authors used the following expression to compute the enthalpy pumping:

$$\dot{H}_{pumping} = 2\pi \int_{R_D}^{R_{cy}} \left(\rho_{f0} Cp_{f0} u_f(T_f)\right) r dr \quad 2.131$$

However, this value may not be correct. Since the flow in both directions, from expansion space to compression space and vice versa, has a loss nature, in the present study, to compute enthalpy pumping, the absolute value of the fluid speed u_f is used as:

$$\dot{H}_{pumping} = 2\pi \int_{R_D}^{R_{cy}} \left(\rho_{f0} Cp_{f0} |u_f|(T_f)\right) r dr \quad 2.132$$

Equation 2.132 physically represents the arithmetic sum of the instantaneous total enthalpy that crosses the displacer-piston gap. T_f will first considered in the equation according to the study of Mabrouk et al. [69] and will also be replaced with $(T_e - T_c)$ to be similar to the method that is used for the coupled model. This provides two methods of enthalpy calculation for the decoupled model that will be compared with the developed coupled model. As stated above, it should be noted that this value of the enthalpy pumping that will be calculated based on Equation 2.132 is not the engine net power loss value that will be taken into account, but just the total enthalpy that will be transferred through the gap. This is the reason that the gas velocity in the gap in both directions (from compression space to expansion space and vice versa) is assumed to be positive, and $|u_f|$ is used for enthalpy pumping computations. To have a better view of the enthalpy and its real effect on the system as a loss, it should be considered in the frame of a complete thermodynamic model.

Now, the results of the decoupled model are presented. As can be seen in Equation 2.132, the gas flow temperature in the gap (T_f) is required to calculate the enthalpy pumping through the original equation (Equation 2.132). Thus, the temperature variations at different times and different gap sizes are presented in Figure 2.24 - Figure 2.27.

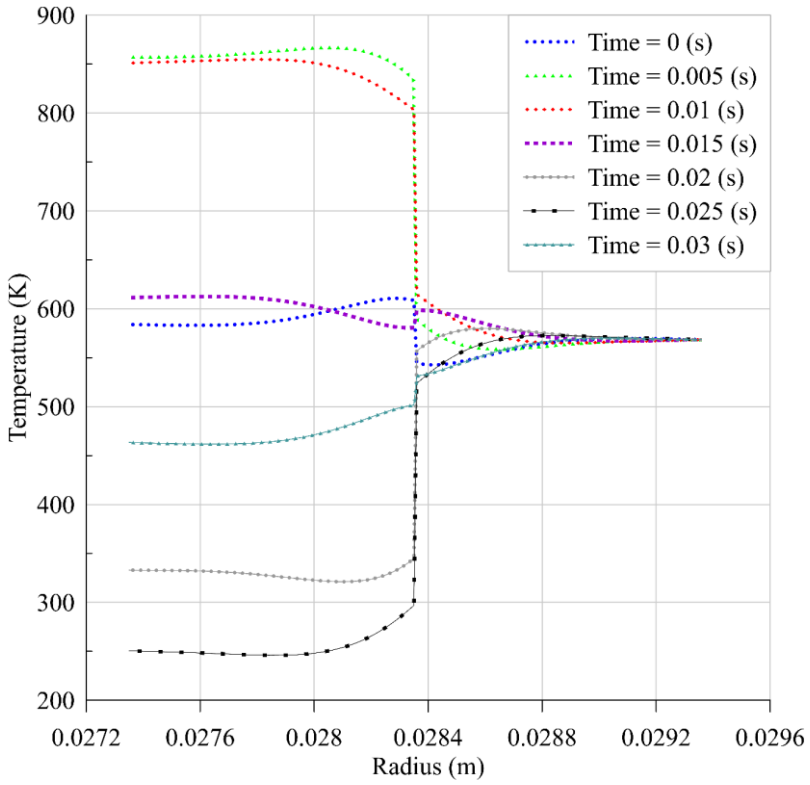

Figure 2.24: Flow temperatures in the gap = 10 μm

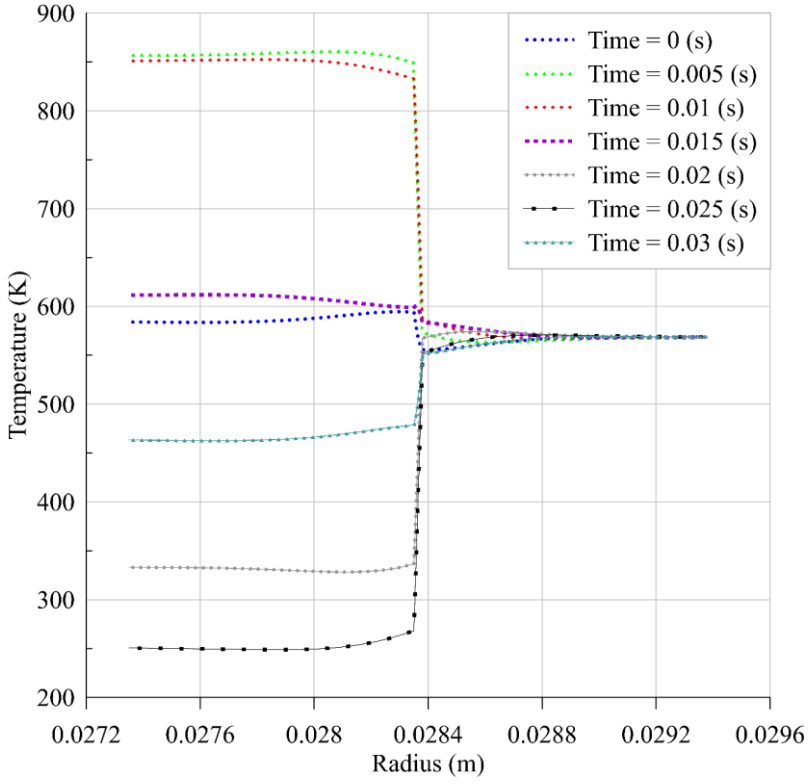

Figure 2.25: Flow temperatures in the gap = 30 μm

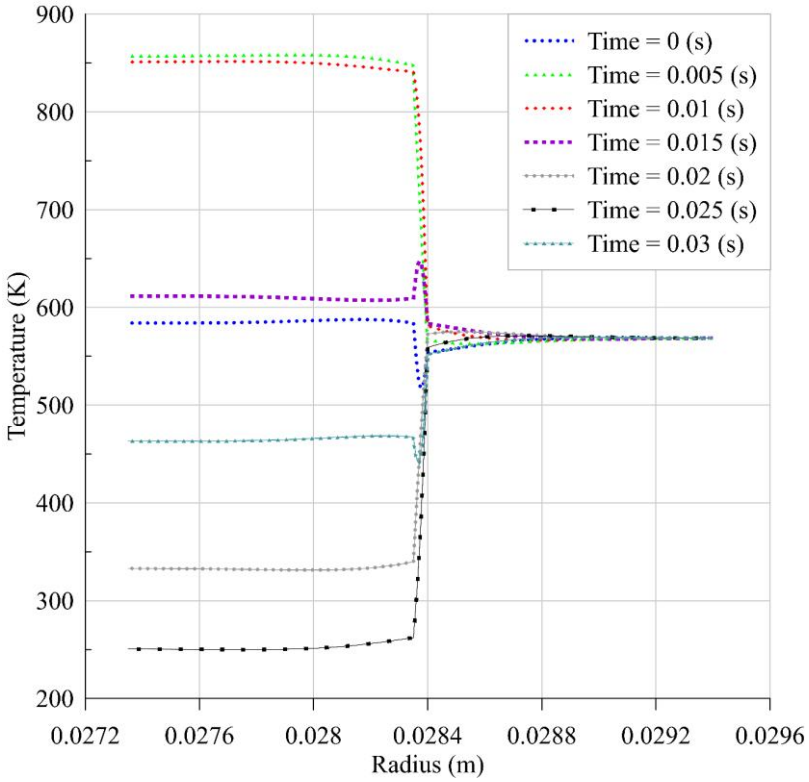

Figure 2.26: Flow temperatures in the gap = 50 μm

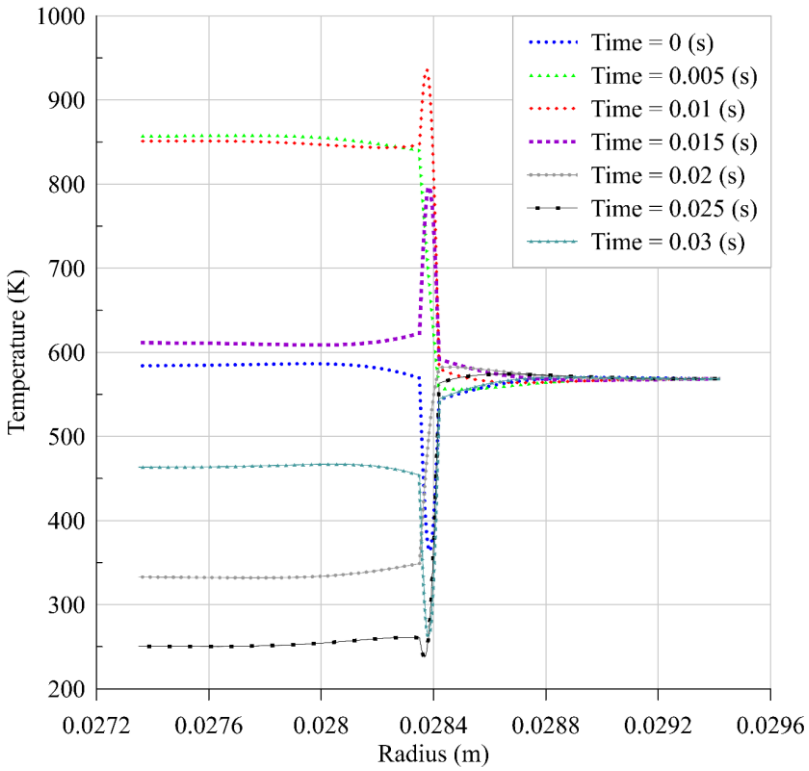

Figure 2.27: Flow temperatures in the gap = 70 μm

As shown in Figure 2.24 - Figure 2.27, the gas follows the boundary conditions and has a continuous temperature. By decreasing the gap size, the shape of the gas temperatures in the gap is getting more linear. Thus, as can be seen in Figure 2.24, for a gap equal to 10 μm, the gas temperature in the gap, that starts at 0.02835 (m), is almost linear at different times. Another important point is that for large gaps, like 70 μm that can be seen in Figure 2.27, the maximum gas temperature in the gap is getting too high/low that may not be physically correct. These results will be discussed later in detail. Here it may be concluded that using T_f in Equation 2.132 might not be precise enough for large gaps. Now, based on these temperatures (T_f), and also the idea of replacing T_f with $(T_e - T_c)$ that was explained after Equation 2.132, the enthalpy pumping is calculated through these methods for different gap sizes, and the results for a steady cycle of the FPSE are presented in Figure 2.28 and Figure 2.29.

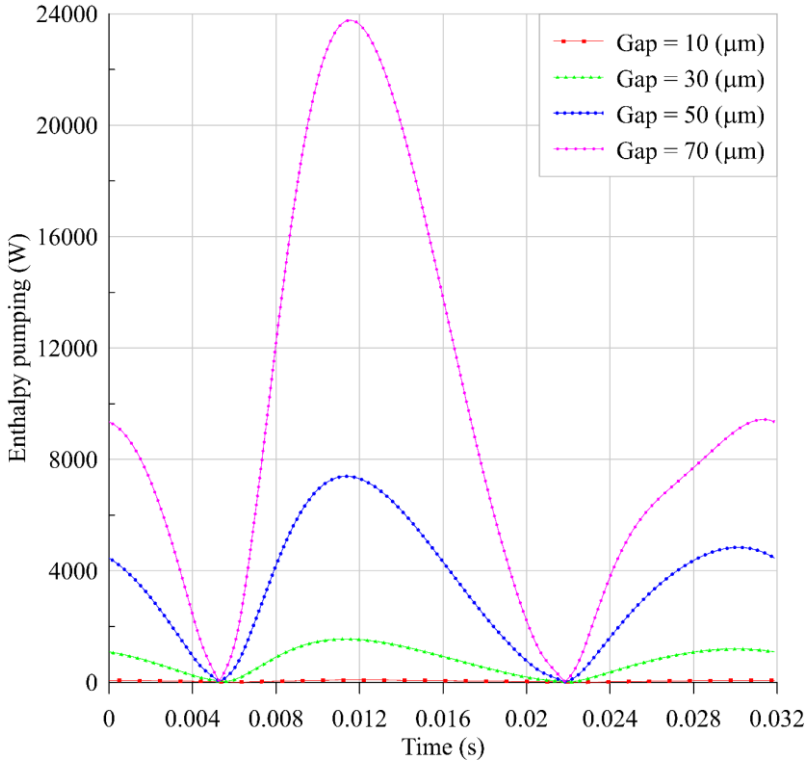

Figure 2.28: Decoupled enthalpy pumping at different gap sizes with T_f

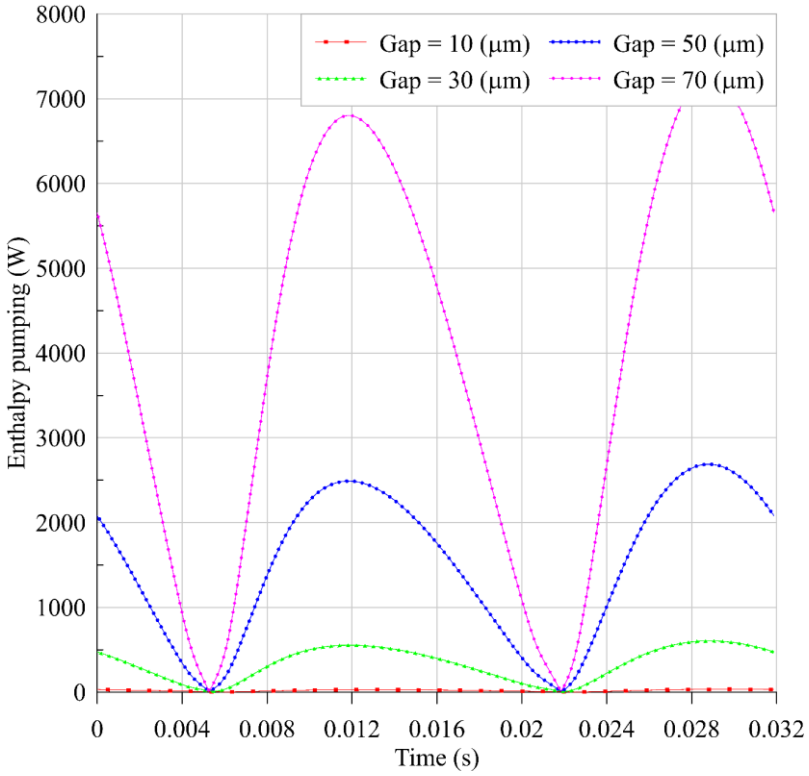

Figure 2.29: Decoupled enthalpy pumping at different gap sizes with $T_e - T_c$

The results of the decoupled model are in the same order as Mabrouk et al. [69] achieved in their research studies. As can be seen in Figure 2.28 and Figure 2.29, the computed values of the enthalpy pumping are too high, especially with the method of T_f computation. A part of this problem may be due to the unrealistic computed gas temperatures in the gap, as already discussed. Having an enthalpy pumping with an instantaneous maximum value of 24 kW for an FPSE with a net power of 1 kW, as it is shown in Figure 2.28, cannot be physically explained. Also, the maximum values around 7,5 kW in Figure 2.29 may not be realistic. This might be due to the fact that there is no interaction between the enthalpy pumping model and the FPSE dynamic model. All these come to the point that the decoupled model may not be the most accurate one for all the conditions, especially when the gap size is large, and another method of enthalpy pumping computation should be developed. Thus, a coupled model to compute the enthalpy pumping will be developed in the next section to consider the interaction between the enthalpy pumping model and the FPSE model.

2.4.2 Coupled Model

In order to have a better estimation of the enthalpy pumping, a new method to calculate it which is based on the instantaneous coupling between the FPSE thermodynamic model and enthalpy pumping model is developed in this section. In the coupled model, to see the thermal effect of the gap, an extra term which is the enthalpy pumping through the gap, will be added to the thermal equations of compression and expansion spaces (2.67 and 2.72). The new thermal balance equations will be as:

$$\dot{T}_c = \left(\frac{\dot{m}_{k\,to\,c} CpT_{kc} - \dot{W}_P + \dot{H}_{pumping}^{instantaneous} \times (u_f > 0)}{Cv} - \dot{m}_c T_c \right) \Big/ m_c \qquad 2.133$$

$$\dot{T}_e = \left(\frac{\dot{m}_{h\,to\,e} CpT_{he} - \dot{W}_D - \dot{H}_{pumping}^{instantaneous} \times (u_f < 0)}{Cv} - \dot{m}_e T_e \right) \Big/ m_e \qquad 2.134$$

$$\dot{H}_{pumping}^{instantaneous} = (\rho_f u_f A_{gap} C_p T_e) \times (u_f > 0) + (\rho_f u_f A_{gap} C_p T_c) \times (u_f < 0) \qquad 2.135$$

The terms of $(u_f > 0)$ and $(u_f < 0)$ will be equal to 1 when the gas velocity in the gap based on the coordinates of Figure 2.1 is positive and negative, respectively; otherwise, it will be equal to 0. The method of u_f calculation for the coupled model will be discussed later (Equation 2.137).

To see the dynamic effect of the gap, an iterative loop is set up to correct the pressure difference between the compression and expansion spaces, as shown in the Flowchart of Figure 2.30.

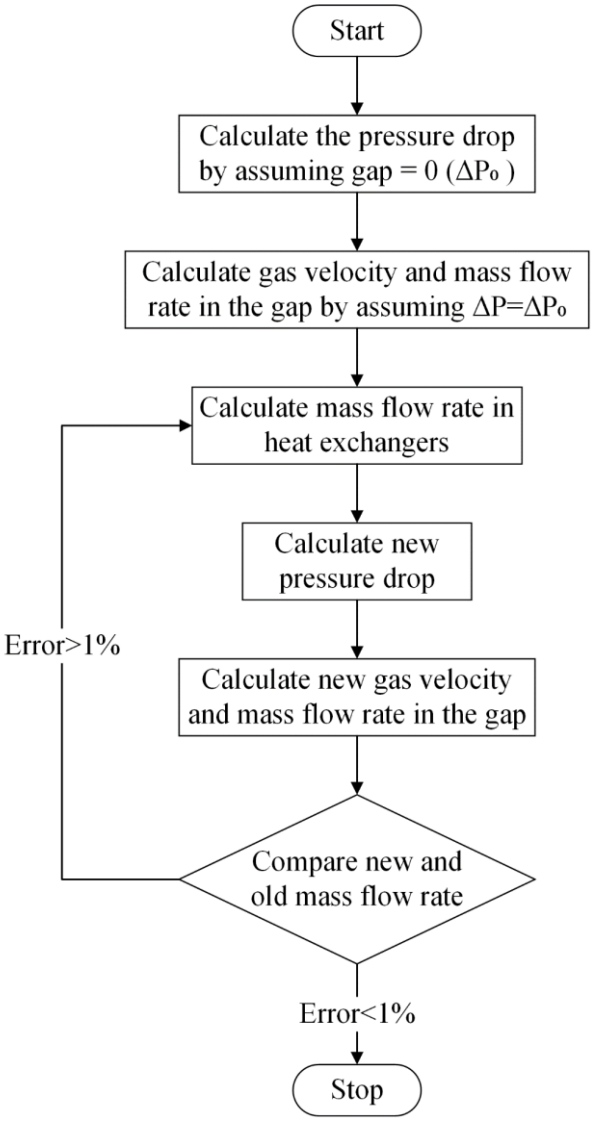

Figure 2.30: Flowchart of pressure drop correction based on the coupled model

In fact, the pressure difference that stands between the compression and expansion spaces depends on the gas velocity through the engine Regenerator-Cooler-Heater path, and this velocity also depends on the gas leakage through the gap that obeys the compression-expansion pressures difference. The interrelationship between these two effects explains the need for an iterative computation procedure.

To calculate the enthalpy pumping in the coupled model, the important parameter that should be calculated is the average gas velocity in the gap with respect to r. To calculate this velocity at each time t, the above-mentioned iterative computing loop is performed as follow: starting with a compression-expansion pressure difference ΔP_0 which is computed assuming no-gas flow leakage through the gap, and the gas mass flow through the Heater-Regenerator-

Cooler path using Darcy law with a classic expression of friction coefficient (Equation 2.41). Then the gas velocity in the displacer-cylinder gap is computed as follow: assuming that the flow of the gas inside this gap consists of an annular Poiseuille flow, the momentum differential equation of the fluid velocity is a Hagen-Poiseuille equation [73]:

$$\frac{1}{r}\frac{\partial}{\partial r}\left(r\frac{\partial u_f}{\partial r}\right)=\frac{1}{\mu}\frac{\partial P_f}{\partial z} \tag{2.136}$$

The analytical solution of this equation is:

$$u_f(r)=-\frac{\Delta P}{4\mu L_D}r^2+D_1\,ln\,r+D_2 \tag{2.137}$$

To calculate the constants, boundaries conditions are needed. For the gas velocity, the non-slip boundary condition is applied:

$$u_f(R_D,t)=u_D(t) \tag{2.138}$$

$$u_f\left(R_{cy},t\right)=0 \tag{2.139}$$

D_1 and D_2 can be calculated based on these boundary conditions as:

$$D_1=\frac{\frac{\Delta P}{4\mu L_D}\left(R_{cy}^2-R_D^2\right)-u_D}{ln\,R_{cy}/R_D} \tag{2.140}$$

$$D_2=\frac{\frac{\Delta P}{4\mu L_D}\left(R_D^2\,ln\,R_{cy}-R_{cy}^2\,ln\,R_D\right)+u_D\,ln\,R_{cy}}{ln\,R_{cy}/R_D} \tag{2.141}$$

The mass flow rate in the gap is computed with the gas velocity given by Equations 2.137, 2.140, and 2.141. Then, to start the next iteration, this mass flow is subtracted from the former mass flow that passes through the Heater-Regenerator-Cooler path. Now, based on this new mass flow rate, the new pressure drop ΔP is calculated (Equation 2.41) to start a new iteration. This iterative procedure shown in Figure 2.30 is done for each time step and allows to rectify the mass flow rates by considering the leakage mass flow rate between the expansion and compression spaces.

When the iteration loop converges, on the one hand, the resulting ΔP is used for the displacer free-motion computation following Equations 2.1 and 2.2, and on the other hand, the resulting gap mass flow is used for the enthalpy pumping calculations.

Knowing the gas velocity in the gap, the advected (i.e., transported) enthalpy by this gas flow may be deduced [69]:

$$\dot{H}_{pumping} = 2\pi \int_{R_D}^{R_{cy}} \left(\rho_{f0} Cp_{f0} |u_f| (T_e - T_c)\right) r dr \qquad 2.142$$

The important point that should be noted here is that the coupled mode, as the decoupled one, use the linear temperature distribution in the gap, but with the instantaneous temperature of the spaces as $\Gamma = (T_e - T_c)/L_D$. Also, the difference between $\dot{H}_{pumping}$ (Equation 2.142) and $\dot{H}_{pumping}^{\text{instantaneous}}$ (Equation 2.135) is that $\dot{H}_{pumping}^{\text{instantaneous}}$ is the instantaneous enthalpy flow from one space to another through the gap while $\dot{H}_{pumping}$ is the enthalpy pumping loss. This is the reason that in the $\dot{H}_{pumping}$ the $(T_e - T_c)$ terms was appeared while in $\dot{H}_{pumping}^{\text{instantaneous}}$ only the temperature of the gas from the space that it comes from was used.

The results of the coupled enthalpy pumping model at different gap sizes are presented in Figure 2.31.

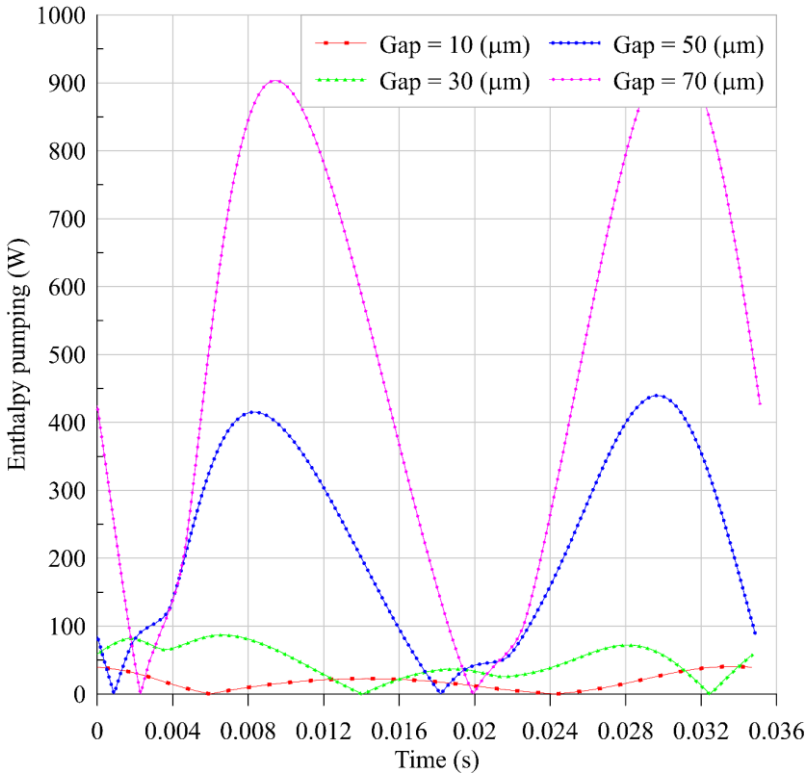

Figure 2.31: Coupled enthalpy pumping at different gap sizes

As can be seen in Figure 2.28, Figure 2.29, and Figure 2.31, the similar behavior for the coupled and decoupled models is that the enthalpy pumping is increasing dramatically with the gap size increment.

As already discussed, in the coupled model, the leakage will affect the system's operating parameters. Here this effect on these parameters is studied. The first is the gas temperature in expansion and compression spaces. The average gas temperature in each space varies due to the gas leakage between two spaces according to the energy balance equation (Equation 2.133 and 2.134). This temperature variation in different gap sizes is shown in Figure 2.32.

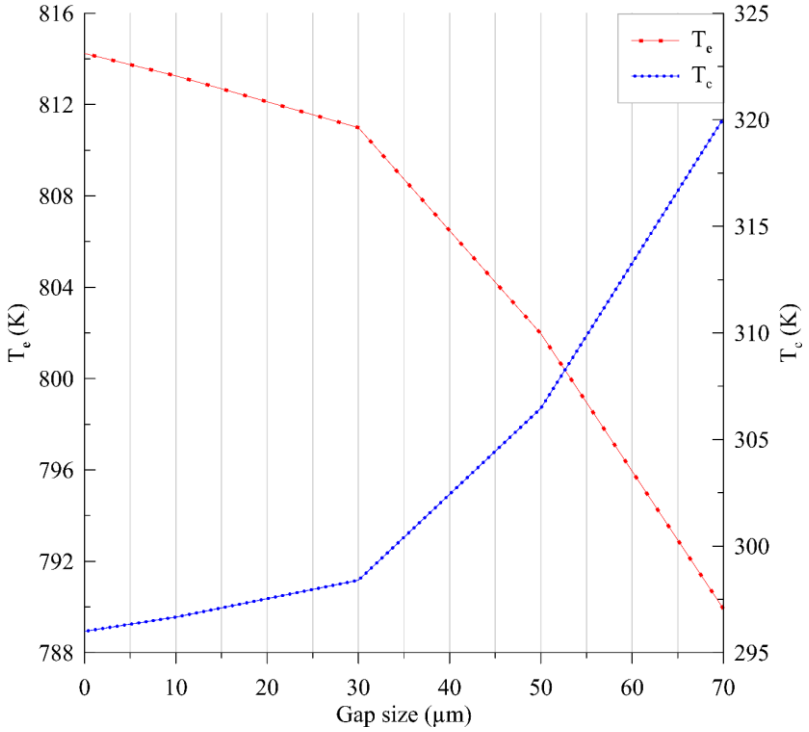

Figure 2.32: Effect of the gap size on the average gas temperature in expansion and compression spaces

As can be seen in Figure 2.32, due to the gas leakage, the average gas temperature in expansion space decreases, and the average gas temperature in compression space increases. This temperature variation without any power production affects the system performance.

The second parameter that is studied here is pressure drop. This parameter is affected by the gas leakage, as was already shown in Figure 2.30. The effect of gap size variations on the pressure drop is shown in Figure 2.33.

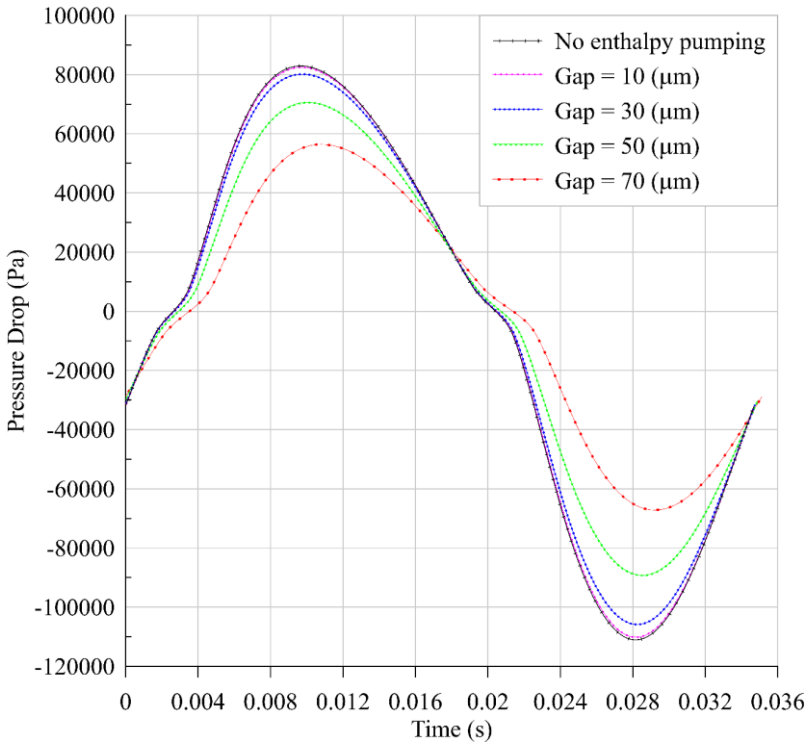

Figure 2.33: Effect of the gap size on the pressure drop

As can be seen in Figure 2.33, by gap size increment, the pressure drop is decreasing. The source of the pressure drop is the gas flow through the heat exchangers and regenerator. Due to the leakage and the short circuit flow between expansion and compression spaces, the gas flow through heat exchangers and regenerator decreases, and as a result, the pressure drop also decreases. As much as the gap size is increasing, the short circuit flow is increasing that results in the pressure drop decrement. This decrease of the pressure drop will decrease the leakage mass flow rate through the gap of the displacer.

The last parameters that the effect of the enthalpy pumping on them is studied are the output power and efficiency. Both recently studied parameters (average gas temperature and pressure drop) affect this final output of the system. The effect of enthalpy pumping on the FPSE power production and efficiency at different gap sizes is shown in Figure 2.34.

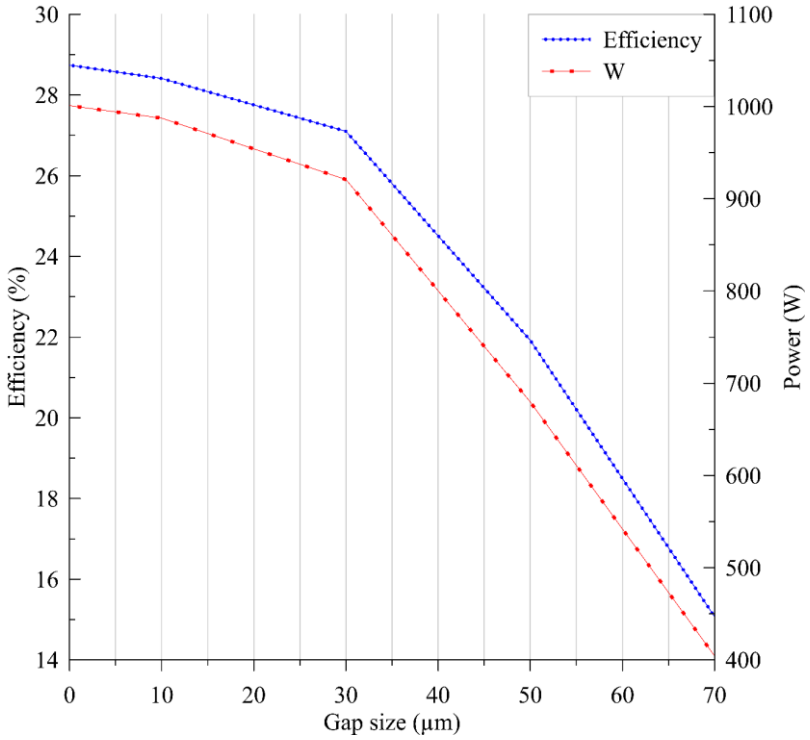

Figure 2.34: Effect of the gap size on the FPSE efficiency and power production

As shown in Figure 2.34, as much as the gap size and enthalpy pumping increase (as shown in Figure 2.31), the output power and efficiency decrease. By gap size increment, since the gas leakage increases, the gas volume that already did work also decreases. Also, the temperatures of the expansion and compression spaces are affected due to this leakage. Thus, the output power of the system and, as a result, the system efficiency decreases because of these two effects.

Now, to have a better comparison between the coupled and decoupled models, the time average values of the enthalpy pumping for one cycle are shown in Figure 2.34 for a gap size of 10-70 μm.

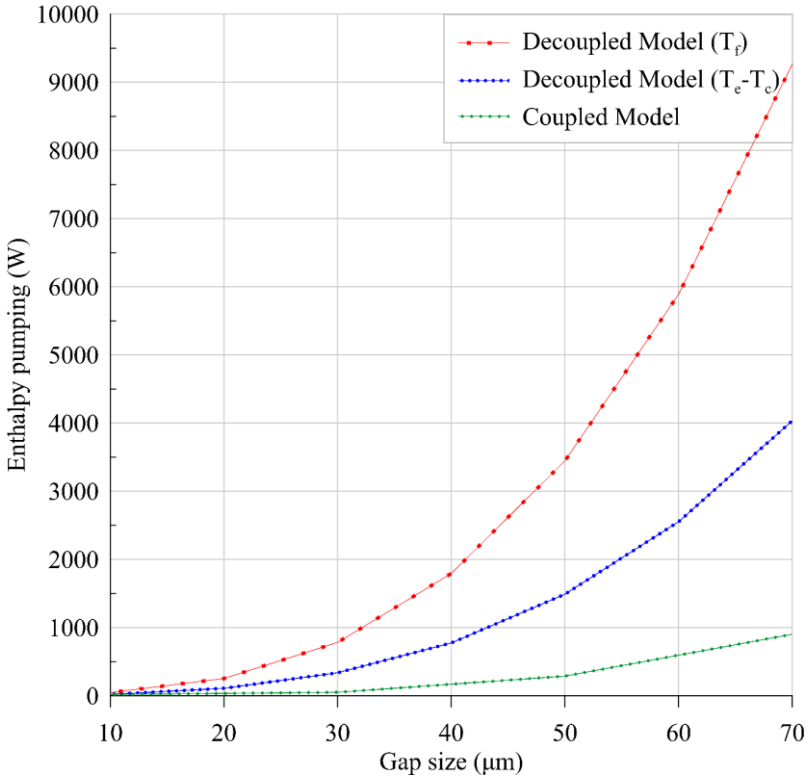

Figure 2.35: Coupled and decoupled enthalpy pumping comparison

It should be noted that the results of Figure 2.34 are extracted at the constant output power of 1 kW for both cases. It means, at different gap sizes, the damper coefficient of the coupled model is modified in a way to always have the output power of 1 kW. Although the fact that the decoupled model gives more details about the gas flow in the gap, it is important to note that for a 1 kW Stirling engine, the amount of enthalpy pumping, which is calculated based on the decoupled models and Equation 2.132, is too high. This can be explained by the fact that it does not take into account the impact of gas leakage on the pressure drop and the temperatures in the compression and expansion spaces. Another important point is that with the gap size variations, since the results of the decoupled model do not have any effect on the Stirling model (on the contrary to the coupled model that will update the pressure drop and temperature and modify the dynamic model), the output power and dynamic behavior of the system remain unchanged. Thus, the output power, amplitude ratio, phase change, frequency, and pressure drops, are not changed by considering the decoupled model. On the other side, as it was already shown for the coupled model, all these operating parameters are affected by the enthalpy pumping, and reversely, this effect is reflected in the enthalpy pumping calculation. Moreover, as it can be seen in Figure 2.31, the values of

enthalpy pumping calculated based on the coupled model are much more consistent for the FPSE compared to the decoupled models that are shown in Figure 2.28 and Figure 2.29 for a 1 kW FPSE. The same remark applies in Figure 2.34, where, even for large gap sizes, the average enthalpy pumping computed using the coupled model stays in a more consistent range.

As a result, it can be concluded that the effect of the enthalpy pumping on the operating parameters of the Stirling Engine is too high to be neglected. Thus, a decoupled model may not be the best alternative to estimate enthalpy pumping values as was used by Mabrouk et al. [69,70]. In their approach, even if the gap flow computation is sophisticated (Equation 2.81 to 2.132), their computation procedure is one-way based and shall be further considered in an iterative frame take into account the compression and expansion spaces pressure and thermal balance correction at each step.

3 FPSE-PMLSM CONTROL

3.1 First Control Method

After developing the thermodynamic model of the FPSE in chapter 2 and the electrodynamic model of the PMLSM and its adapted control in section 1.3, these two systems can be combined as already shown in Figure 1.26 and repeated here in Figure 3.1.

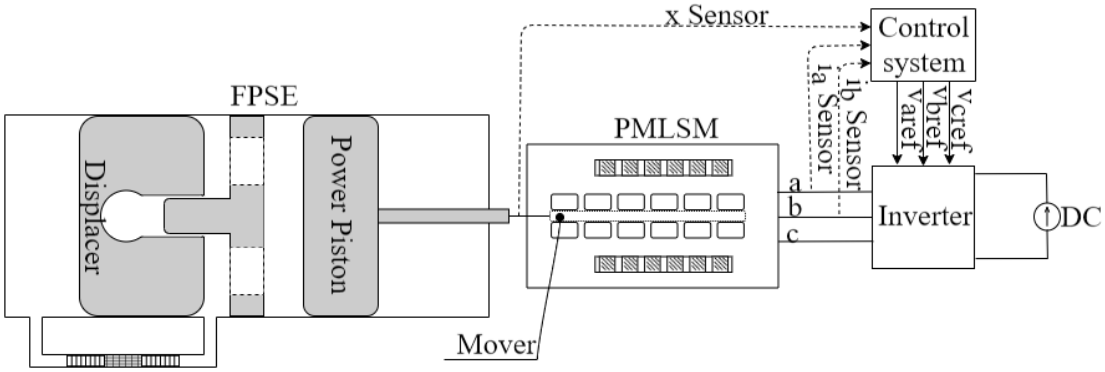

Figure 3.1: The FPSE-PMLSM combined system schematic

With the combined system the dynamic of the power piston which is the same as the mover is fully imposed by the control system of the PLMSM. It is due to the rigid connection between the power piston and the mover which provides a linkage between the two systems.

As can be seen in Figure 3.1, three sensors are used in the control system: two current sensors and one position sensor. The control system compares $d-q$ currents (already discussed in section 1.3) and the mover velocity with the required reference . It allows the control system to deliver the three-phase reference voltages that should be produced by the

inverter. Inverter, which can be seen as a constant unit gain (already discussed in section 1.3), feeds the PMLSM with these voltages.

Here, for the linear machine, the idea of controlling the motor torque like for a rotary machine can be applied. Thus, $i_{d\,reference} = 0$ and $i_{q\,reference}$ is the result of the speed control. So, a reference velocity $\dot{x}_{mover\,reference}$ for the mover will be defined. In defining this reference velocity, the limited reciprocating motion of the FPSE pistons should be considered. Since the nature of the speed is alternative, a Proportional Resonance (PR) controller is more adapted for speed controlling.

So, the PMLSM currents controllers are two Proportional Integral (PI) and velocity controller is a Proportional Resonance (PR) one that can be defined as:

$$PI = K_{p_{PI}} + K_{i_{PI}} \frac{1}{s} \qquad 3.1$$

$$PR = K_{p_{PR}} + K_{i_{PR}} \frac{s}{s^2 + \omega_0^2} \qquad 3.2$$

The K_p and K_i are the controller gains and ω_0 is the resonance frequency that at each instant will be equal to the reference velocity frequency. The block diagram of Figure 3.2 describes the control system which is used beside the PMLSM model.

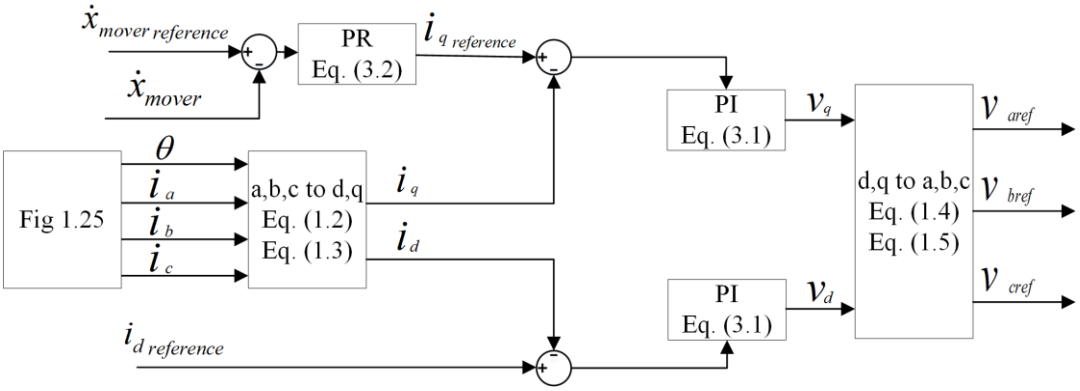

Figure 3.2: The PMLSM control block diagram

As can be seen in Figure 3.2, one PR and two PI controllers are used. One controller for the velocity ($\dot{x}_{mover}$) and two controllers for the currents (i_d and i_q). $\dot{x}_{mover\,reference}$ and $i_{d\,reference}$ are the inputs. For the present study, $\dot{x}_{mover\,reference}$ is assumed to be a sinusoidal wave and $i_{d\,reference} = 0$. i_a, i_b, and i_c are the results of the PMLSM modeling and v_{aref}, v_{bref}, and v_{cref} are the results of the system control. As can be seen, based on the

input and output data of Figure 3.2 and Figure 1.25, these two figures can be easily placed beside each other.

To identify the PI controllers' gains, the MATLAB Simulink® tuning method is used (PID tuner app) and their values are given in Table 3.1. The decoupling method allows controlling the currents separately [74]. The downside of the Figure 3.3 which corresponds to the q current control, is the schematic of the decoupled model that can be simplified as the light gray colored part of Figure 3.4.

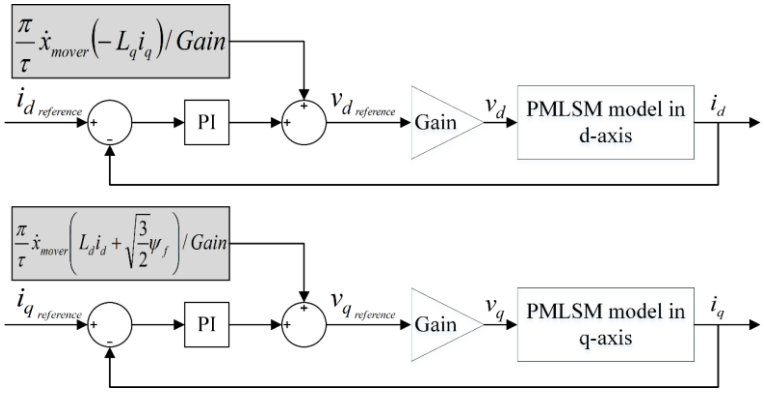

Figure 3.3: Decoupled PMLSM model for i_d and i_q

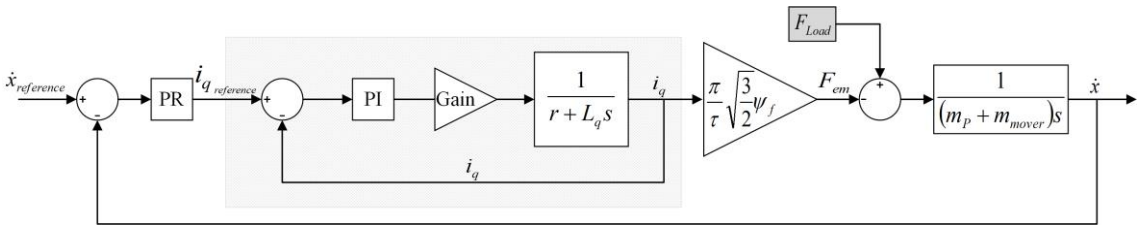

Figure 3.4: Schematic of the control system for velocity

In Figure 3.3 and Figure 3.4, the Gain, which is equal to 1 , is the inverter model (already discussed in section 1.3). The goal of Figure 3.4 is to identify PR gains. In order to identify the PR gains that match the FPSE-PMLSM combined system, the stability of the system should be considered. In Figure 3.4 the FPSE force (F_{Load}) is modeled as a force which is seen by the system as a perturbation. As the fundamental component of this force has the same frequency as the resonance frequency of the PR, it will be easily rejected and won' t perturbs the control. The piston mass is considered besides the mover mass. This is due to the coupled dynamic equation between FPSE and PMLSM (Equation 3.3).

The frequency response of the open-loop system of Figure 3.4, by ignoring the perturbations and assuming $\dot{x}_{reference}$ as the open loop input and $\dot{x}$ as the open loop output, is studied. Then, the effect of the setting of the PR coefficients ($K_{p_{PR}}$ and $K_{i_{PR}}$) on the gain and phase margins is evaluated. The results show that there is a zone in the bode diagram where the phase margin its maximum value, and the system is stable with maximum margin. Since these PR gains will be used in the combined system, and the FPSE system behavior is treated as a perturbation, it is proposed to be in the safest place in this zone which is the middle of the zone. The bode diagram of Figure 3.4 with $K_{p_{PR}}$ and $K_{i_{PR}}$ gains given in Table 3.1 is shown in Figure 3.5. In Figure 3.5, the input and output of the Bode diagram based on Figure 3.4 are $\dot{x}_{reference}$ and $\dot{x}$, respectively.

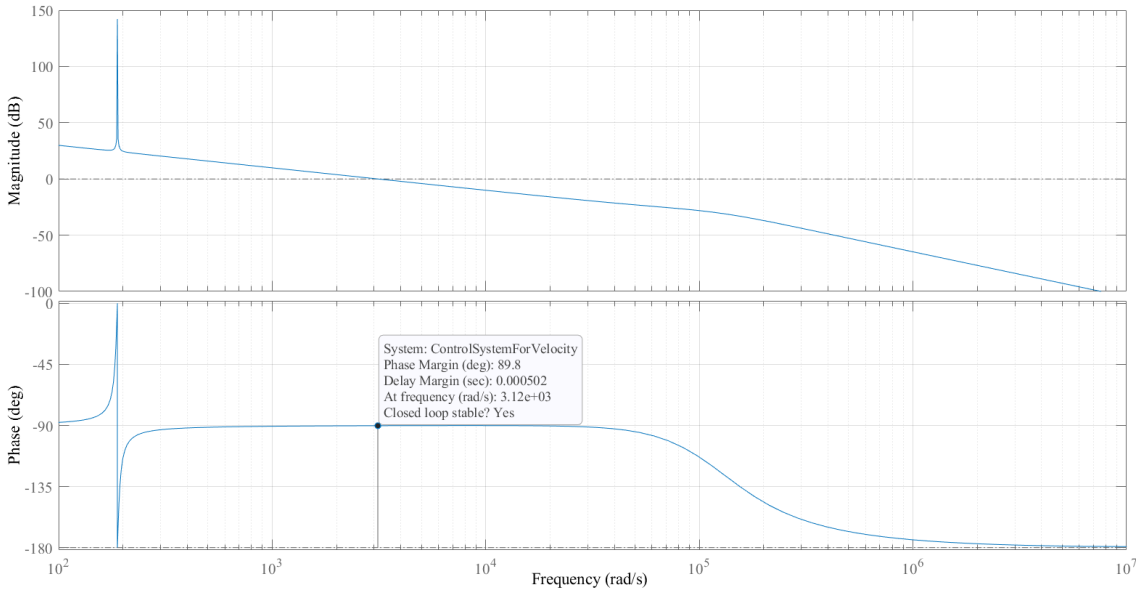

Figure 3.5: Bode diagram of Figure 3.4

As can be seen in Figure 3.5, with the defined values of PR gains that are presented in Table 3.1, the system phase margin is almost in the middle of the zone which is the safest pace.

Table 3.1: Controller gains

i_d controller		i_q controller		$\dot{x}$ controller	
$K_{p_{PI}}$	4×10^4	$K_{p_{PI}}$	554.1	$K_{p_{PR}}$	1×10^3
$K_{i_{PI}}$	1×10^8	$K_{i_{PI}}$	47062993.6	$K_{i_{PR}}$	1×10^4

After defining the control parameters, the behavior and response of the combined system can be analyzed.

The input data of the FPSE system are the same that was already provided in Table 2.3. The input data of the PMLSM system are also presented in Table 3.2.

Table 3.2: PMLSM input data [12]

r	0.1 (Ω)	L_q	3.01 (mH)	L_d	1.77 (mH)
ψ_f	0.0513 (Wb)	B_v	10	m_{mover}	0.824 (kg)

As it was already discussed, the coupling between the FPSE and the PMLSM is due to the rigid rode that connects the power piston to the mover. Thus, in order to couple these two systems, their dynamic equations related to the power piston and the mover should be combined. After combining these two equations (Equation 1.10 and 2.1) that results in the Equation 3.3, the set of combined system equations will be as:

$$(m_P + m_{mover})\ddot{x}_P = A_P(P_c - P_b) + F_{em} - B_v\dot{x}_p \quad 3.3$$

$$m_D\ddot{x}_D = A_D(P_e - P_c) + A_{rod}(P_c - P_{gs}) \quad 3.4$$

$$v_d = L_d\frac{di_d}{dt} + ri_d - \frac{\pi}{\tau}\dot{x}_P L_q i_q \quad 3.5$$

$$v_q = L_q\frac{di_q}{dt} + ri_q + \frac{\pi}{\tau}\dot{x}_P\left(L_d i_d + \sqrt{3/2}\psi_f\right) \quad 3.6$$

$$F_{em} = \frac{\pi}{\tau}\left(\sqrt{3/2}\psi_f i_q + (L_d - L_q)i_d i_q\right) \quad 3.7$$

$$Power_{em} = F_{em}\dot{x}_P \quad 3.8$$

$$Power_{el} = v_q i_q + v_d i_d \quad 3.9$$

$$\eta = \frac{Power_{el}}{\dot{Q}_h} \quad 3.10$$

As can be seen, the only equation which is different compared to the previous set of equations is Equation 3.3.

Now, the results of the combined FPSE-PMLSM system considering the developed control model will be presented. It should be noted that the reference velocity value has an

amplitude equal to 1 and frequency equal to 30 Hz as $\dot{x}_{P\,reference} = 1 \times sin(30 \times 2\pi \times t)$. This is the frequency that the FPSE system was validated in Section 2.3 and also is almost equal to the FPSE resonance frequency.

First, the results of the controlled currents and velocity with their absolute error values are presented to show that the control system is well designed.

In Figure 3.6, the power piston velocity, its reference value, and the displacer velocity are shown. Furthermore, in Figure 3.7, the absolute error between power piston velocity and its reference value is presented.

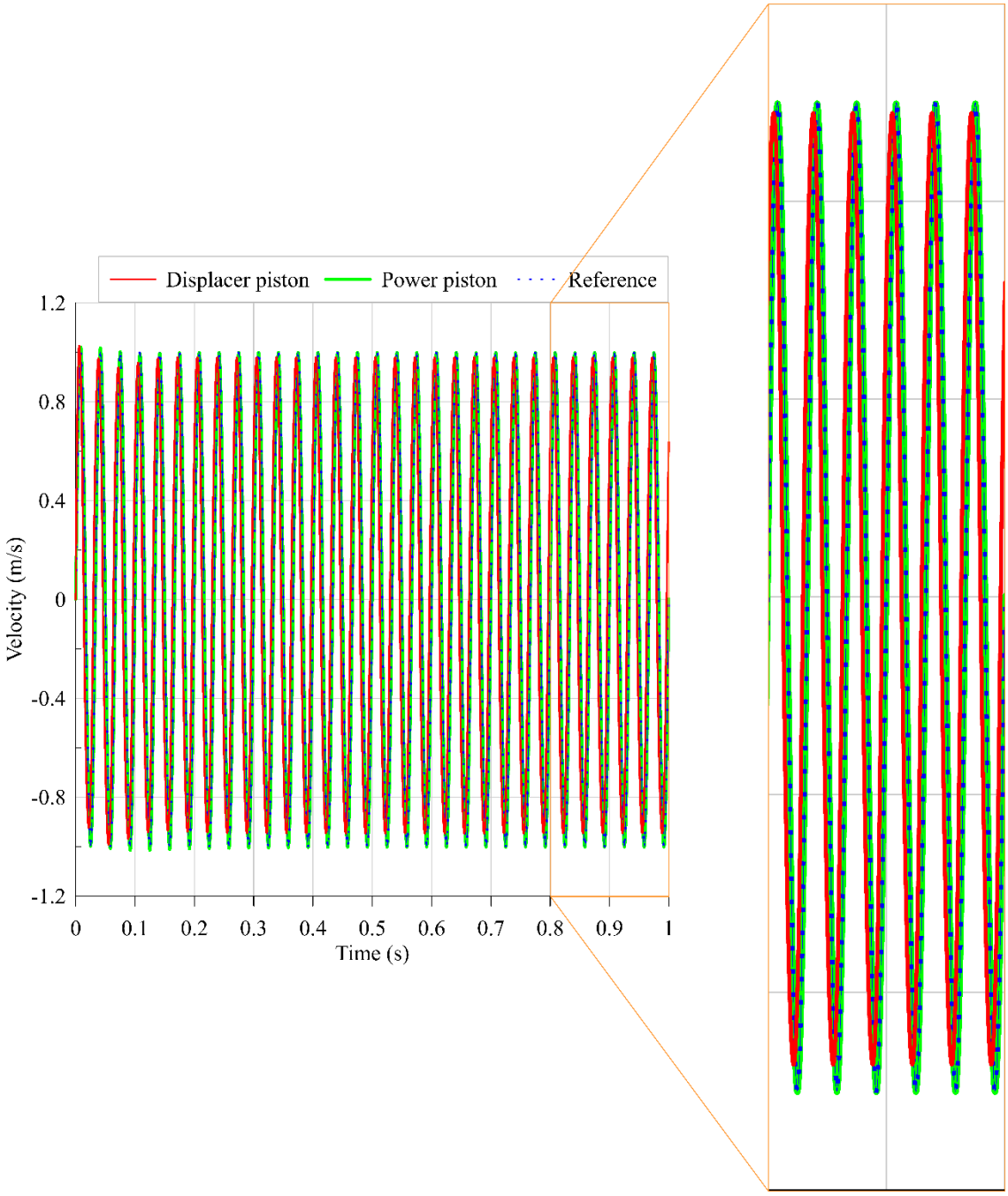

Figure 3.6: Pistons' velocity and the reference velocity of the FPSE-PMLSM system

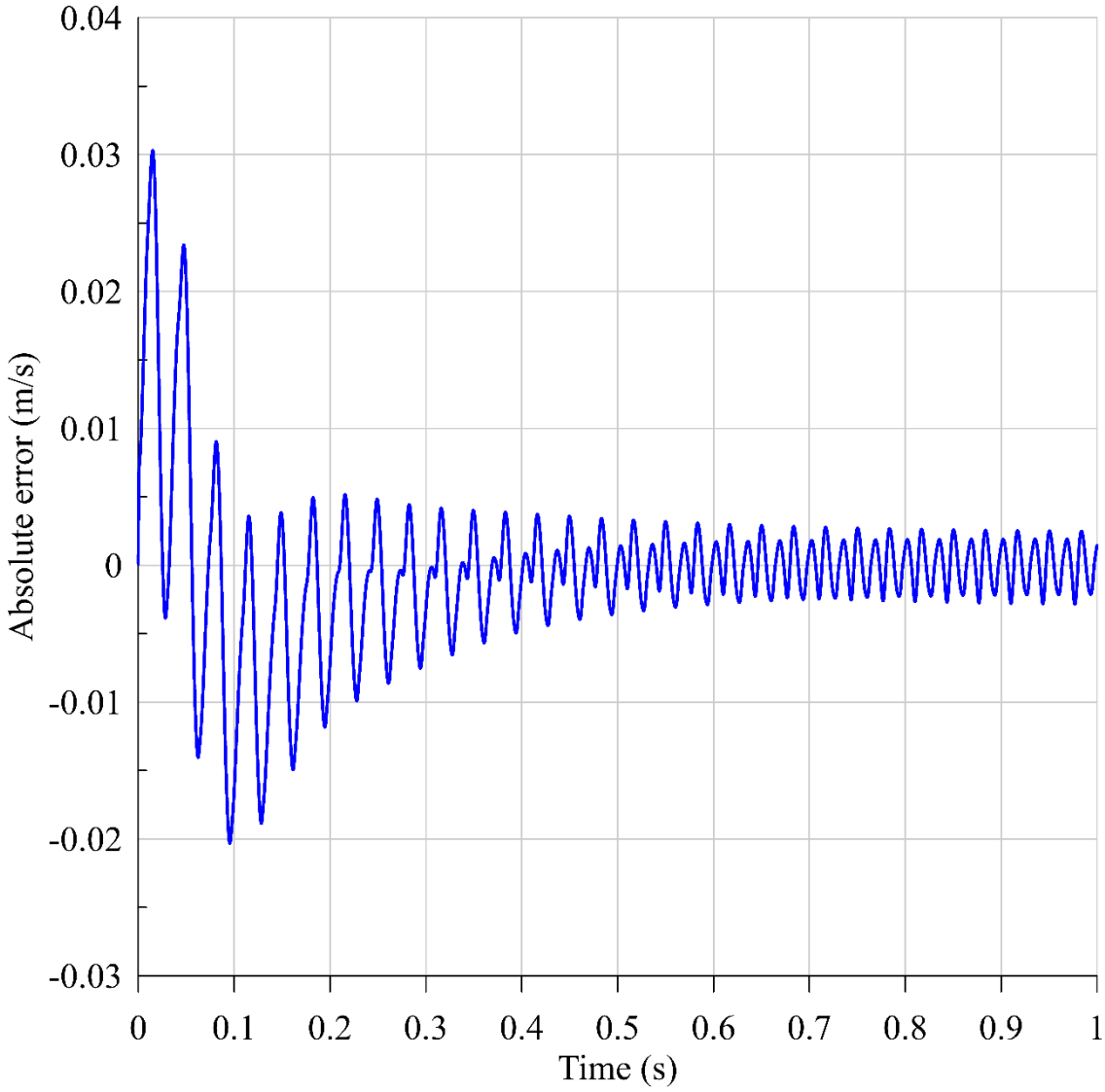

Figure 3.7: The absolute error between the power piston velocity and its reference value

As can be seen in Figure 3.6, the transient period is satisfying for this kind of application. In the transient period, as shown in Figure 3.7, the error also has its maximum value. Based on Figure 3.6 and Figure 3.7, since the absolute error is very small compared to the velocity amplitude and the transient mode is fast, it can be concluded that the PR controller of the velocity is well designed and the setting of the PR gains (based on Table 3.1) are well adapted.

Now the results of the PI controllers of the currents are studied in Figure 3.8 to Figure 3.10.

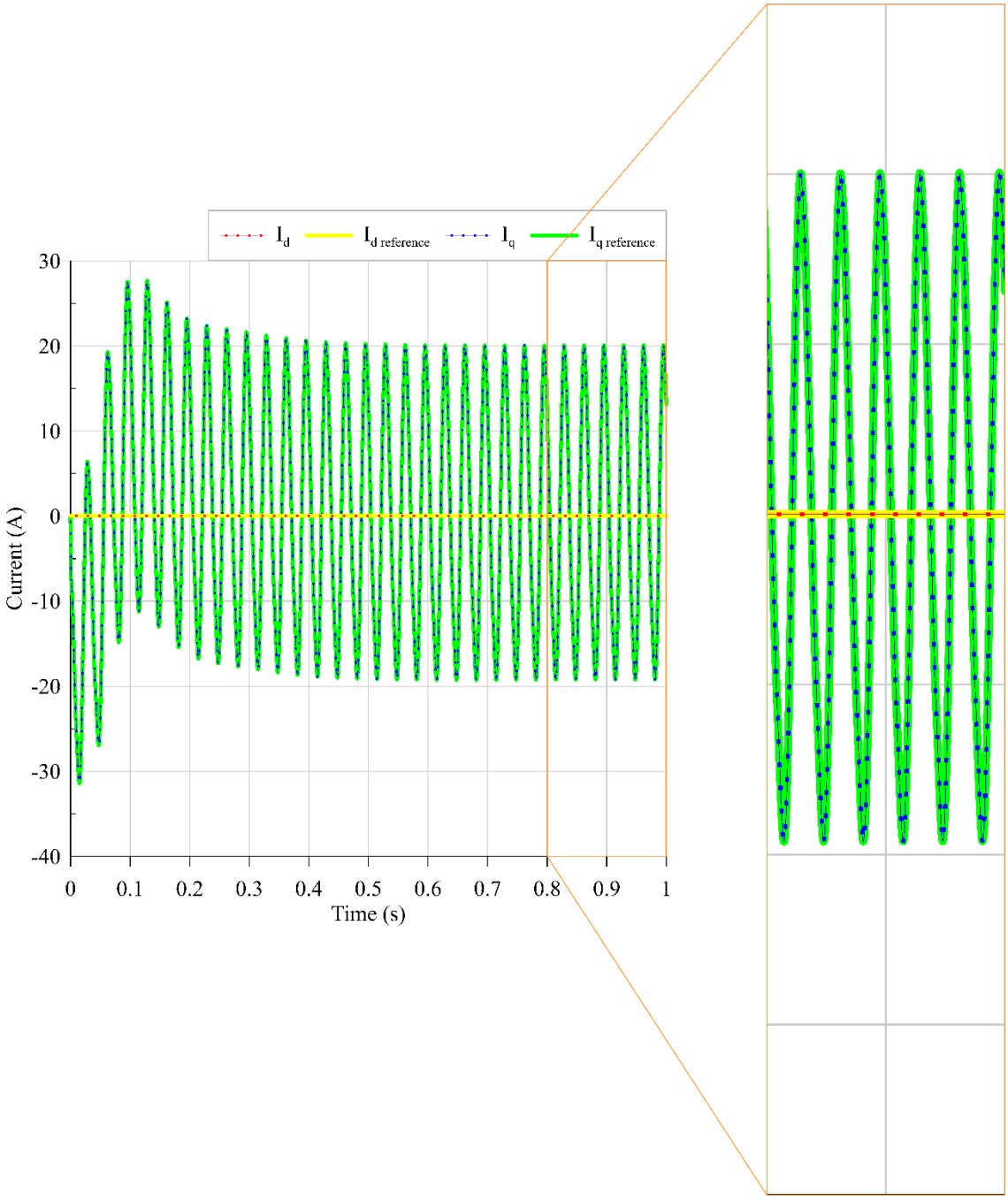

Figure 3.8: Currents and their reference values of the FPSE-PMLSM system

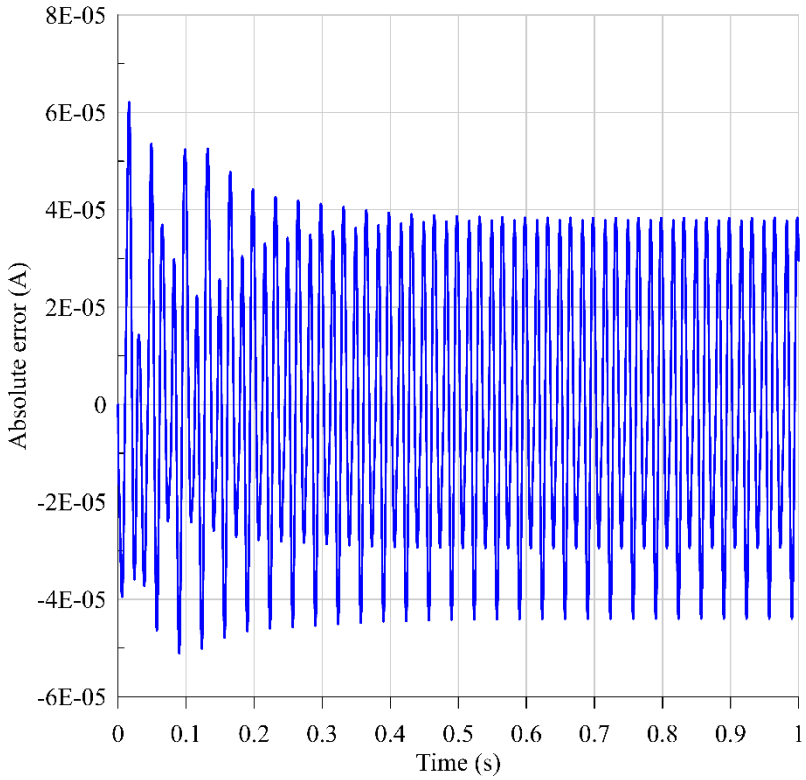

Figure 3.9: The absolute error of the d current

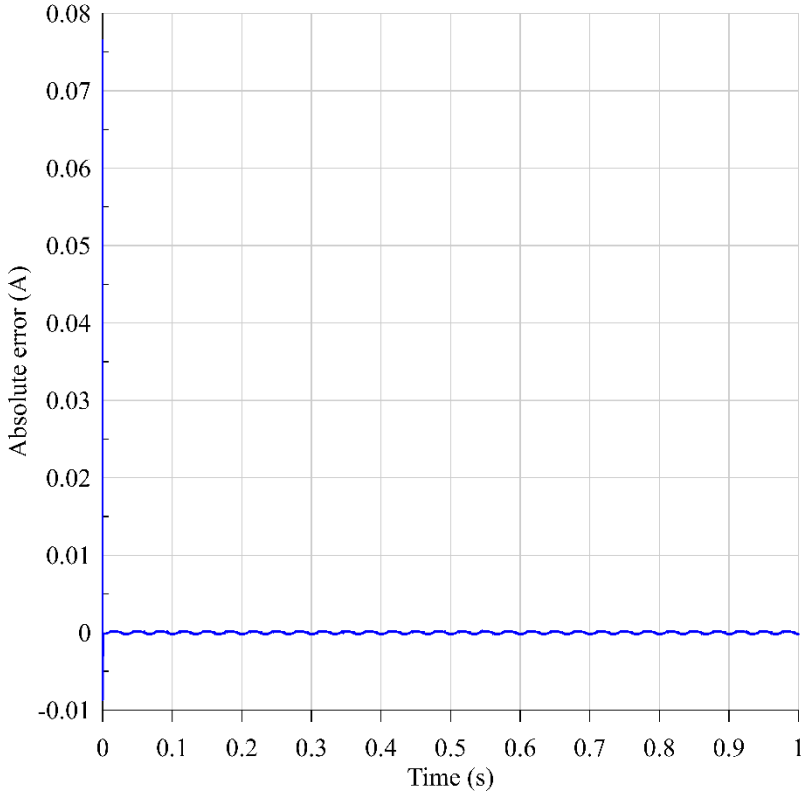

Figure 3.10: The absolute error of the q current

As can be seen in Figure 3.9 and Figure 3.10, and as already discussed, the maximum error happens at the starting and transient phases. However, these errors are very small compared to the reference values. As shown in Figure 3.8, since the transient phase is fast and in this phase, there are not high jumps for the currents, and also based on Figure 3.9 and Figure 3.10 the errors are very small, the PI current controllers are well designed, and their gains are well-tuned using MATLAB Simulink PID tuning method.

Now that it was shown that the controllers were well designed and the combined system was well controlled, the results of the combined FPSE-PMLSM system are shown. First, the displacer and power piston displacements are shown in Figure 3.11.

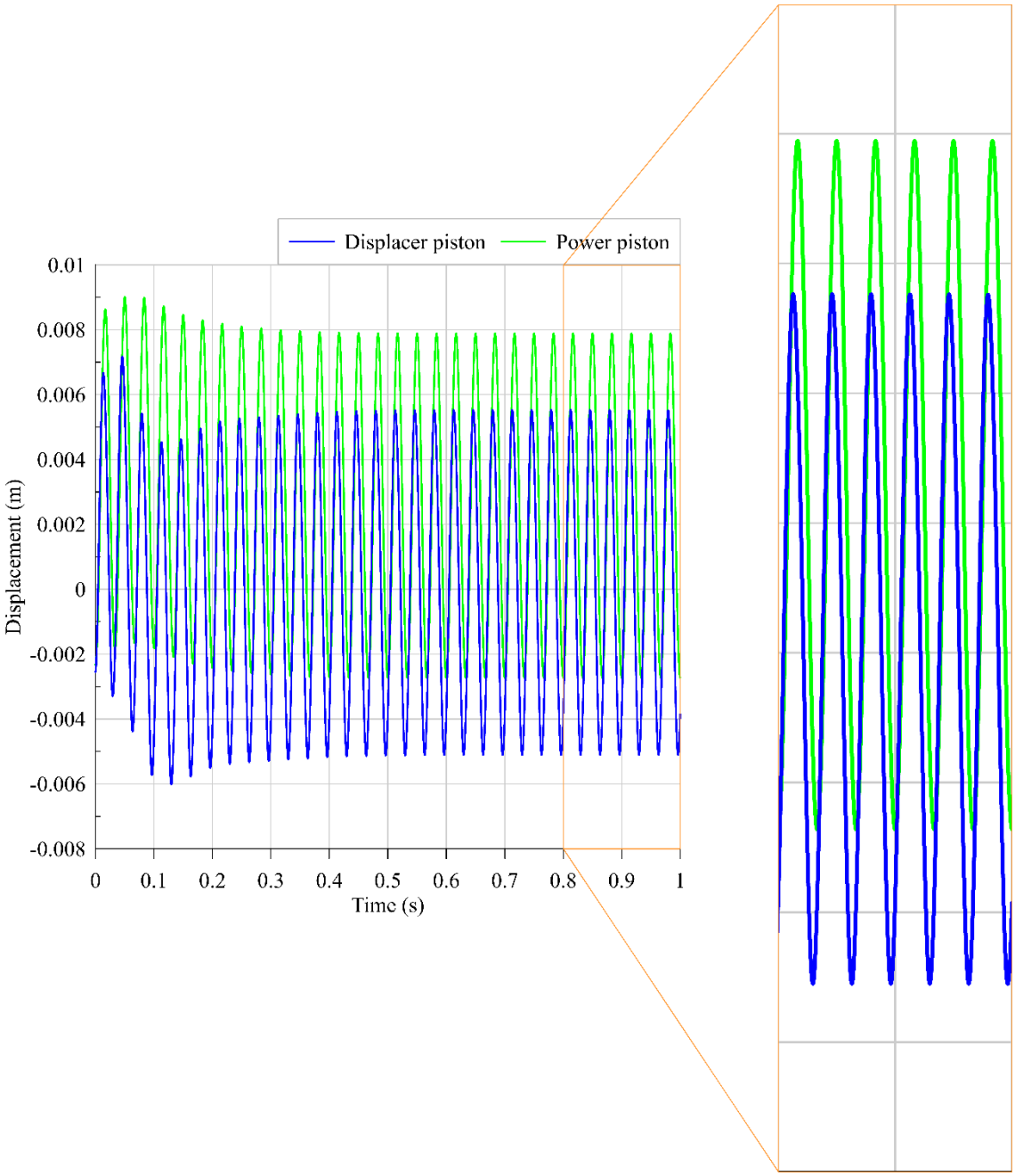

Figure 3.11: Displacer and power piston displacements of the FPSE-PMLSM system

As can be seen in Figure 3.11, and already discussed, the transient is satisfying for this kind of application.

The pressure drops are also shown in Figure 3.12.

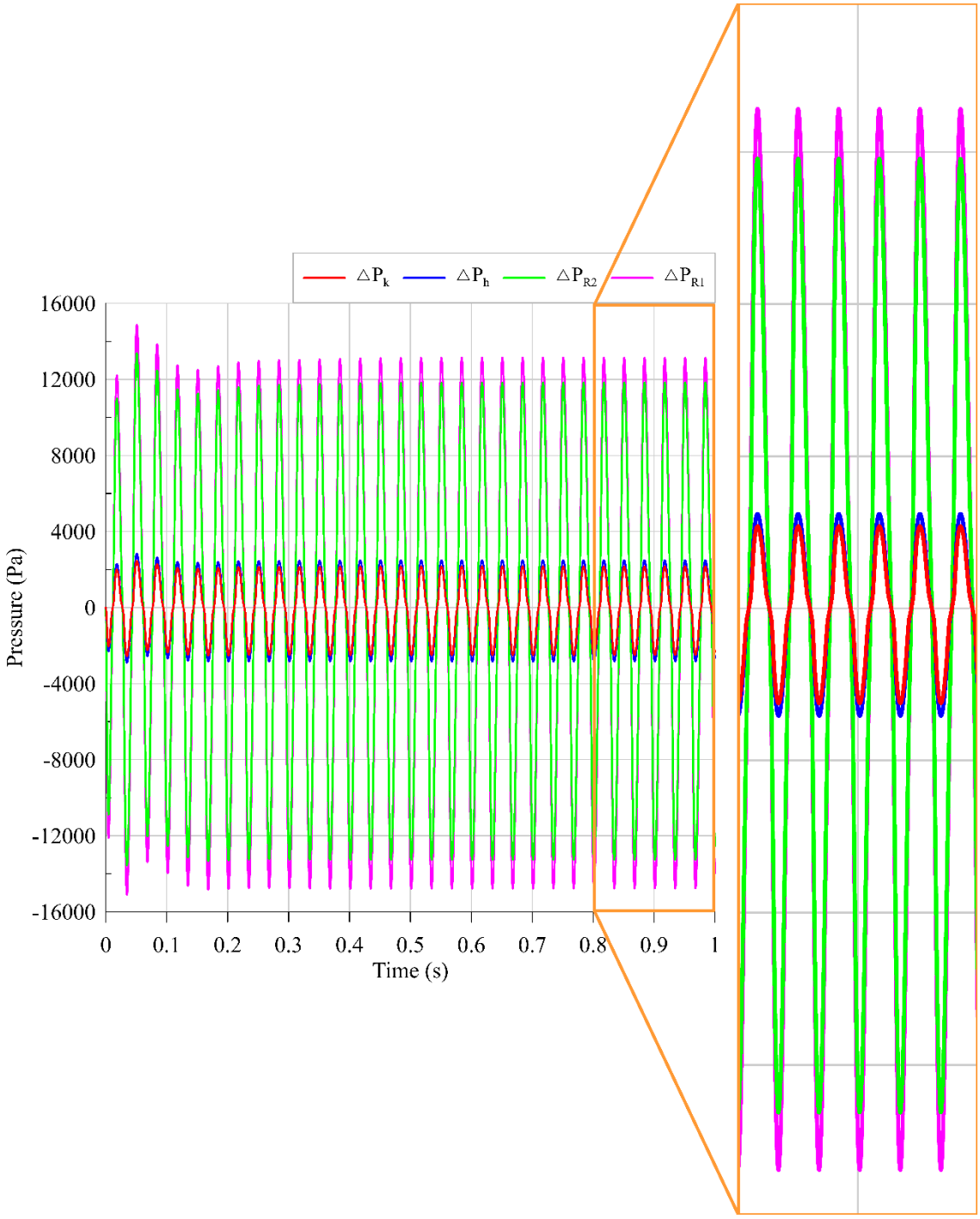

Figure 3.12: Pressure drops of the FPSE in the combined system

As can be seen in Figure 3.12, as it was already shown in chapter 2, the regenerators have the maximum pressure drops and the pressure drops in the heater and cooler are in the same range. Also, there is no phase shift between the pressure drops which can be explained based on the gas velocity calculation method.

The temperature variations in spaces and also heat transfers are shown in Figure 3.13 - Figure 3.16.

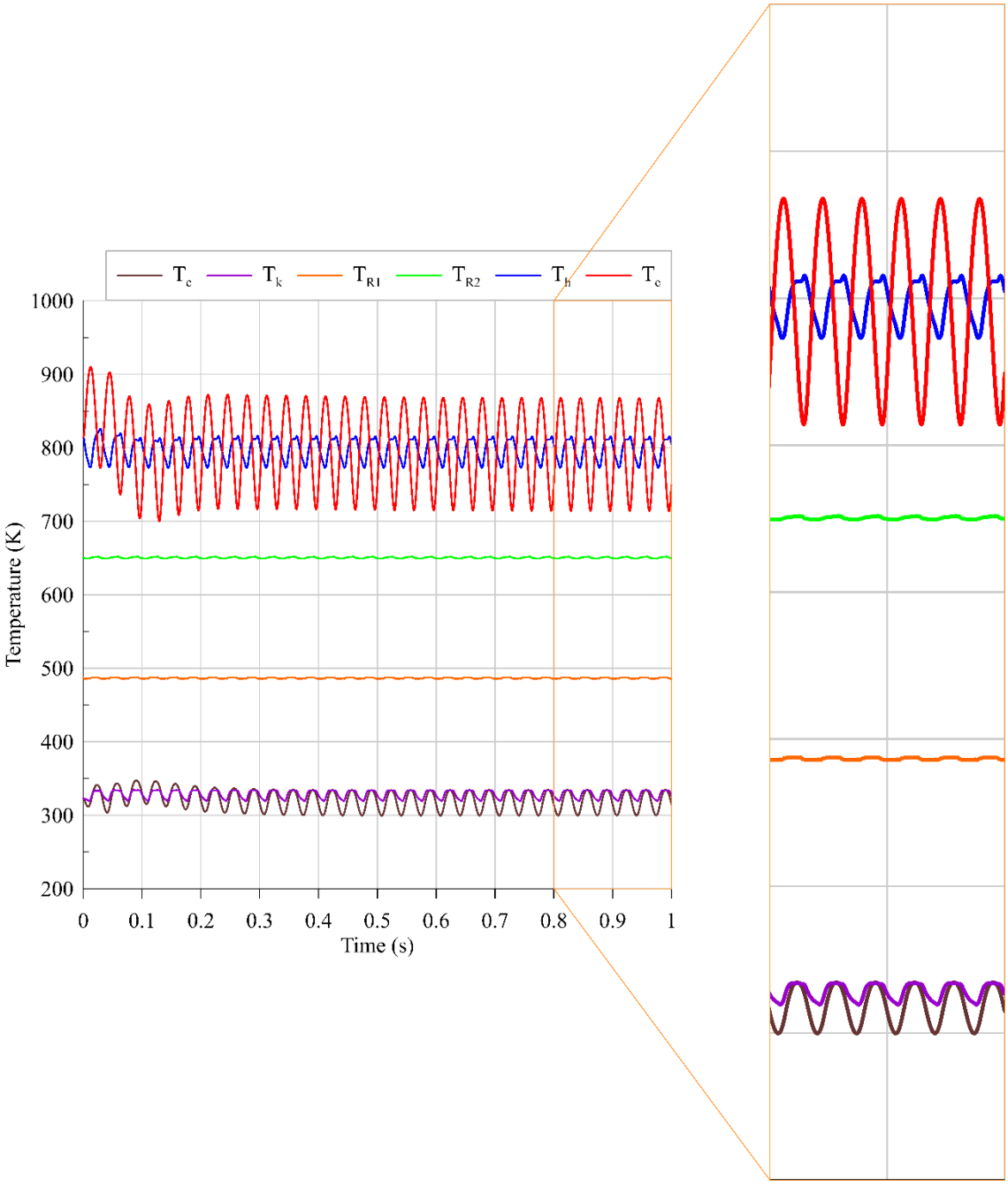

Figure 3.13: Spaces' temperature variations of the FPSE-PMLSM system

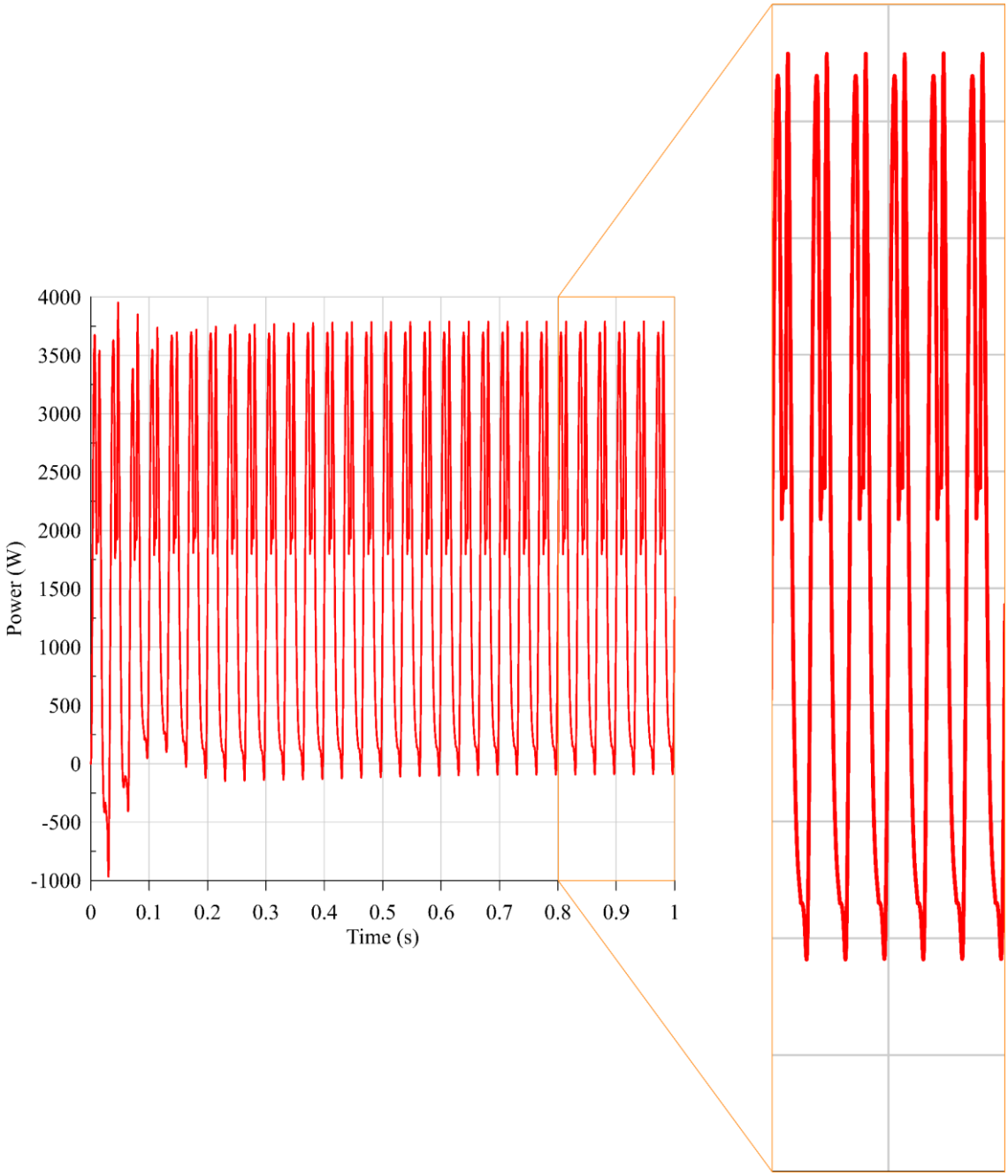

Figure 3.14: Heat transfer rate of the heater of the FPSE-PMLSM system

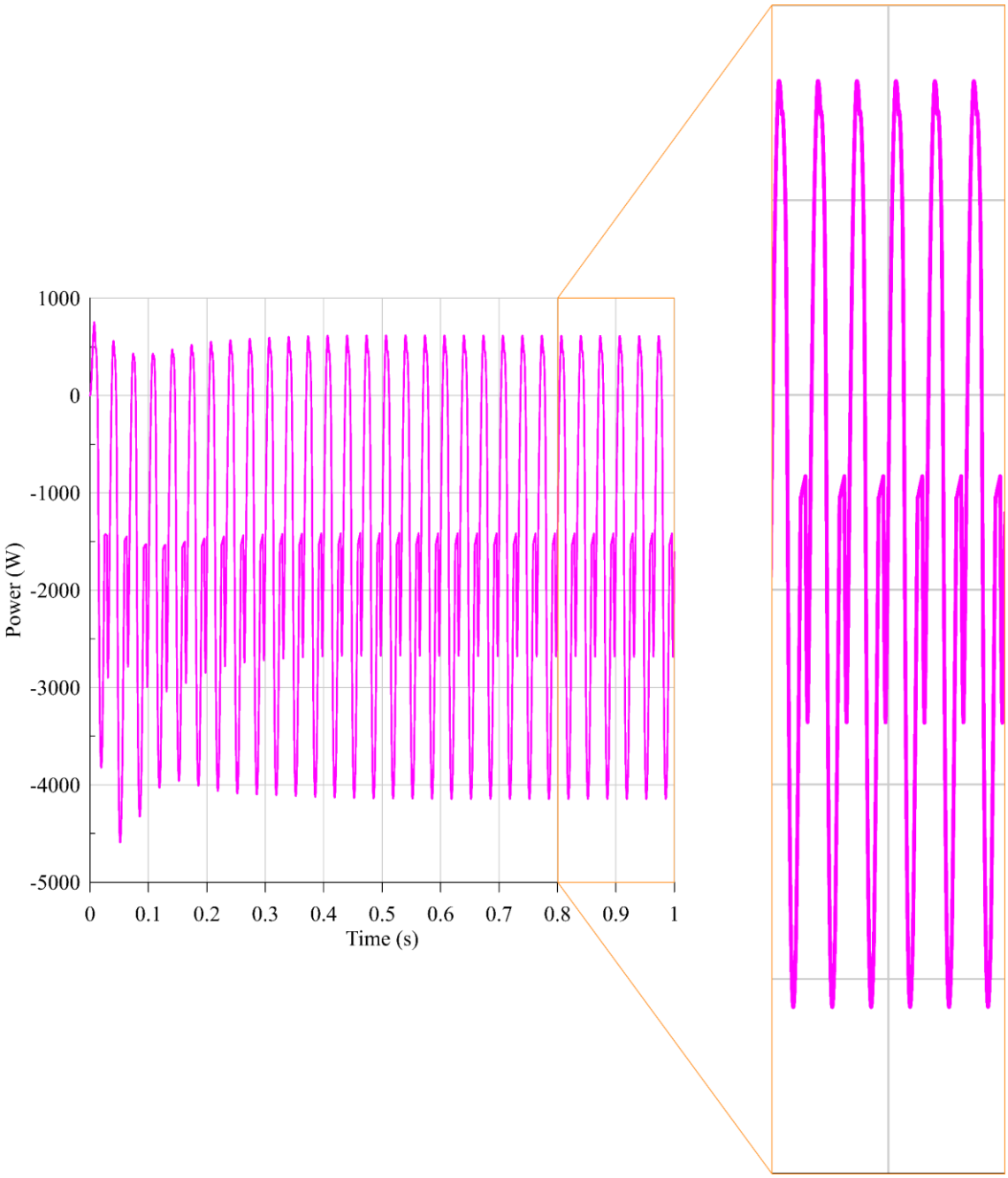

Figure 3.15: Heat transfer rate of the cooler of the FPSE-PMLSM system

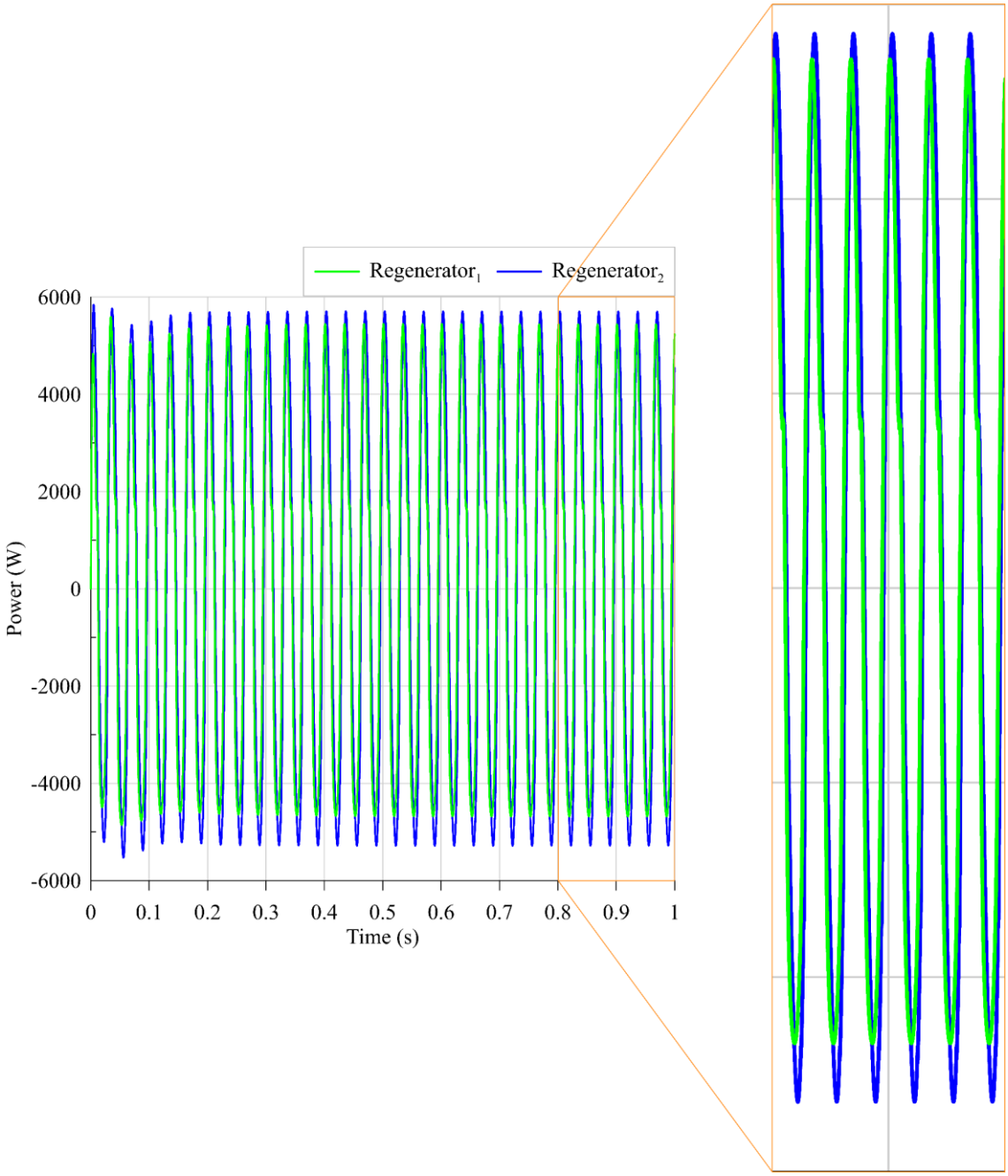

Figure 3.16: Heat transfer rate of the regenerators of the FPSE-PMLSM system

Now, the electrical results, which are the three-phase currents and voltages, are presented in Figure 3.17 - Figure 3.22.

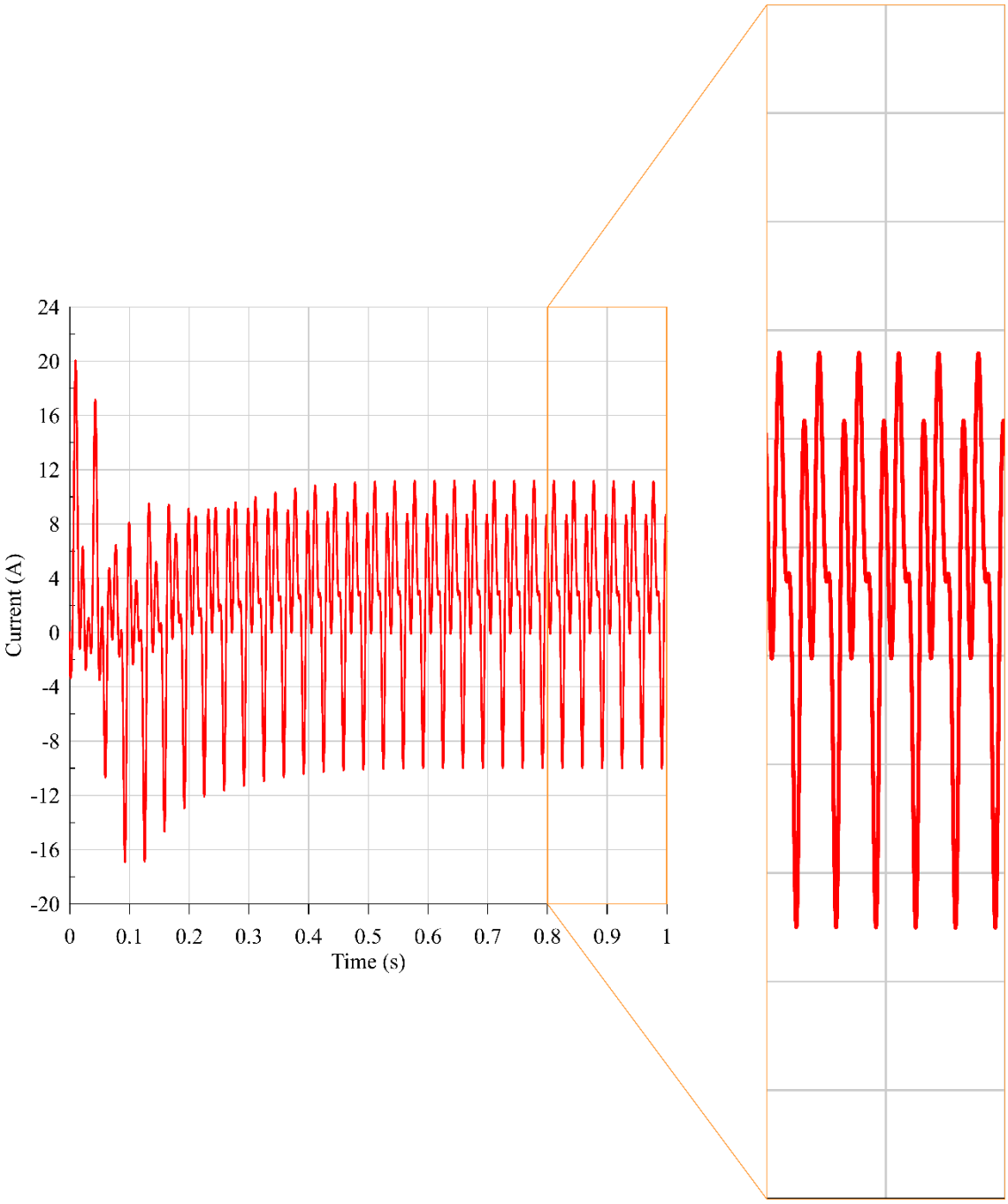

Figure 3.17: i_a current of the FPSE-PMLSM system

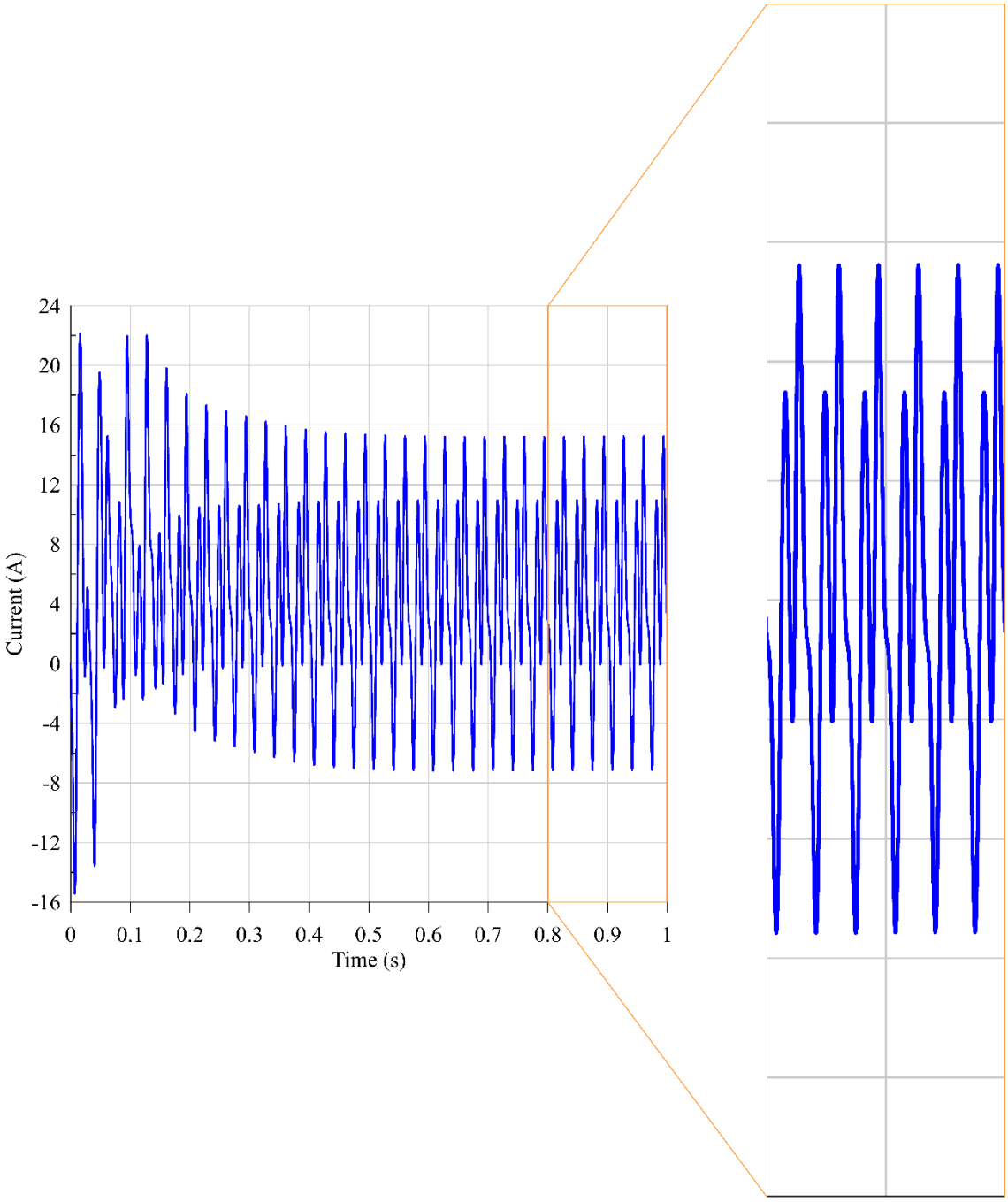

Figure 3.18: i_b current of the FPSE-PMLSM system

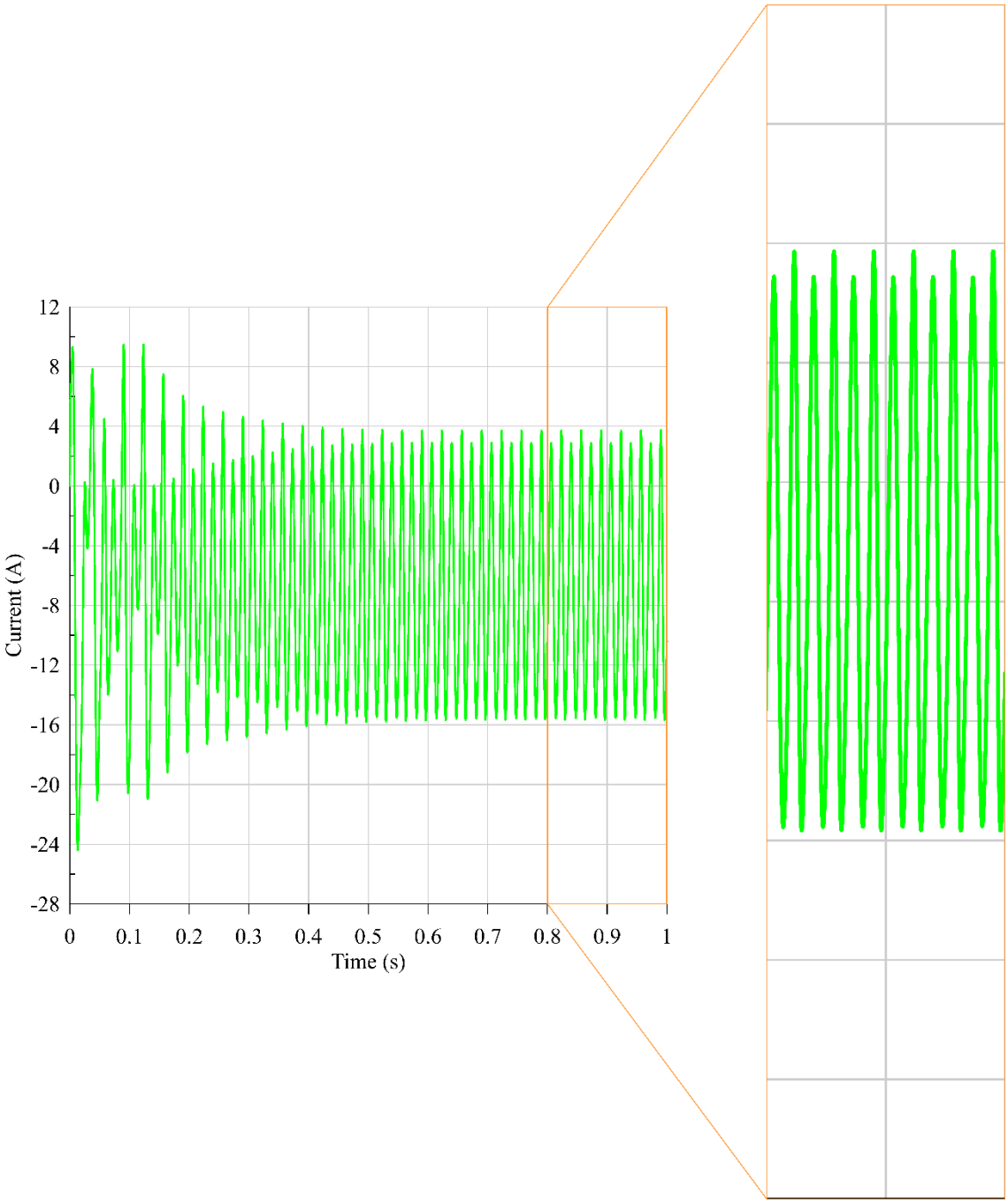

Figure 3.19: i_c current of the FPSE-PMLSM system

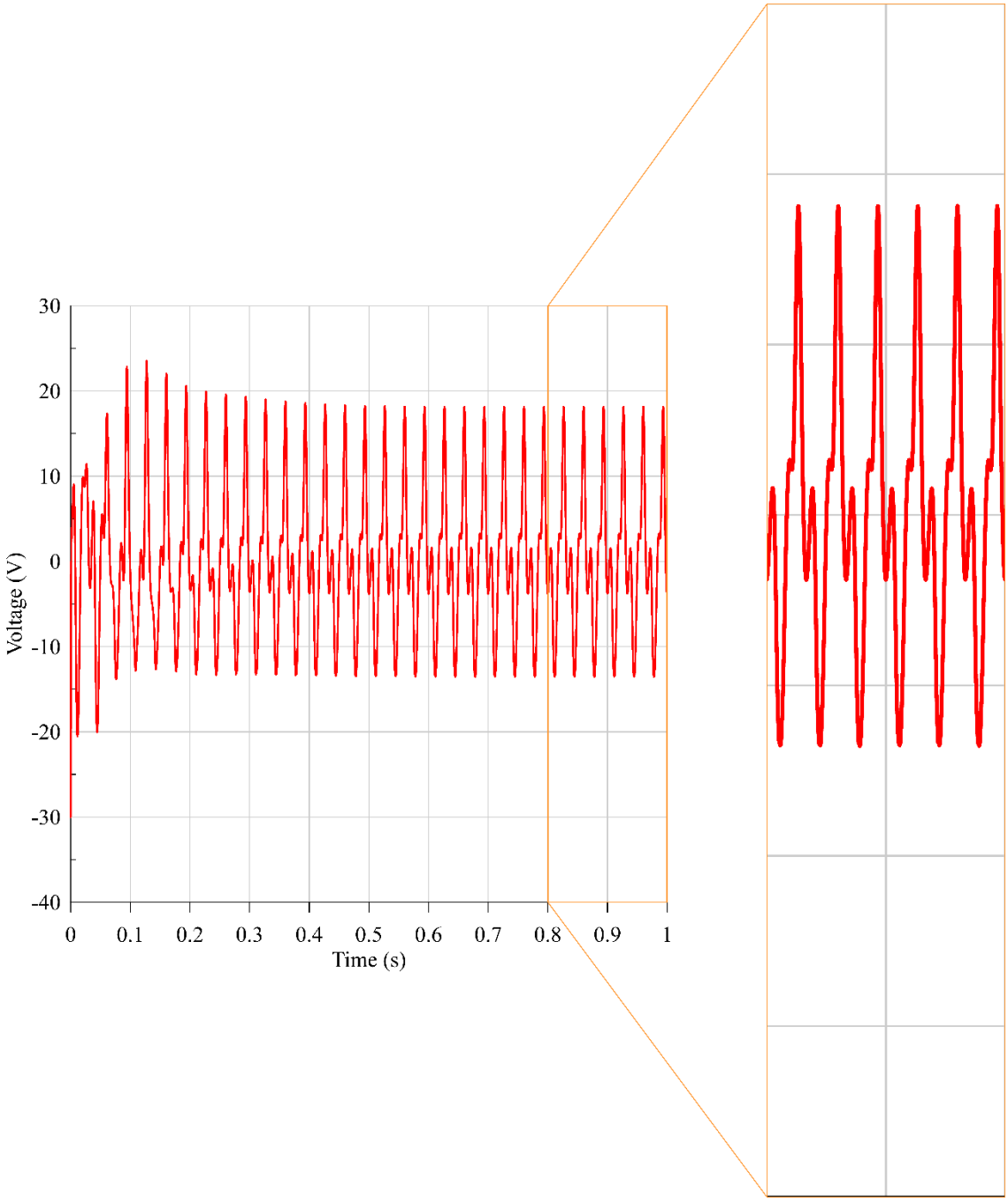

Figure 3.20: v_a voltage of the FPSE-PMLSM system

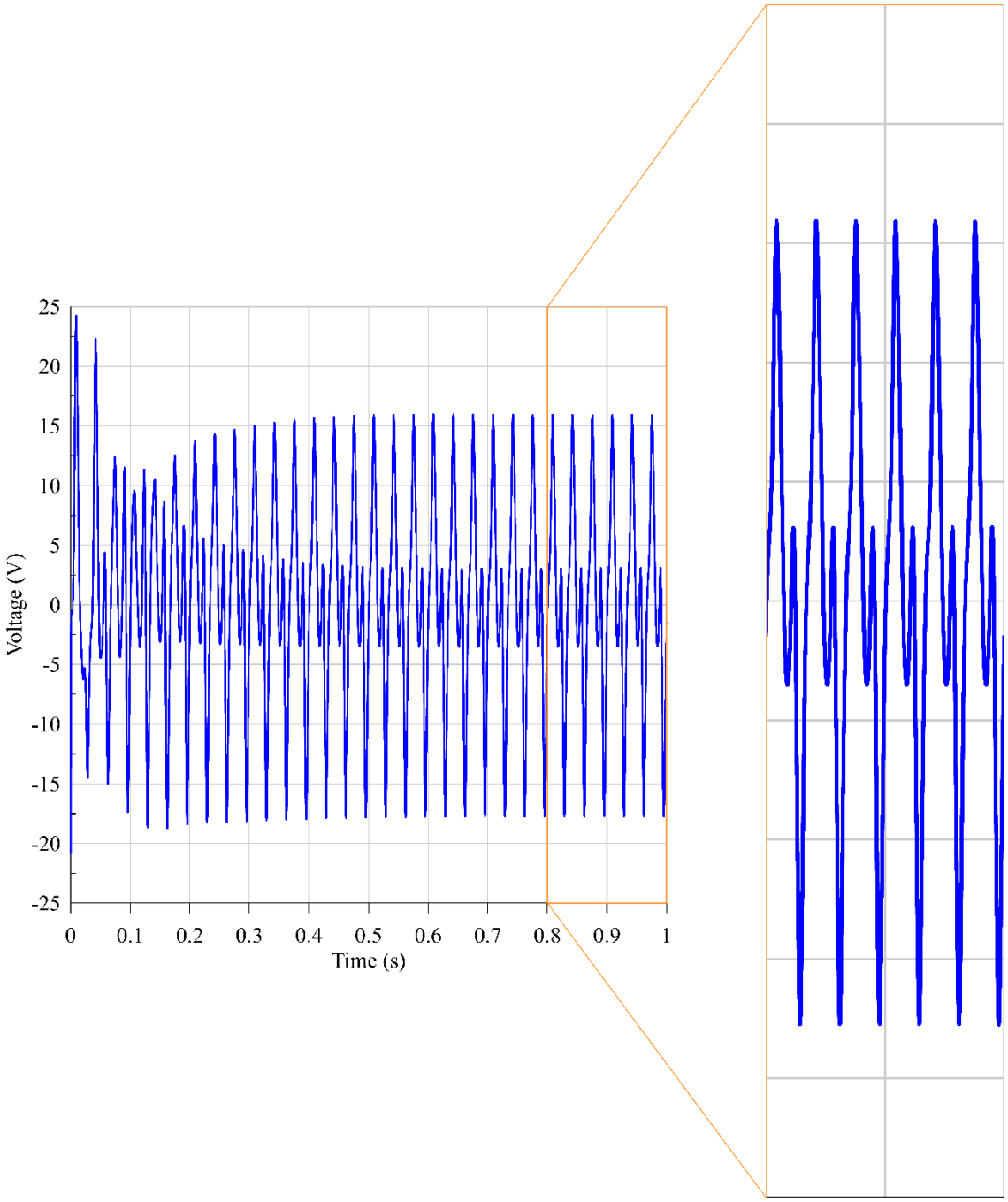

Figure 3.21: v_b voltage of the FPSE-PMLSM system

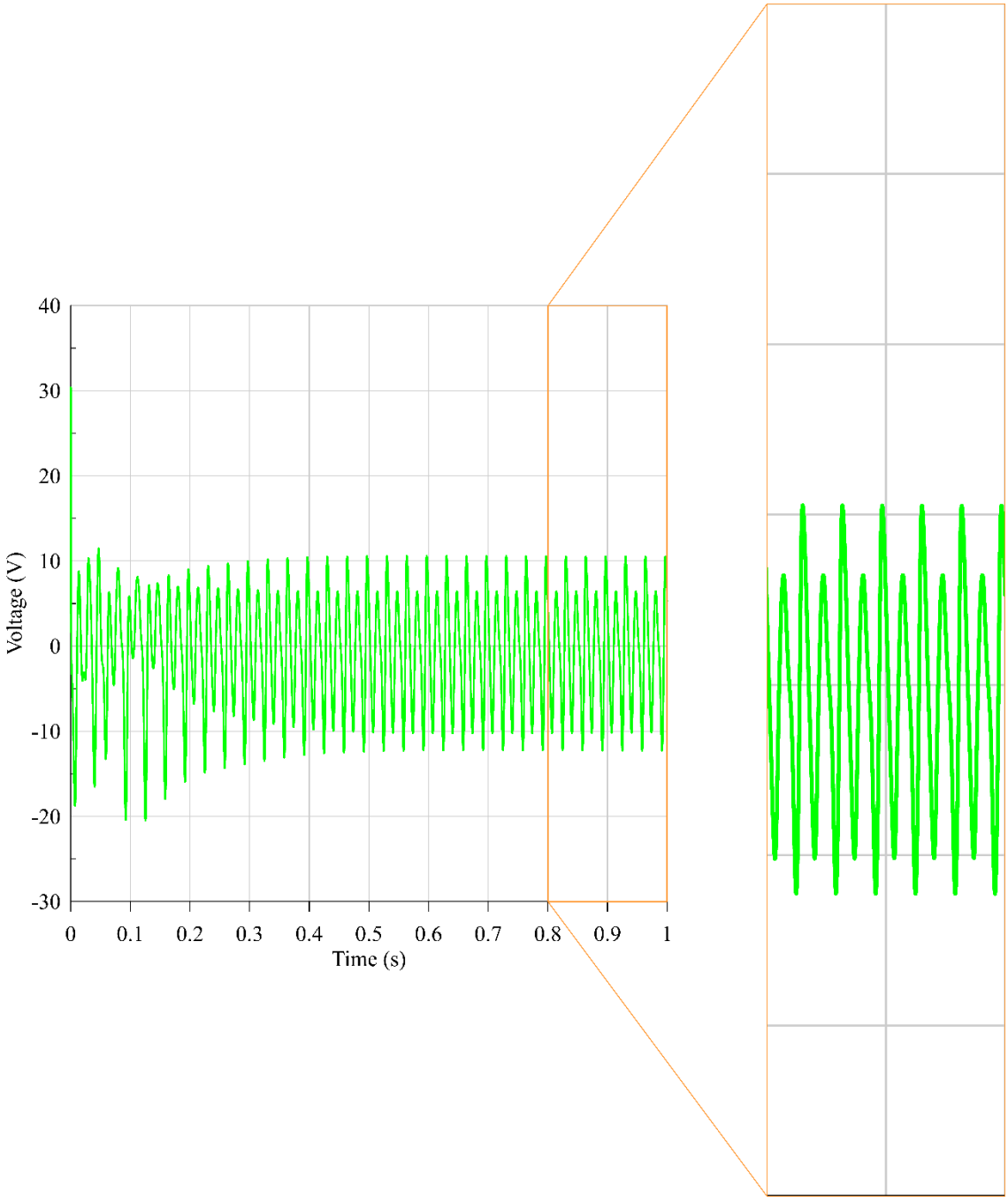

Figure 3.22: v_c voltage of the FPSE-PMLSM system

As can be seen in Figure 3.17 - Figure 3.22, there is a jump for currents and voltages at the starting point, but after a few cycles, the system is stabilized.

Furthermore, the results of the electrical power (3.9), electromagnetic power (3.8), and the piston power (2.80) are shown in Figure 3.23 - Figure 3.25.

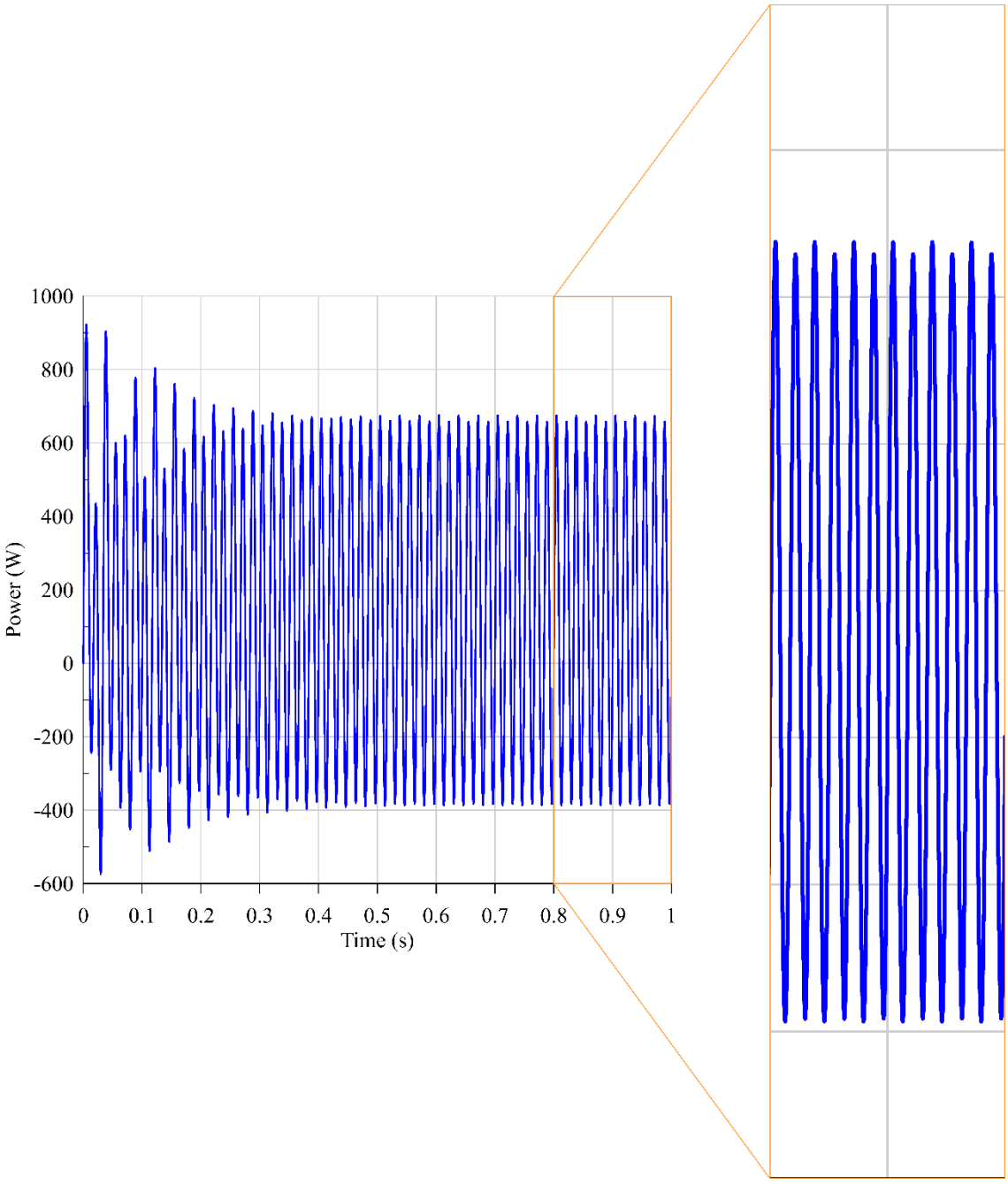

Figure 3.23: The power produced by power piston of the FPSE-PMLSM system

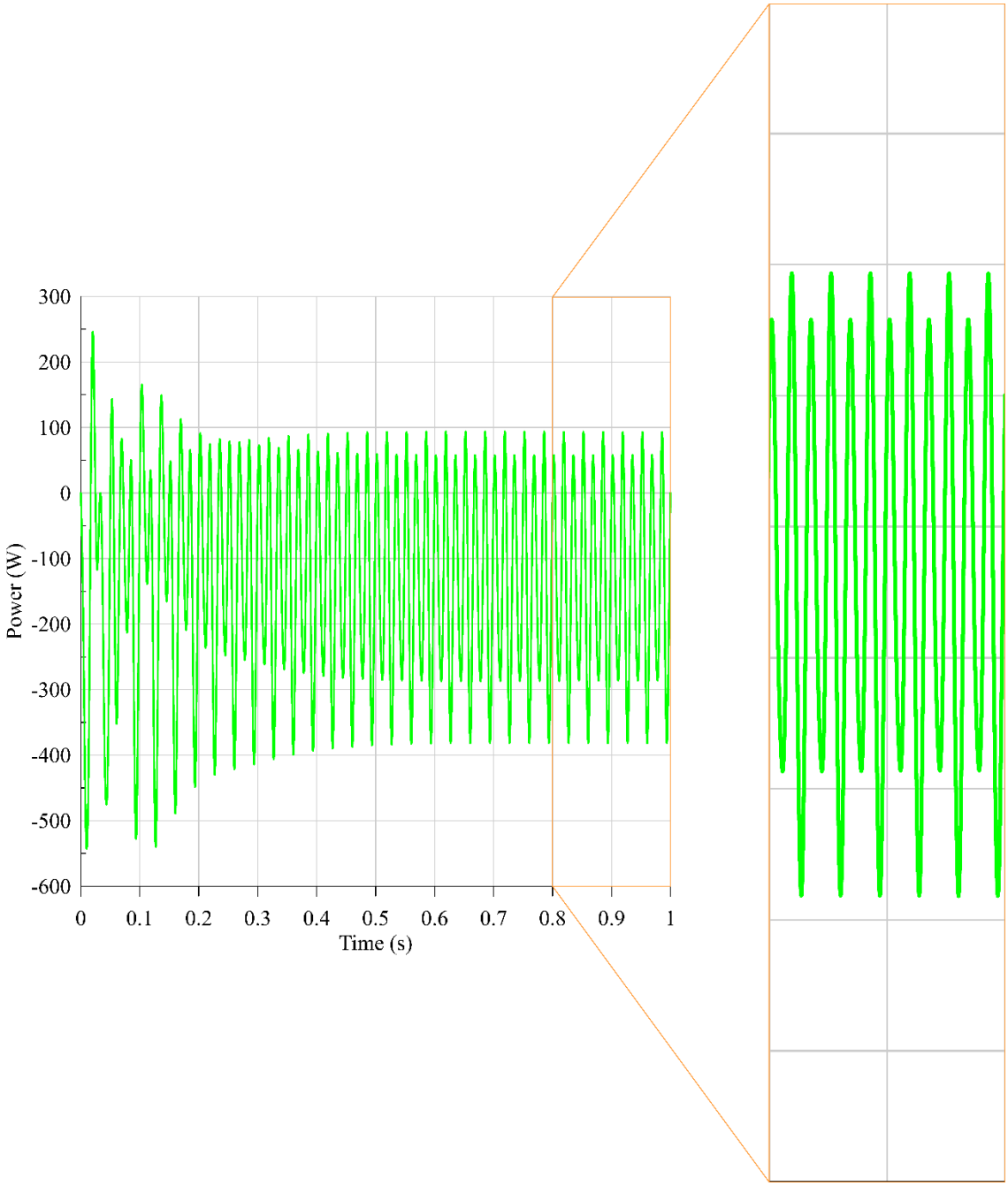

Figure 3.24: The electromagnetic produced power by the FPSE-PMLSM system

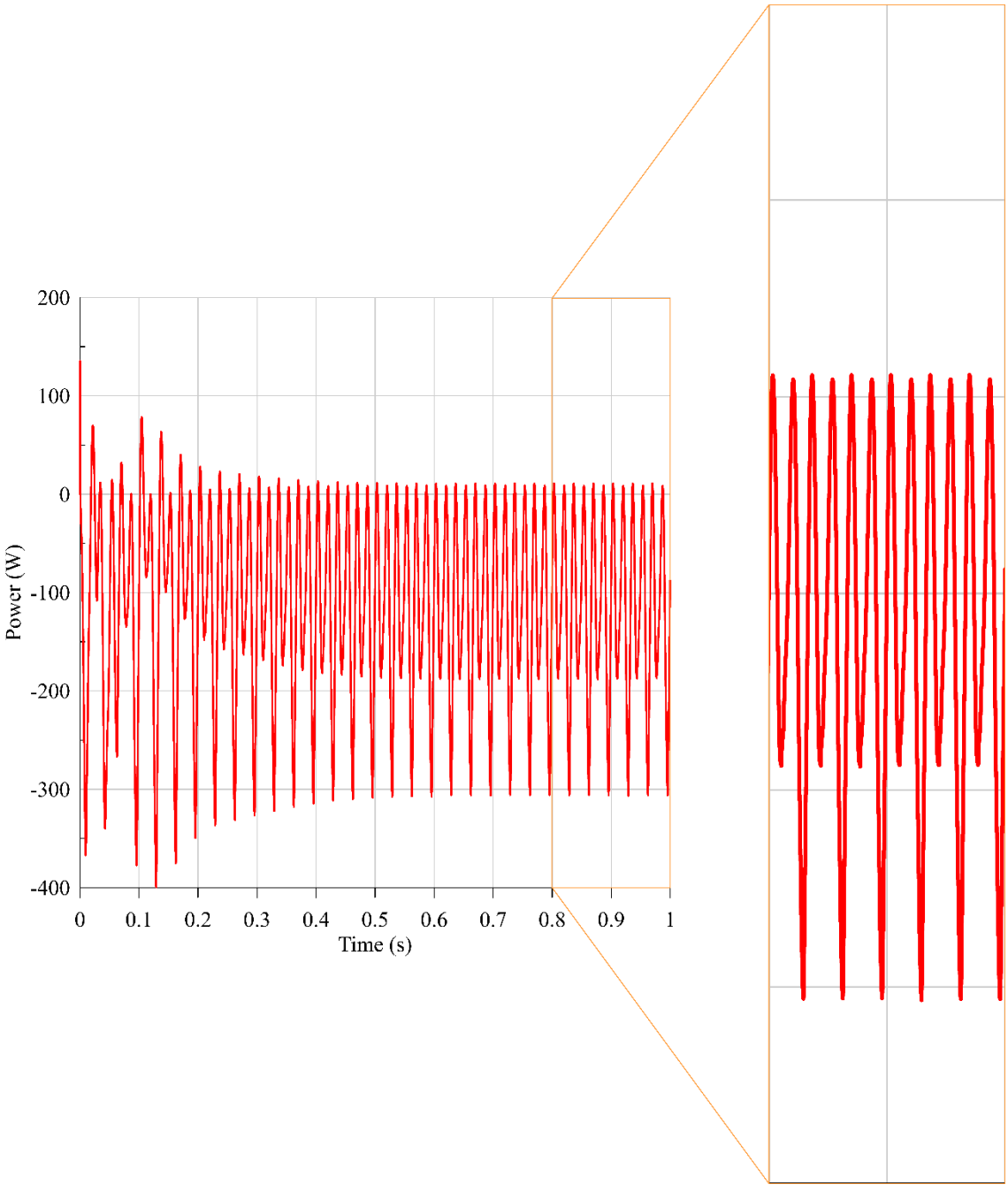

Figure 3.25: The electrical produced power by the FPSE-PMLSM system

As can be seen in Figure 3.25, most of the time, the electrical power is negative that shows the system is producing electrical power according to the used motor convention for the PMLSM in the present study, but in some points, it is positive, which means the PMLSM works as a motor. This happens especially in the transient phase and at the starting point. Finally, the results of the power piston force and electromagnetic forces are shown in Figure 3.26.

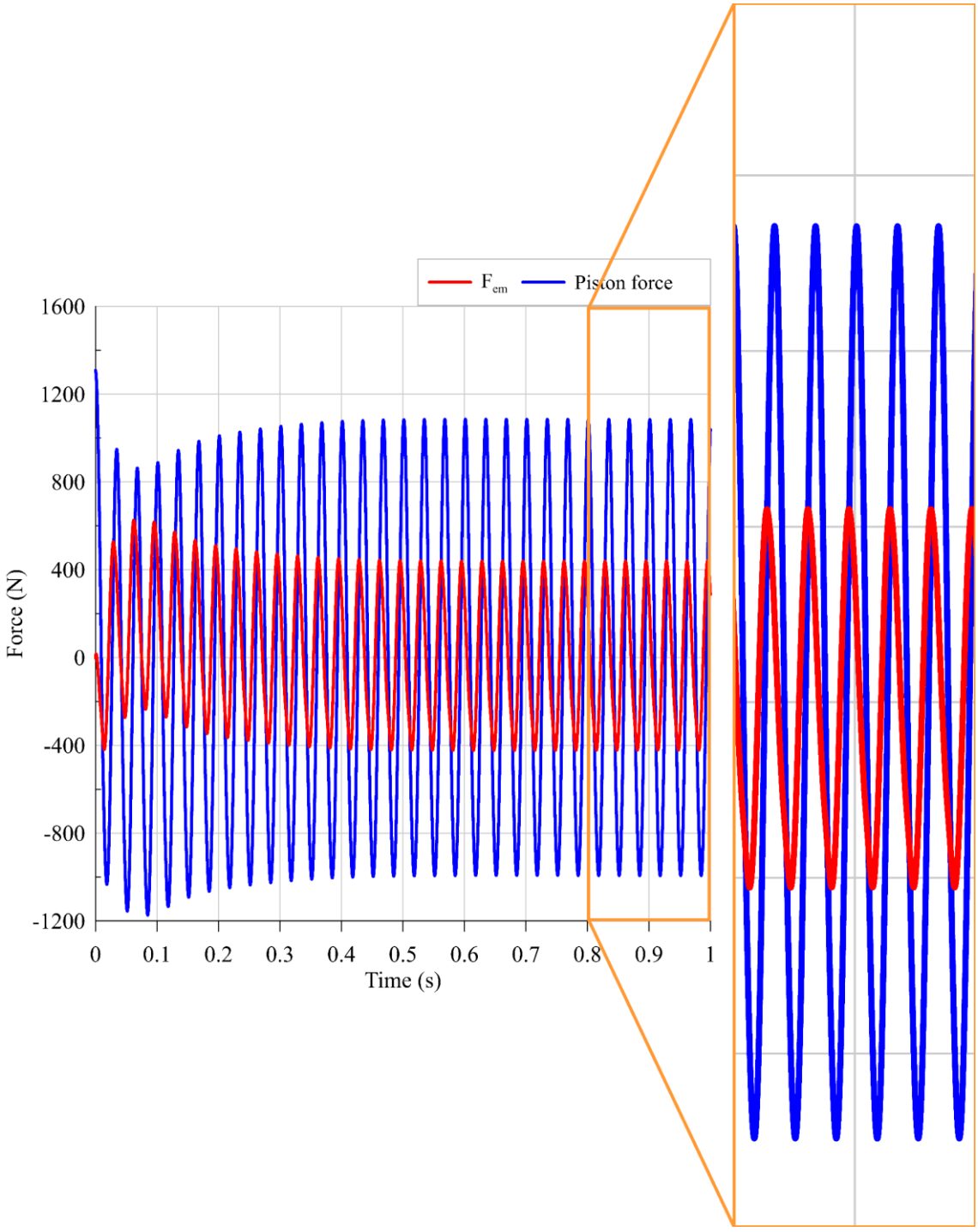

Figure 3.26: The electromagnetic and power piston forces in the FPSE-PMLSM combined system

As can be seen in Figure 3.26, the piston force is bigger than the electromagnetic force. This is logical since the system is in generating power phase. On these curves we can see the phase shift between two forces.

3.1.1 Performance Analysis

After modeling and validating the control method, the performance (efficiency and output power) of the FPSE-PMLSM combined system will be analysed based on the control system selected. It should be noted that the proposed control may not be the best one, but the present study allows us to analyze the performance of the combined system. As it was already discussed (Figure 3.2), there are three controllers in the combined system: two current controllers that are PI controllers, and one velocity controller, which is a PR controller. For the d current, the reference value, as it was already discussed in the beginning of the this chapter, is equal to zero. The reference value for the q current is the result of the velocity control (Figure 3.2). It means, for the currents' reference values no change can be applied in the present system. On the other side, the reference velocity is a sinusoidal wave whose amplitude and frequency should be identified. These two parameters based on the system performance can be defined to find the best system performance. One important point that should be considered in this identification is the physical limitations of the system, which are the maximum possible strokes of the two pistons. To do the performance analysis, it is assumed that the maximum strokes for power and displacer pistons are 0.014 m and 0.0154 m, respectively. The maximum strokes are chosen in a way to be in the most secure zone concerning the physical limitations of the FPSE to be able to develop the performance analyses after.

Now, two control methods can be applied based on the setting of the reference velocity. These control methods are based on the fact that with maximum electromagnetic power extraction (defined already in Equation 3.8) of the system, the system will have its best performance. Now, it is assumed that the reference velocity and electromagnetic force have a sinusoidal behavior with the same frequency and they can be defined as (the piston movement is assumed to be $x_P = X_P\, sin(\omega t + \varphi_0)$):

$$F_{em} = F\, sin(\omega t + \varphi_1) \tag{3.11}$$

$$\dot{x}_P = X_P \omega\, sin(\omega t + \varphi_2) \tag{3.12}$$

It should be noted that F and X_P are the maximum possible values at each frequency considering the system physical limitations. Now, Equation 3.8 can be rewritten as:

$$Power_{em} = FX_P\omega\, sin(\omega t + \varphi_1)\, sin(\omega t + \varphi_2) = \frac{FX_P\omega}{2}(cos(\varphi_1 - \varphi_2) - cos(2\omega t + \varphi_1 + \varphi_2)) \quad 3.13$$

To have the maximum electromagnetic power, it should be maximized during each period. Thus, its integration in a period should be maximum. The mean power in a period by $\omega t = \theta$ can be calculated as:

$$\frac{1}{2\pi}\int_0^{2\pi} Power_{em}\, d\theta = \frac{FX_P\omega}{4\pi}\int_0^{2\pi}(cos(\varphi_1 - \varphi_2) - cos(2\theta + \varphi_1 + \varphi_2))d\theta = \frac{FX_P\omega}{4\pi}\left(\theta\, cos(\varphi_1 - \varphi_2) - \frac{1}{2}sin(2\theta + \varphi_1 + \varphi_2)\right)\Big|_0^{2\pi} = \frac{FX_P\omega}{2}cos(\varphi_1 - \varphi_2) \quad 3.14$$

From Equation **3.14**, it can be concluded that the maximum electromagnetic power is a function of F, X_P, ω, and $cos(\varphi_1 - \varphi_2)$. Unlike F, other parameters including X_P, ω, and $cos(\varphi_1 - \varphi_2)$ can be defined directly. Two control method are developed to identify these parameters.

In the first method, the input variables (speed control references) are X_P (position magnitude) and ω (speed frequency and resonance frequency of the PR) and other parameters will be the result of this setting. In this method, the system behaviour with different reference values considering its physical limitation is studied to find the best frequency-amplitude pair for the reference velocity.

In the second method, that will be explained later, the focus is on identifying the X_P and $cos(\varphi_1 - \varphi_2)$. To maximize $cos(\varphi_1 - \varphi_2)$, the phase difference between φ_1 and φ_2 ($\varphi_1 - \varphi_2$) should be 0 or π. Phase difference equal to 0 is for the motor case that the electromagnetic force is the cause of the movement, and as a result, the velocity has the same direction as the force. Here, since the PMLSM is a generator, the phase difference should be equal to π. So the second method is based on a control method that imposed a phase shift equal to π and also the maximum possible X_P. This method will be explained in detail as the second control method.

In the first control method the performance of the system is analyzed, the reference velocity amplitude and frequency are varied independently to find the best system response according to its physical limitations. First, based on these limitations, the effect of the reference velocity amplitude and frequency on the system efficiency will be studied

separately. To achieve this goal, the velocity amplitude or the frequency is fixed, and the other one is changed considering the physical limitations to see its effect on the system performance.

Figure 3.27 and Figure 3.28 are the results of the reference velocity parameter variations. In Figure 3.27, the reference velocity amplitude is constant while its frequency is varying, and in Figure 3.28, the velocity frequency is constant while its amplitude is varying.

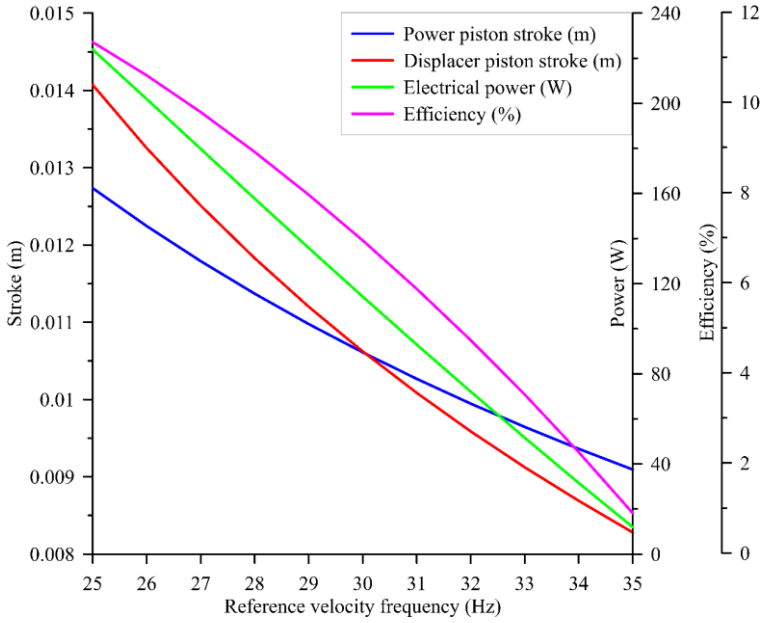

(a)

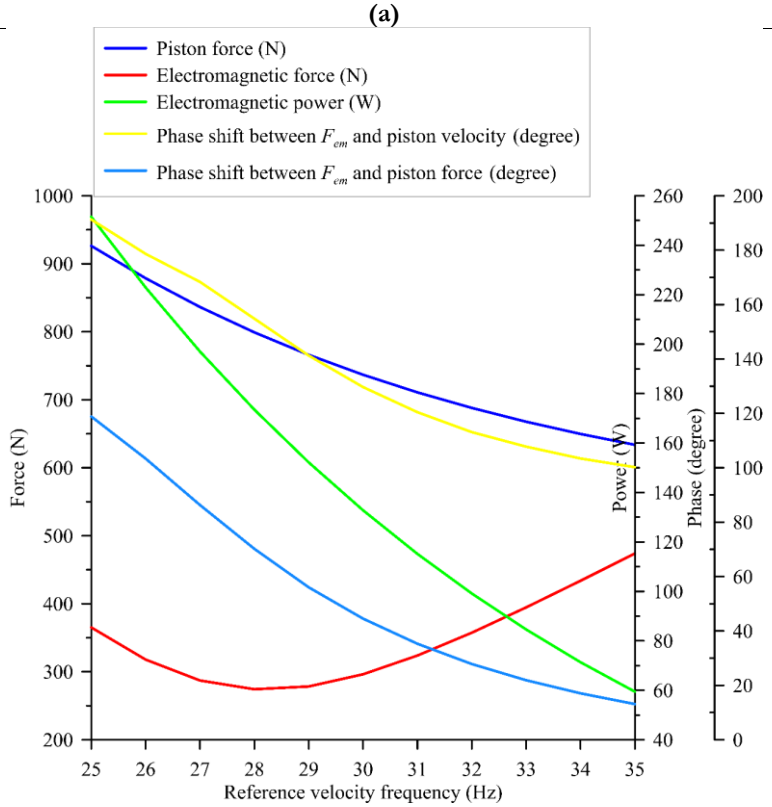

(b)

Figure 3.27: FPSE-PMLSM results at constant reference amplitude of 1 m/s and variable frequency

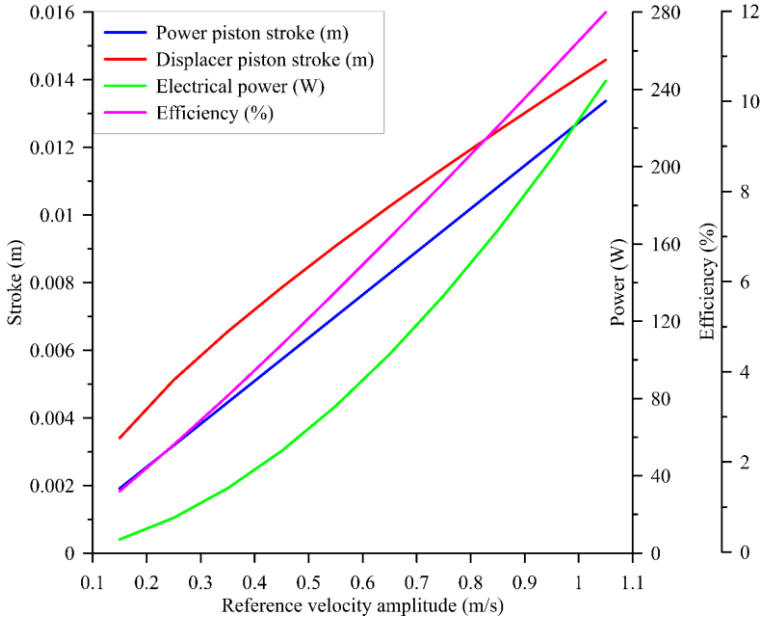

(a)

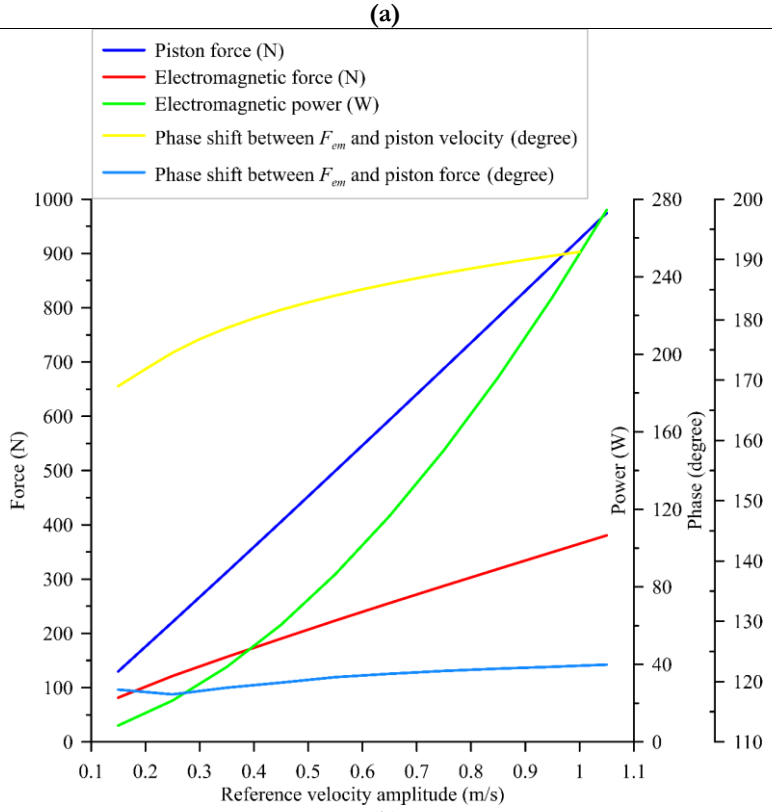

(b)

Figure 3.28: FPSE-PMLSM results at a constant reference frequency of 25 Hz and variable amplitude

As shown in Figure 3.27 and Figure 3.28, the frequency decrement at constant amplitude, and the amplitude increment at constant frequency improve the system performance (efficiency and produced power). This increment or decrement continues until one of the pistons gets to its maximum stroke. Under these conditions, when the system meets its physical limitation, more amplitude increment or frequency decrement is not possible. For the given conditions (thermodynamic), the Stirling engine delivers a force which is a function of the frequency and amplitude. It should be noted that there are two parameters in electromagnetic force that plays a vital role to calculate the power and efficiency: its phase shift with the FPSE force and with the velocity and its magnitude. It is the reason that for some frequencies, the electromagnetic force can increase (Figure 3.27) and the electromagnetic power, electrical power, and efficiency decrease. For the forces, their RMS (Root Mean Square) values are used. Furthermore, as can be seen in Figure 3.27 and Figure 3.28, the phase shift between electromagnetic force and piston force is almost constant by reference velocity amplitude variation at constant frequency, and is decreasing by reference velocity frequency increment at its constant amplitude. It means the frequency plays the most important role in the phase shift identification between forces.

In Figure 3.29 the variations of the forces (electromagnetic force and power piston force) by time for two steady state cycles are shown. Figure 3.30 also shows the variation of the piston velocity and electromagnetic force by time for two steady state cycles. These results are for the reference velocity amplitude as $\dot{x}_{P\,reference} = 1 \times sin(30 \times 2\pi \times t)$.

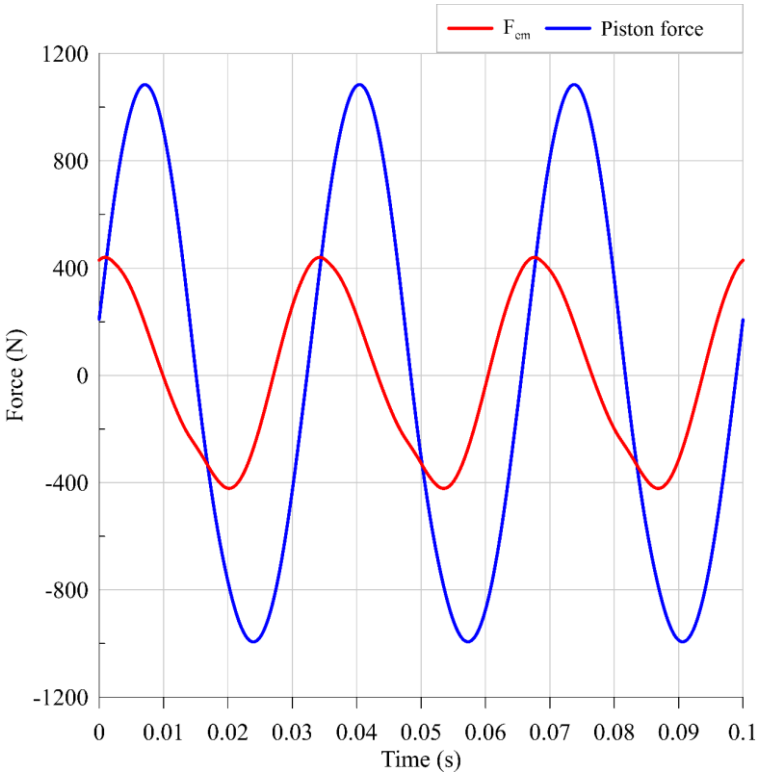

Figure 3.29: Electromagnetic and piston forces in steady state cycles for frequency = 30 Hz and velocity amplitude = 1

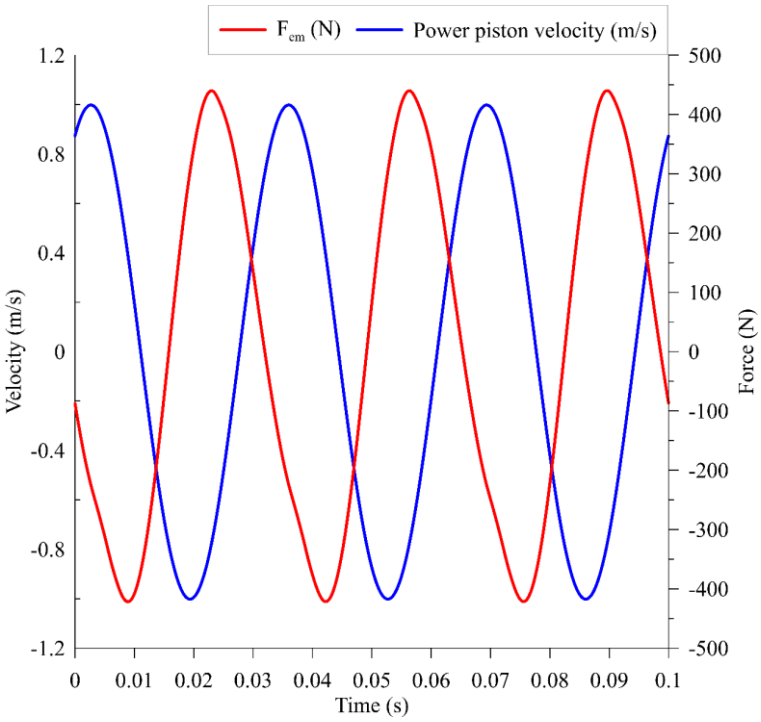

Figure 3.30: Electromagnetic force and power piston velocity in steady state for frequency = 30 Hz

As can be seen in Figure 3.29 and Figure 3.30, there is a phase shift between forces and also between electromagnetic force and piston velocity. Also, the behavior of the forces is almost sinusoidal. It justifies the choice of a sinusoidal reference velocity. More of such results are presented in Appendix 2.

The first important result extracts from Figure 3.27 and Figure 3.28 is that the best performance of the system at the defined physical conditions, is obtained when the reference velocity amplitude is maximum, and the frequency should be minimum. The second important point is that there is a direct link between pistons' strokes and the system performance. Thus, the frequency and amplitude pairs of the reference velocity should be defined in a way that at least one of the pistons gets to its maximum possible stroke. There are many frequency-amplitude pairs for the reference velocity that can meet these conditions, which obviously all of them are not the optimum points, and the best pair should be identified. Thus, at each frequency, the maximum possible amplitude of the reference velocity to meet the physical limitations is found to identify all the pairs. Then, the output power and efficiency are calculated for each pair. Finally, the results of the system modeling for all pairs are shown in Figure 3.31 and Figure 3.32.

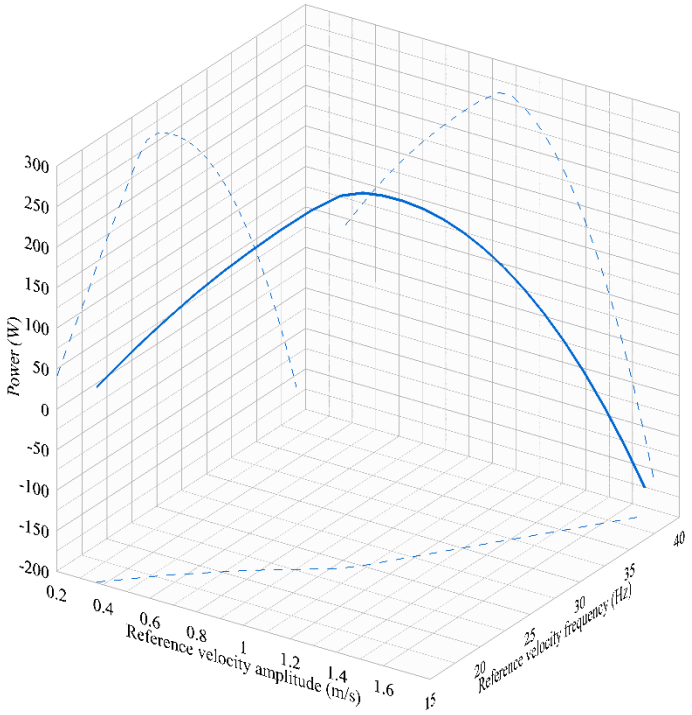

Figure 3.31: FPSE-PMLSM output power at different amplitude-frequency pairs of the reference velocity

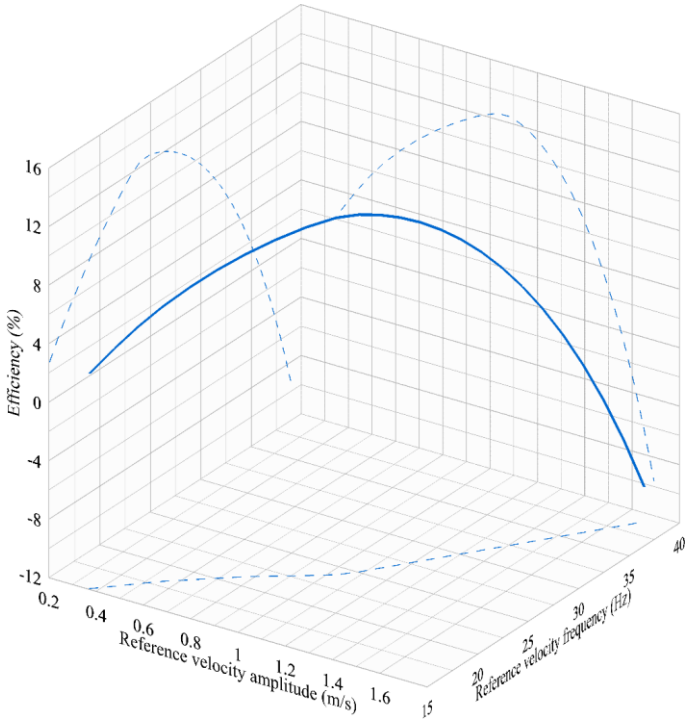

Figure 3.32: FPSE-PMLSM efficiency at different amplitude-frequency pairs of the reference velocity

Based on Figure 3.31 and Figure 3.32, the maximum output power (260.8 W) and efficiency (12.47 %) are related to the same amplitude-frequency pair of 1.085 m/s - 25 Hz. All the amplitude-frequency pairs of Figure 3.31 and Figure 3.32 are concerned with the physical limitations of the system. To show which piston's stroke identifies the physical limit of the system of each pair, Figure 3.33 is presented.

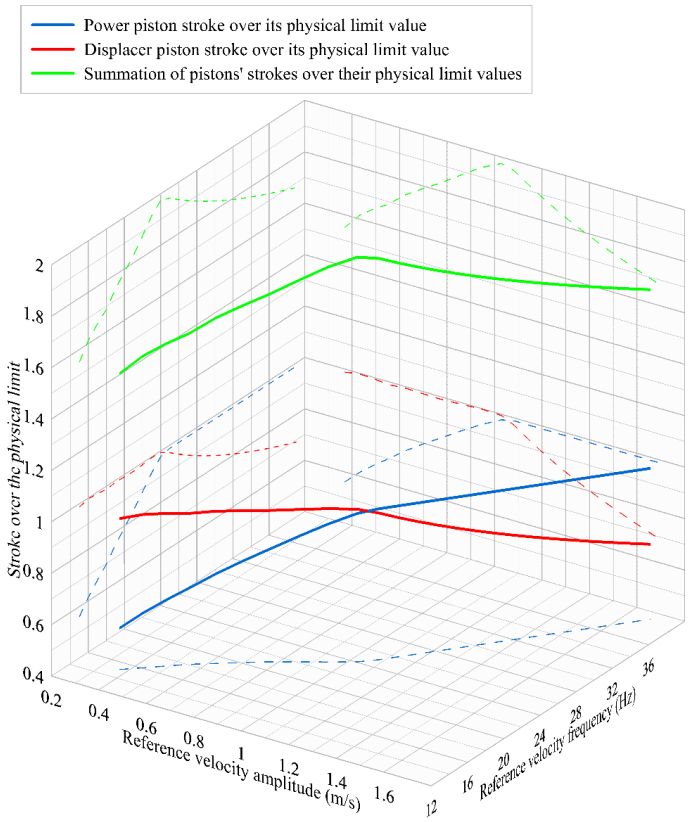

Figure 3.33: System physical limitation at each frequency-amplitude reference value pair

As can be seen in Figure 3.33, for each frequency-amplitude pair of the reference velocity, at least one of the pistons gets to its maximum possible stroke. At high frequencies (more than 24 Hz), the physical limit is applied by the power piston, and at the small frequencies (less than 24 Hz), this limit is applied by the displacer piston. As can be seen in Figure 3.33, the maximum of the summation of pistons' strokes divided by their physical limit value happens at velocity amplitude-frequency pair of 1.031 m/s - 24 Hz. This point is very close to the optimum point (1.085 m/s - 25 Hz) that was already found in Figure 3.31 and Figure 3.32. The system output power and efficiency at the point with the maximum summation of the strokes are equal to 260.65 W and 12.45 %, respectively. These results have less than 0.1 % difference with the optimum ones (260.8 W-12.46 %).

An interesting and important result that can be obtained here is that in the FPSE-PMLSM combined system, the both piston strokes are important. It means, since the power piston is connected to the PMLSM mover, it should not be concluded that the power piston stroke should be increased regardless of the displacer piston stroke.

At the end, the phase shift between electromagnetic force and reference velocity ($\varphi_1 - \varphi_2$) for the reference amplitude-frequency pairs of the Figure 3.33 is shown in Figure 3.34.

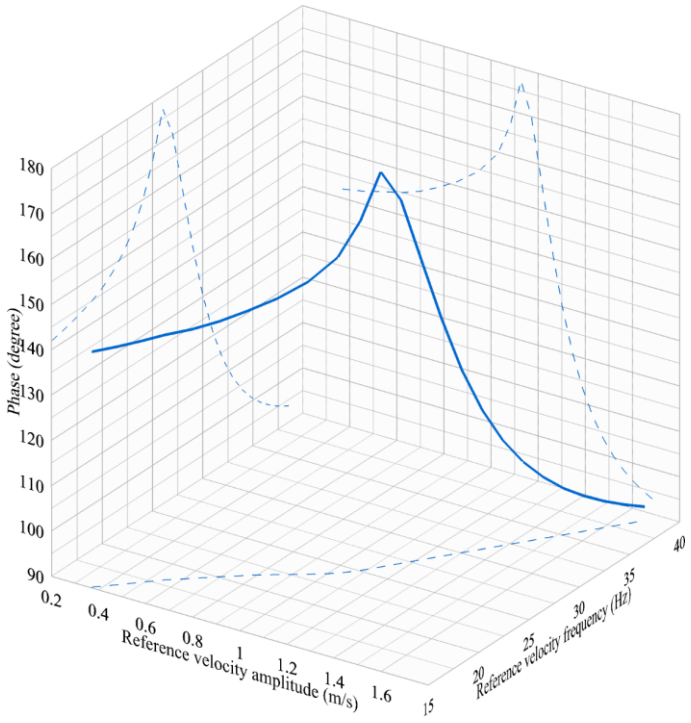

Figure 3.34: Phase difference between electromagnetic force and reference velocity at each frequency-amplitude reference value pair

As can be seen in Figure 3.34, the phase difference between reference velocity and electromagnetic force at the optimum point (1.085 m/s - 25 Hz) is equal to 167.31 degree and it has its maximum value at the 1.129 m/s - 26 Hz which is equal to 177.33 degree. The output power and efficiency at this point (1.129 m/s - 26 Hz) are equal to 253 W and 12.20 %, respectively.

The first control method shows that first of all, an optimum point exists for the combined system. At this optimum point, the power and efficiency have their maximum values. Also, the results show that this point is almost the same point that the sum of piston and displacer strokes has its maximum value. Furthermore, at this point, the phase shift between electromagnetic force and velocity is very close to π.

3.2 Second Control Method & Performance Analysis

In this method, as it was already discussed, a phase shift equal to π is applied between the electromagnetic force and the reference velocity considering X_P. To apply this phase shift, since $sin(\theta - \pi) = -sin\,\theta$, with a negative gain for electromagnetic force, the required phase shift can be obtained for the reference velocity. Also, the X_P value can be controlled through the gain magnitude. The schematic of the reference velocity identification based on the electromagnetic force is shown in Figure 3.35.

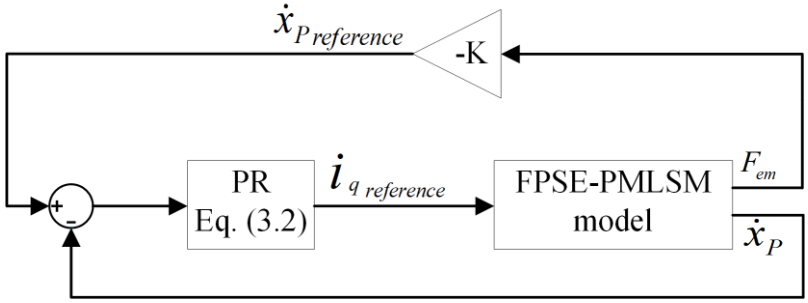

Figure 3.35: Identifying reference velocity based on electromagnetic force

In Figure 3.35, the coefficient K is a very small (compared to 1) positive constant that is used to identify reference velocity considering the physical limitations of the system (power and displacer pistons' maximum strokes of 0.014 m and 0.0154 m, respectively). This value is found to be equal to 1/418.6 to have power and displacer pistons' maximum strokes equal to 0.014 m and 0.01454 m. Since with this value of K the system meets its physical limitations, it is not possible to increase it. It should be noted that the PR frequency is equal to 26 Hz and is constant.

The results of the system modeling considering this method of control shows the output power and efficiency equal to 255.4 W and 12.27 %, respectively. These results are very close to the result of the previous optimization method (260.8 W - 12.46 %). In this proposed method, the velocity amplitude and frequency were equal to 1.16 m/s and 26.3 Hz, respectively, which are also close to the previous results.

The advantage of the first control method is that the stability analysis for it is done and also since the control parameters were chosen to be at the safest zone, it is not very sensitive to the system parameters and in general will be stable. The disadvantage of the first method is that since two parameters should be identified (velocity amplitude and frequency), it is

numerically time-consuming analysis. The advantage of the second method is since just one coefficient should be identified, it is much faster compared to the first method from numerical point of view. This method gave an efficiency smaller that the first method, but the difference is negligible. Concerning the second method, the stability of the system under this running condition is not studied (lack of time), so there is no information about the robustness of this control. Anyway, this method seems harder to be applied directly to a real system, because there is a strong probability that the value of the K constant (Figure 3.35) must be updated online according to the evolution of the external parameters of the FPSE to ensure the optimum condition of oscillation. In simulation this method allows to quickly find the neighborhood of the maximum efficiency point.

4 APPLICATION

In this chapter, the FPSE-PMLSM system will be studied from the application point of view. First, a sensitivity study will be done to see the effect of different parameters on the system response. This study is valuable from the practical point of view. When the theoretical model is going to be validated with the experimental setup, some physical parameters may not be well estimated or well measured. Thus, the effect of these parameters on system response will be studied. Then, the FPSE-PMLSM system will be used as a heat recovery option in a tri-generation IRSOFC based system to see its application in a combined system.

4.1 Sensitivity Study

As it was already discussed, when a model is going to be validated with an experimental setup, due to bad estimation/measurement of different parameters, there might be a difference between the results. Here, the effect of variations of different thermal, electrical, and physical parameters on the system is studied to see the sensitivity of the system response to each parameter and how bad estimation of each parameter will affect the system response. There will be some parameters that they may not need precise measurement/estimation, and some of them may need more precision. Furthermore, it gives an idea of that by changing which parameters it would be possible to have a better system response.

Here, the precision of the used equations is not the subject of the study, and it is assumed that they have the required precision, but if there is a difference, it comes from the input parameters that were measured or estimated. Thus, the combined FPSE-PMLSM system response to 10% variation of the input data of Table 2.3 and Table 3.2 with $\dot{x}_{P\,reference} = 1 \times sin(30 \times 2\pi \times t)$ is studied. The presentation order of the parameters implied into the

sensitivity study is based on the alphabetic order. The presented results are the percentage of variations of system output power and efficiency by varying the parameters compared to the base case (by input data of Table 2.3 and Table 3.2).

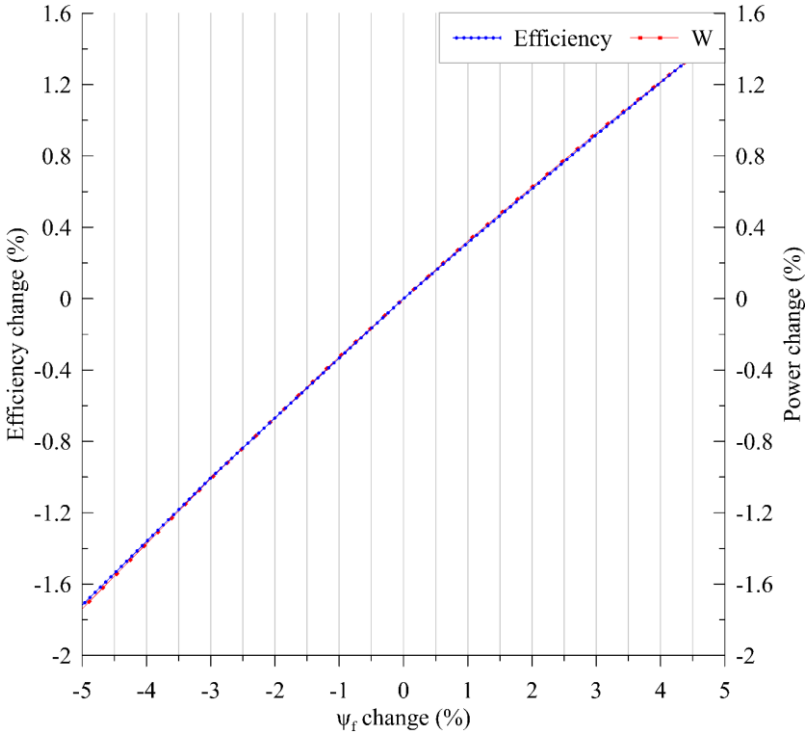

Figure 4.1: Sensitivity of the system to the ψ_f

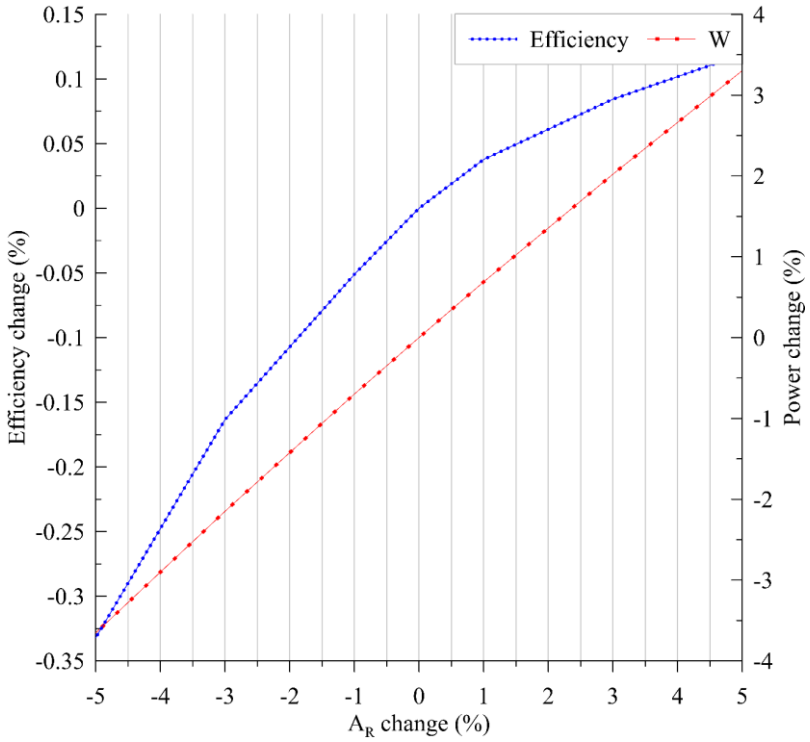

Figure 4.2: Sensitivity of the system to the A_R

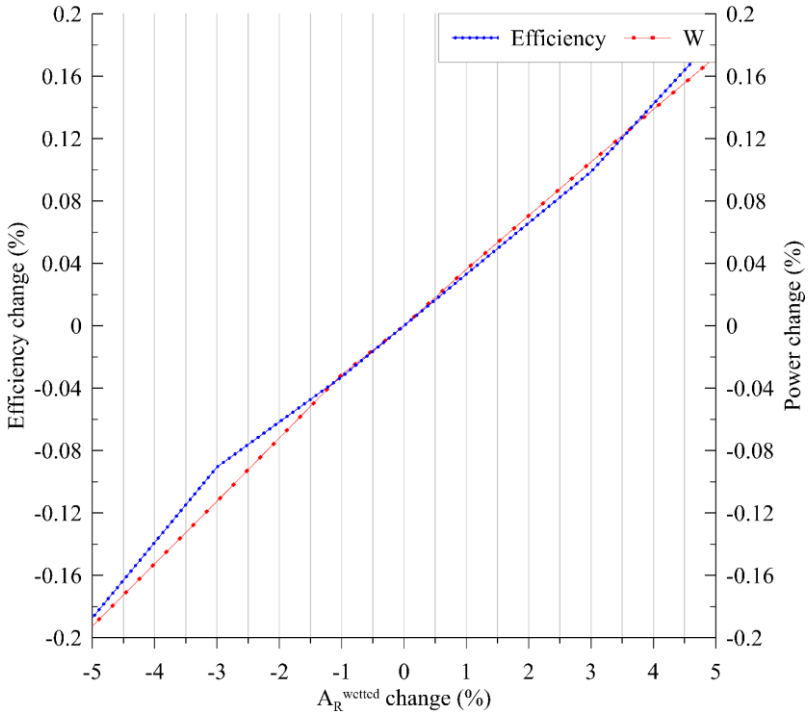

Figure 4.3: Sensitivity of the system to the A_R^{wetted}

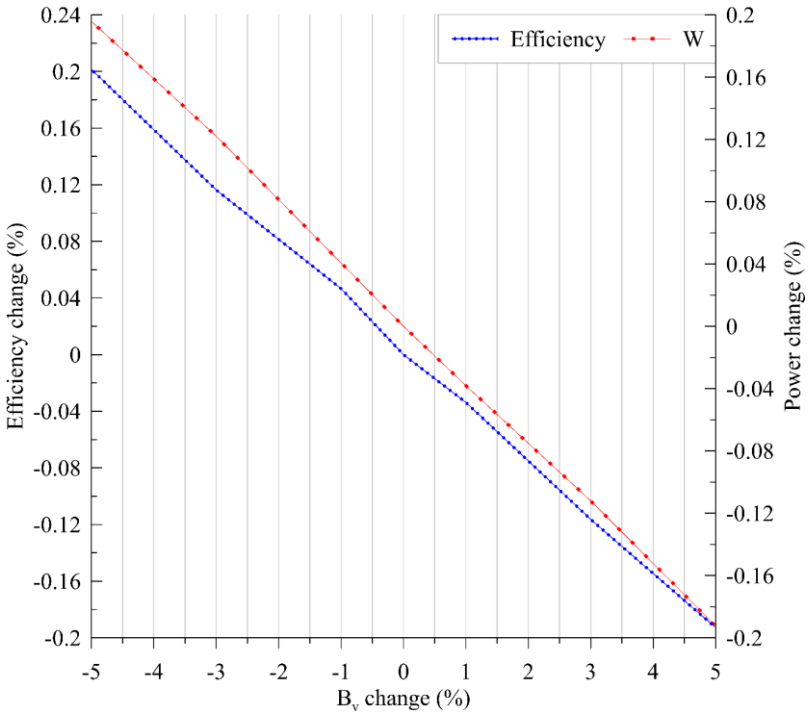

Figure 4.4: Sensitivity of the system to the B_v

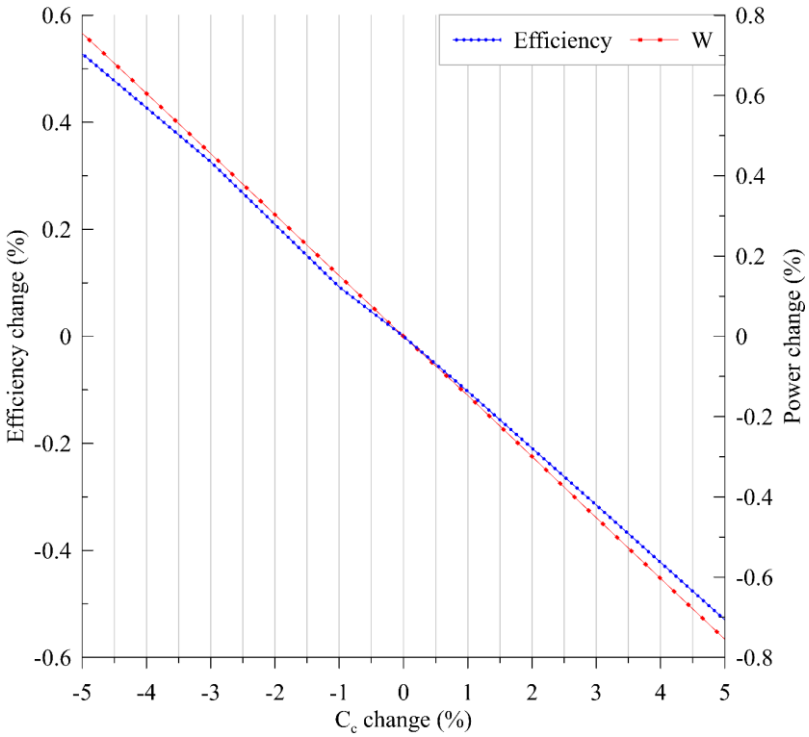

Figure 4.5: Sensitivity of the system to the C_c

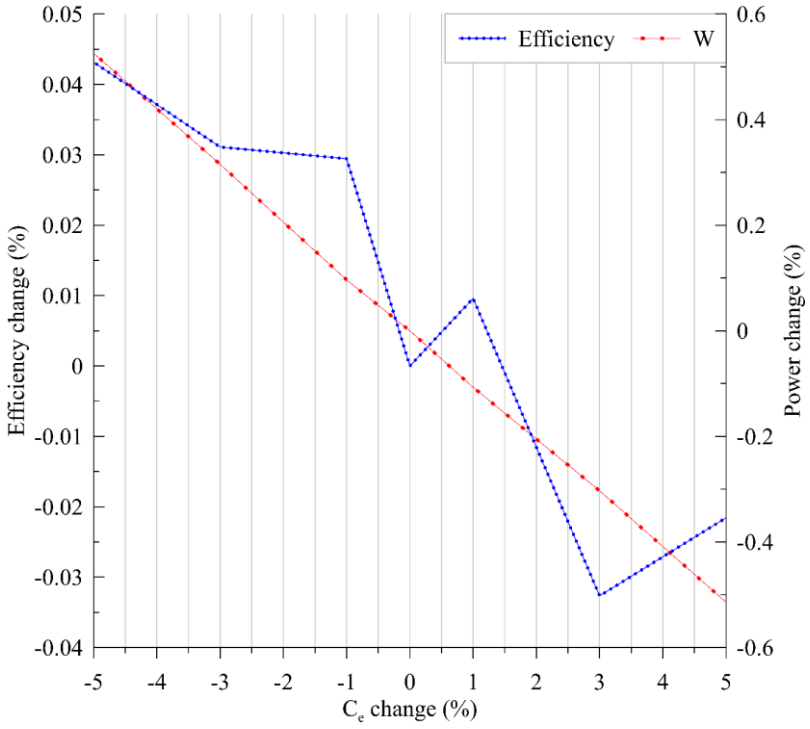

Figure 4.6: Sensitivity of the system to the C_e

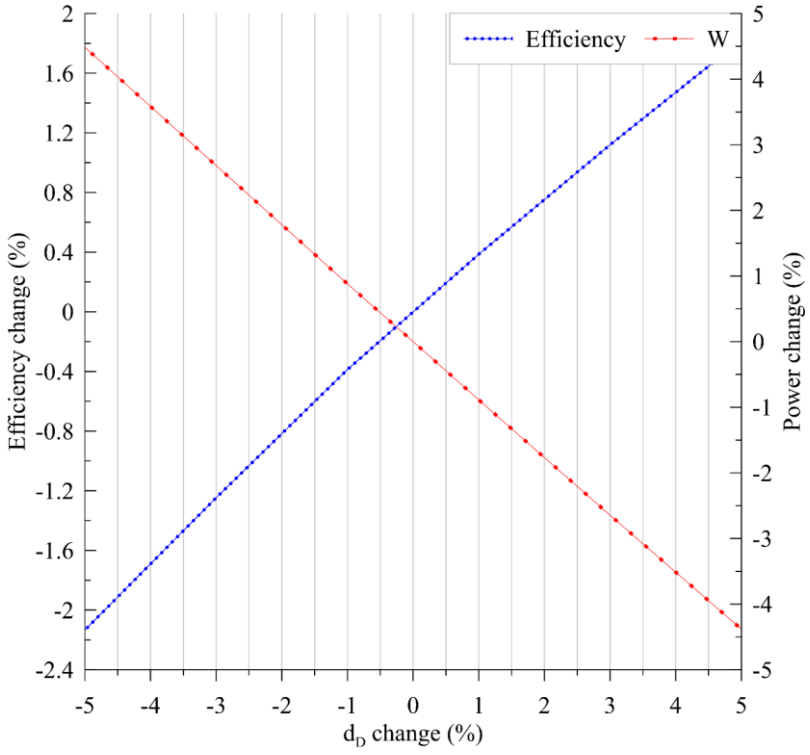

Figure 4.7: Sensitivity of the system to the d_D

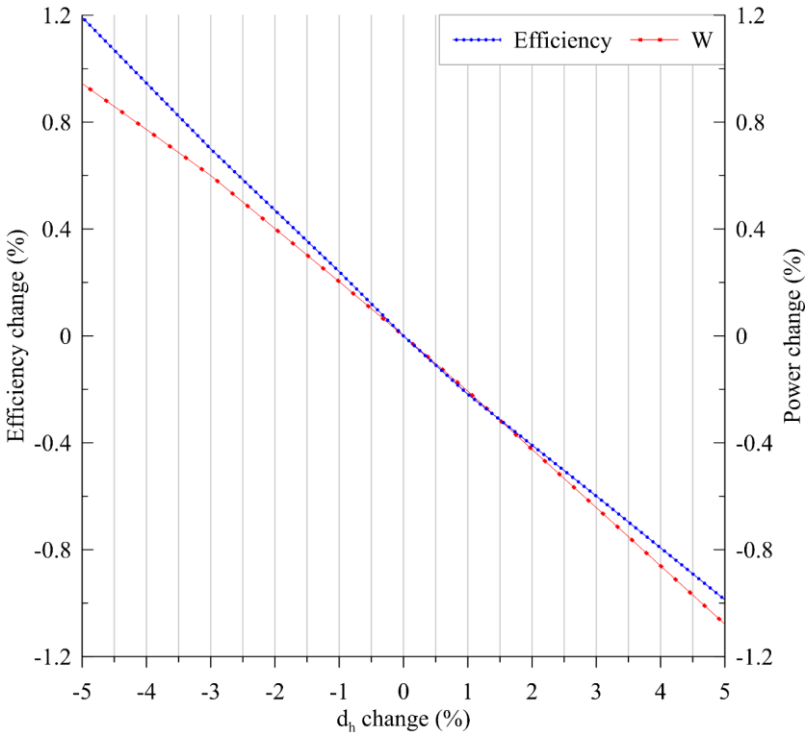

Figure 4.8: Sensitivity of the system to the d_h

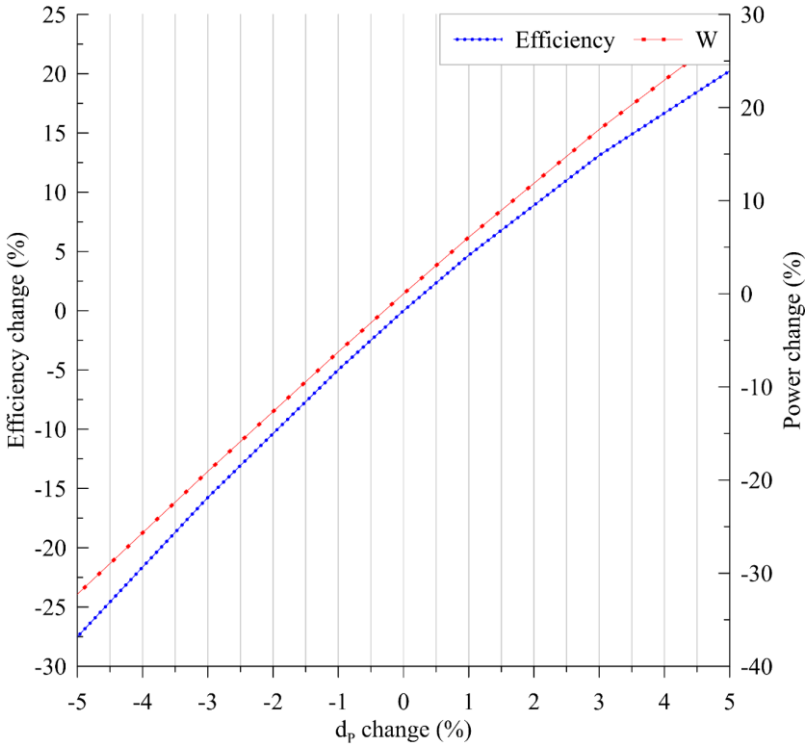

Figure 4.9: Sensitivity of the system to the d_P

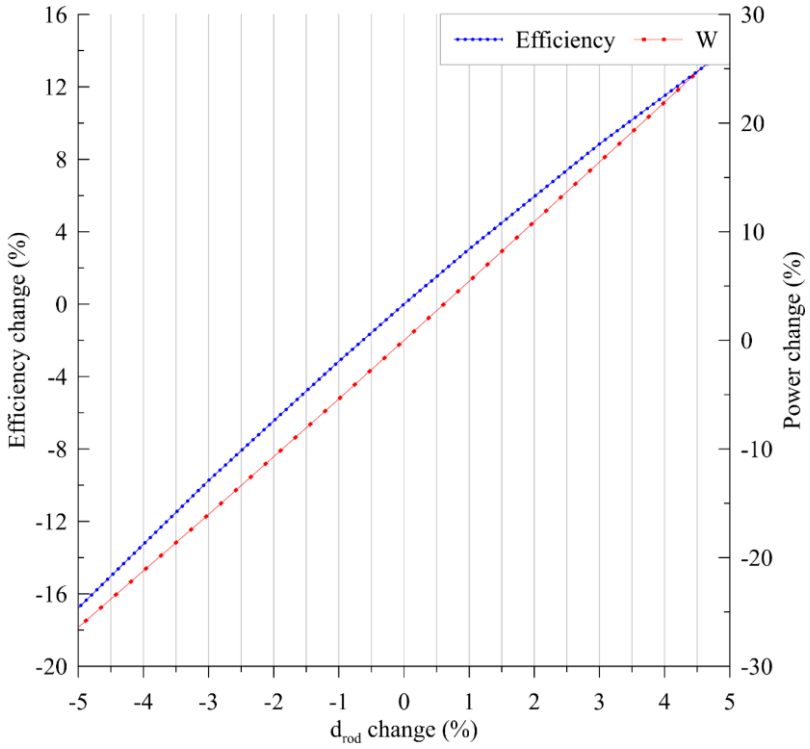

Figure 4.10: Sensitivity of the system to the d_{rod}

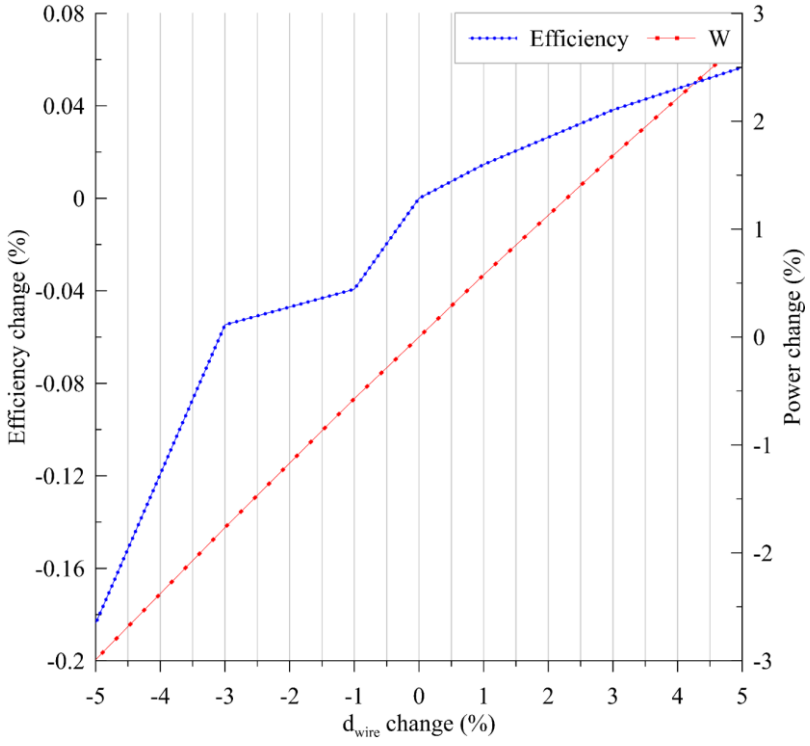

Figure 4.11: Sensitivity of the system to the d_{wire}

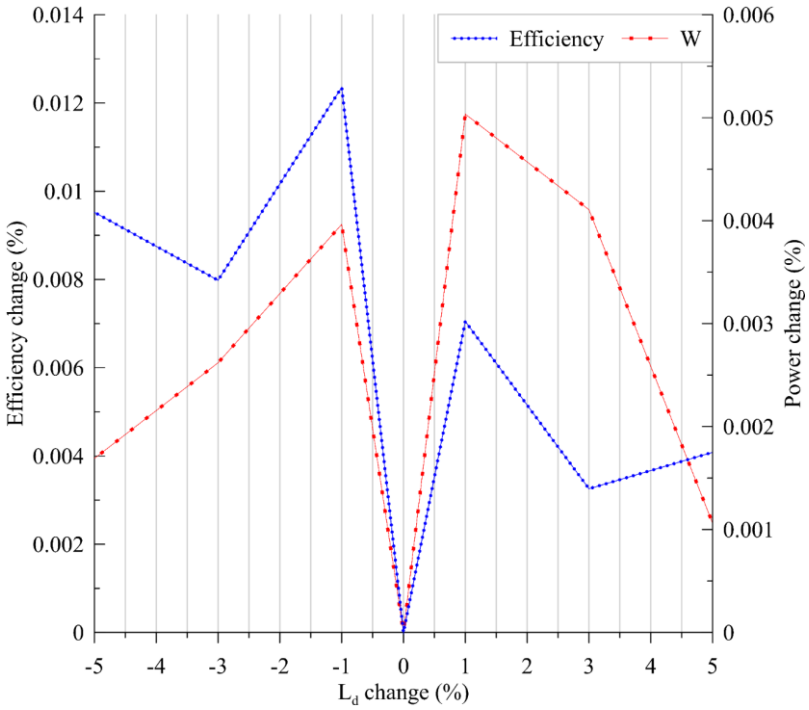

Figure 4.12: Sensitivity of the system to the L_d

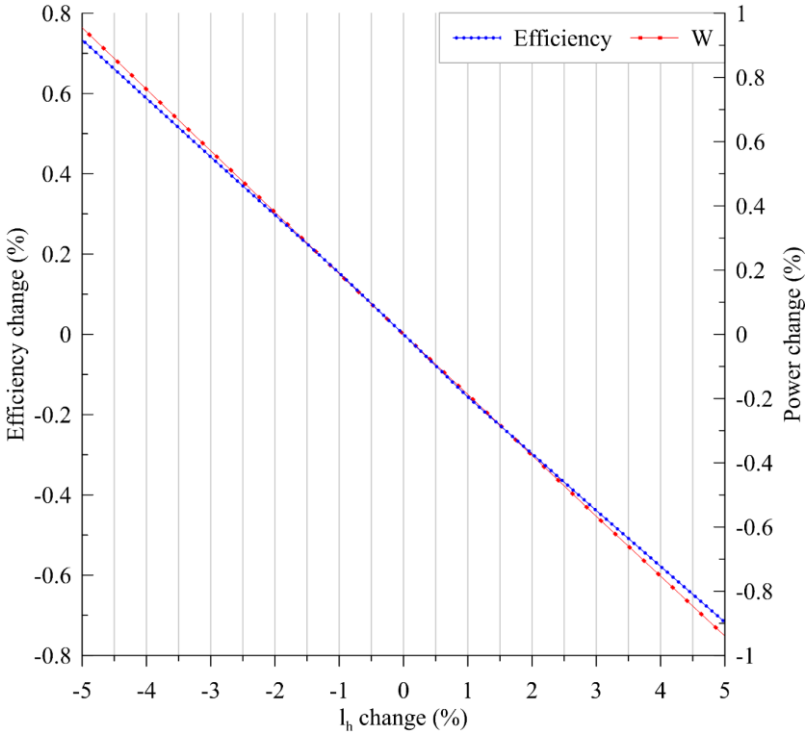

Figure 4.13: Sensitivity of the system to the l_h

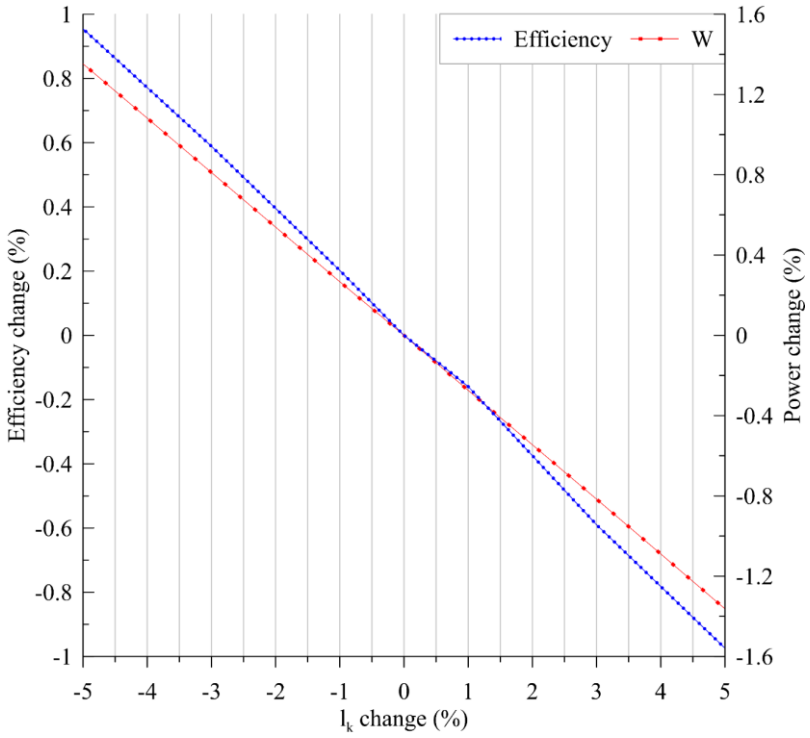

Figure 4.14: Sensitivity of the system to the l_k

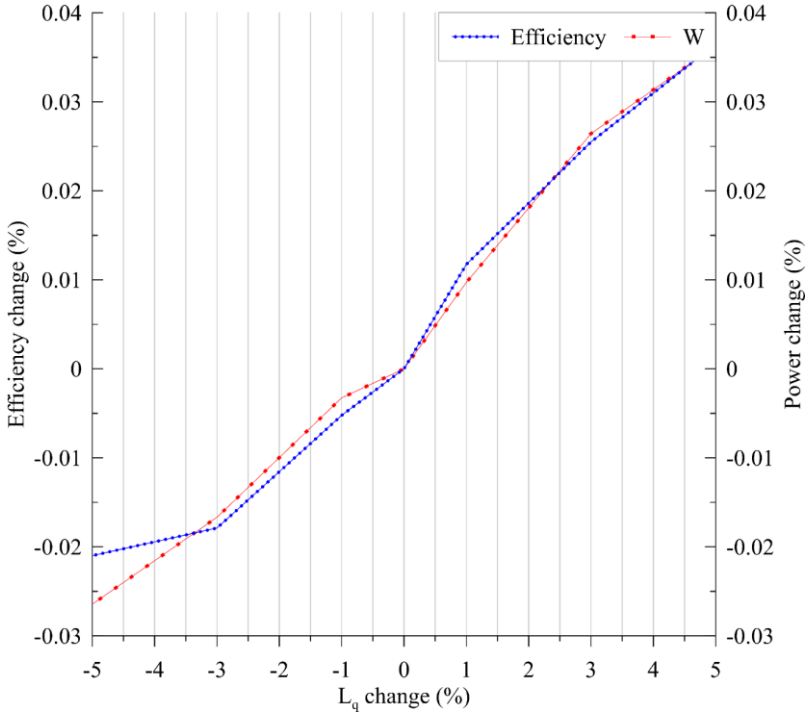

Figure 4.15: Sensitivity of the system to the L_q

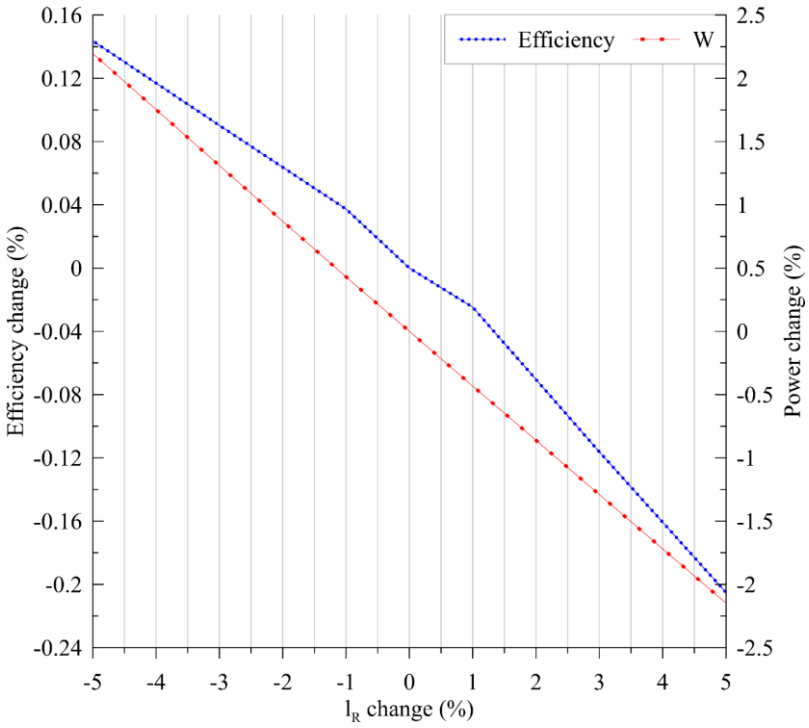

Figure 4.16: Sensitivity of the system to the l_R

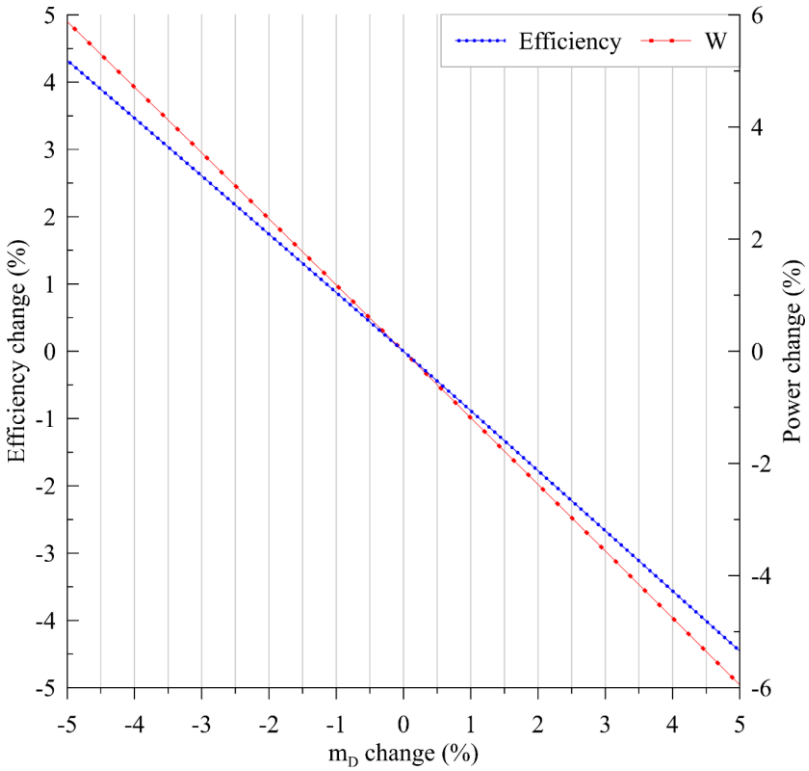

Figure 4.17: Sensitivity of the system to the m_D

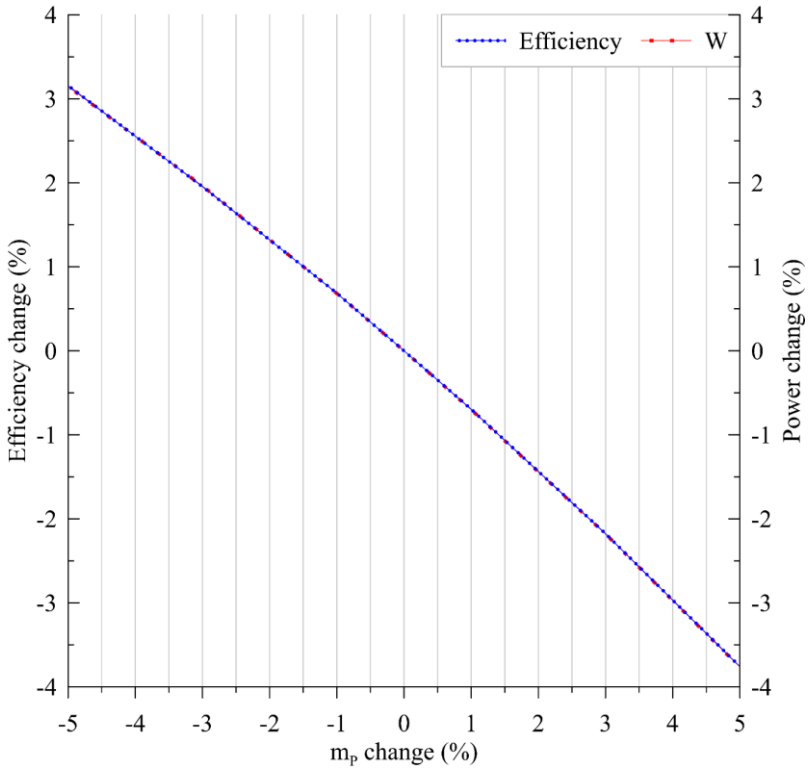

Figure 4.18: Sensitivity of the system to the m_P

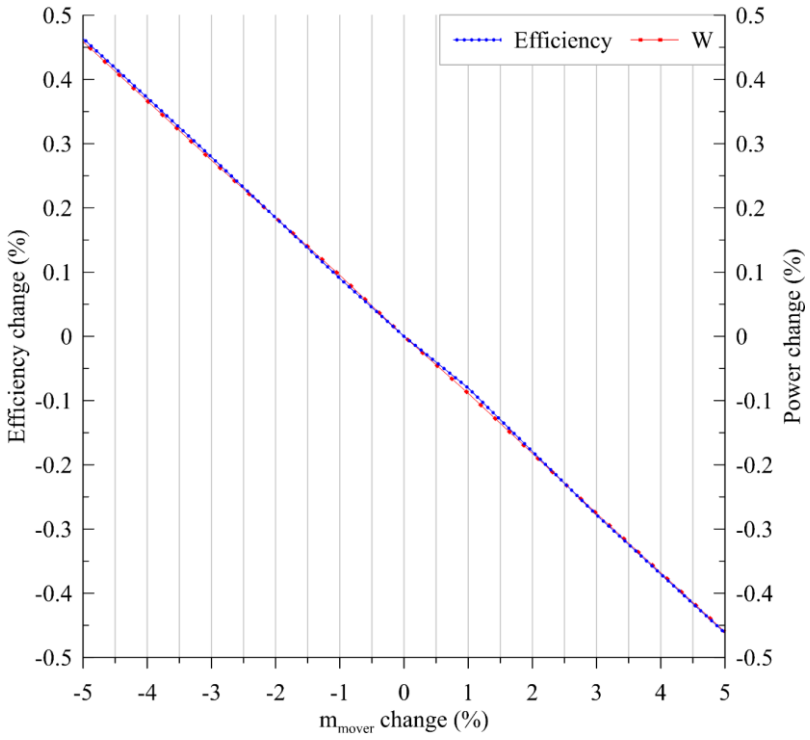

Figure 4.19: Sensitivity of the system to the m_{mover}

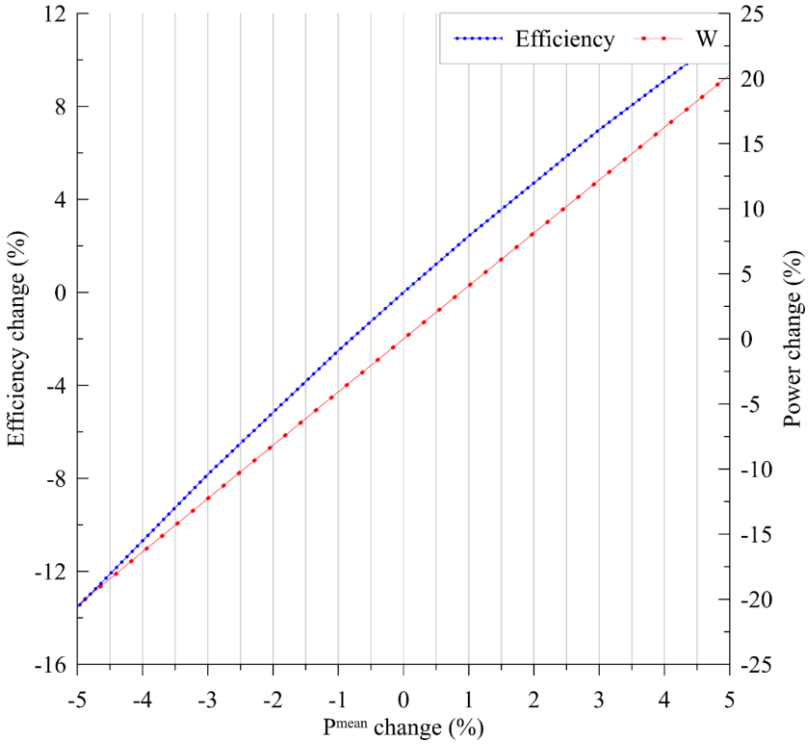

Figure 4.20: Sensitivity of the system to the P^{mean}

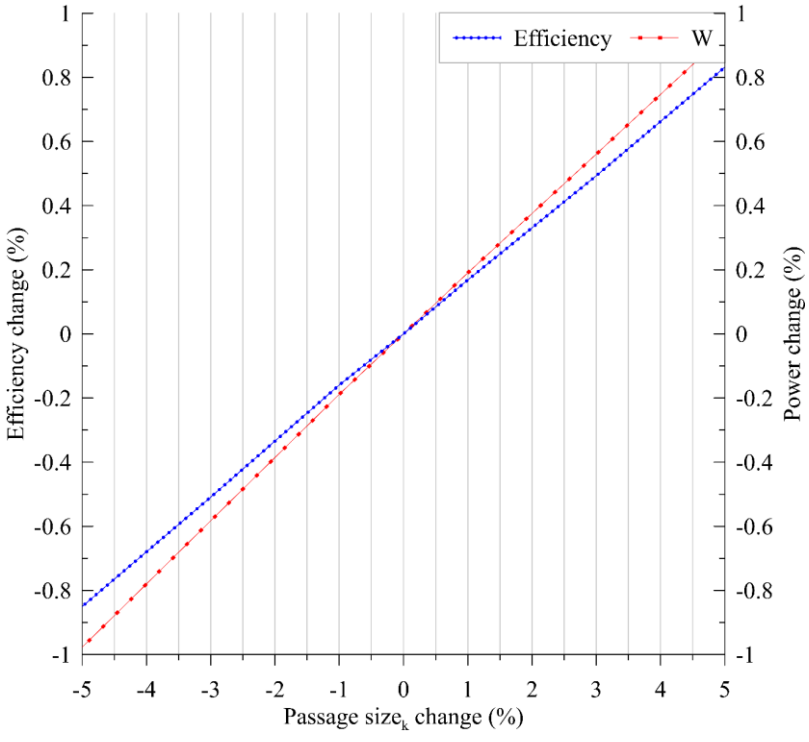

Figure 4.21: Sensitivity of the system to the $Passage\ size_k$

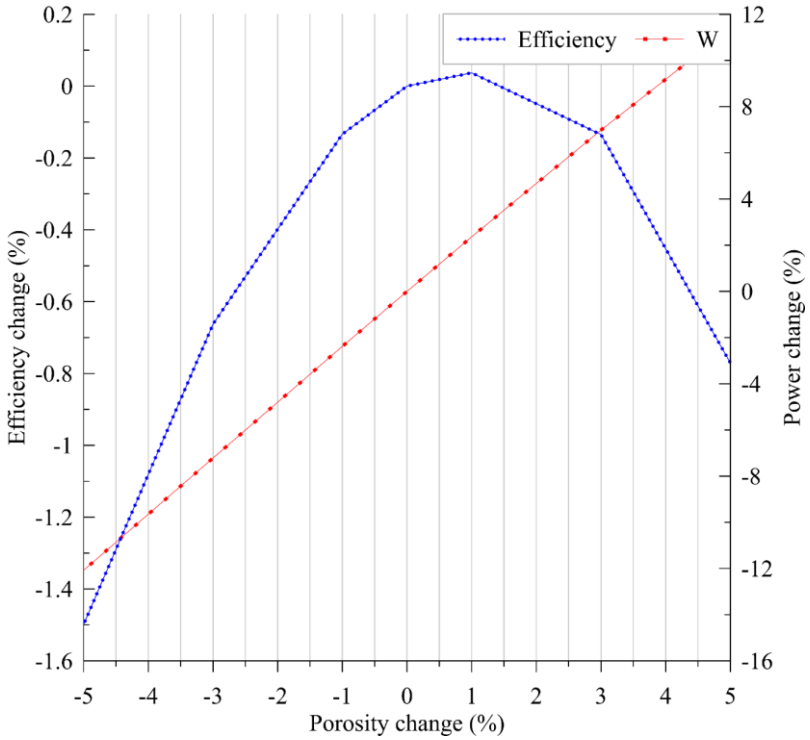

Figure 4.22: Sensitivity of the system to the *Porosity*

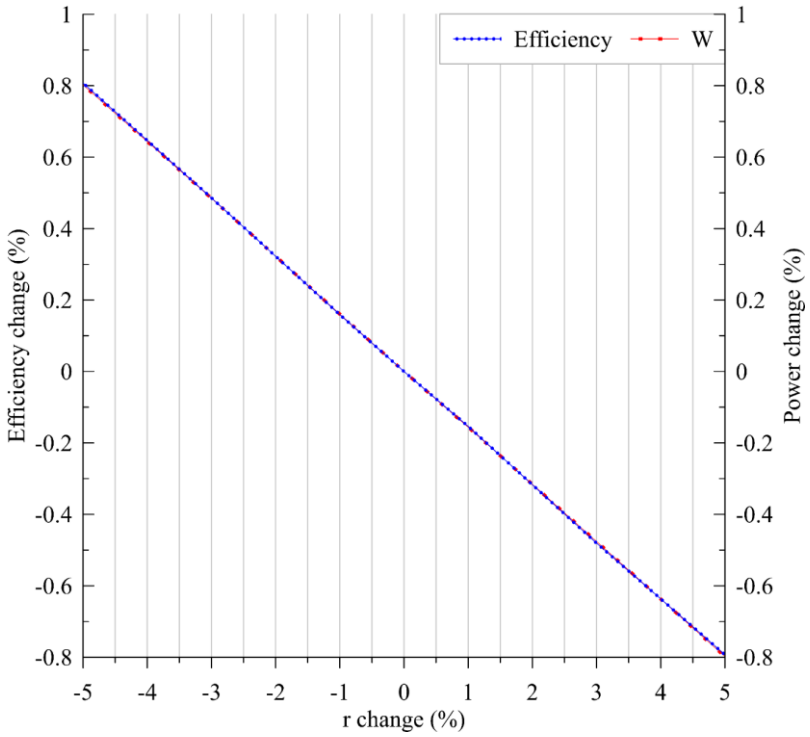

Figure 4.23: Sensitivity of the system to the *r*

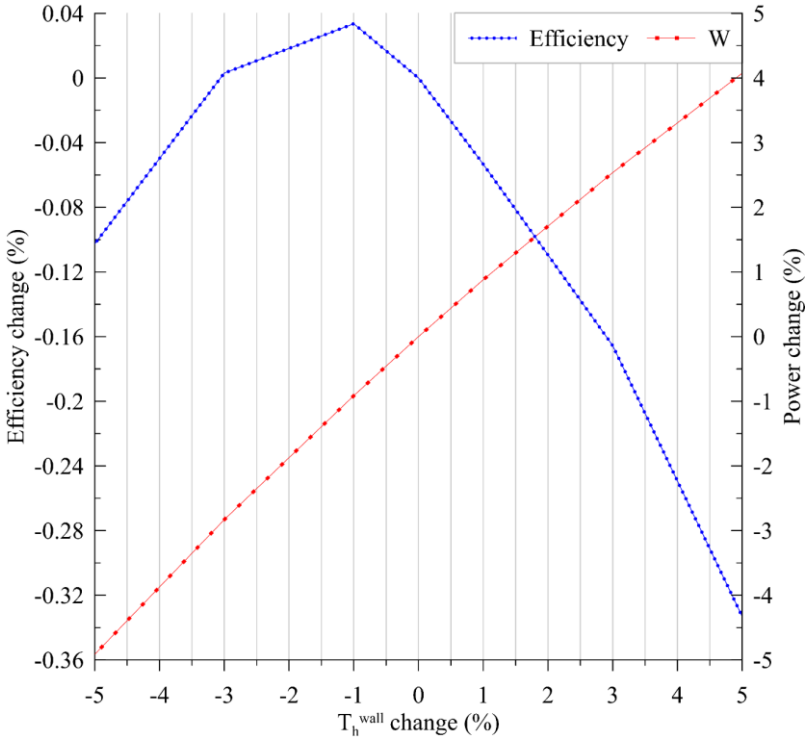

Figure 4.24: Sensitivity of the system to the T_h^{wall}

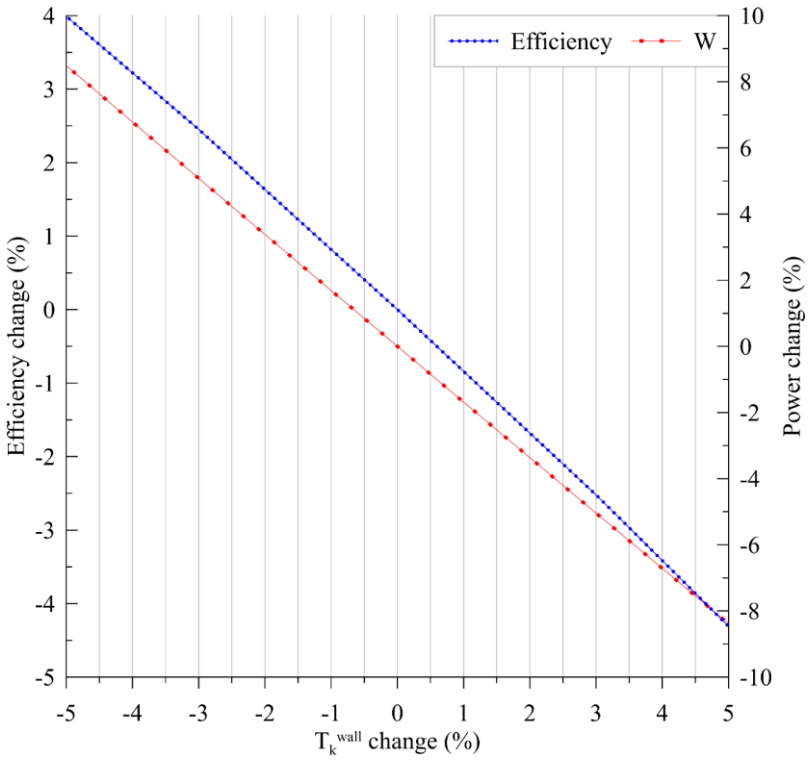

Figure 4.25: Sensitivity of the system to the T_k^{wall}

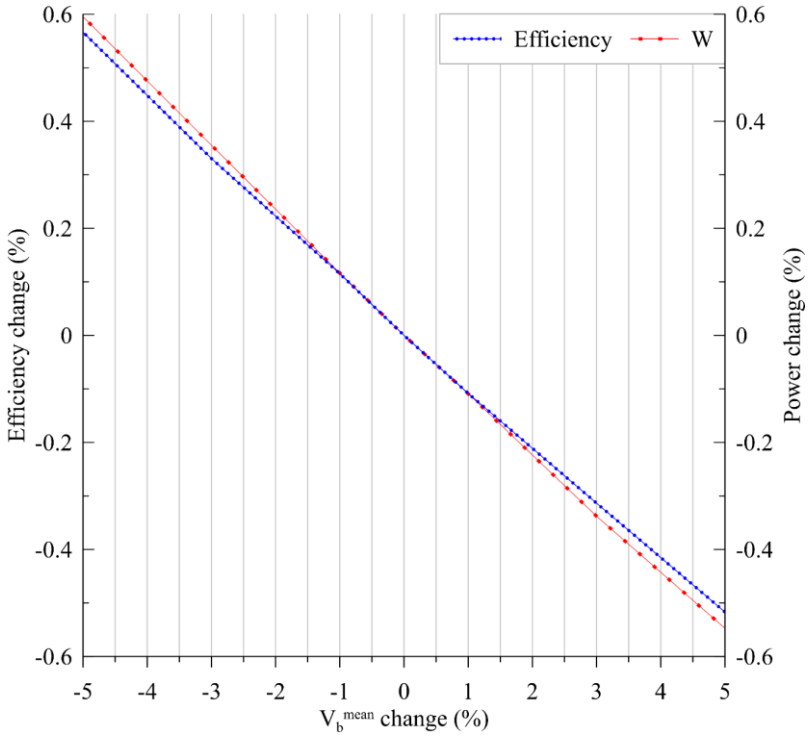

Figure 4.26: Sensitivity of the system to the V_b^{mean}

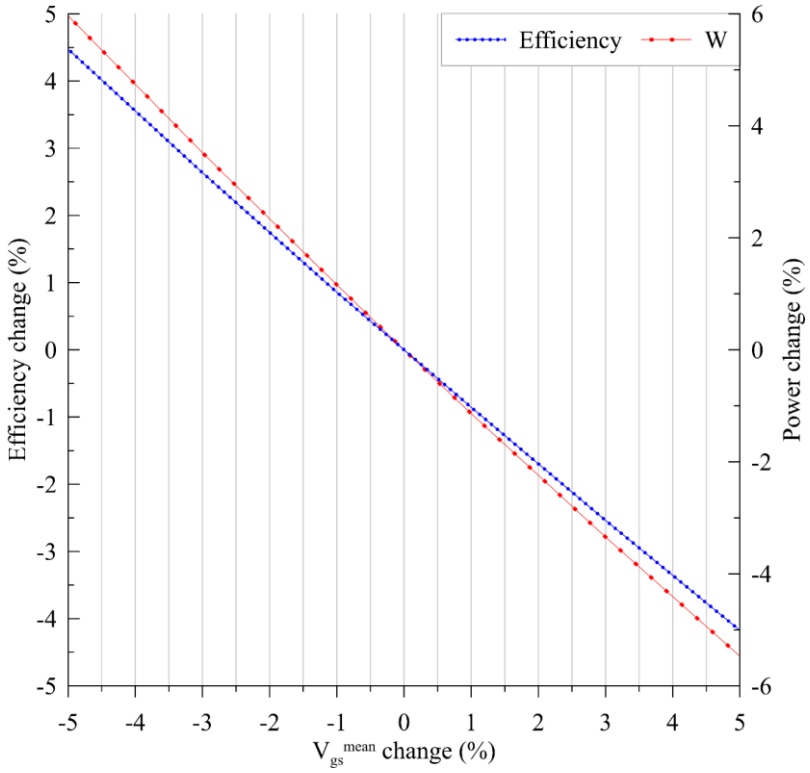

Figure 4.27: Sensitivity of the system to the V_{gs}^{mean}

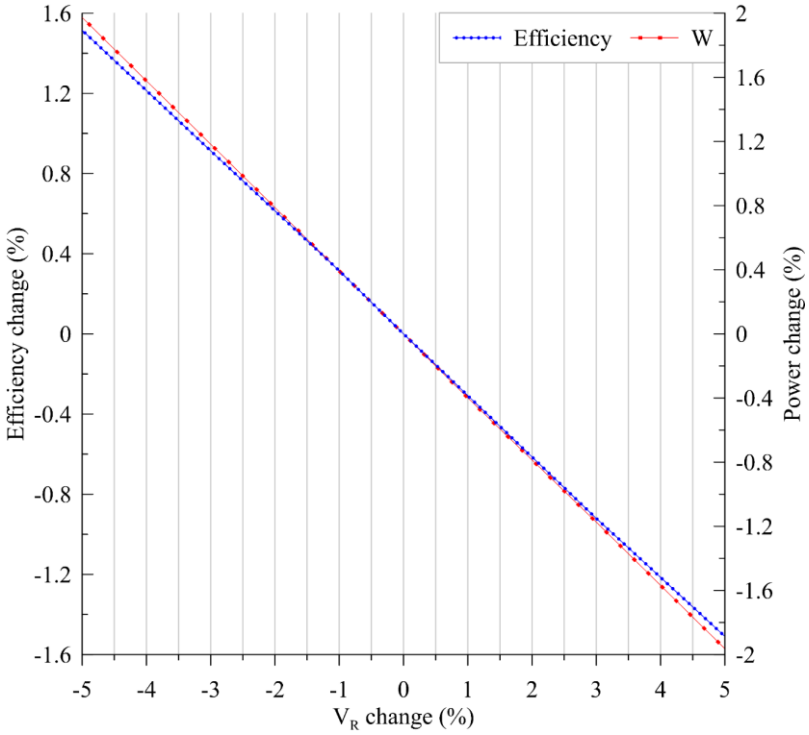

Figure 4.28: Sensitivity of the system to the V_R

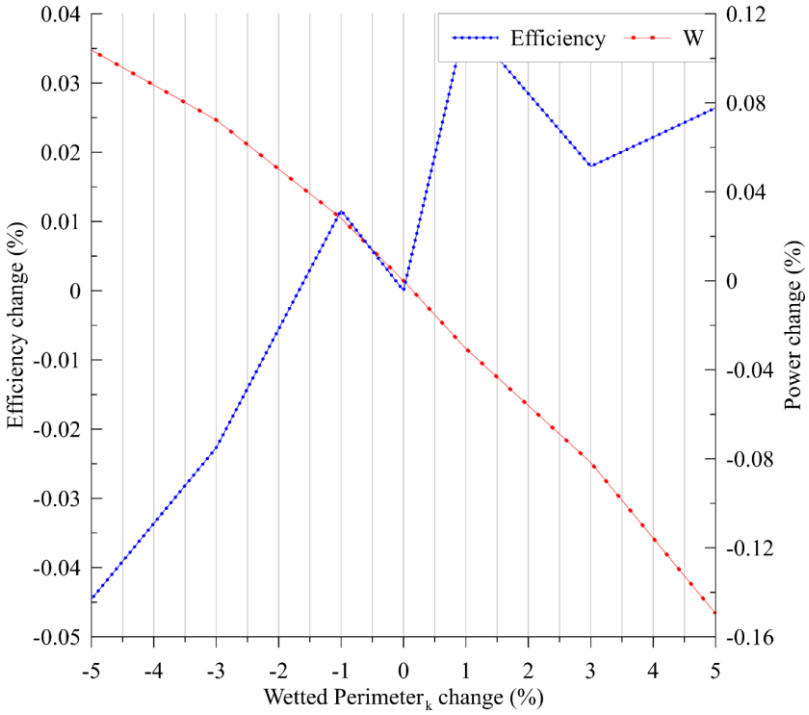

Figure 4.29: Sensitivity of the system to the $Wetted\ Perimeter_k$

As can be seen in Figure 4.1-Figure 4.29, system sensitivity to some parameters is high and to some of them is low. Also, the sensitivity to some parameters is linear that makes it

easy to predict the system response by changing them and get to the requested one, while to some others is not linear. To have a brief review of the system sensitivity to different parameters, a summary of Figure 4.1-Figure 4.29 is presented in Table 4.1 that the system sensitivity to each of the parameters is shown and sorted from high to low. Here, the output power is chosen as the system response to study its sensitivity.

Table 4.1: Sensitivity study of the FPSE-PMLSM combined system at 30 Hz

Parameter with 10% of change	Output power change (%)	Parameter with 10% of change	Output power change (%)	Parameter with 10% of change	Output power change (%)
d_P	60.51	m_P	6.91	C_c	1.51
d_{rod}	53.84	d_{wire}	5.73	V_b^{mean}	1.14
P^{mean}	40.76	l_R	4.34	C_e	1.04
$Porosity$	23.46	V_R	3.94	m_{mover}	0.92
T_k^{wall}	16.87	ψ_f	3.24	B_v	0.39
m_D	11.83	l_k	2.71	A_R^{wetted}	0.36
V_{gs}^{mean}	11.43	d_h	2.02	$Wetted\ Perimeter_k$	0.25
T_h^{wall}	8.99	$Passage\ size_k$	1.91	L_q	0.06
d_D	8.87	l_h	1.89	L_d	0.005
A_R	6.96	r	1.60		

As can be seen in Table 4.1, the sensitivity of the system to some parameters like L_d, L_q, $Wetted\ Perimeter_k$, A_R^{wetted}, and B_v is very low that can be ignored, while the system sensitivity to d_P, d_{rod}, P^{mean}, and $Porosity$ is very high. To have a better study of the sensitivity analysis and identify the sensitive parameters, all the parameters are categorized in three groups: 1- High sensitive parameters, which are the parameters with more than 10% of system sensitivity to their variations (highlighted by orange). 2- Low sensitive parameters, which are the parameters with a system sensitivity between 5% and 10% to their variations (highlighted by yellow). 3- Not sensitive parameters, with the system sensitivity less than 5% to them (highlighted by green).

It should be noted that the output power variation based on the high sensitive parameters is linear that makes it possible to predict the output power after changing each of them or modifying the output power based on them. Since the system is nonlinear (already discussed in Section 2.1.1), the results of sensitivity analysis may vary by frequency variation. To show how frequency variation may change the sensitivity of the system to the different parameters, this analysis is re-done at 25 Hz. The results are shown in Table 4.2 with the same order of Table 4.1 to have a better comparison.

Table 4.2: Sensitivity study of the FPSE-PMLSM combined system at 25 Hz

Parameter with 10% of change	Output power change (%)	Parameter with 10% of change	Output power change (%)	Parameter with 10% of change	Output power change (%)
d_P	25.49	m_P	0.87	C_c	0.72
d_{rod}	29.68	d_{wire}	6.75	V_b^{mean}	0.07
P^{mean}	20.86	l_R	5	C_e	0.73
$Porosity$	27.96	V_R	2.16	m_{mover}	0.11
T_k^{wall}	13.80	ψ_f	2.5	B_v	0.18
m_D	4.51	l_k	1.67	A_R^{wetted}	0.15
V_{gs}^{mean}	6.13	d_h	0.7	$Wetted\ Perimeter_k$	0.25
T_h^{wall}	10.36	$Passage\ size_k$	1.5	L_q	0.01
d_D	13.45	l_h	1.28	L_d	0.003
A_R	8.11	r	1.24		

Again, high (highlighted by orange, ≥10%), low (highlighted by yellow, between 5% and 10%) and not-sensitive (highlighted by green, ≤5%) parameters are shown in Table 4.2. As can be seen in Table 4.2, the value of system sensitivity to the parameters are changed, but there is not many changes in the predefined sensitivity groups. All the not-sensitive parameters are still in the same group. From low sensitive parameters, the sensitivity to m_P is reduced and now it is known as a non-sensitive parameter. Also, d_D and T_h^{wall} are now in the category of high sensitive parameters. From high sensitive parameter, one (V_{gs}^{mean}) is moved to the low and one (m_D) is moved to the non-sensitive parameter. However due to the nonlinearity in the system, the sensitivity of the system to

the parameters will change, but this study still remains helpful since the variation between sensitivity groups is limited.

4.2 Heat Recovery in a Tri-generation IRSOFC Based System

In the present section, the application of this system as a heat recovery option for a tri-generation system is presented, and its effect on the general system performance is studied.

The proposed tri-generation system produces electricity by an Internal Reforming Solid Oxide Fuel Cell (IRSOFC), cooling by a Double Effect Absorption Chiller (DEACH), and hot water through a heat exchanger. The FPSE-PMLSM system is added after IRSOFC to recover the high-quality thermal energy of it as electricity which is the main product of this tri-generation system.

The schematic of the tri-generation system after adding the FPSE-PMLSM system to it is shown in Figure 4.30.

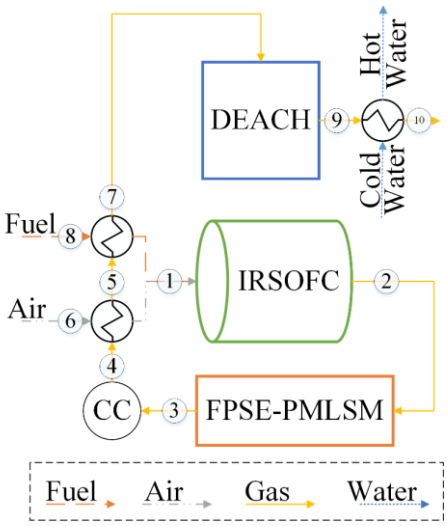

Figure 4.30: Combined tri-generation system [8]

As shown in Figure 4.30, at first, air and fuel are fed to IRSOFC ① to produce electricity. The exhaust gas of the Internal Reforming Solid Oxide Fuel Cell (IRSOFC) ② has a high temperature that is used in a Free Piston Stirling Engine combined with a Permanent Magnet Linear Synchronous Machine (FPSE-PMLSM) to produce electricity. Then, the gas leaves the FPSE-PMLSM system ③ with a decreased temperature. Since this gas still contains

burnable substances, a Combustion Chamber (CC) is used to burn them and increase the gas temperature ④. Then, this gas passes through a heat exchanger ⑤ to preheat the input air ⑥. After that, it passes through another heat exchanger ⑦ to preheat the input fuel ⑧. This gas still has enough energy to run a Double Effect Absorption Chiller (DEACH) ⑨. The final low-quality thermal energy heats the water ⑩ and provides hot water.

Now, the IRSOFC and DEACH will be modeled and validated. Since there was no need to have a high-pressure fuel cell, the IRSOFC in the combined system works at atmospheric pressure. Since electricity production was the main interest of the proposed combined system which is a part of a microgrid, to recover the high-quality heat of the IRSOFC, the FPSE-PMLSM system is put before the IRSOFC gas/air preheaters.

4.2.1 IRSOFC Analysis

Here a zero-dimensional model of IRSOFC is developed. The following assumptions are made to model the IRSOFC system:

- The IRSOFC operates at a steady-state
- The IRSOFC is isolated and has no heat transfer with the environment
- It is a tubular IRSOFC
- The radiation heat transfer between solid structure and gas channels is ignored
- The contact resistances are ignored

4.2.1.1 Internal Reformer

An internal reformer, compared to an external one, has higher efficiency and lower cost [75]; thus, an internal reformer was chosen. The three main reactions that happen inside the reformer and SOFC are:

$$a \Longrightarrow CH_4 + H_2O \longrightarrow CO + 3H_2 \tag{4.1}$$

$$b \Longrightarrow CO + H_2O \longrightarrow CO_2 + H_2 \tag{4.2}$$

$$c \Longrightarrow H_2 + 1/2\ O_2 \longrightarrow H_2O \tag{4.3}$$

In these equations, a, b and c are extents of reforming, shifting, and electrochemical reactions (mol/s), respectively. The equilibrium constants of reforming (r subscript- Equation 4.1) and shifting (s subscript- Equation 4.2) reactions can be calculated based on

partial pressures of gasses in the reactions which are related to their equilibrium molar concentrations:

$$K_r = (P^{CO}(P^{H_2})^3)/(P^{CH_4}P^{H_2O}) = \left(X_{eq}^{CO}\left(X_{eq}^{H_2}\right)^3\right)/\left(X_{eq}^{CH_4}X_{eq}^{H_2O}\right) \times (P/P_0)^2 \quad 4.4$$

$$K_s = (P^{CO_2}P^{H_2})/(P^{CO}P^{H_2O}) = \left(X_{eq}^{CO_2}X_{eq}^{H_2}\right)/\left(X_{eq}^{CO}X_{eq}^{H_2O}\right) \quad 4.5$$

These coefficients are also a function of temperature:

$$ln\, K = \underline{A}T^4 + \underline{B}T^3 + \underline{C}T^2 + \underline{D}T + \underline{E} \quad 4.6$$

$\underline{A}$, $\underline{B}$, $\underline{C}$, $\underline{D}$, and $\underline{E}$ are constants, and their values are presented in Table 4.3.

Table 4.3: Constants to calculate equilibrium constants of equations (Equation 4.6) [76]

	Reforming (for K_r)	Shifting (for K_s)
$\underline{A}$	-2.63121×10^{-11}	5.47301×10^{-12}
$\underline{B}$	1.24065×10^{-7}	-2.57479×10^{-8}
$\underline{C}$	-2.25232×10^{-4}	4.63742×10^{-5}
$\underline{D}$	1.95028×10^{-1}	-3.91500×10^{-2}
$\underline{E}$	-6.61395×10	1.32097×10

Since in Equations 4.4 and 4.5, partial gas pressures are related to their equilibrium molar concentrations, and these equations are rewritten based on equilibrium molar concentrations, the first step to model the reformer is to calculate gas compositions at different channels of Figure 4.31. Since the chemical reactions in the anode need water as a reactant, and the output gas mixtures of the anode ($An4$) has high water content, the fuel ($An1$) before entering the anode mixes with the recirculated gas mixture ($An2$). Also, the oxidant is fed to cathode ($Ca1$).

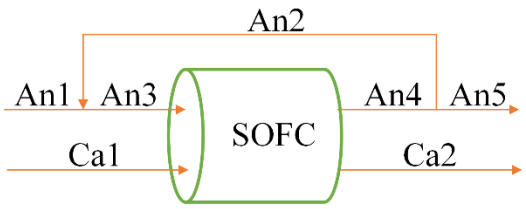

Figure 4.31: SOFC flow channels [8]

Based on Figure 4.31, the molar gas flow rate for $An3$ and $An4$ for each gas (i) can be calculated as [77]:

$$\dot{n}^i_{An3} = \dot{n}^i_{An1} + \dot{n}^i_{An2} = \dot{n}^i_{An1} + X^i_{eq}\dot{n}_{An2} = \dot{n}^i_{An1} + X^i_{eq}\left(\overline{\overline{Re}}\dot{n}_{An4}\right) \quad 4.7$$

$$\dot{n}^i_{An4} = \dot{n}^i_{An3} + d^i \rightarrow \dot{n}_{An4} = \dot{n}_{An3} + 2a \quad 4.8$$

Here $\dot{n}^i_j$ is the molar flow rate of component i in channel j and $\dot{n}_j$ is the total molar flow rate in channel j. The values of d^i based on a, b, and c are given in Table 4.4.

Table 4.4: d^i values to calculate $An4$ gas flow rates [77]

d^{CH_4}	$-a$	d^{CO_2}	b
d^{H_2O}	$-a-b+c$	d^{H_2}	$3a+b-c$
d^{CO}	$a-b$	d^{N_2}	0

Thus, the total gas flow rate in $An3$ is [77]:

$$\dot{n}_{An3} = (\dot{n}_{An1} + 2aRe)/\left(1-\overline{\overline{Re}}\right) \quad 4.9$$

$\overline{\overline{Re}}$ is the recirculation ratio that here is assumed to be equal to 0.6. Combination of Equations 4.7 and 4.8 allows calculating the equilibrium gas molar composition in $An4$ Channel [77]:

$$X^i_{eq} = \left(\dot{n}^i_{An4}\right)/(\dot{n}_{An4}) = \left(\dot{n}^i_{An1} + d^i\right)/(\dot{n}_{An1} + 2a) \quad 4.10$$

For CH_4, CO_2, CO, and N_2, the d^i values are based on Table 4.4, and for H_2O and H_2 the equilibrium gas molar compositions in $An4$ are as [77]:

$$X^{H_2}_{eq} = \left(\dot{n}^{H_2}_{An1} + 3a + b\right)/(\dot{n}_{An1} + 2a) \times \left(\left(1-\overline{\overline{Re}}\right)\left(1-U_f\right)\right)/\left(1-\overline{\overline{Re}} + \overline{\overline{Re}}U_f\right) \quad 4.11$$

$$X^{H_2O}_{eq} = \left(\dot{n}^{H_2O}_{An1} + \left(-a-b+U_f\left(\dot{n}^{H_2}_{An1} + 3a + b\right)/\left(1-\overline{\overline{Re}} + \overline{\overline{Re}}U_f\right)\right)\right)/(\dot{n}_{An1} + 2a) \quad 4.12$$

U_f in these equations is the fuel utilization factor, which is assumed to be equal to 0.85. For the cathode side (air channel), gases molar flow rates and equilibrium gases molar compositions are as [77]:

$$\dot{n}^{O_2}_{Ca1} = c/(2U_{ox}) \quad 4.13$$

$$\dot{n}_{Ca1}^{N_2} = c/(2U_{ox}) \times 79/21 \quad 4.14$$

$$\dot{n}_{Ca2}^{O_2} = c/(2U_{ox}) - c/2 \quad 4.15$$

$$\dot{n}_{Ca2}^{N_2} = c/(2U_{ox}) \times 79/21 \quad 4.16$$

Here U_{ox} is the air utilization factor, which is assumed to be 0.25. The unknown variables of these equations are a, b, and total mass flow rate in $An1$. These variables can be found by solving the Equations 4.4, 4.5, and the following Equation at the same time [77]:

$$i_{cell}A_{cell} = 2cFr = 2\left(\left(\left(\dot{n}_{An1}^{H_2} + 3a + b\right)U_f\right)/\left(1 - \overline{\overline{Re}} + \overline{\overline{Re}}U_f\right)\right)Fr \quad 4.17$$

Unknown parameters of these equations are a, b and fuel flow rate ($\dot{m}_{fuel}$) which is needed to calculate $\dot{n}_{An1}^{i}$. Since c can be calculated based on a and b, it is not an independent parameter. The flow chart of the internal reformer modeling procedure is shown in Figure 4.32.

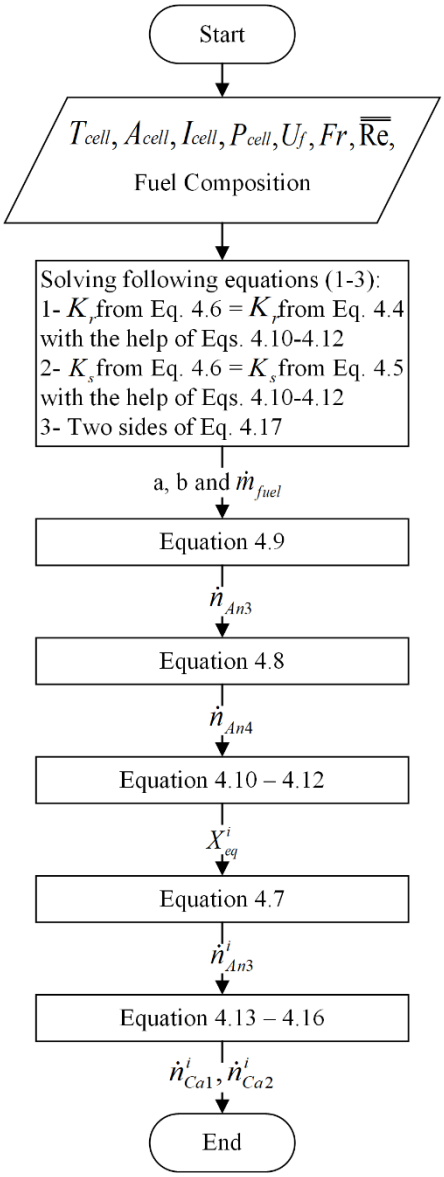

Figure 4.32: Internal reformer flow chart [8]

4.2.1.2 SOFC Voltage

The reversible voltage of the cell can be calculated based on the Nernst equation [78]:

$$v_{rev} = v_0 + \Delta v = -\Delta G_0/(n_e Fr) - \Delta G/(n_e Fr) = -\Delta G_0/(2Fr) + (RT)/(2Fr)\, ln(P^{H_2}(P^{O_2})^{0.5}/P^{H_2O}) \quad 4.18$$

n_e is the number of electrons that here is equal to 2. Partial pressures of gasses are related to their molar concentrations in $An4$ that were already calculated in section 4.2.1.1. Due to irreversibilities, the actual voltage is smaller than this value and is equal to [78]:

$$v = v_{rev} - (v_{Act} + v_{Ohm} + v_{Conc}) \quad 4.19$$

As can be seen, there are three different polarization types: activation (Act subscription), ohmic (Ohm subscription), and concentration ($Conc$ subscription). Activation polarization can be calculated as [76]:

$$\begin{aligned} v_{Act} &= v_{Act,An} + v_{Act,Ca} \\ &= 2RT/(n_e Fr)\, sinh^{-1}\big(i/\big(2i_{0,An}\big)\big) \\ &+ 2RT/(n_e Fr)\, sinh^{-1}\big(i/\big(2i_{0,Ca}\big)\big) \end{aligned} \quad 4.20$$

$$i_{0,An} = \Upsilon_{An}(P^{H_2}/P_0)(P^{H_2O}/P_0)exp\big(-E_{Act,An}/(RT)\big) \quad 4.21$$

$$i_{0.Ca} = \Upsilon_{Ca}(P^{O_2}/P_0)^{0.25} exp\big(-E_{Act,Ca}/(RT)\big) \quad 4.22$$

Υ_i are exchange current density pre-exponential factor and $E_{Act,i}$ are activation energies [79]. Partial pressures of gasses are related to their molar concentrations in $An4$ that were already calculated in section 3.1. Then for ohmic and concentration polarization following equations can be written [80,81].

$$v_{Ohm} = \sum ir = \sum i\delta \underline{A} \times exp\big(\underline{B}/T\big) \quad 4.23$$

$$v_{Conc} = (RT/(n_e Fr))(1 - i/i_l) \quad 4.24$$

Constants to calculate ohmic polarization are presented in Table 4.5.

Table 4.5: Constants to calculate ohmic polarization [80,81]

	$\underline{A}(\Omega.cm)$	$\underline{B}(K)$	$\delta(cm)$
Anode	0.00298	1392	0.01
Cathode	0.00814	-600	0.19
Electrolyte	0.00294	-10350	0.004
Internal connections	0.1256	-4690	0.0085

Now to calculate cell voltage, at first based on Equations 4.20 - 4.22 activation polarization (v_{Act}), based on Equation 4.23, ohmic polarization (v_{Ohm}), and based on Equation 4.24, concentration polarization (v_{Conc}) should be calculated. Then these values based on Equation 4.19 are extracted from the reversible voltage (v_{rev}) that can be calculated based on Equation 4.18 to calculate cell voltage (v).

4.2.1.3 IRSOFC Temperature

IRSOFC temperature can be calculated based on a trial and error method. The energy balance is based on the idea that the heat generation inside IRSOFC should be equal to the energy increment of gasses pass through it. Thus, thermal energy generation/consumption due to three main equations inside IRSOFC (Equations 4.1 - 4.3) and due to irreversibilities of polarizations should be calculated and compared to the required energy to increase the temperature of reactants and products to the cell temperature. Based on this idea, the temperature of the IRSOFC is calculated [82]. The heat production due to irreversibilities and also electrochemical reaction inside IRSOFC are as follows:

$$Q_{rxn} = i_{cell} A_{cell} (v_{Act} + v_{Ohm} + v_{Conc}) + T_{cell} \Delta S \quad 4.25$$

$$\Delta S = \left(S_0^{H_2O} - S_0^{H_2} - (1/2)\, S_0^{O_2}\right) - R\, ln(P^{H_2}(P^{O_2})^{0.5}/P^{H_2O}) \quad 4.26$$

the required heat for reforming and shifting processes can also be calculated as:

$$Q_r = a(H^{CO} + 3H^{H_2} - H^{H_2O} - H^{CH_4}) \quad 4.27$$

$$Q_s = b(H^{CO_2} + H^{H_2} - H^{H_2O} - H^{CO}) \quad 4.28$$

The produced heat (Equation 4.25) is used to provide required heat for the reforming and shifting reactions (Equation 4.27 and 4.28), and also, to heat the gas streams, that can be calculated as:

$$Q_{heat\ up} = \left(\dot{n}_{An,re} \int_{T_{An}}^{T_{cell}} Cp\ dT\right)_{re} + \left(\dot{n}_{An,pr} \int_{T_{An}}^{T_{cell}} Cp\ dT\right)_{pr} + \left(\dot{n}_{Ca,re} \int_{T_{Ca}}^{T_{cell}} Cp\ dT\right)_{re} + \left(\dot{n}_{Ca,pr} \int_{T_{Ca}}^{T_{cell}} Cp\ dT\right)_{pr} \quad 4.29$$

Now, the remaining thermal energy of the reactions is compared to the required energy for the heat up to calculate the cell temperature through a trial and error procedure. The heat transfer with the surrounding is also ignored.

$$Error = \left(Q_{heat\ up} - (Q_{rxn} - Q_r - Q_s)\right)/(Q_{rxn} - Q_r - Q_s) < 1\% \quad 4.30$$

The procedure of the temperature calculation is shown in Figure 4.33.

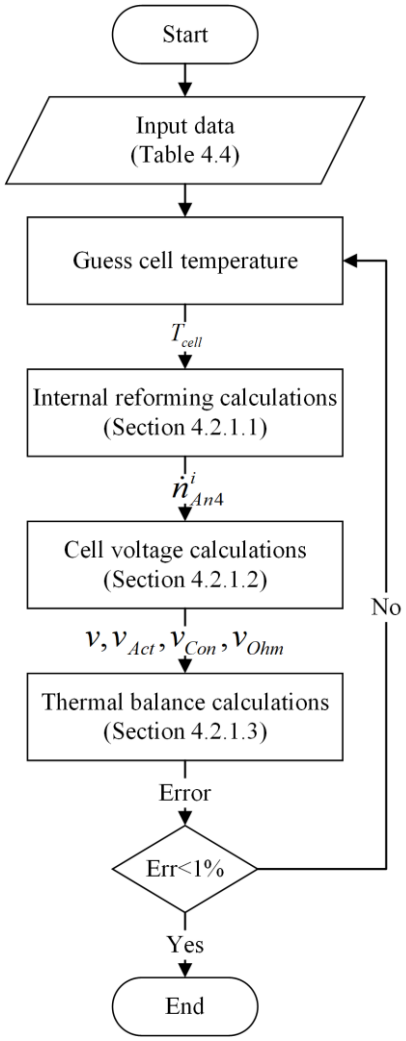

Figure 4.33: Flowchart of trial and error procedure for IRSOFC temperature calculation [8]

4.2.1.4 IRSOFC Results and Validation

The IRSOFC is modeled in MATLAB® with the equations presented in the previous section. In order to validate it, the results of the modeling are compared with Pirkandi et al. [82] ones (Figure 4.34-Figure 4.38), considering the same input data, which is shown in Table 4.6.

Table 4.6: IRSOFC input data for validation [82]

U_f	0.85
U_{ox}	0.25
$\overline{\overline{Re}}$	60 %

P	1 bar
A_{cell}	0.10362 m²
i_l	9000 A/m²
Number of cells	8792

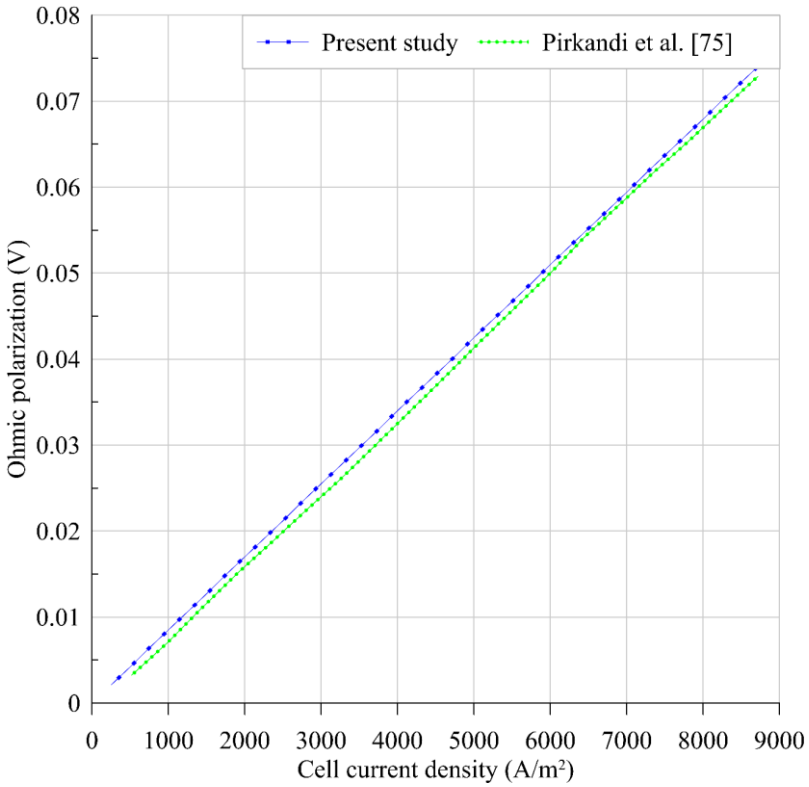

Figure 4.34: Validation of ohmic polarization

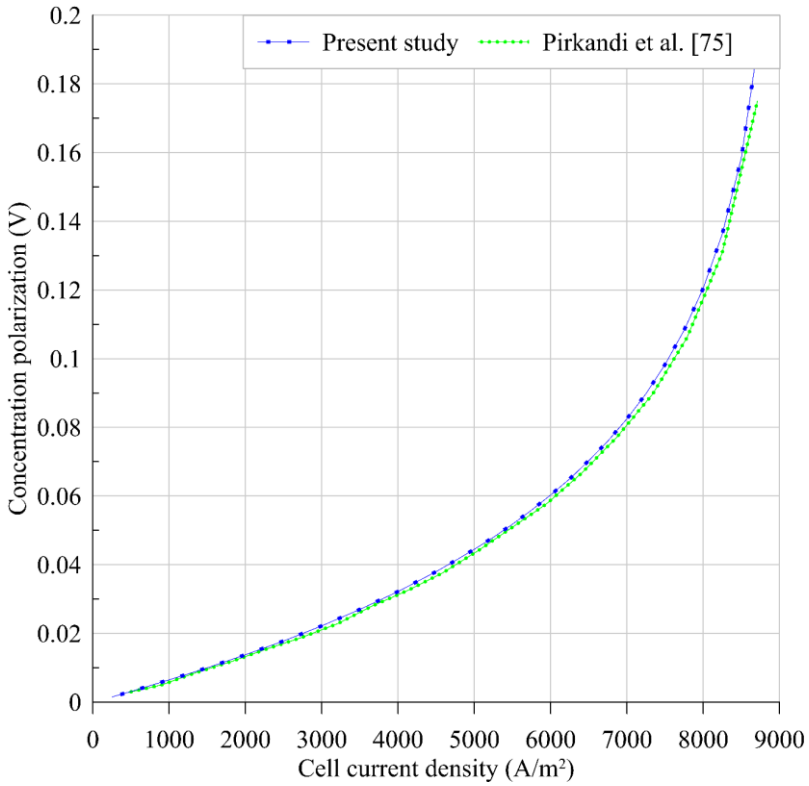

Figure 4.35: Validation of concentration polarization

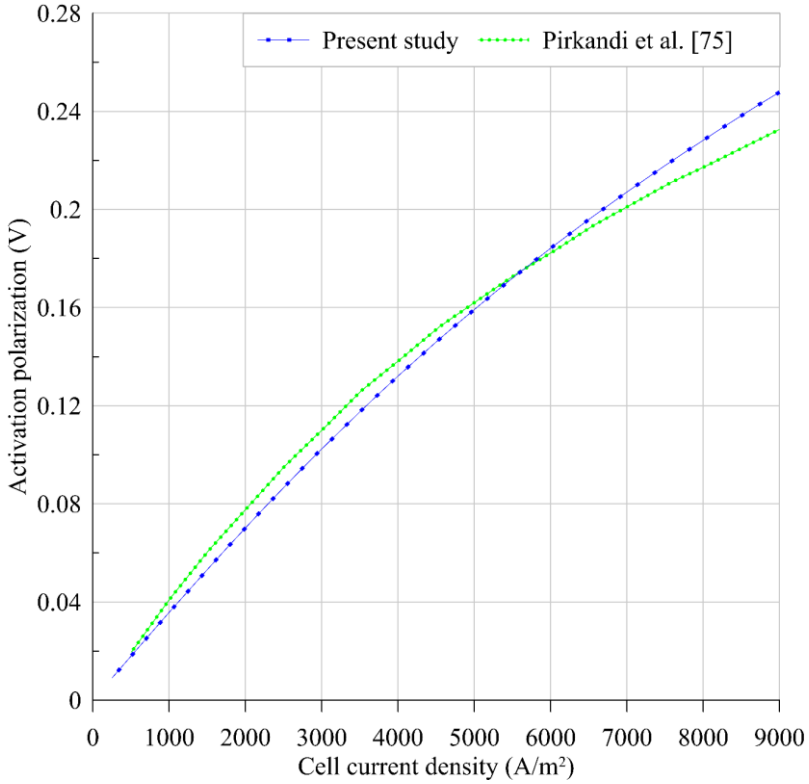

Figure 4.36: Validation of activation polarization

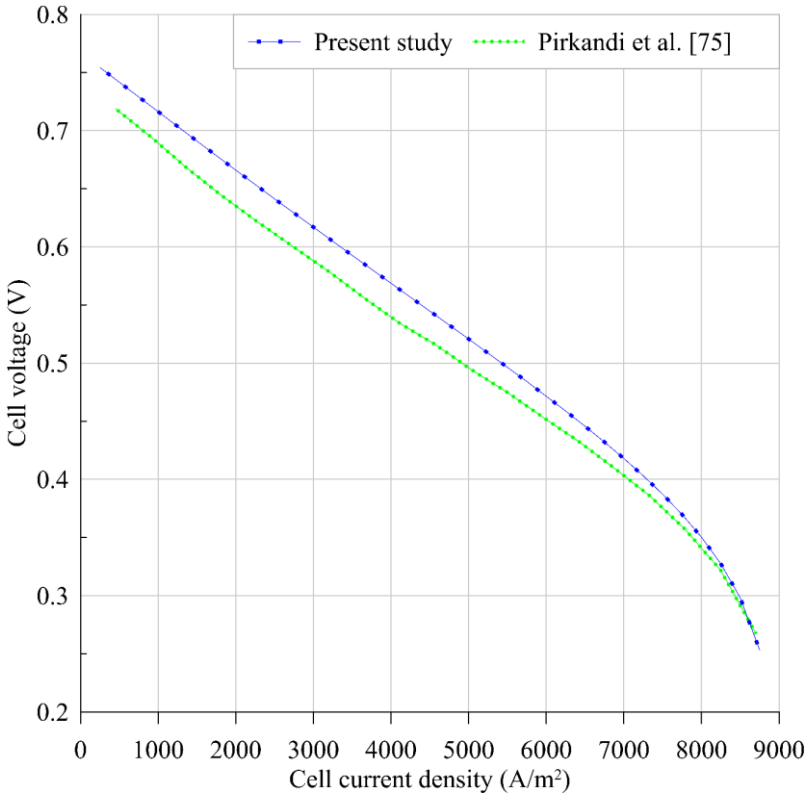

Figure 4.37: Validation of cell voltage

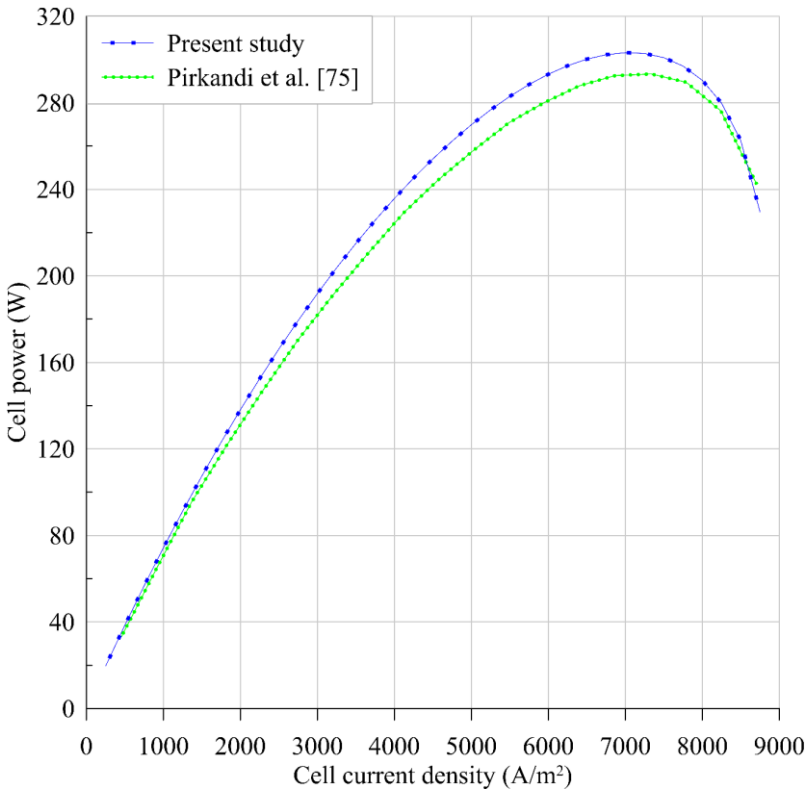

Figure 4.38: Validation of cell power

As can be seen in Figure 4.34-Figure 4.38, there is a good agreement between the present study and Pirkandi et al. [82] results that shows the IRSOFC model is valid. The effect of the current density on the power and voltage is also shown. By increasing the current density, the voltage of the cell is continuously decreasing. Also, this increment increases the power by a point, and after that (around 7500 A/m^2), the power decreases. It is important to choose an appropriate working current density for the system to satisfy the requirements.

4.2.2 DEACH Analysis

The Schematic of the DEACH is shown in Figure 4.39. The refrigerant and the absorbents are water and lithium bromide, respectively. The following assumptions are made to model the DEACH system:

- The system operates at steady-state
- The refrigerant that leaves the condenser is saturated liquid
- The refrigerant that leaves the evaporator is saturated vapor
- The pressure drop inside tubes is neglected
- The pump work is neglected
- The heat transfer with outside happens only in the evaporator, condenser, absorber, and high-pressure generator
- The processes in expansion valves are enthalpy constant

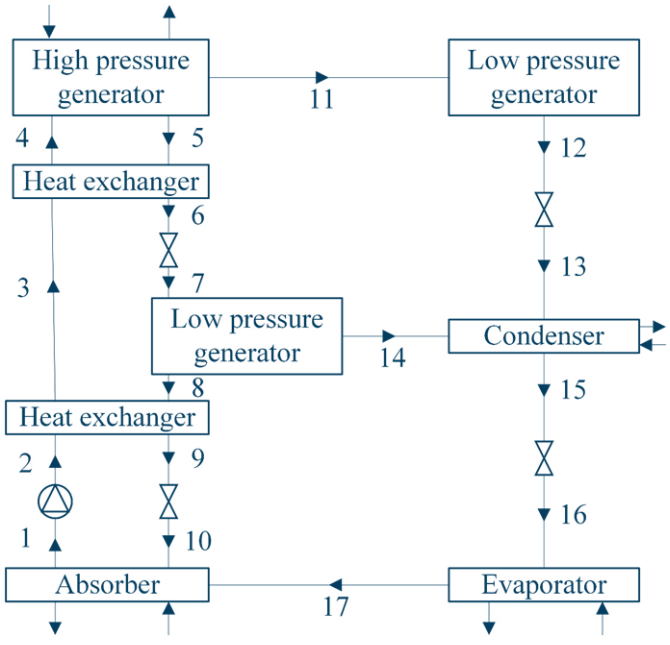

Figure 4.39: Schematic of DEACH [8]

Components of the DEACH are in three pressure levels and five temperature levels [83]. For each component, the laws of conservation of mass and energy are applied by calculating each flow's properties. For a lithium bromide solution, the enthalpy can be calculated as [84]:

$$H = 2.326\{\underline{A}_1 + \underline{A}_2(1.8T + 32) + \underline{A}_3(1.8T + 32)^2\} \quad 4.31$$

$\underline{A}_i$ can be calculated as [84]:

$$\underline{A}_i = \underline{a}_0 + \underline{a}_1 Xm + \underline{a}_2 Xm^2 + \underline{a}_3 Xm^3 + \underline{a}_4 Xm^4 \quad 4.32$$

Table 4.7: Constants to calculate the enthalpy of lithium bromide solution [84]

	$\underline{A}_1$	$\underline{A}_2$	$\underline{A}_3$
$\underline{a}_0$	-1015.07	4.68108	-4.9107×10^{-3}
$\underline{a}_1$	79.5387	-3.037766×10^{-1}	3.83184×10^{-4}
$\underline{a}_2$	-2.358016	8.44845×10^{-3}	-1.078963×10^{-5}
$\underline{a}_3$	0.03031583	-1.047721×10^{-4}	1.3152×10^{-7}
$\underline{a}_4$	-1.400261×10^{-4}	4.80097×10^{-7}	-5.897×10^{-4}

Xm is the mass concentration of lithium bromide in the solution. T is the solution temperature, which can be calculated as [84]:

$$T = T_{Dew\ Point} \sum_{n=0}^{3} \underline{A}_n Xm^n + \sum_{n=0}^{3} \underline{B}_n Xm^n \quad 4.33$$

$T_{Dew\ Point}$ can be calculated based on Holmgren code [85]. $\underline{A}_n$ and $\underline{B}_n$ are constants that are shown in Table 4.8.

Table 4.8: Constants of solution temperature formula [84]

n	$\underline{A}_n$	$\underline{B}_n$
0	-2.00755	124.934
1	0.16976	-7.7165
2	-3.13336× 10^{-3}	0.152286
3	1.97668× 10^{-5}	-7.9509× 10^{-4}

Table 4.9: Five-level temperatures of DEACH

Evaporator	280.15 K
Absorber	305.15 K
Low-pressure generator	340.95 K
High-pressure generator	381.05 K
Condenser	305.35 K

Table 4.10: DEACH validation

Flow number	Temperature (K)		Pressure (kPa)		Concentration (%)		Enthalpy (kJ/kg)	
	Present study	Gebreslassie et al. [83]	Present study	Gebreslassie et al. [83]	Present study	Gebreslassie et al. [83]	Present study	Gebreslassie et al. [83]
1	305.15	305.15	1.0021	1.0021	53.95	53.95	73.583	73.1
2	305.15	305.15	31.575	31.575	53.95	53.95	73.583	73.2
3	337.055	337.95	31.575	31.575	53.95	53.95	140.46	142.3
4	378.39	379.15	31.575	31.575	53.95	53.95	227.43	230.9
5	381.05	382.95	31.575	31.575	55.92	55.92	235.96	241.4
6	337.055	338.15	31.575	31.575	55.92	55.92	145.82	148.3
7	337.055	338.15	4.8133	4.8133	55.92	55.92	145.82	148.3
8	340.95	343.75	4.8133	4.8133	57.65	57.65	159.61	167
9	305.15	305.35	4.8133	4.8133	57.65	57.65	88.152	91.1
10	305.15	305.35	1.0021	1.0021	57.65	57.65	88.152	91.1
11	381.05	381.05	31.575	31.575	-	-	2700.1	2700
12	343.426	343.95	31.575	31.575	-	-	294.17	296.4
13	305.35	305.35	4.8133	4.8133	-	-	294.17	296.4
14	340.95	340.95	4.8133	4.8133	-	-	2627.1	2627.1
15	305.35	305.35	4.8133	4.8133	-	-	134.94	134.9

16	280.15	280.15	1.0021	1.0021	-	-	134.94	134.9
17	280.15	280.15	1.0021	1.0021	-	-	2513.7	2513.7

Also, the *COP* of the Gebreslassie et al. [83] model was 1.655, while the present study has a *COP* of 1.6012. It should be noted that to calculate the COP, as Gebreslassie et al. [83] study, the pump work was neglected. As can be seen, the present model of the DEACH is valid and presents almost the same results as the study of Gebreslassie et al. [83]. The model of the DEACH is developed in MATLAB®.

4.2.3 Tri-generation System Analysis

After modeling, presenting the results, and validating each system, they are coupled based on Figure 4.30. At first, the high-quality output heat of the IRSOFC is used for running the FPSE-PMLSM system. Then to increase the temperature and burn the left output gas of the IRSOFC, it passes through a combustion chamber. After that, the reheated gas is used for preheating the input air and fuel of the IRSOFC. Then, it provides the required heat of the DEACH. The final low-quality heat is used to produce the required hot water.

The input parameters of the FPSE-PMLSM system are the same that was already presented in Table 2.3. Also, for DEACH, the same condition as Table 4.9 is applied. For IRSOFC the input data of Table 4.6 is used, but the cell area, number of cells, and the working currents are equal to 0.0834 m^2, 26, and 2000 A/m^2 (to be in the zone with maximum output voltage and minimum voltage drop) [8,86], respectively. Based on these input data, the combined tri-generation system is modeled. For IRSOFC, the calculated operating temperature is 1000 K. The output of each system in the combined mode is shown in Table 4.11.

Table 4.11: Tri-generation system results

IRSOFC	1981 W
FPSE-PMLSM	279.4 W
DEACH	1366.6 W
Hot water	0.27 kg/s
Input heat	6165.4 W

As can be seen, IRSOFC and FPSE-PMLSM electricity production, DEACH cooling production, and produced hot water flow rate are shown in Table 4.11. The equation which is used to calculate IRSOFC power production is as follows:

$$Power_{IRSOFC} = (Number\ of\ Cells) \times i_{cell} A_{cell} v \quad 4.34$$

PSE-PMLSM power production is also calculated based on Equation 3.9. The hot water thermal flowrate also can be calculated as:

$$\dot{Q}_{Hotwater} = \dot{m}_{water} Cp_{water} \times (T_{water\ hot} - T_{water\ cold}) \quad 4.35$$

It is assumed that the hot water temperature ($T_{water\ hot}$) is 333.15 K that should be achieved from the cold water ($T_{water\ cold}$) at 298.15 K. Also, the input thermal energy is calculated based on the input fuel (CH_4) flow rate to IRSOFC and its LHV (Lower Heating Value).

$$\dot{Q}_{Input} = \dot{m}_{CH_4} LHV \quad 4.36$$

Now, the efficiency of this combined system can be calculated. To calculate efficiency, two methods can be defined based on the following equation:

$$\eta = \frac{Power_{IRSOFC} + Power_{FPSE-PMLSM} + \dot{Q}_{DEACH} + \dot{Q}_{Hotwater}}{\dot{Q}_{Input}} \quad 4.37$$

In this equation, powers are output electrical powers, and $\dot{Q}_{Hotwater}$ is the amount of heat that was recovered by heating the water. $\dot{Q}_{DEACH}$ can be defined as the heat that is used in DEACH or the cooling that is produced by it. If it is assumed that $\dot{Q}_{DEACH}$ is the consumed heat in DEACH, the whole combined system efficiency is equal to 63.82 %, but if $\dot{Q}_{DEACH}$ is the cooling production, the efficiency of the combined system is equal to 72.14%. Comparing this system with a standalone IRSOFC, which has an efficiency of 32.13%, shows that the total efficiency of the system based on the first and the second method of efficiency calculation is increased by 31.7% and 40%, respectively. Also, the electrical efficiency of the combined system is 36.66%, which shows around 14.1% increment compared to the standalone IRSOFC. All these results show a significant improvement of the IRSOFC performance when it works in a combined system with an FPSE-PMLSM, a DEACH, and a heat exchanger to produce hot water.

5 Conclusion & Perspectives

One of the challenges which is tried to solve in this thesis is recovering waste heat of industries and micro-grids. For this purpose, a Free Piston Stirling Engine combined with a Permanent Magnet Linear Synchronous Machine is proposed.

In Chapter 1, first the idea of Internet Of Energy (IOE) was introduced which is the base of the thesis. It was discussed that IOE is moving from the conventional centralized/unidirectional networks to the decentralized/bidirectional ones. After presenting this idea, the role of the present study in this idea was identified. Then, the systems, which are Free Piston Stirling Engine (FPSE) and Permanent Magnet Linear Synchronous Machine (PMLSM), were selected. After presenting the electrodynamic model of the PMLSM system, the coupled FPSE-PMLSM system was introduced.

In Chapter 2, the focus was on the FPSE modeling. First, a general dynamic analysis of the system was presented. Then, a linearized set of equations were solved as already discussed in the literature. Furthermore, the nonlinear equations were used directly as a new approach in the present study. Comparing the results of these models showed that linearized model is not adapted to the present study cannot identify the realistic behavior of the FPSE. After selecting the new nonlinear proposed model as the base dynamic model, the thermic model of the system is developed based on that. Then, the thermodynamic model of the FPSE was validated with the existed experimental results. At the end, the effect of enthalpy pumping loss on the system was studied using two scenarios. The first scenario that already explained in the literature was based on the decoupled model between the loss and the thermodynamic one. The second scenario which is a new one is introduced in the present study, was based

on the coupled model between the loss and the thermodynamic one. Comparing the results showed that the second model is more adapted to the present study and the first one does not present logical results.

In Chapter 3, the control of the combined FPSE-PMLSM system was introduced. Two Proportional-Integral (PI) controllers for currents and one Proportional-Resonance (PR) controller for the power piston/mover velocity were used to control the system using three sensors: two current sensors and one position sensor. For the first time in the present study a PR controller is used for such a system. Then, two different control methods were introduced to identify the reference velocity and a performance analysis of the FPSE-PMLSM system was done based on them. The first control method was based on the direct identification of the reference velocity amplitude and frequency. The PR gains for this control method was set with the stability analysis of the system. The second method was based on the auto oscillating of the system and identifying the reference velocity based on the system response. The performance analyses showed the optimum points that were close to each other's.

In Chapter 4, which is the last chapter, the application of the FPSE-PMLSM system was shown. First, a sensitivity analysis was done to see the effect of different parameters on system. It helps to see how each parameter affects the system output and to adapt the model to an experimental setup, which parameters should be measured more precisely. Furthermore, to see how this system can be used as a waste heat recovery option coupled with another power sources, it was used beside a tri-generation with a Solid Oxide Fuel Cell (SOFC) as a power source, a Double Effect Absorption Chiller (DEACH) for cooling production, and a heat exchanger to provide heating needs. The results showed that how FPES-PMLSM system improve the performance of the system.

In continuation of this thesis, following improvements are proposed:

For the modeling of the electric part, providing a more precise model of the PMLSM as well as for the inverter should help to find more accurate values of the efficiency and power. For the FPSE, more losses can be studied an effect of them on the FPSE system can be analyzed. This will help to identify the most important losses and try to find a solution to minimize them. Furthermore, gas compressibility can be taken into account. Concerning the control of the system, the stability analysis of the second control method that was based on

the auto oscillating system should be studied. Furthermore, an optimization method can be applied to the FPSE-PMLSM system based on the control method. Furthermore, based on the sensitivity analysis that was done, an optimization method can be developed to find the best parameters for the system.

The future of the current study will be the adaptation of the model to an experimental setup to the model and also to test and to improve the developed control method on it. This experimental setup should have the following characteristics. This experimental setup should have the following characteristics:

- A small size system that delivers around 1-2 kW of power will be needed.
- The heater of the Stirling engine should be a combustion chamber with controllable flow to control the temperature.
- Two position sensors should be placed. One for power piston and one for displacer inside the Stirling engine.
- Two pressure sensors should be placed. One for the high pressure space and one for the low pressure space inside the Stirling engine.
- Two temperature sensors should be placed. One for cooler and one for heater of the Stirling engine.

Such a system will provide the required information to develop an adapted control system.

6 REFERENCES

[1] G. Shu, Y. Liang, H. Wei, H. Tian, J. Zhao, L. Liu, A review of waste heat recovery on two-stroke IC engine aboard ships, Renew. Sustain. Energy Rev. 19 (2013) 385–401. https://doi.org/10.1016/J.RSER.2012.11.034.

[2] H. Chen, D.Y. Goswami, E.K. Stefanakos, A review of thermodynamic cycles and working fluids for the conversion of low-grade heat, Renew. Sustain. Energy Rev. 14 (2010) 3059–3067. https://doi.org/10.1016/J.RSER.2010.07.006.

[3] I. Urieli, D. Berchowitz, Stirling Cycle Engine Analysis, A. Hilger Bristol, 1984.

[4] S. Zhu, G. Yu, K. Liang, W. Dai, E. Luo, A review of Stirling-engine-based combined heat and power technology, Appl. Energy. 294 (2021) 116965. https://doi.org/10.1016/J.APENERGY.2021.116965.

[5] M.A. Al-Nimr, W.A. Al-Ammari, A novel hybrid and interactive solar system consists of Stirling engine/vacuum evaporator/thermoelectric cooler for electricity generation and water distillation, Renew. Energy. 153 (2020) 1053–1066. https://doi.org/https://doi.org/10.1016/j.renene.2020.02.072.

[6] A.C. Ferreira, J. Silva, S. Teixeira, J.C. Teixeira, S.A. Nebra, Assessment of the Stirling engine performance comparing two renewable energy sources: Solar energy and biomass, Renew. Energy. 154 (2020) 581–597. https://doi.org/10.1016/j.renene.2020.03.020.

[7] M. Rokni, Thermodynamic and thermoeconomic analysis of a system with biomass gasification, solid oxide fuel cell (SOFC) and Stirling engine, Energy. 76 (2014) 19–31. https://doi.org/10.1016/j.energy.2014.01.106.

[8] M. Majidniya, B. Remy, T. Boileau, M. Zandi, Free Piston Stirling Engine as a new heat recovery option for an Internal Reforming Solid Oxide Fuel Cell, Renew. Energy. 171 (2021) 1188–1201. https://doi.org/https://doi.org/10.1016/j.renene.2021.02.082.

[9] Ł. Bartela, J. Kotowicz, L. Remiorz, A. Skorek-Osikowska, K. Dubiel, Assessment of the economic appropriateness of the use of Stirling engine as additional part of a cogeneration system based on biomass gasification, Renew. Energy. 112 (2017) 425–443. https://doi.org/https://doi.org/10.1016/j.renene.2017.05.028.

[10] M. Marion, H. Louahlia, H. Gualous, Performances of a CHP Stirling system fuelled with glycerol, Renew. Energy. 86 (2016) 182–191. https://doi.org/10.1016/j.renene.2015.08.012.

[11] M. Majidniya, T. Boileau, B. Remy, M. Zandi, Performance simulation by a nonlinear thermodynamic model for a Free Piston Stirling Engine with a linear generator, Appl. Therm. Eng. 184 (2021) 116128. https://doi.org/10.1016/j.applthermaleng.2020.116128.

[12] M. Majidniya, T. Boileau, B. Remy, M. Zandi, Nonlinear modeling of a Free Piston Stirling Engine combined with a Permanent Magnet Linear Synchronous Machine, Appl. Therm. Eng. 165 (2020) 114544. https://doi.org/10.1016/j.applthermaleng.2019.114544.

[13] M. Majidniya, T. Boileau, B. Remy, M. Zandi, Performance simulation by a nonlinear thermodynamic model for a Free Piston Stirling Engine with a Linear Generator, Appl. Therm. Eng. (2020) 116128.

[14] J.E. Thorsen, J. Bovin, H. Carlsen, 3 kW Stirling engine for power and heat production, in: IECEC 96. Proc. 31st Intersoc. Energy Convers. Eng. Conf., 1996: pp. 1289–1294 vol.2. https://doi.org/10.1109/IECEC.1996.553902.

[15] M. Pålsson, H. Carlsen, Development of a wood powder fuelled 35 kW Stirling CHP unit, in: Proc. 11th ISEC (International Stirling Engine Conf., Department of Mechanical and Aeronautical Engineering, University of Rome …, 2003: pp. 221–230.

[16] H. Carlsen, N. Ammundsen, J. Traerup, 40 kW Stirling engine for solid fuel, in:

IECEC 96. Proc. 31st Intersoc. Energy Convers. Eng. Conf., IEEE, 1996: pp. 1301–1306.

[17] N. Jensen, J. Werling, H. Carlsen, U. Henriksen, CHP from updraft gasifier and Stirling engine, in: Proc. 12th Eur. Biomass Conf. ETA-Florence WIP-Munich, 2002: pp. 726–729.

[18] F. Biedermann, H. Carlsen, M. Schöch, I. Obernberger, Operating experiences with a small-scale CHP pilot plant based on a 35 kWel hermetic four cylinder Stirling engine for biomass fuels, in: Proc. 11th Int. Stirling Engine Conf., 2003: pp. 248–254.

[19] K. Sato, N. Ohiwa, A. Ishikawa, H. Shimojima, A. Nishiyama, Y. Moriya, Development of small-scale CHP plant with a wood powder-fueled Stirling engine, J. Power Energy Syst. 2 (2008) 1221–1231.

[20] M. Urciuolo, R. Chirone, F. Saverio Marra, R. Solimene, Power generation by Stirling engine during fluidized bed combustion of wood pellets, Combust. Sci. Technol. 191 (2019) 263–274.

[21] G. Angrisani, C. Roselli, M. Sasso, Distributed microtrigeneration systems, Prog. Energy Combust. Sci. 38 (2012) 502–521. https://doi.org/10.1016/j.pecs.2012.02.001.

[22] N. Carbon Trust, Micro-CHP accelerator: interim report, Carbon Trust London London, UK. (2007).

[23] A. Baumuller, F.X. Borras, P. Eskilson, M. Nilsson, A. Verner, Upgrading of Stirling Engine Dynamic Seals-Swedish Development since 40 years, in: 17th Int. Stirling Engine Conf.(ISEC), 2016.

[24] G. Magri, C. Di Perna, G. Serenelli, Analysis of electric and thermal seasonal performances of a residential microCHP unit, Appl. Therm. Eng. 36 (2012) 193–201. https://doi.org/10.1016/J.APPLTHERMALENG.2011.11.025.

[25] R. Van der WOude, E. ten Haaken, S. Zutt, B. Vriesema, G. Beckers, A.V. BV, Intermediate results of the Enatec micro cogeneration system field trials, in: Proc. Int. Stirling Forum, 2004.

[26] K. Mahkamov, Thermal-engine-based small and micro combined heat and power (CHP) systems for domestic applications: modelling micro-CHP deployment, in:

Small Micro Comb. Heat Power Syst., Elsevier, 2011: pp. 459–509.

[27] J. Harrison, E. On, Stirling engine systems for small and micro combined heat and power (CHP) applications, in: Small Micro Comb. Heat Power Syst., Elsevier, 2011: pp. 179–205.

[28] D.W. Kirkley, Determination of the optimum configuration for a Stirling engine, J. Mech. Eng. Sci. 4 (1962) 204–212.

[29] L.-L. Lemaire, Miniaturized Stirling engines for waste heat recovery, McGill University (Canada), 2012.

[30] C.S. Vineeth, Stirling Engines: A Beginners Guide, Vineeth CS, 2011.

[31] R.J. Meijer, The Philips hot-gas engine with rhombic drive mechanism, 1960.

[32] J.R. Senft, A mathematical model for Ringbom engine operation, (1985).

[33] S. Zare, A.R. Tavakolpour-Saleh, Frequency-based design of a free piston Stirling engine using genetic algorithm, Energy. 109 (2016) 466–480. https://doi.org/10.1016/j.energy.2016.04.119.

[34] K. Wang, S.R. Sanders, S. Dubey, F.H. Choo, F. Duan, Stirling cycle engines for recovering low and moderate temperature heat: A review, Renew. Sustain. Energy Rev. 62 (2016) 89–108. https://doi.org/10.1016/j.rser.2016.04.031.

[35] A.J. Organ, Stirling Cycle Engines: Inner Workings and Design, Stirling Cycle Engines Inn. Work. Des. 2 (2013) 1–268. https://doi.org/10.1002/9781118818428.

[36] G. Walker, Stirling engines, (1980).

[37] J. Subramanian, G. Heiskell, F. Mahmudzadeh, P. Famouri, Study of radial and axial magnets for linear alternator - Free piston engine system, in: 2017 North Am. Power Symp. NAPS 2017, IEEE, 2017: pp. 1–6. https://doi.org/10.1109/NAPS.2017.8107293.

[38] R. Redlich, A summary of twenty years experience with linear motors and alternators, Sunpower Inc. (1995) 1–9.

[39] E.Y. Loktionov, A.A. Martirosyan, M.D. Shcherbina, Solar powered free-piston stirling-Linear alternator module for the lunar base, in: 2016 2nd Int. Conf. Ind. Eng. Appl. Manuf. ICIEAM 2016 - Proc., IEEE, 2016: pp. 1–6.

https://doi.org/10.1109/ICIEAM.2016.7910983.

[40] J. Boucher, F. Lanzetta, P. Nika, Optimization of a dual free piston Stirling engine, Appl. Therm. Eng. 27 (2007) 802–811. https://doi.org/10.1016/j.applthermaleng.2006.10.021.

[41] H. Karabulut, M. Okur, A.O. Ozdemir, Performance prediction of a Martini type of Stirling engine, Energy Convers. Manag. 179 (2019) 1–12. https://doi.org/10.1016/j.enconman.2018.10.059.

[42] A. Souissi, I. Abdennadher, A. Masmoudi, Linear synchronous machines: application to sustainable energy and mobility, Springer, 2019.

[43] C.K. Alexander, M.N.O. Sadiku, e-Text Fundamentals of Electric Circuits, McGraw-Hill Higher Education, 2001. https://books.google.fr/books?id=SBdigDfQB5cC.

[44] T.T. Dang, M. Ruellan, L. Prévond, H. Ben Ahmed, B. Multon, Sizing Optimization of Tubular Linear Induction Generator and Its Possible Application in High Acceleration Free-Piston Stirling Microcogeneration, IEEE Trans. Ind. Appl. 51 (2015) 3716–3733. https://doi.org/10.1109/TIA.2015.2427284.

[45] M.H. Rashid, Power electronics handbook, Butterworth-Heinemann, 2017.

[46] S.-H. Kim, Electric motor control: DC, AC, and BLDC motors, Elsevier, 2017.

[47] R. Luis, J.C. Quadrado, On PM tubular linear synchronous motor modelling., WSEAS Trans. Circuits Syst. 3 (2004) 1852–1857.

[48] J.M. Kim, J.Y. Choi, K.S. Lee, S.H. Lee, Design and analysis of linear oscillatory single-phase permanent magnet generator for free-piston stirling engine systems, AIP Adv. 7 (2017) 56667. https://doi.org/10.1063/1.4977888.

[49] P. Zheng, B. Yu, S. Zhu, Q. Gong, J. Liu, Research on control strategy of free-piston stirling-engine linear-generator system, in: Electr. Mach. Syst. (ICEMS), 2014 17th Int. Conf., IEEE, 2014: pp. 2300–2304.

[50] T.T. Dang, P. François, L. Prévond, H. Ben Ahmed, Theoretical and experimental results of tubular linear induction generator for stirling cogenerator system, in: 19th Int. Conf. Electr. Mach. ICEM 2010, IEEE, 2010: pp. 1–7. https://doi.org/10.1109/ICELMACH.2010.5607832.

[51] T.T. Dang, M. Ruellan, H. Ben Ahmed, L. Prevond, B. Multon, Sizing optimization of tubular linear induction generator for a new stirling micro-cogenerator system, in: 2014 Int. Symp. Power Electron. Electr. Drives, Autom. Motion, SPEEDAM 2014, IEEE, 2014: pp. 1362–1367. https://doi.org/10.1109/SPEEDAM.2014.6871993.

[52] W.P. Hew, J. Jamaludin, M. Tadjuddin, K.M. Nor, Fabrication and testing of linear electric generator for use with a free-piston engine, in: Natl. Power Eng. Conf. PECon 2003 - Proc., IEEE, 2003: pp. 277–282. https://doi.org/10.1109/PECON.2003.1437457.

[53] W. Ye, X. Wang, Y. Liu, J. Chen, Analysis and prediction of the performance of free-piston Stirling engine using response surface methodology and artificial neural network, Appl. Therm. Eng. 188 (2021) 116557. https://doi.org/10.1016/J.APPLTHERMALENG.2021.116557.

[54] W. Ye, X. Wang, Y. Liu, Application of artificial neural network for predicting the dynamic performance of a free piston Stirling engine, Energy. 194 (2020) 116912. https://doi.org/10.1016/j.energy.2020.116912.

[55] S. Zare, A.R. Tavakolpour-Saleh, M.H. Sangdani, Investigating limit cycle in a free piston Stirling engine using describing function technique and genetic algorithm, Energy Convers. Manag. 210 (2020) 112706. https://doi.org/10.1016/j.enconman.2020.112706.

[56] P. Zheng, C. Tong, J. Bai, B. Yu, Y. Sui, W. Shi, Electromagnetic design and control strategy of an axially magnetized permanent-magnet linear alternator for free-piston stirling engines, IEEE Trans. Ind. Appl. 48 (2012) 2230–2239. https://doi.org/10.1109/TIA.2012.2226858.

[57] S. Zhu, G. Yu, O. Jongmin, T. Xu, Z. Wu, W. Dai, E. Luo, Modeling and experimental investigation of a free-piston Stirling engine-based micro-combined heat and power system, Appl. Energy. 226 (2018) 522–533. https://doi.org/10.1016/j.apenergy.2018.05.122.

[58] M. Majidniya, T. Boileau, R. Benjamin, M. Zandi, Thermoelectric modeling of a Free Piston Stirling Engine (FPSE) combined with a Permanent Magnet Linear Synchronous Machine (PMLSM) with its control system, in: Int. Conf. Renew. Energy Distrib. Gener. Iran, 2019.

[59] M. Majidniya, T. Boileau, R. Benjamin, M. Zandi, Modélisation thermo-électrique d'un moteur Stirling à piston libre et d'une machine synchrone linéaire à aimant permanent avec sa commande, in: Congrès Annu. La Société Française Therm., 2019.

[60] J. Schreiber, TESTING AND PERFORMANCE CHARACTERISTICS OF A 1-kW FREE PISTON STIRLING ENGINE., NASA Tech. Memo. (1983).

[61] W.R. Martini, Stirling engine design manual. US Department of Energy, DOE/NASA/3152-78/1, NASA, CR-13518, 1978.

[62] D.P. Sekulic, Compact heat exchangers, Handb. Therm. Sci. Eng. (2018) 1501–1520. https://doi.org/10.1007/978-3-319-26695-4_36.

[63] H. Petersen, The properties of helium: density, specific heats, viscosity, and thermal conductivity at pressures from 1 to 100 bar and from room temperature to about 1800 K, Jul. Gjellerup Copenhagen, 1970.

[64] S. Anvoner, Solution of problems in mechanics of machines, Pitman Paperbacks, 1970.

[65] F.A. Creswick, Thermal Design of Stirling-Cycle Machines, SAE Technical Paper, 1965.

[66] J. Sauer, H.D. Kuehl, Theoretically and experimentally founded simulation of the appendix gap in regenerative machines, Appl. Therm. Eng. 166 (2020) 114530. https://doi.org/10.1016/j.applthermaleng.2019.114530.

[67] R.W. Redlich, D.M. Berchowitz, Linear Dynamics of Free-Piston Stirling Engines., Proc. Inst. Mech. Eng. Part A. Power Process Eng. 199 (1985) 203–213. https://doi.org/10.1243/PIME_PROC_1985_199_025_02.

[68] G. Walker, J.R. Senft, Free-piston Stirling engines, in: Free Pist. Stirling Engines, Springer, 1985: pp. 23–99.

[69] M.T. Mabrouk, A. Kheiri, M. Feidt, Displacer gap losses in beta and gamma Stirling engines, Energy. 72 (2014) 135–144. https://doi.org/10.1016/j.energy.2014.05.017.

[70] M.T. Mabrouk, A. Kheiri, M. Feidt, Effect of leakage losses on the performance of a β type Stirling engine, Energy. 88 (2015) 111–117. https://doi.org/10.1016/j.energy.2015.05.075.

[71] J.P. Ward, Modern mathematics for engineers and scientists, CRC Press, 2003. https://doi.org/10.1093/teamat/22.1.37.

[72] M.N.L. Narasimhan, Pulsating magnetohydrodynamic flow superposed on the steady laminar motion of an incompressible viscous fluid in an annular channel, J. Phys. Soc. Japan. 19 (1964) 117–120. https://doi.org/10.1143/JPSJ.19.117.

[73] C.K. Batchelor, G.K. Batchelor, An Introduction to Fluid Dynamics, Cambridge university press, 1959. https://doi.org/10.1063/1.3060769.

[74] J. Zheng, J. Chen, P. Zheng, H. Wu, C. Tong, Research on control strategy of free-piston Stirling power generating system, Energies. 10 (2017) 1609.

[75] G. Brus, P.F. Raczkowski, M. Kishimoto, H. Iwai, J.S. Szmyd, A microstructure-oriented mathematical model of a direct internal reforming solid oxide fuel cell, Energy Convers. Manag. 213 (2020) 112826. https://doi.org/10.1016/j.enconman.2020.112826.

[76] P. Costamagna, K. Honegger, Modeling of Solid Oxide Heat Exchanger Integrated Stacks and Simulation at High Fuel Utilization, J. Electrochem. Soc. 145 (1998) 3995–4007. https://doi.org/10.1149/1.1838904.

[77] C.O. Colpan, I. Dincer, F. Hamdullahpur, Thermodynamic modeling of direct internal reforming solid oxide fuel cells operating with syngas, Int. J. Hydrogen Energy. 32 (2007) 787–795. https://doi.org/10.1016/j.ijhydene.2006.10.059.

[78] S. Motahar, A.A. Alemrajabi, Exergy based performance analysis of a solid oxide fuel cell and steam injected gas turbine hybrid power system, Int. J. Hydrogen Energy. 34 (2009) 2396–2407. https://doi.org/10.1016/j.ijhydene.2008.12.065.

[79] A. Arsalis, M.R. Von Spakovsky, F. Calise, Thermoeconomic modeling and parametric study of hybrid solid oxide fuel cell-gas turbine-steam turbine power plants ranging from 1.5 MWe to 10 MWe, J. Fuel Cell Sci. Technol. 6 (2009) 0110151–01101512. https://doi.org/10.1115/1.2971127.

[80] F. Calise, M. Dentice d'Accadia, A. Palombo, L. Vanoli, Simulation and exergy analysis of a hybrid Solid Oxide Fuel Cell (SOFC)-Gas Turbine System, Energy. 31 (2006) 3278–3299. https://doi.org/10.1016/j.energy.2006.03.006.

[81] S.H. Chan, K.A. Khor, Z.T. Xia, Complete polarization model of a solid oxide fuel

cell and its sensitivity to the change of cell component thickness, J. Power Sources. 93 (2001) 130–140. https://doi.org/10.1016/S0378-7753(00)00556-5.

[82] J. Pirkandi, M. Ghassemi, M.H. Hamedi, R. Mohammadi, Electrochemical and thermodynamic modeling of a CHP system using tubular solid oxide fuel cell (SOFC-CHP), J. Clean. Prod. 29–30 (2012) 151–162. https://doi.org/10.1016/j.jclepro.2012.01.038.

[83] B.H. Gebreslassie, M. Medrano, D. Boer, Exergy analysis of multi-effect water-LiBr absorption systems: From half to triple effect, Renew. Energy. 35 (2010) 1773–1782. https://doi.org/10.1016/j.renene.2010.01.009.

[84] L.A. McNeely, Thermodynamic Properties of Aqueous Solutions of Lithium Bromide., ASHRAE Trans. 85 (1979) 413–434.

[85] M. Holmgren, X Steam, Thermodynamic properties of water and steam, MathWorks, Natick, MA, Accessed Dec. 2 (2007) 2014.

[86] M. Majidniya, K. Gharali, K. Raahemifar, A Comparison of Off-Grid-Pumped Hydro Storage and Grid-Tied Options for an IRSOFC-HAWT Power Generator, Int. J. Rotating Mach. 2017 (2017). https://doi.org/10.1155/2017/4384187.

7 Appendices

APPENDIX 1: THESIS SUMMARY IN FRENCH

À ce jour, les réseaux énergétiques les plus courants, par exemple le réseau énergétique qui existe en France, sont basés sur une structure centralisée fournisseur-consommateur. Dans cette structure, l'énergie est toujours produite par un fournisseur centralisé et est acheminée vers les consommateurs. Aujourd'hui, avec l'aide des énergies renouvelables, les consommateurs peuvent produire localement leur énergie. Cette production d'énergie peut perturber le fonctionnement du réseau. Pour résoudre ce problème, le projet d'Internet Of Energy (IOE) est introduit à l'UL-ENSEM (Université de Lorraine-L'École Nationale Supérieure d'Électricité et de Mécanique) couplé à la chaire scientifique TIE (Territoire Industrie Energie) (LEMTA-CNRS). L'IOE passe des réseaux conventionnels centralisés/unidirectionnels aux réseaux décentralisés/bidirectionnels. La Figure 7.1 présente le schéma de l'IOE et sa comparaison avec les systèmes énergétiques courants.

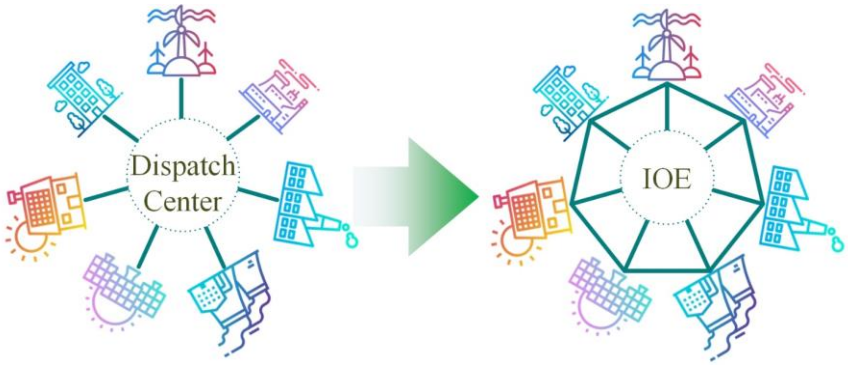

Figure 7.1: Schéma de l'IOE et du réseau énergétique commun

Grâce à l'IOE, les connexions entre les consommateurs avec un fournisseur et aussi avec d'autres consommateurs seront dynamiques et multidirectionnelles. Cela signifie que, par une stratégie de contrôle efficace, un consommateur peut, par le biais de l'IOE, alimenter un autre consommateur pour satisfaire ses demandes sans perturber la fonction du réseau.

Le concept IOE est un contenu large/multidisciplinaire qui doit être divisé en différentes sections. Ces sections peuvent être identifiées comme étant la capture de l'énergie, la conversion de l'énergie, la distribution/transport de l'énergie, le stockage de l'énergie et les systèmes de contrôle. Chaque section peut également être divisée en sous-sections ; par exemple, la section sur la conversion de l'énergie peut être divisée en sous-sections sur la modélisation et l'optimisation des systèmes. La section sur le contrôle peut également être divisée en deux parties : le contrôle de chaque système et le contrôle de l'intégration des

systèmes/réseaux. Un autre point est que pour chaque section, différents systèmes/méthodes peuvent être appliqués. De même, différentes méthodes de contrôle et d'optimisation peuvent être utilisées. Les systèmes définis dans le projet IOE et devant être contrôlés sont présentés dans la Figure 7.2.

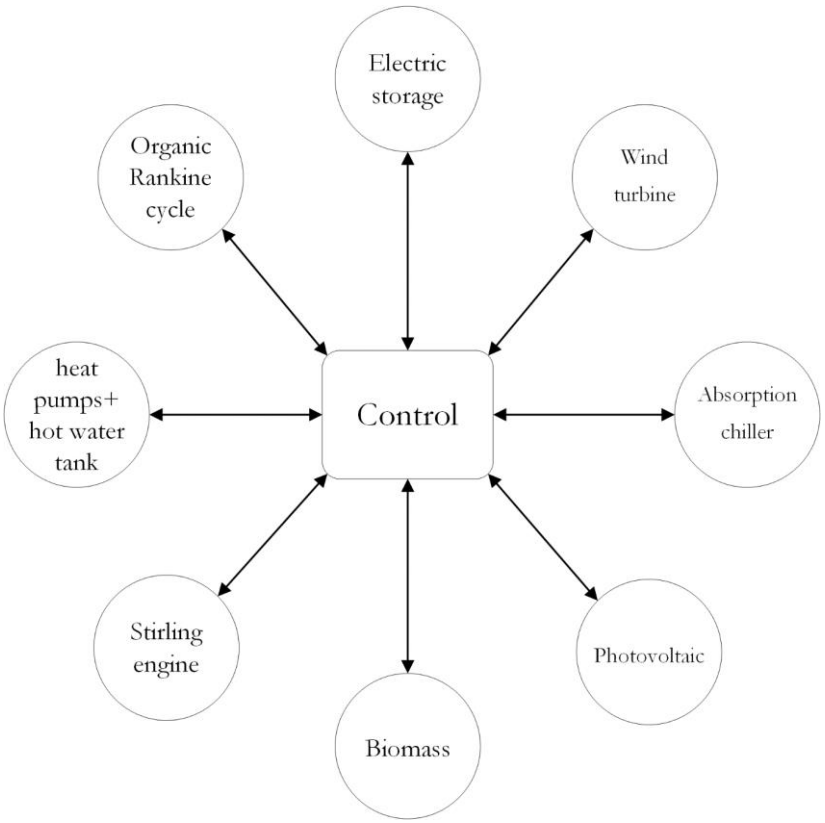

Figure 7.2: Schéma de contrôle de l'IOE

Un point crucial à noter est que les conditions de fonctionnement des systèmes sont dynamiques, les modèles doivent donc être des modèles dynamiques détaillés pour être capables de prédire le comportement réaliste des systèmes/réseaux.

Dans la présente thèse, en tant que partie du projet IOE, l'étude a été faite en trois sections : section de conversion d'énergie, section de contrôle, et section d'optimisation.

Du point de vue de la conversion d'énergie, différents systèmes peuvent être étudiés, notamment le moteur Stirling et le cycle organique de Rankine (ORC). L'ORC est un cycle en boucle fermée qui, comparé à la turbine à vapeur conventionnelle du cycle de Rankine, présente les avantages suivants [1,2] :

- Compatible avec des sources de chaleur à plus basse température.

- Durée de vie plus longue.
- Moins de maintenance est nécessaire.
- Des échangeurs de chaleur plus petits et moins chers sont nécessaires, ce qui donne un système plus petit.
- Le moteur Stirling est également un système en boucle fermée qui présente les avantages suivants :
- Fonctionnement silencieux et pratiquement sans vibrations [3].
- Pollution minimale. Grâce à la combustion externe, le combustible peut être brûlé de manière plus suffisante [4].
- Rendement maximal atteignable par rapport aux moteurs thermiques fonctionnant entre la même différence de température [3].
- Comme il s'agit d'un système à combustion externe, la source d'énergie peut être de n'importe quelle forme, pourvu qu'elle soit disponible à une température suffisamment élevée. Les moteurs Stirling peuvent fonctionner avec de l'énergie solaire [5,6], des piles à combustible à haute température [7,8], des systèmes de gazéification [9], des systèmes de combustion [10], et aussi avec de nombreuses industries qui traitent directement ou indirectement de l'énergie thermique comme les industries sidérurgiques ou chimiques [11].
- Haute fiabilité [3].
- Simplicité mécanique [3].
- La production de travail spécifique la plus élevée de tous les cycles régénératifs fermés [3].

Puisque, en comparaison avec l'ORC, le Stirling a un rendement potentiel plus élevé, un rendement spécifique plus élevé, une plus grande fiabilité, et l'avantage de la simplicité mécanique [3], la présente étude se concentrera sur ce système et son alternateur adapté.

Du point de vue du contrôle, un alternateur avec un système de contrôle dédié sera introduit pour le moteur Stirling. De plus, du point de vue de l'optimisation, les performances du système en tenant compte des paramètres de contrôle seront optimisées.

Dans le chapitre 1, les systèmes, qui sont le moteur Stirling à piston libre (FPSE) et la machine synchrone linéaire à aimant permanent (PMLSM), ont été sélectionnés. Après avoir

présenté le modèle électrodynamique du système PMLSM, le système couplé FPSE-PMLSM a été introduit.

Dans le chapitre 2, l'accent a été mis sur la modélisation du FPSE. Tout d'abord, une analyse dynamique générale du système a été présentée. Ensuite, un ensemble d'équations linéarisées a été résolu comme cela a déjà été discuté dans la littérature. En outre, les équations non linéaires ont été utilisées directement comme une nouvelle approche dans la présente étude. La comparaison des résultats de ces modèles a montré que le modèle linéarisé n'est pas adapté à la présente étude et ne peut pas identifier le comportement réaliste de l'EPSF. Après avoir sélectionné le nouveau modèle non linéaire proposé comme modèle dynamique de base, le modèle thermique du système est développé sur cette base. Ensuite, le modèle thermodynamique du FPSE a été validé avec les résultats expérimentaux existants. Enfin, l'effet de la perte par pompage d'enthalpie sur le système a été étudié en utilisant deux scénarios. Le premier scénario, déjà expliqué dans la littérature, était basé sur le modèle découplé entre la perte et le modèle thermodynamique. Le deuxième scénario, qui est un nouveau scénario introduit dans la présente étude, était basé sur le modèle couplé entre la perte et la thermodynamique. La comparaison des résultats a montré que le second modèle est plus adapté à la présente étude et que le premier ne présente pas de résultats logiques.

Dans le chapitre 3, le contrôle du système combiné FPSE-PMLSM a été introduit. Deux contrôleurs Proportionnels-Intégraux (PI) pour les courants et un contrôleur Proportionnel-Résonance (PR) pour la vitesse du piston moteur/moteur ont été utilisés pour contrôler le système en utilisant trois capteurs : deux capteurs de courant et un capteur de position. Pour la première fois dans cette étude, un contrôleur PR est utilisé pour un tel système. Ensuite, deux méthodes de contrôle différentes ont été introduites pour identifier la vitesse de référence et une analyse des performances du système FPSE-PMLSM a été réalisée sur cette base. La première méthode de contrôle est basée sur l'identification directe de l'amplitude et de la fréquence de la vitesse de référence. Les gains PR de cette méthode de contrôle ont été calculés sur la base de l'analyse de stabilité du système. La deuxième méthode est basée sur l'auto-oscillation du système et l'identification de la vitesse de référence en fonction de la réponse du système. Les analyses de performance ont montré les points optimaux qui étaient proches les uns des autres.

Dans le chapitre 4, qui est le dernier chapitre, présente l'application du système FPSE-PMLSM. Tout d'abord, une analyse de sensibilité a été effectuée pour voir l'effet des

différents paramètres sur le système. Cela permet de voir comment chaque paramètre affecte la sortie du système et si ce modèle va être adapté à une configuration expérimentale, quels paramètres doivent être mesurés plus précisément. De plus, pour voir comment ce système peut être utilisé comme une option de récupération de la chaleur perdue couplée à d'autres sources d'énergie, il a été utilisé à côté d'une tri-génération avec une pile à combustible à oxyde solide (SOFC) comme source d'énergie, un refroidisseur à absorption à double effet (DEACH) pour la production de froid, et un échangeur de chaleur pour répondre aux besoins de chauffage. Les résultats ont montré que le système FPES-PMLSM améliore les performances du système.

Dans la continuité de cette thèse, les améliorations suivantes sont proposées :

Pour la modélisation du PMLSM, fournir un modèle plus précis peut affecter les résultats et présenter plus d'informations concernant le système proposé. Pour le FPSE, plus de pertes peuvent être étudiées et leur effet sur le système FPSE peut être analysé. Cela permettra d'identifier les pertes les plus importantes et d'essayer de trouver une solution pour les minimiser. En ce qui concerne le contrôle du système, l'analyse de la stabilité de la deuxième méthode de contrôle qui était basée sur le système auto-oscillant doit être étudiée. En outre, une méthode d'optimisation peut être appliquée au système FPSE-PMLSM sur la base de la méthode de contrôle. En outre, sur la base de l'analyse de sensibilité qui a été faite, une méthode d'optimisation peut être développée pour trouver les meilleurs paramètres pour le système.

En général, la principale amélioration de l'étude actuelle sera de fournir un dispositif expérimental pour adapter le modèle et tester la méthode de contrôle développée. Ce dispositif expérimental devrait avoir les caractéristiques suivantes :

- Un système de petite taille qui fournit environ 1-2 kW de puissance sera nécessaire.
- Le chauffage du moteur Stirling devrait être une chambre de combustion avec un flux contrôlable pour contrôler la température.
- Deux capteurs de position doivent être placés. Un pour le piston moteur et un pour le plongeur à l'intérieur du moteur Stirling.
- Deux capteurs de pression doivent être placés. Un pour l'espace haute pression et un pour l'espace basse pression à l'intérieur du moteur Stirling.

- Deux capteurs de température doivent être placés. Un pour le refroidisseur et un pour le réchauffeur du moteur Stirling.

Un tel système fournira les informations nécessaires pour développer un système de contrôle adapté.

APPENDIX 2: MORE RESULTS OF THE FIRST CONTROL METHOD PERFORMANCE ANALYSIS

Here, more results of the first control method concerning the electromagnetic and piston forces and also electromagnetic force and piston velocity. These results are presented at steady state and for three reference velocity frequencies (25 Hz, 28 Hz, and 35 Hz) at constant reference velocity amplitude of 1 m/s, and for three reference velocity amplitudes (0.15 m/s, 0.55 m/s, and 1.05 m/s) at constant reference velocity frequency of 25 Hz.

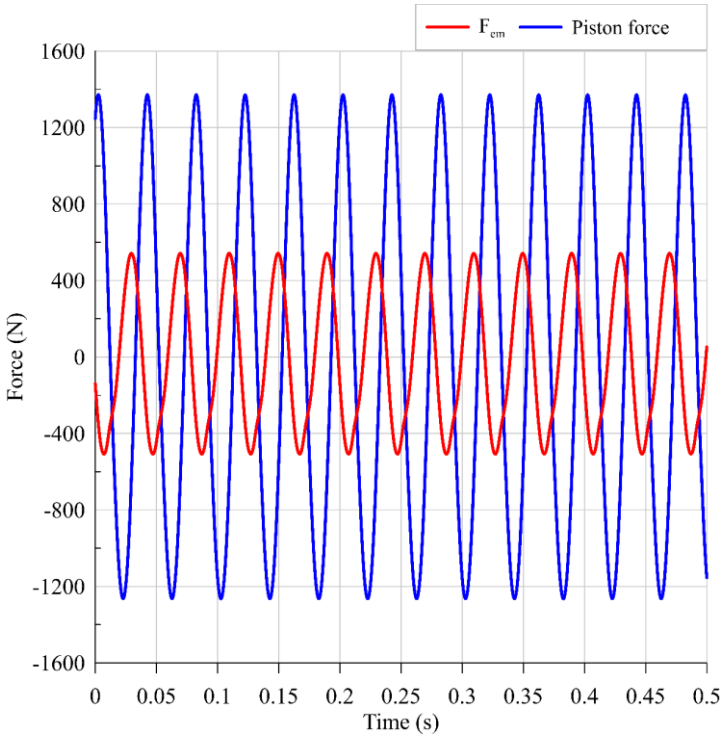

Figure 7.3: Variation of the electromagnetic and piston forces in steady state condition at reference velocity frequency of 25 Hz and amplitude of 1 m/s

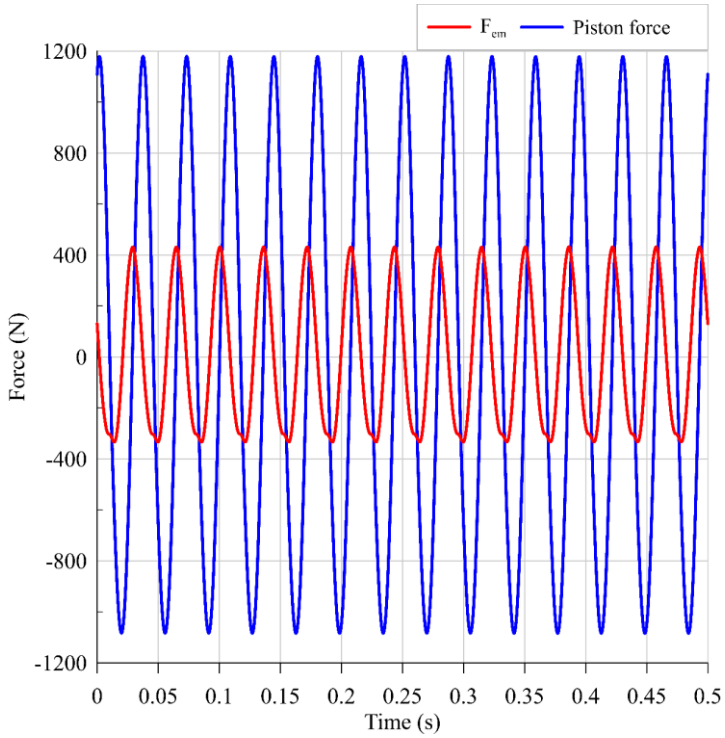

Figure 7.4: Variation of the electromagnetic and piston forces in steady state condition at reference velocity frequency of 28 Hz and amplitude of 1 m/s

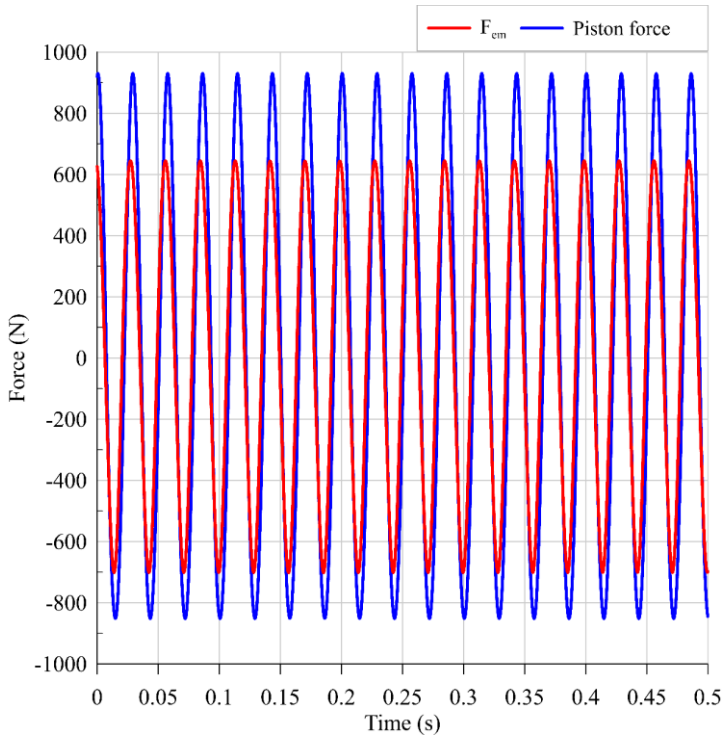

Figure 7.5: Variation of the electromagnetic and piston forces in steady state condition at reference velocity frequency of 35 Hz and amplitude of 1 m/s

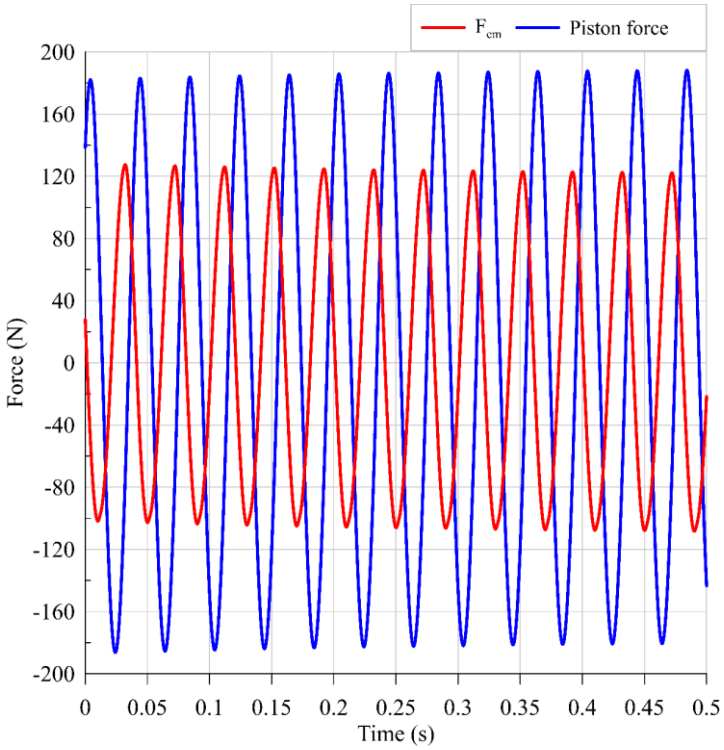

Figure 7.6: Variation of the electromagnetic and piston forces in steady state condition at reference velocity frequency of 25 Hz and amplitude of 0.15 m/s

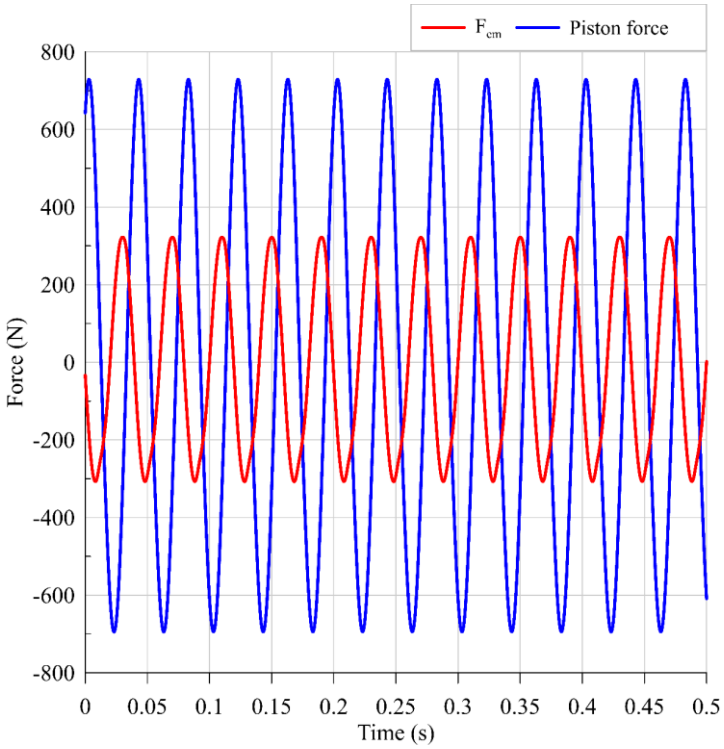

Figure 7.7: Variation of the electromagnetic and piston forces in steady state condition at reference velocity frequency of 25 Hz and amplitude of 0.55 m/s

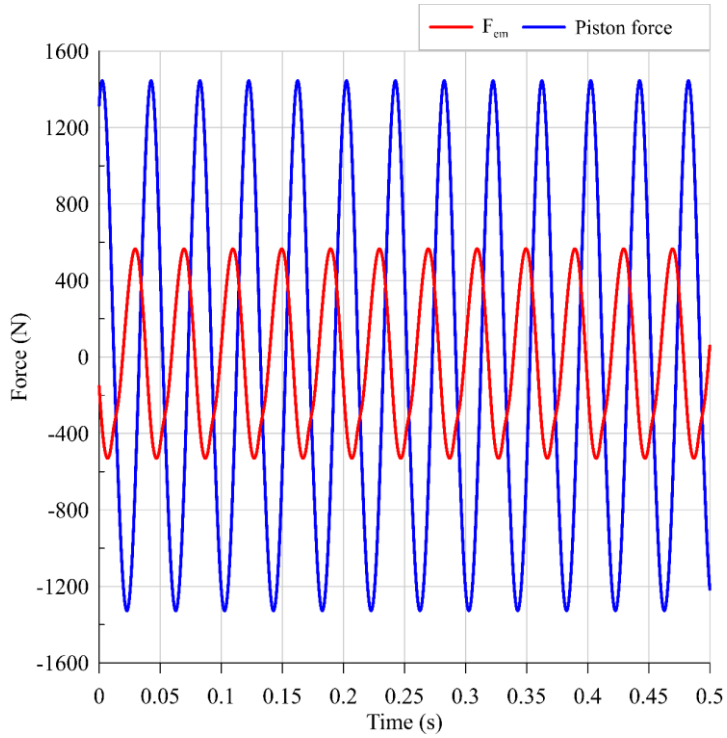

Figure 7.8: Variation of the electromagnetic and piston forces in steady state condition at reference velocity frequency of 25 Hz and amplitude of 1.05 m/s

As can be seen in Figure 7.3 - Figure 7.8, the phase shift between forces (electromagnetic force and piston force) with reference velocity frequency variation is varying while with reference velocity amplitude variation the phase shift is almost constant. Furthermore, Furthermore, it can be seen that the system behavior is almost sinusoidal at 25 Hz which is less the case at 28 Hz, it shows non-linear behavior of the system.

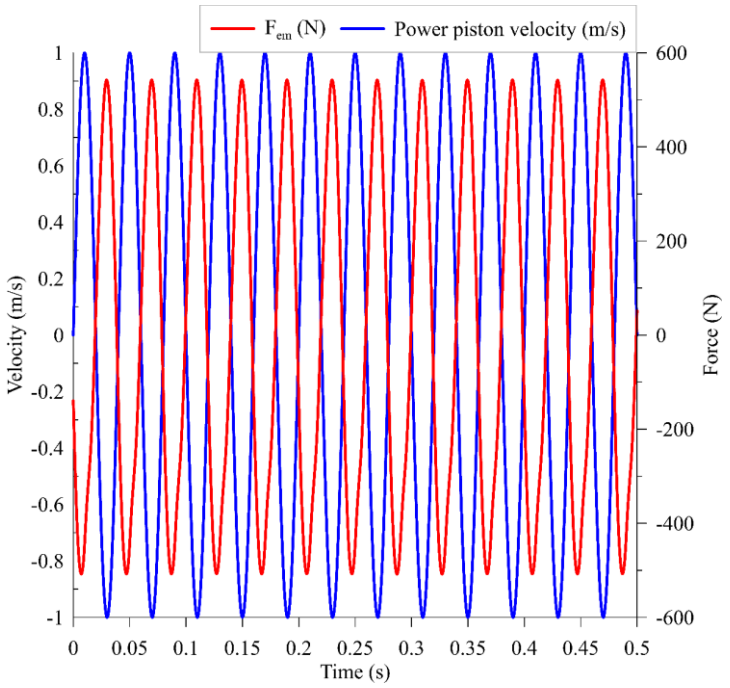

Figure 7.9: Variation of the electromagnetic force and piston velocity in steady state condition at reference velocity frequency of 25 Hz and amplitude of 1 m/s

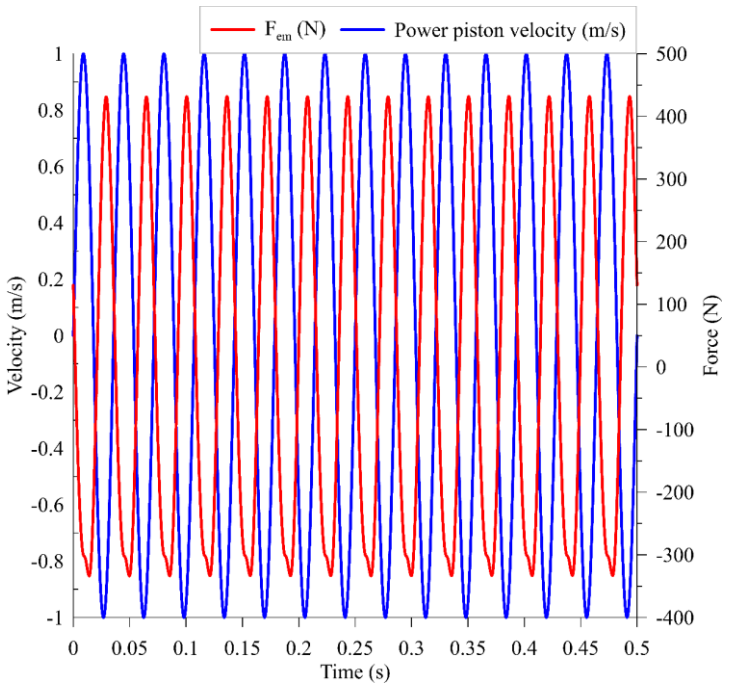

Figure 7.10: Variation of the electromagnetic force and piston velocity in steady state condition at reference velocity frequency of 28 Hz and amplitude of 1 m/s

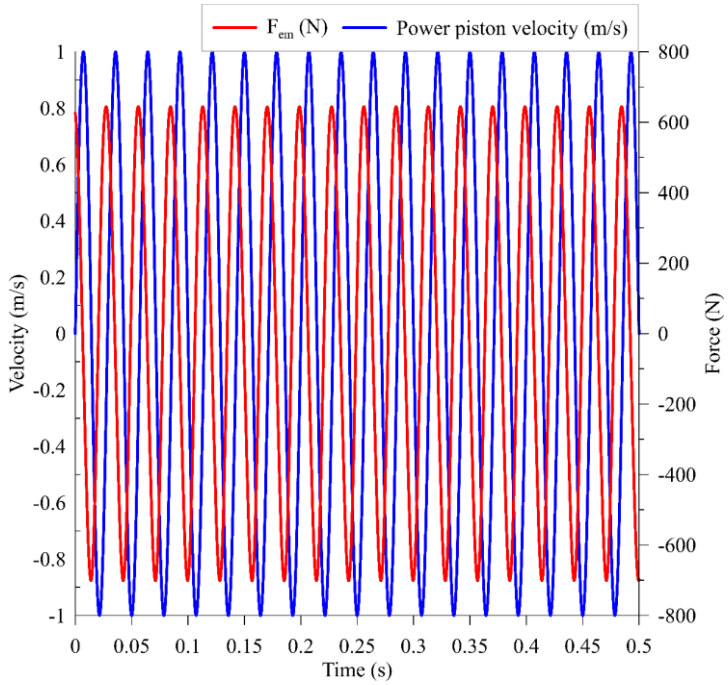

Figure 7.11: Variation of the electromagnetic force and piston velocity in steady state condition at reference velocity frequency of 35 Hz and amplitude of 1 m/s

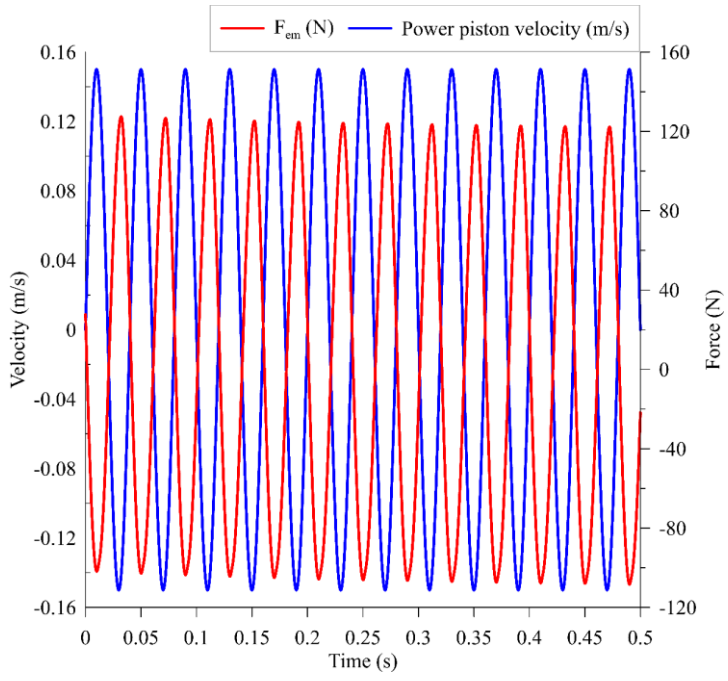

Figure 7.12: Variation of the electromagnetic force and piston velocity in steady state condition at reference velocity frequency of 25 Hz and amplitude of 0.15 m/s

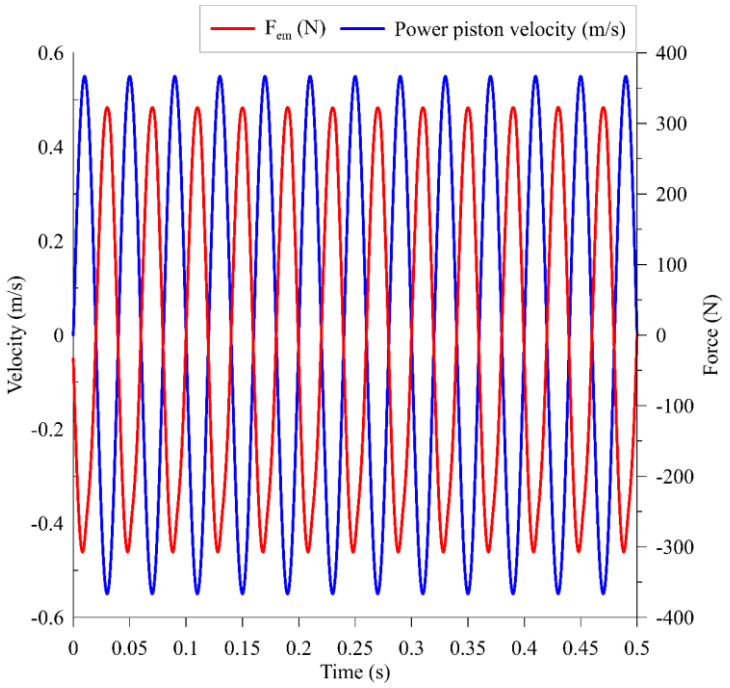

Figure 7.13: Variation of the electromagnetic force and piston velocity in steady state condition at reference velocity frequency of 25 Hz and amplitude of 0.55 m/s

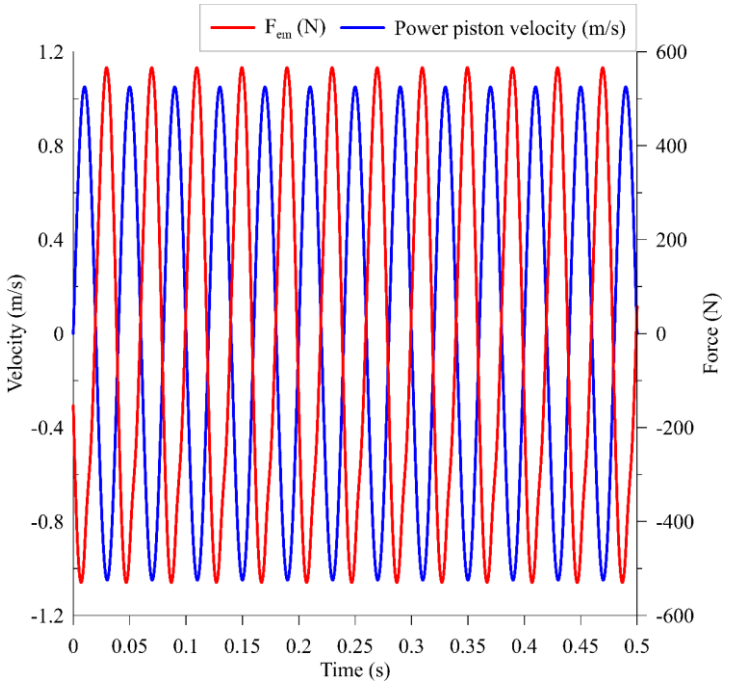

Figure 7.14: Variation of the electromagnetic force and piston velocity in steady state condition at reference velocity frequency of 25 Hz and amplitude of 1.05 m/s

As can be seen in Figure 7.9 - Figure 7.14, the phase shift variation between power piston velocity and electromagnetic force is more sensitive to the reference velocity frequency variation that the reference velocity amplitude variation.

APPENDIX 3: LIST OF THE PUBLICATIONS

Book Chapter

Majidniya, M., Remy, B., & Boileau, T. (2022). Introducing a new system for energy recovery of high and mid-temperature renewable energy sources: Free Piston Stirling Engine Combined with a Permanent Magnet Linear Synchronous Machine. In M. Amidpour, M. Ebadollahi, F. Jabari, M.-R. Kolahi, H. Ghaebi, (Eds.), Synergy Development in Renewables Assisted Multi-carrier Systems, Springer International Publishing.

Journal Papers

Majidniya, M., Remy, B., Boileau, T., & Zandi, M. (2021). Free Piston Stirling Engine as a new heat recovery option for an Internal Reforming Solid Oxide Fuel Cell. Renewable Energy, 171, 1188-1201.

Majidniya, M., Boileau, T., Remy, B., & Zandi, M. (2020). Performance simulation by a nonlinear thermodynamic model for a Free Piston Stirling Engine with a linear generator. Applied Thermal Engineering, 116128.

Majidniya, M., Boileau, T., Remy, B., & Zandi, M. (2020). Nonlinear modeling of a Free Piston Stirling Engine combined with a Permanent Magnet Linear Synchronous Machine. Applied Thermal Engineering, 165, 114544

Conference Papers

Majidniya, M., Remy, B., Boileau, T., & Zandi, M. (2021). FREE PISTON STIRLING ENGINE (FPSE): A GENERAL SURVEY FROM MODELLING TO APPLICATION. International Conference on MATERIALS & ENERGY (ICOME21), Virtual Conference, France.

Majidniya, M., Remy, B., Boileau, T., & Zandi, M. (2021). Thermodynamic Modeling And Controlling Of A Combined Free Piston Stirling Engine System (FPSE) With A Permanent Magnet Linear Synchronous Machine (PMLSM). 8th European Thermal Sciences Conference (EUROTHERM2021), Virtual Conference, France.

Majidniya, M., Boileau, T., Remy, B., & Zandi, M. (2019). Modélisation thermo-électrique d'un moteur Stirling à piston libre et d'une machine synchrone linéaire à aimant permanent avec sa commande. 27ième Congrès français de thermique, France, Nantes. (In French)

Majidniya, M., Boileau, T., Remy, B., & Zandi, M. (2019). Thermoelectric modelling of a Free Piston Stirling Engine (FPSE) Combined with a Permanent Magnet Linear Synchronous Machine (PMLSM) with its control system. International Conference on Renewable Energy & Distributed Generation of Iran (ICREDG), Tehran, Iran. (In Persian).

Abstract:

Energy Storage & Conversion: Waste heat recovery in microgrids by a Free Piston Stirling Engine

In this study, a combined system of an FPSE and a PMLSM is investigated. First, the linear and nonlinear models of the FPSE are developed, and then the most suitable model for the study is chosen. Then, the FPSE model is validated with available experimental results. After validating the model, two scenarios (an existed decoupled one and a newly introduced coupled one) are applied to study the enthalpy pumping loss on this system, and then the best one is presented. After that, the FPSE system is coupled with the presented PMLSM model. To combine these systems, their equations are combined, solved, and the coupled system is controlled in MATLAB Simulink®. Controlling such a system makes it possible to avoid conditions leading to FPSE instability. Moreover, it is feasible to control the system in transient operating modes to get the best performance. After combining FPSE with PMLSM, two performance analysis method based on the control system are introduced, and the results of the two methods are compared. An application of such a system is presented, it is used as a waste heat recovery system in a Solid Oxide Fuel Cell (SOFC) based tri-generation system. Finally, a study of the sensitivity to the parameters of such a system is performed

Résumé:

Stockage d'Energie et Conversion : Récupération de la chaleur fatale dans les Microgrids par un Moteur Stirling à Piston Libre

Dans cette étude, un système combiné d'un moteur Striling à piston libre (MSPL) et d'une Machine linéaire synchrone à aimants permanents (MLSAP) est étudié. Tout d'abord, les modèles linéaires et non-linéaires de MSPL sont développés, puis le modèle le plus adapté à l'étude est choisi. Ensuite, le modèle MSPL est validé avec les résultats expérimentaux disponibles. Après validation du modèle, deux scénarios (un premier « découplé » existant dans la littérature et un cas « couplé » nouvellement introduit) sont envisagés pour étudier la perte par pompage d'enthalpie sur ce système et puis le meilleur cas est présenté. Par la suite, le système MSPL est couplé avec le modèle de MLSAP présenté. Pour combiner ces systèmes, leurs équations sont combinées, résolues, et le système couplé est contrôlé dans MATLAB Simulink®. Le contrôle d'un tel système permet d'éviter les conditions conduisant à l'instabilité du MSPL. De plus, il est possible de contrôler le système dans des modes de fonctionnement transitoires pour obtenir de meilleures performances. Après avoir combiné le MSPL avec MLSAP, deux méthodes d'analyse des performances basées sur le système de contrôle sont proposées, les résultats des deux méthodes sont comparés. Ensuite un exemple d'application d'un tel système est présenté, il est utilisé comme système de récupération de chaleur dans un système de tri-génération basé sur une pile à combustible à oxyde solide (PCOS). Finalement, une étude de la sensibilité aux paramètres d'un tel système est réalisée.